Nuclei of Nearby Active Galaxies:

NIR and Sub-mm Views

and

Finalizing the LINC-NIRVANA Fringe and Flexure Tracking System:

Flexure and Temperature Behavior

INAUGURAL - DISSERTATION

zur

Erlangung des Doktorgrades

der Mathematisch-Naturwissenschaftlichen Fakultät

der Universität zu Köln

vorgelegt von

Semir Smajić

aus Bijeljina, Bosnien und Herzegowina

Köln 2015

Abstract

The work presented in my thesis addresses the two cornerstones of modern astronomy: Observation and Instrumentation.

Part I deals with the observation of two nearby active galaxies, the Seyfert 2 galaxy NGC 1433 and the Seyfert 1 galaxy NGC 1566, both at a distance of ~ 10 Mpc, which are part of the Nuclei of Galaxies (NUGA) sample. It is well established that every galaxy harbors a super massive black hole (SMBH) at its center. Furthermore, there seems to be a fundamental correlation between the stellar bulge and SMBH masses. Simulations show that massive feedback, e.g., powerful outflows, in Quasi Stellar Objects (QSOs) has an impact on the mutual growth of bulge and SMBH. Nearby galaxies follow this relation but accrete mass at much lower rates. This gives rise to the following questions: Which mechanisms allow feeding of nearby Active Galactic Nuclei (AGN)? Is this feeding triggered by events, e.g., star formation, nuclear spirals, outflows, on ~ 500 pc scales around the AGN? Does feedback on these scales play a role in quenching the feeding process? Does it have an effect on the star formation close to the nucleus?

To answer these questions I have carried out observations with the Spectrograph for INtegral Field Observation in the Near Infrared (SINFONI) at the Very Large Telescope (VLT) situated on Cerro Paranal in Chile. I have reduced and analyzed the recorded data, which contain spatial and spectral information in the H-band ($1.45\ \mu m - 1.85\ \mu m$) and K-band ($1.95\ \mu m - 2.45\ \mu m$) on the central $10'' \times 10''$ of the observed galaxies. Additionally, Atacama Large Millimeter/Sub-millimeter Array (ALMA) data at 350 GHz (~ 0.87 mm) as well as optical high resolution Hubble Space Telescope (HST) images are used for the analysis.

For NGC 1433 I deduce from comparison of the distributions of gas, dust, and intensity of highly ionized emission lines that the galaxy center lies ~ 70 pc north-northwest of the prior estimate. A velocity gradient is observed at the new center, which I interpret as a bipolar outflow, a circum nuclear disk, or a combination of both. At least one dust and gas arm leads from a $r \sim 200$ pc ring towards the nucleus and might feed the SMBH. Two bright warm H_2 gas spots are detected that indicate hidden star formation or a spiral arm-arm interaction. From the stellar velocity dispersion (SVD) I estimate a SMBH mass of $\sim 1.74 \times 10^7\ M_\odot$.

For NGC 1566 I observe a nuclear gas disk of $\sim$ 150 pc in radius with a spiral structure. I estimate the total mass of this disk to be $\sim 5.4 \times 10^7$ M$_\odot$. What mechanisms excite the gas in the disk is not clear. Neither can the existence of outflows be proven nor is star formation detected over the whole disk. On one side of the spiral structure I detect a star forming region with an estimated star formation rate of $\sim 2.6 \times 10^{-3}$ M$_\odot$ yr^{-1}. From broad Brγ emission and SVD I estimate a mean SMBH mass of $\sim 5.3 \times 10^6$ M$_\odot$ with an Eddington ratio of $\sim 2 \times 10^{-3}$.

Part II deals with the final tests of the Fringe and Flexure Tracker (FFTS) for LBT INterferometric Camera and the NIR/Visible Adaptive iNterferometer for Astronomy (LINC-NIRVANA) at the Large Binocular Telescope (LBT) in Arizona, USA, which I conducted. The FFTS is the subsystem that combines the two separate beams of the LBT and enables near-infrared interferometry with a significantly large field of view. The FFTS has a cryogenic system and an ambient temperature system which are separated by the baffle system. I redesigned this baffle to guarantee the functionality of the system after the final tests in the Cologne cryostat. The redesign did not affect any scientific performance of LINC-NIRVANA. I show in the final cooldown tests that the baffle fulfills the temperature requirement and stays < 110 K whereas the moving stages in the ambient system stay > 273 K, which was not given for the old baffle design. Additionally, I test the tilting flexure of the whole FFTS and show that accurate positioning of the detector and the tracking during observation can be guaranteed.

Zusammenfassung

Ich befasse mich in meiner Doktorarbeit mit den Grundsäulen moderner Astronomie: Beobachtung und Instrumentierung.

Teil I der Arbeit behandelt die Beobachtung zweier nahe gelegener aktiver Galaxien, die Seyfert 2 Galaxie NGC 1433 und die Seyfert 1 Galaxie NGC 1566, die sich in einer Entfernung von $\sim$ 10 Mpc befinden und Teil des "Nuclei of Galaxies" (NUGA) Projektes sind. Es ist allgemein anerkannt, dass jede Galaxie ein supermassives schwarzes Loch (SMSL) in ihrem Zentrum beherbergt. Des Weiteren scheint es eine Grundkorrelation zwischen den Massen des stellaren Bulges und der SMSL zu geben. Simulationen zeigen, dass intensives Feedback, z.B. durch intensive Materieflüsse, in quasi-stellaren Objekten (QSOs) dieses gemeinsame Wachstum erklären kann. Nahe gelegene aktive Galaxiekerne (AGK) folgen dieser Relation, akkretieren jedoch Masse mit viel niedrigeren Raten. Daher stellen sich folgende Fragen: Welche Mechanismen ermöglichen die Akkretion für nahe AGK? Wird der Akkretionsprozess angestoßen, z.B. durch Sternentstehung, Spiralarme oder Materieflüsse auf $\sim$ 500 pc Skalen um die AGK? Wirkt Feedback auf diesen Skalen dämpfend für den Akkretionsprozess und hat es einen Einfluss auf die Sternentstehung nahe am Kern?

Um mich mit diesen Fragen zu befassen habe ich Beobachtungen mit dem "Spectrograph for INtegral-Field Observation in the Near Infrared" (SINFONI) durchgeführt am "Very Large Telescope" (VLT) auf dem Cerro Paranal in Chile. Die aufgezeichneten Daten habe ich reduziert und analysiert. Die Daten umfassen räumliche und spektrale Information im H-Band (1.45μm $- 1.85\mu$m) und K-Band (1.95μm $- 2.45\mu$m) für die zentralen $10'' \times 10''$ der beobachteten Galaxien. Zusätzlich werden "Atacama Large Millimeter/Sub-millimeter Array" (ALMA) Daten bei 350 GHz ($\sim$ 0.87 mm) sowie hoch aufgelöste optische "Hubble Space Telescope" (HST) Bilder für die Analyse verwendet.

Für NGC 1433 finde ich, anhand eines Vergleiches der Gas- und Staubverteilungen und der Intensitätsverteilung hoch ionisierter Emissionslinien, heraus, dass das Galaxiezentrum $\sim$ 70 pc nord-nordwestlich im Vergleich zu vorherigen Bestimmungen liegt. Im neuen Zentrum wird ein Geschwindigkeitsgradient beobachtet und für dessen Ursache ich einen bipolaren Materiefluss, eine circumnukleare Scheibe, oder eine Kombination dieser diskutiere. Mindestens ein Spiralarm führt von einem $r \sim$ 200 pc Ring in Richtung des Kerns und könnte so Gas zum SMSL bringen. Zwei stark strahlende Bereiche, welche aus war-

mem H_2-Gas bestehen, sind detektiert worden. Diese deuten auf ein verborgenes Sternentstehungsgebiet oder zeigen die Interaktion der Spiralarme. Aus der stellaren Geschwindigkeitsdispersion (SGD) bestimme ich eine Masse des SMSL zu $\sim 1.74 \times 10^7$ M$_\odot$.

Im Zentrum von NGC 1566 habe ich eine Gasscheibe mit Radius $r \sim 150$ pc und einer Spiralstruktur beobachtet. Die Gesamtmasse der Gasscheibe bestimme ich zu $\sim 5.4 \times 10^7$ M$_\odot$. Welche Prozesse das Gas in dieser Scheibe anregen bleibt unklar. Es können weder Beweise für einen Materiefluss gefunden werden noch wird Sternentstehung innerhalb der gesamten Scheibe beobachtet. Lediglich auf einer Seite der Spiralstruktur identifiziere ich ein Sternentstehungsgebiet, welches eine geschätzte Sternentstehungrate von $\sim 2.6 \times 10^{-3}$ M$_\odot$ yr^{-1} hat. Aus der Emission der breiten Brγ Linie und der SGD bestimme ich eine mittlere Masse des SMSL zu $\sim 5.3 \times 10^6$ M$_\odot$ mit einem Eddingtonverhältnis von $\sim 2 \times 10^{-3}$.

Teil II dieser Arbeit befasst sich mit den, von mir durchgeführten, finalen Tests des "Fringe and Flexure Trackers" (FFTS) für "LBT INterferometric Camera and the NIR/Visible Adaptive iNterferometer for Astronomy" (LINC-NIRVANA) am "Large Binocular Telescope" (LBT) in Arizona, USA. Das FFTS ist das Teilsystem, das die beiden getrennten Strahlen des LBT vereint und dadurch Interferometrie im nahen Infrarot mit einem großen Gesichtsfeld erlaubt. Das FFTS besteht aus einem kryogenen Teil und einem Teil was bei Umgebungstemperatur arbeitet, welche durch ein Bafflesystem getrennt sind. Ich habe dieses Baffle neu konzipiert, um sicher zu stellen, dass dessen Funktionalität bereits in Köln durch finale Tests im Kryostaten gegeben ist. Die Neugestaltung hat keinen Einfluss auf die wissenschaftliche Leistung von LINC-NIRVANA. Ich zeige in den finalen Kühltests, dass das Baffle die Temperaturanforderung $T < 110$ K erfüllt, wohingegen die beweglichen Bauteile im warmen Systemteil eine Temperatur von 273 K nicht unterschreiten. Zusätzlich habe ich die Verbiegung beim Verkippen des gesamten FFTS mit zufriedenstellenden Ergebnissen getestet. Alle Anforderungen für die genaue Positionierung des Detektors und das Nachführen während einer Beobachtung sind erfüllt.

Contents

Part I

The Central Region in Seyfert Galaxies

Introduction

This chapter introduces the main characteristics and methods that are used, described, and discussed later on in the analysis. It is based on astrophysical textbooks, e.g., Dopita & Sutherland (2003); Osterbrock & Ferland (2006); Peterson (1997); Mihalas & Binney (1981), as well as review papers by Ho (2008); Kennicutt & Evans (2012); Sofue & Rubin (2001); Fabian (2012); Kormendy & Ho (2013), which I highly recommend as a source for a thorough overview on the topics mentioned here.

I will start with the description of astrophysical spectra focusing mainly on the optical[1], which is the best studied wavelength regime, and the Near-Infrared (NIR)[2], which is the wavelength regime that is mainly used in the analysis in this thesis. I will talk about the different emission mechanisms that are typical in observed spectra.

Thereafter, I will introduce the type of galaxies that are investigated in this thesis, active galaxies. These galaxies harbor an Active Galactic Nucleus (AGN) at their center. They contain ionized gas, e.g., H ɪɪ regions, whose ionization cannot be attributed clearly and directly to stars, in their nuclear regions. Hence, the existence of different energetic phenomena, e.g., the accretion disk around a Super Massive Black Hole (SMBH), has been claimed.

I will present the Unified Model (UM) which combines all observed characteristics of AGN and explains them as different phenomena that stem from the same model but are perceived differently due to orientation effects. This model can explain the perceived differences in AGN themselves, but not the different hosts in which they reside.

Afterwards, I will explain how the Black Hole (BH) mass can be estimated, then I will talk about the contribution of star formation to the nuclear region in different galaxies and how this can be disentangled and then I introduce rotation in galaxies.

---

[1] Wavelength range of $\sim 4000 - 7500$ Å.

[2] Wavelength range of $\sim 7500 - 50000$ Å or $\sim 0.75 - 5.0$ μm.

1.1 Astrophysical Spectra

The word "spectrum" describes the fact that there are different subgroups to a specific group. For example in politics there are parties that range from leftist parties over liberals and conservatives to rightist parties, this is called the political spectrum. In science, especially with regard to light, the word spectrum is used to describe dispersion of light. For example the different colors of a rainbow which are created by dispersion of white light from the sun by water drops in the atmosphere. This is the effect used to analyze the light from distant stars and galaxies. The observed light is dispersed to gain information not only on the intensity but also on the energy distribution of the incoming photons.

I will describe the different emission mechanisms that are typical in astrophysics and explain the emission mechanisms which are discussed in this study. A galaxy spectrum is a linear combination of radiation from different components, e.g., black body emission, electron continuum, hydrogen atoms and molecules, which are explained below, and other emission and absorption lines from a zoo of helium, metals, and molecules.

1.1.1 Continuum Radiation

The emission that is continuous over a wider wavelength range is termed continuum radiation. There are several processes that create continuous emission which will be discussed in the following.

Black Body Emission

The rainbow colors, violet to red, are those that the human eye is sensitive to, which covers a wavelength range of $\sim 4000 - 7000$ Å. But stellar light is not confined to only this range. Stellar emission can be very well described as black body emission which is characterized by the Planck function

$$B_\lambda(T) = \frac{2hc^2}{\lambda^5} \frac{1}{\exp\left(\frac{hc}{\lambda kT}\right) - 1}$$

with the Planck constant $h = 6.626 \times 10^{-34}$ J s, the speed of light $c \approx 3 \times 10^{10}$ cm s^{-1}, the wavelength λ, the black body Temperature T in Kelvin, and the Boltzmann constant $k = 1.38 \times 10^{-19}$ cm^2 kg s^{-2} K^{-1}. From the Planck function it becomes apparent that even a single star with a specific temperature radiates at every wavelength. The sun's black body emission temperature[3] is $T_\odot = 5778$ K.

_____

[3]In the following effective temperature will be used for this term as is usual in other literature.

Following Wien's displacement law

$$\lambda_{max}T = 0.29 \text{ cm K}$$

the peak intensity for the sun is found at a wavelength of ~ 5019 Å

$$\lambda_{max} = \frac{0.29 \text{ cm K}}{T_\odot}$$

$$\Rightarrow \lambda_{max} = \frac{0.29 \text{ cm K}}{5778 \text{ K}} = 5.019 \times 10^{-5} \text{ cm.}$$

Figure 1.1 shows the black body emission of the sun and the black body emission of bodies at temperatures of $T = 1200$ K and $T = 10000$ K.
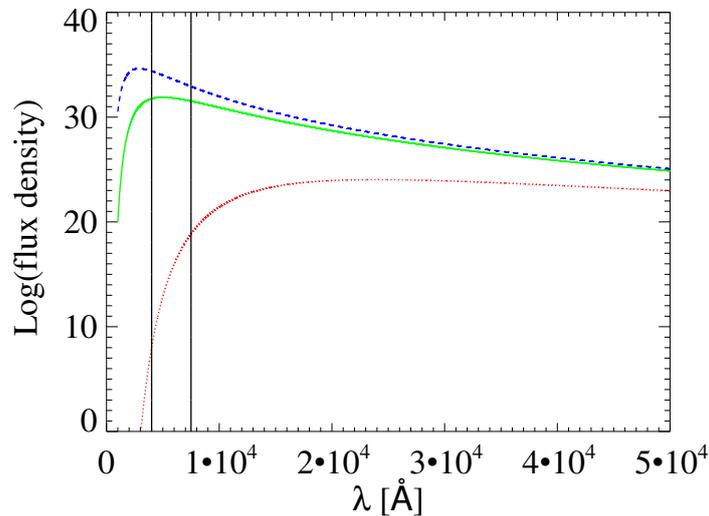
Figure 1.1: Black body emission of the sun $T_\odot = 5778$ K (green - solid line) and black body emission at effective temperatures of $T = 10000$ K (blue - dashed line) and $T = 1200$ K (red - dotted line). The vertical lines mark the visible wavelength range. Note that the flux density scales with the temperature at every wavelength.

The black body emission is a very important contributor of emission over a large wavelength range. Young hot stars with effective temperatures > 10000 K peak in the UltraViolet (UV). These are bright stars that have lifetimes of a few Mega years and are only seen in very young star forming regions. Stars with effective temperatures of $5000 - 10000$ K and lifetimes of $> 10^9$ yr peak in the optical. These stars are mostly main sequence stars[4]. Stars at temperatures below

---

[4]The term dwarf will be used from now on when referring to main sequence stars.

5000 K peak in the NIR. These stars make up most of the dwarf population. However, giants and supergiants can show the same effective temperature as the aforementioned dwarfs. For longer wavelengths down to the sub-mm black body emission from dust is observed.

The main contribution to the continuum in the later discussed NIR stems from an already evolved stellar population or from very hot dust. However, for hot dust to become prominent in a galaxy spectrum, a strong ionizing source is needed to heat up a lot of dust (e.g., the torus structure around an AGN, see Sect. 1.2). This is explained by the black body emission where at a higher temperature the flux density is higher over the whole wavelength range. This becomes apparent from Fig. 1.1, where the $T = 1200$ K black body is several magnitudes weaker compared to the hotter black body plots although the black body peak emission follows Wien's displacement law and peaks with lower temperature at a higher wavelength. Another reason is that dust is not as good a black body as a star and its black body emission has to be multiplied by an emissivity factor $\epsilon < 1$, which weakens the dust intensity.

Electron Continuum

A charged particle, e.g., an electron, will radiate if it is accelerated. This happens for example when an electron interacts with the Coulomb potential of a positive ion, e.g., H II. This interaction produces a continuum from *free-free* radiation. The electron before and after the interaction is free but its energy level changes due to the de- or acceleration[5] with the Coulomb potential. The change in energy is not quantized hence the radiated spectrum is continuous.

The *free-bound* interaction, where the electron is free and is then captured by the ion, also creates continuous radiation due to the dependence of the emission coefficient on the velocity of the captured electron.

Synchrotron radiation is another form of accelerated electron radiation. It occurs when electrons spiral around magnetic fields. Due to the spiral movement the velocity vector changes its direction hence an acceleration occurs. The radiation depends on the electron energy and can occur throughout the spectrum. When synchrotron emission becomes important there is not a single electron at a specific energy creating a synchrotron spectrum but several electrons with different energies which combined create a *power-law* shape described by

$$F_\nu = C\nu^{-\alpha}$$
$$F_\lambda = C'\lambda^{\alpha-2}.$$

---

[5]In the case of deceleration the effect is called bremsstrahlung.

Where C and C' are constants and α is the power-law index typically in the range of $0 \leq \alpha \leq 1$ for quasar spectra.

In the galaxies studied in this thesis electron continuum radiation is weak compared to the black body emission from background stars and is therefore not important for this study. However, the electron continuum becomes important for the study of isolated nebulae or for the study of galaxies with strong jets.

1.1.2 Line Emission

In addition to the continuum radiation, atoms and molecules, which are found in clouds and nebulae throughout the InterStellar Medium (ISM), emit photons at specific wavelengths. This emission is added to the underlying continuum and results in local emission maxima at wavelengths and energies corresponding to the transitions energy. However, absorption minima can occur as well when photons from the underlying continuum are absorbed by the nebulae. Very important and well studied emission lines are the hydrogen recombination lines, e.g., Balmer series in the optical or Brackett series in the NIR, and molecular rotational-vibrational emission, e.g., molecular hydrogen, H_2, in the NIR or carbonmonoxide, CO, in the Millimeter to sub-mm wavelength regime. Important absorption lines are found in mentioned recombination lines from nebulae and optically thick clouds or in stellar atmospheres, e.g., CaT $\lambda 8500$ Å or CO(2-0) $\lambda 2.29\,\mu$m.

I will describe emission lines of atomic and molecular hydrogen that are important for this work. However, the spectrum of galaxies is populated by several other species which are briefly mentioned here.

Recombination Lines

Recombination lines are mainly observed in atomic gas, i.e., from atomic gas clouds, which are found throughout the ISM. Hydrogen is the most abundant element in the universe therefore these clouds consist mainly of hydrogen, $\sim$ 90%, followed by helium, $\sim$ 10%, and metals, e.g., oxygen (O), carbon (C), iron (Fe), with numbers of $10^{-4} - 10^{-3}$ relative to hydrogen.

Photoionization

Photoionization describes the effect that photons with an energy above a given threshold, e.g., $E \sim 13.6$ eV or $\lambda \sim 912$ Å for a hydrogen atom, can remove electrons from the atom they are interacting with, thereby ionizing the atom. This interaction is called bound-free photon absorption. The easiest and most illustrative example in astrophysics is a hydrogen cloud close to a young hot

star that emits strong UV radiation. All photons above the energy threshold of $E \sim 13.6$ eV and directed towards the cloud can ionize hydrogen atoms in the nearby cloud. However, not every photon will interact with a hydrogen atom. The photoionization cross section is highest around the threshold frequency of $v_0 \sim 3.29 \times 10^{15}$ s^{-1} and drops off with approximately v^{-3} above this threshold.

The free electrons follow a Maxwell-Boltzmann velocity distribution

$$f(u) = \frac{4}{\sqrt{\pi}} \left(\frac{m}{2kT} \right)^{\frac{3}{2}} u^2 \exp\left(-\frac{mu^2}{kT} \right),$$

with the velocity u, mass m, and temperature T of the electrons, because the cross section for elastic scattering collisions between electrons is much larger than any other involved cross section, e.g., recombination cross section. Hence, the recombination coefficient to a specific hydrogen level $\alpha_{n\,^2L}(H^0, T)$ is the integral over the velocities du of the Maxwell-Boltzmann energy distribution $f(u)$, the recombination cross section $\sigma_{n\,^2L}(H^0, u)$ of this specified level, and the velocity of the electrons u

$$\alpha_{n\,^2L}(H^0, T) = \int\limits_0^\infty u \, \sigma_{n\,^2L}(H^0, u) \, f(u) \, du.$$

The recaptured electrons emit radiation depending on their velocities and create continuum emission (see Sect. 1.1.1). The electrons then cascade downwards to the ground level emitting photons with specific energies that equal the gaps between the levels. These photons create the observed line emission of hydrogen recombination lines, e.g the Brackett Series in the NIR. For a single hydrogen atom the lifetime of an excited state is of the order of 10^{-4} s $- 10^{-8}$ s whereas the lifetime of a hydrogen atom against ionization is of the order of 10^8 s. Therefore a recombined electron in an excited hydrogen atom will cascade down to the ground level before the hydrogen atom is going to be photoionized.

Molecular Emission Lines

It is deemed wise to study the H_2 molecule, the most abundant molecular species. Emission lines can be observed in the NIR, e.g., H_2(1-0)S(1) $\lambda 2.12$ μm. The excitation energy of H_2 corresponds to a temperature ≥ 500 K, hence H_2 can be detected in a direct way only in hot gas, e.g., around star forming regions. Therefore, CO (monoxide) transitions with an excitation temperature ≥ 5.6 K are used instead of H_2 to measure the H_2 distribution in cooler regions, e.g., spiral arms. This is possible since H_2 plays an important role in the production

of CO. The most important and fastest way is the radiative association of C^+ with H_2 forming CH or CH_2 and neutral exchange reaction of CH and O (oxygen) to CO and H. The lowest rotational transition has a wavelength of $\lambda 2.59$ mm due to the low excitation energy of CO. Therefore, it is easier to excite CO collisionally to much higher rotational levels than H_2, e.g., CO(3-2).

Collisional Excitation

In the case of weak radiation fields molecular rotational-vibrational excitation is due to collisions. The very important case for this work is the hydrogen molecule which can be excited by collisions with other molecules or electrically neutral atoms. The density has to be low enough to allow radiative processes to de-excite these ro-vibrational levels instead of being de-excited collisionally. Furthermore, the emission line flux of these transitions is then proportional to the temperature T in the medium because the probability depends on the collisional excitation cross section integrated over the energy distribution of the colliding species. In thermal equilibrium the energy follows the Maxwell-Boltzmann distribution and the levels are populated according to the Boltzmann equilibrium

$$\frac{N_2}{N_1} = \frac{g_2}{g_1} \exp\left(\frac{-E_{12}}{kT}\right)$$

with levels N_i, where N_1 is the ground state, statistical weights g_i and the energy difference between the two states, here E_{12}. Afterwards, the molecule will radiate a photon corresponding to its rotational-vibrational spectrum and return to the ground state.

UV-flourescence of Molecular Hydrogen

This process occurs in PhotoDissociation Regions (PDRs), i.e. the region that is adjacent to H II regions. The ionization of the gas in the PDR is due to transmitted stellar continuum and the emission produced in the H II region, e.g., free-bound and free-free emission. The Lyman-Werner bands of molecular hydrogen lie between the Lyman limit $\sim$ 912 Å and $\sim$ 1500 Å in the UV and are therefore populated in this process. Furthermore, the Lyα emission falls into this region which additionally can excite molecular hydrogen. The H_2 molecule has to be already in a vibrationally and rotationally excited state, i.e. at temperatures $\gtrsim$ 1000 K by collisional excitation, to achieve a good resonance with the Lyα line. Most of the hydrogen ($\sim$ 90%) decays into excited bound rotational-vibrational levels whereas the rest decays into unbound continuum levels.

1.1.3 Absorption

The intensity I received from the observed source is usually not the initial intensity I_0 of this source as defined by the mechanisms described above. The absorption of photons with a specific energy was mentioned in Sect. 1.1.2 leading to absorption lines. The photons also encounter and interact with dust clouds on their way to the observer. This interaction leads to absorption of high energetic photons from UV and optical bands and reemission in infrared bands, e.g., at $\approx 60\,\mu$m. As a simplification these clouds can be seen as a dust screen with constant density n_d of the dust grains and a constant path length x_d. When it is assumed that scattering of photons is negligible the observed intensity I is defined as

$$I = I_0 \exp(-\tau)$$

where τ is the optical depth, which depends on the effective cross section of the dust grains and the column density $N = n_d x_d$ of the dust cloud. The extinction in the visual, $A_v = 1.086\tau$, is usually used to give a measure for the absorbed light. However, the extinction varies with wavelength; Cardelli et al. (1989) give a solution A_λ for the extinction curve at wavelength λ in the optical and NIR. The UV and optical bands are much more prone to extinction than the NIR bands. Hence, dark dust lanes in the optical tend to disappear when the same region is viewed in the NIR.

1.2 AGN Taxonomy

It is widely believed that all galaxies harbor a SMBH at their center. However, only a fraction of these are in an active accretion phase which marks them as an AGN. The closest SMBH is the black hole at the center of the Milky Way, also known as Sagittarius A* (SgrA*). It is usually observable in radio and in X-ray but very faint in other wavelength regimes when it is not flaring, i.e. no accretion event is taking place. The mass of SgrA* is calculated to $\sim 10^6$ M$_\odot$ from observed stellar orbits (Eckart & Genzel 1996; Genzel et al. 1997; Eckart et al. 2002; Schödel et al. 2009). It is these orbits that constrain the space in which the central mass has to be confined and lead to the only possible assumption that the central mass has to be a SMBH.

SgrA* is so low in activity that the associated radiation would not be detectable if it were in another galaxy. The topic of this thesis, however, is extragalactic AGNs of which there are several types distinguished mainly by luminosity but also in spectral features (e.g., strong or faint radio emission) that will

be introduced in the following. The main difference of AGNs and H II regions, which are ionized by young, bright, and hot stars, is the wide range and strength in ionization, e.g., the ionization of the coronal line [Si VI] $\lambda 1.963$ μm with an ionization potential of 167 eV which cannot be achieved by stars. An important attribute is the emission line ratio of the emission lines [O III] $\lambda 5007$ Å over Hβ $\lambda 4861$ Å and [S II] $\lambda\lambda 6716$ Å, 6731 Å over Hα $\lambda 6563$ Å with typical values for AGNs of [O III]/Hβ > 3 and/or [S II]/Hα > 0.4.

1.2.1 Active Galaxies

Seyfert galaxies

Seyfert galaxies are named after Carl Seyfert who observed a sample of galaxies with stellar-appearing cores (high central surface brightness) using optical spectroscopy in 1948. He found that several of these galaxies show strong high-excitation nuclear emission lines and that the hydrogen lines are sometimes broader than others. The definition of a Seyfert galaxy is that its absolute B-band magnitude $M_B > -21.5 + 5 \log h_0$ (Schmidt & Green 1983) and that strong, high-ionization lines are present. In general, a Seyfert host galaxy is clearly detectable but the nucleus is very bright and has the appearance of a superimposed star. Because the host is resolved stellar absorption features, e.g., Si I $\lambda 1.59$ μm, CO(2-0) $\lambda 2.29$ μm, created mainly by evolved bulge populations, can be detected.

There are two types of Seyfert galaxies, Seyfert 1 and Seyfert 2 galaxies. Their main difference is the appearance or non-appearance of broad permitted lines in the nuclear spectrum, e.g., Hα line emission with a Full Width at Half Maximum (FWHM) > 1000 km s^{-1}. These *broad lines* are seen in Seyfert 1 nuclei. Since exclusively permitted lines are observed the electron density n_e in the emitting region has to be of the order of $n_e \geq 10^9$ cm^{-3}. At these densities the non-electric-dipole transitions are suppressed by collisions. Broad lines are detected in several atoms, e.g., H I, He I, He II, Fe II.

Narrow emission lines are seen in both types, Seyfert 1 and Seyfert 2 nuclei. They have widths of several hundred km s^{-1} and are broader than emission lines originating in planetary nebulae or classical H II regions. Narrow emission lines in nuclear spectra are observed in all kinds of atoms and in both permitted and forbidden transitions. Hence, the electron density in this region cannot be as high as in the broad line emitting region and corresponds to $n_e = (10^3 - 10^6)$ cm^{-3}. Forbidden lines are for example [O III] $\lambda\lambda 4595$ Å, 5007 Å or [Fe II] $\lambda 1.644$ μm and permitted lines are H$\alpha \lambda 6563$ Å, He II$\lambda 4686$ Å, or Br$\gamma \lambda 2.166$ μm.

Other differences are a usually strong absorption component in the X-ray regime ($N_H > 10^{22}$ cm^{-2}) in Seyfert 2 nuclei and weak AGN continuum in the

11

optical and UV. Hence, Seyfert 1 nuclei show stronger X-ray emission and a prominent power-law continuum from the AGN in the optical and UV.

Quasars

Quasi Stellar Radio sources (Quasars) or Quasi Stellar Objects (QSOs) are defined as having an absolute magnitude $M_B < -21.5 + 5 \log h_0$. They are the most luminous subclass of AGNs. In contrast to Seyfert galaxies QSOs outshine their host galaxies by more than a factor 100 hence the host is either not detected or only a faint stellar emission halo can be perceived. Due to their brightness QSOs can be observed at very high redshifts $z > 7$ which can be used to retrieve information about the galactic and cosmological environment in the early universe.

Radio Galaxies

There are radio loud galaxies that exhibit similar optical spectra to Seyfert galaxies. These are called the Narrow-Line Radio Galaxy (NLRG) as the counterpart to Seyfert 2 galaxies and the Broad-Line Radio Galaxy (BLRG) as the counterpart to Seyfert 1 galaxies. The BLRGs usually show a composite nuclear spectrum, indicating strong star formation in the center whereas the NLRGs show almost no difference to Seyfert 2 galaxies except that they are usually ellipticals.

Low-Ionization Narrow Emission Region Galaxies

Low Ionization Nuclear Emission Region (LINER) galaxies are those AGNs that exhibit an [O III]/Hβ < 3 ionization but with an [S II]/Hα > 0.4 ratio. The latter ratio distinguishes these galaxies from H II galaxies whereas the first one distinguishes them from other AGNs, e.g., Seyfert galaxies, that show [O III]/Hβ > 3 ratios (see also Sect. 1.4 and Fig. 1.3). There are other ratios that can distinguish H II galaxies and LINERs but these can be affected by strong extinction effects.

From Surveys it seems that the youngest galaxies of Hubble type Sc are predominantly (> 80%) H II galaxies whereas this trend turns for Sb and Sa galaxies toward an ~ 80% LINER fraction. For ellipticals the fraction of nuclear LINER spectra is at about 46%.

Although LINERs are usually compared to Seyfert 2 galaxies, which might have historical reasons, there are type 1 and type 2 LINERs similar to Seyfert galaxies.

Blazars

Blazars show almost no signs of emission or absorption lines, although with high signal-to-noise ratios weak nebular emission or stellar absorption features can be

detected. These sources show large polarization of a few percent whereas usual AGN show less than one percent polarization. The variability is strong with sometimes more than 0.1 magnitudes on time scales as short as a day. These effects probably stem from very strong relativistically beamed components close to the line-of-sight. It seems that all blazars also show strong radio emission.

1.2.2 The Unified Model

All the above mentioned characteristics describe one phenomenon, the AGN. The question arises: Are all these AGNs different or do they only appear to be different? The thing that all AGNs have in common is the very bright nuclear region. This bright continuum emission is responsible for the ionization of the Broad-Line Region (BLR) and Nroad-Line Region (NLR). In Seyfert 1s the broad emission is highly correlated with continuum fluxes which is why it is used for reverberation mapping[6] calculations. In Seyfert 2s the AGN featureless continuum at 4800Å and the narrow Hα emission are logarithmically correlated with a slope of ~ 1 (Shuder 1981). These observations imply that both, NLR and BLR, are ionized by the AGN continuum.

Another intriguing observation was first made by Antonucci & Miller (1985), who observed the Seyfert 2 galaxy NGC 1068 in polarized light. In other observations NGC 1068 did not show any sign of broad emission lines hence its classification as a Seyfert 2 galaxy. However, in polarized light broad emission lines did become apparent. This detection was not the only one of a BLR in polarized light and implied strongly that Seyfert 1 and 2 nuclei are intrinsically the same.

The UM tries to explain the characteristics mentioned in Sect. 1.2.1 by orientation effects. This is possible since AGNs show rather an axial than a spherical symmetry. An example from which this can be inferred are observations of nearby AGNs and their NLRs which show a cone-like structure. Other examples are radio jets in radio loud AGN. One effect of this axial symmetry would be the unobservable BLR in Seyfert 2 galaxies (except for polarized straylight) and the high column densities from X-ray observations in Seyfert 2 galaxies in contrast to low column densities in Seyfert 1 galaxies.

The sketch in Fig. 1.2 shows an example of how the composition of the central few parsec[7] of an AGN might look and how the viewing angle changes the observed characteristics. I will describe these different components in detail in the following.

---

[6]Reverberation mapping measures the light travel-time delay between an intensity changing continuum source and the responding BLR clouds. From this time delay the size of the BLR can be inferred and further on an estimate can be given for the mass of the SMBH.

[7]1 pc$\approx 3.1 \times 10^{18}$ cm
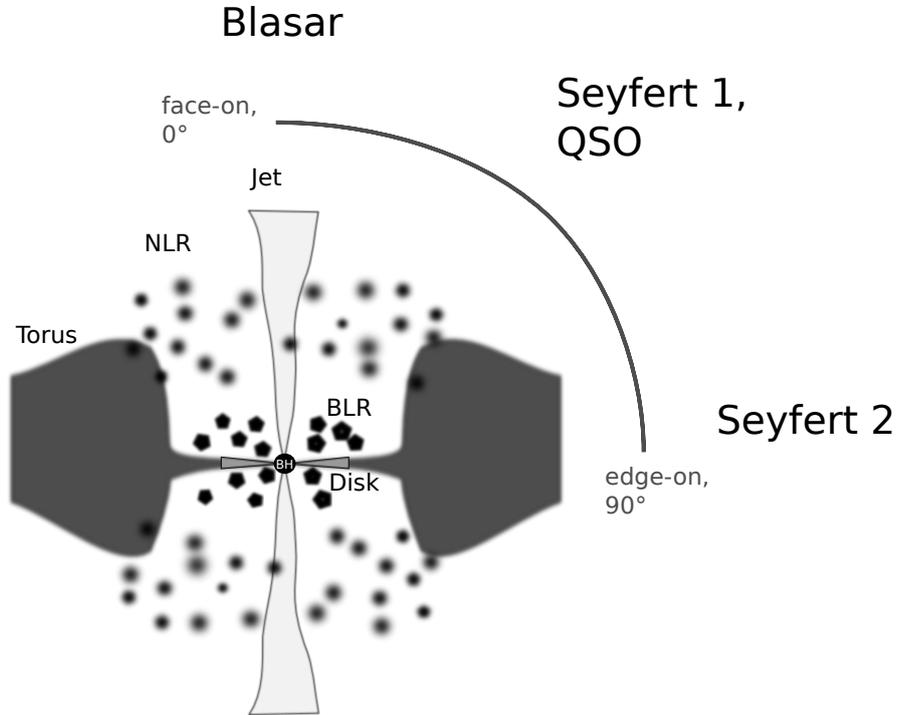
Figure 1.2: A sketch of the different components of an active galactic nucleus. Note that the scales are adapted to be able to show all components. For more detail see text.

The Super Massive Black Hole

Direct proof for SMBHs is lacking but the evidence, e.g., very high continuum luminosities, points toward gravitational accretion of matter by a central mass, the SMBH. Typical values for the mass of these black holes are 10^6 M$_\odot$ in nearby AGN and more than 10^9 M$_\odot$ in more distant and massive galaxies. The mass can be inferred assuming isotropy and a stability of the source. When assuming spherical accretion onto the SMBH the highest possible luminosity depends on the mass of the SMBH and is called the Eddington luminosity

$$L_E \leq \frac{4\pi G m_p c}{\sigma_e} M,$$

with the gravitational constant G, proton mass m_p, the speed of light c, and the Thomson scattering cross-section σ_e. This is derived by considering that the radiation pressure force cannot be higher than the gravitational force of the SMBH for material to be accreted onto it. Analogue the Eddington mass M_E is

defined which gives the lowest possible mass to an observed luminosity

$$M_{\mathrm{E}} = 8 \times 10^5 L_{44} M_\odot$$

with L_{44} as the bolometric luminosity of the central source in units of 10^{44} erg s^{-1}. The fueling of the SMBH can be approximated from the energy available in a mass M, $E = \eta M c^2$, where η is a scaling factor for the efficiency of mass to energy conversion.[8] The time derivative of this energy gives $L = \eta \dot{M} c^2$ and an Eddington accretion rate of

$$\dot{M}_E = \frac{L_E}{\eta c^2}$$

using the Eddington luminosity L_E.

The Accretion Disk

The accretion disk is of the size of $\sim 10^{15}$ cm and its structure depends on several parameters, e.g., magnetic field strength, accretion rate, disk corona, and jets. The energy of a given particle is supposed to be dissipated locally at a radius r to the black hole. The medium of the accretion disk is supposed to be optically thick. Then local black body emission at radius r in the disk can be assumed. For black holes with a mass of 10^8 $M_\odot$ and accretion rates close to their Eddington accretion the temperature peaks at about 5×10^5 K in the innermost parts of the accretion disk. It is assumed that the big blue bump, seen in the optical and UV is thermal emission at temperatures of $10^{5\pm1}$ K. From these estimations the peak luminosity of the black body emission is situated at about 100 Å, the extreme UV. For Low-Luminosity AGNs (LLAGNs) with a mass of 5×10^6 $M_\odot$ and accretion rates of 10^{-4} with respect to their Eddington accretion the peak is at slightly longer wavelengths ~ 200 Å. For these typical accretion rates the disk can be seen as thin and the efficiency at which it radiates is high ($\eta \approx 0.1$). The spectrum is then a composite of black body emission at the temperatures that exist in the disk.[9] At low accretion rates the disk can become optically thin which allows for an ion-torus to develop. These ion-tori and its magnetic field properties are regarded as important tools towards the creation of jets.

---

[8] A typical value for η is 0.1, which implies an efficiency of 10% for the conversion rate. Compared conversion efficiency of nuclear fusion, which is less than 1%, accretion is 10 times more efficient.

[9] The temperature dependency on the disk radius, distance r from the BH, is $T(r) \sim (r/R_S)^{-3/4}$ for an optically thick disk.

The Broad Line Region

The broad line region are clouds of temperature $T \sim 10^4 K$ and an electron density of 10^8 cm^{-3} $< n_e < 10^{11}$ cm^{-3}. They are at a distance of lightdays, in Seyferts, and can be at a distance of lightyears, for QSOs, to the SMBH.[10] These clouds absorb the ionizing UV continuum emission of the central source, e.g., the accretion disk, and show characteristic line emission and variability in accordance to the continuum variability. The spectral lines observed originate mostly from allowed transitions. This fact is used to derive the mentioned lower and upper limits for the electron density in the BLR clouds. The name 'broad line' stems from the emission lines' FWHM which is typically ~ 5000 km s^{-1}. The width of the lines is usually associated with differential Doppler shifts of the bulk motion of individual clouds. The bulk motion is assumed to be determined by the SMBH, e.g., Keplarian orbits, but the specific structure, e.g., a BLR disk, is unknown.

From reverberation mapping[11] the actual size of the BLR can be deduced. Since the BLR is thought to be very close to the center its motion can be seen as virialized hence the black hole mass can be estimated using the virial theorem when velocity v and distance r are known. The velocity can be measured from the broad-line widths. This estimate gives a much better and usually about one magnitude higher mass of the SMBH than the estimated Eddington mass. Kaspi et al. (2000) showed empirically that the featureless continuum luminosity at 5100 Å correlates with the radius of the BLR. Inferring further Greene & Ho (2005) show that the broad Hα correlates with the featureless continuum luminosity at 5100 Å. This allows the use of broad-line characteristics only to determine the black hole mass, for more detail see Sect. 1.3.2.

The Obscuring Torus

Beyond the BLR the optically thick torus awaits. The torus consists of dust and gas which means that it has a lower limit for its distance to the ionizing central source of $r \gtrsim 10^{17}$ cm where the dust sublimation temperature $T \approx 1300$ K is reached. How far the torus extends is not clear but observations of Seyfert galaxies using infrared interferometry (e.g., Burtscher et al. 2013; Tristram et al. 2014, and references therein) show dust emission on parsec to few parsec scales. The structure of the gas and dust is believed to be toroidal around the central source, hence introducing a rather axial than spherical structure to the AGN en-

---

[10]One lightyear corresponds to $\approx 9.5 \times 10^{17}$ cm or 0.3 pc.

[11]Reverberation mapping is the time resolution of luminosity change in the BLR with respect to continuum variation.

vironment. The torus is supposed to be responsible for the observed differences in Seyfert 1 and Seyfert 2 nuclei by blocking the emission of the inner sources, e.g., continuum emission from the accretion disk and broad emission lines from the BLR.

The Narrow Line Region

The narrow line region is located at the polar regions of the toroidal structure and extends from a few lightyears ($\gtrsim 10^{18}$ cm) distance to the central source up to several hundred pc. These clouds show line emission of allowed and forbidden line transitions. The observed transitions imply an electron density of $n_e \sim 10^4$ cm^{-3} and temperatures of $T \sim 10^4$ K. The NLR is the only part of this AGN environment described here that can be resolved in optical and NIR wavelengths, simply due to its strong emission and large spatial scale. The line emission from this region is used to discriminate AGNs from star forming regions and galaxies by emission line ratios and simply by the ionization potential of some transitions, e.g., [Si VI] $\lambda 1.96\,\mu$m with an ionization potential of 167 eV.

Jets

Jets are powerful energy outflows which are usually highly collimated and are directed towards the polar openings left by the torus. These energy outflows are best studied with interferometers in the radio regime where high spatial resolution can be achieved, e.g., the Very Long Baseline Interferometer (VLBI) at a few $10\,\mu$as angular resolution. Jets directed almost along the line of sight of the observer are the probable explanation to the occurrence of Blazars. They can cause the observed effects of high luminosity, strong polarization, and variability.

1.3 Black Hole Mass Estimators

The best estimator for a BH mass is a star orbiting undisturbed in the potential of the SMBH. To observe this is impossible, since there are always a lot more stars that will have an influence on the orbit due to their potential. Nevertheless, in the Milky Way single stars can be observed and the BH mass is estimated from their orbital properties (e.g., Eckart & Genzel 1996; Genzel et al. 1997; Eckart et al. 2002; Schödel et al. 2009) with corrections taken into account.[12] This method

---

[12]The first fully observed orbit was of the star S0-2 which will have its next periapse in the end of 2017. The only other star for which all orbital elements are known is S0-102, however, this star 16 times dimmer than S0-2 and is more challenging to observe due to confusion with other sources.

cannot be used for other galaxies hence other properties, e.g., BH mass - host galaxy relations and BLR characteristics, have to be invoked.

1.3.1 Black Hole Mass to Host Galaxy Relations

The SMBHs studied here are of the order of $10^6 - 10^7$ $M_\odot$. Their sphere of influence[13] ranges from 0.5 to 5.0 pc according to $R_{BH} = GM_{BH}/\sigma_\star^2$ with the gravitational constant G, the black hole mass M_{BH}, and the stellar velocity dispersion of the bulge $\sigma_\star$ and is therefore not resolved in the observed data. This means that a BH mass estimate from dynamical means, e.g., stellar orbits, cannot be determined. Furthermore, the SMBH is directly influencing only a very small fraction of the host galaxy. Nevertheless, several empirical relations have been found that connect the BH mass and the bulge properties of the host.

The $M - \sigma_\star$ Relation

The relation that nonetheless is relying on dynamics is the $M - \sigma_\star$ relation. It was first found by Ferrarese & Merritt (2000); Gebhardt et al. (2000) which found different slopes of $M \sim \sigma_\star^{4.8}$ and $M \sim \sigma_\star^{3.75}$ respectively. It was later improved by Tremaine et al. (2002). Ferrarese & Merritt (2000) argue that this correlation might stem from a fundamental connection between BH mass and bulge mass with the stellar dispersion $\sigma_\star$ being a good predictor of the bulge mass with the idea that early-type[14] galaxy masses scale with their luminosities $M \sim L^{5/4}$ and the luminosity scales with $L \sim \sigma^4$. Another idea is that the dispersion represents a measure of the potential well depth in which the BH formed. This is supported by simple BH-host galaxy growth models (e.g., Silk & Rees 1998). Both explanations lead to a dependency of $M \sim \sigma_\star^5$.

The latest relation found by Gültekin et al. (2009) from a sample of 49 galaxies is

$$M_\bullet = 10^{8.12 \pm 0.08} \times \left(\frac{\sigma_\star}{200 \text{ kms}^{-1}} \right)^{4.24 \pm 0.41} M_\odot$$

where they notice a significantly lower scatter in a subpopulation of ellipticals. This difference is not clear but might arise from systematic errors in BH mass measurements of late type galaxies or because ellipticals lie closer to the ridge line of the $M_\bullet - \sigma_\star$ relation.

---

[13]The sphere of influence of a BH is the region where the gravitational potential of the BH dominates over the stellar gravitational potential.

[14]Early-type galaxies are elliptical and lenticular galaxies after the Hubble classification.

Recently Graham & Scott (2013) found that a significant fraction of barred galaxies show a factor of two different relation from non-barred galaxies. However, they do not find if barred galaxies harbor undermassive BHs or if they tend to towards brighter luminosities.

Other $M_\bullet$ – Bulge Relations

The BH mass seems to be related not just to the velocity dispersion of the bulge but also to the luminosity L_{bulge} (e.g., Marconi & Hunt 2003), mass M_{bulge} (e.g., Häring & Rix 2004), and the Sérsic index n (e.g., Graham & Driver 2007). After first empirical investigations it was believed that only the $M_\bullet - \sigma_\star$ relation showed a scatter that was tight enough to be acceptable as a correlation between $M_\bullet$ and the $\sigma_\star$.

Marconi & Hunt (2003) had the idea to correlate the L_{bulge} in the NIR to the BH mass. Earlier works (Magorrian et al. 1998) have concentrated, probably out of historical reasons, on the B-band luminosity. The NIR is far less affected by extinction effects and traces much better the mass dominating stellar population, e.g., due to a lower variation of the M/L ratio (Gavazzi 1993). Additionally, they introduced two-dimensional bulge-disk decomposition to determine the needed parameters. Furthermore, they find that the $M_\bullet$-M_{bulge} shows a tight relation with the simple assumption that the virial bulge mass $M_{bulge} = R_e \sigma_e$, with the effective bulge radius R_e and effective Stellar Velocity Dispersion (SVD) σ_e. Häring & Rix (2004) tightened the $M_\bullet$-M_{bulge} relation by modeling of the bulge parameters, e.g., the SVD.

The $M_\bullet$-n relation is based on the concentration of stars where the Sérsic index n is the parameter from an $R^{1/n}$ light profile fit (Graham & Driver 2005, and references therein). The idea behind this approach is that it is presumably easy to obtain, i.e., only images are needed to derive the Sérsic index n, and that it is less affected by kinematical effects, e.g., from substructures in the bulge and the underlying disk.

1.3.2 Broad Line Region Relations

Extragalactic sources, i.e., other galaxies than the Milky Way, are too far away to resolve single stars. However, in AGN properties of regions that are within the sphere of influence of the BH, e.g., the BLR, can be observed due to their high luminosity. From the characteristics of these regions a mass of the SMBH can be inferred. As mentioned in Sect. 1.2.2 the exact structure of the BLR is not known therefore an assumption which has to be made is that the BLR clouds are virialized and on Keplerian orbits around the SMBH. This assumption gives

a mass estimate depending on the velocity of the clouds v and the distance r to the SMBH.

$$M_\bullet = \frac{r\,v^2}{G}.$$

Keplerian orbits are assumed for the BLR clouds hence the FWHM of the broad lines is supposed to be created by Doppler shift. The velocity can then be obtained from the measured FWHM of an observed broad line. To account for using half the FWHM and for velocities in three dimensions the velocity derived from the FWHM is corrected by a factor of $\sqrt{3}/2$.

The radius can be obtained by reverberation mapping for some AGN. Reverberation mapping (Blandford & McKee 1982; Wandel et al. 1999; Kaspi et al. 2000) analyzes the time response of the ionization lines in the BLR to the variable ionizing continuum, i.e., emission from the accretion disk, assuming an expansion of the continuum photons at the speed of light, and a free path way between continuum source and BLR. This method is limited only by time, i.e., time needed for an adequate signal-to-noise[15] and an appropriate time resolution of the variability and response.

Wandel et al. (1999) and Kaspi et al. (2000) investigate the BLR radius to continuum luminosity $\lambda 5100$ Å relation empirically and find differing slopes for their correlations ($R \sim L^{0.5}$ and $R \sim L^{0.7}$ respectively). The problem with the continuum luminosity at $\lambda 5100$ Å is that it can be contaminated, e.g., star formation in the host. Bentz et al. (2006, 2009) revisit this relation and find that with proper host starlight correction the relation is $R \sim L^{0.52}$ similar to Wandel et al. (1999) and similar to simple photoionization models.

To omit the contamination issue Greene & Ho (2005) analyze the relation of the Hα and Hβ broad emission lines to the $\lambda 5100$ Å continuum and to each other respectively regarding luminosity and width. Their empirical approach proves the single epoch mass estimates by Dibai (1977) who used a basic photoion-

---

[15] The signal-to-noise ratio can be improved by adding up several observations taken one after the other if the observed signal can be assumed constant. The idea behind this is that the random noise will cancel out whereas the signal grows by summation. This is inferred from simple error propagation

$$\frac{S}{N} = \frac{nS}{\sqrt{n\sigma^2}} = \sqrt{n}\frac{S}{\sigma}$$

with S the signal, N the noise in one measurement, n the number of summed observations, and σ the standard deviation of a single measurement. However, not all noise in a system is random, e.g., noise introduced by vibrations at specific frequencies, therefore this method has limits to improving the signal-to-noise ratio.

ization model[16]. Kim et al. (2010) update the relations found in Greene & Ho (2005) by using the radius-continuum relation by Bentz et al. (2009), which is recalibrated using proper continuum decomposition. They find a relation of

$$M_\bullet = 10^{6.88\pm0.57} \left(\frac{L_{\mathrm{H}\beta}}{10^{42}\ \mathrm{erg\ s^{-1}}} \right)^{0.46\pm0.05} \left(\frac{FWHM_{\mathrm{H}\beta}}{10^3\ \mathrm{km\ s^{-1}}} \right)^2 \mathrm{M_\odot}$$

with the Hβ luminosity and FWHM $L_{\mathrm{H}\beta}$ and $FWHM_{\mathrm{H}\beta}$. They go on and derive new mass estimators from the NIR Paα and Paβ lines to avoid contamination by dust obscuration and imperfect extinction correction.

1.4 Star Formation in Galaxies

Star formation is the process that turns hydrogen into metals therefore changing the composition of the gas in a galaxy. Hence, star formation is the important process in galaxy evolution, e.g., young galaxies show bluer colors due to hot young stars than old galaxies which are red in color due to old cool stars. This process is usually a local phenomenon in a galaxy where out of molecular gas clouds several millions of stars can form. For a molecular cloud to collapse and fragment into dense cores it needs to be cooled and the angular momentum of the cloud has to be lowered sufficiently. The gas is cooled by collisions with dust particles or metals which then emit photons hence taking away kinetic energy and transforming it into emission which then can leave the molecular cloud. The angular momentum problem is still unsolved but on large scales density waves, i.e., spirals or bars, can induce transport of angular momentum and allow for a collapse of molecular clouds.

1.4.1 Diagnostic Diagram

There are also cases where across the whole galaxy star formation is taking place almost simultaneously, on galactic scales. These are called Starburst galaxies

---

[16] The ionization parameter U is defined as:

$$U = \frac{Q}{4\pi r^2 c n_e}$$

with the Q the number of ionizing photons, r the distance to the ionizing source, c the speed of light, and n_e the electron density. The average energy of an ionizing photon can be written as $\bar{E} = L_{\mathrm{ion}}/Q$ with the ionizing luminosity L_{ion}. Hence, the equation above can be written as

$$U = \frac{L_{\mathrm{ion}}}{4\pi r^2 \bar{E} c n_e}$$

and distance to the ionizing source and luminosity should be related as $r \sim L^{0.5}$.

and they are very bright in the UV regime, i.e., direct light from young stars, e.g., OB type stars, is seen, or in the Far-Infrared (FIR) regimes due to high emission from dust by reemitted UV photons. Since it is not easy for star formation to occur even locally, it must be drastic events that trigger star formation all over the galaxy at the same timescales, e.g., galaxy-galaxy encounters, where huge tidal forces act on the gas distribution in the participating galaxies. Due to the strong UV and optical emission it is not easy to distinguish starburst from Seyfert galaxies by their color. As mentioned above Starburst galaxies show strong emission in UV but also in spectral emission lines. To distinguish between Starburst and Seyfert galaxies emission line ratios in diagnostic diagrams, also Baldwin, Phillips & Terlevich (BPT) diagrams, are used. The most famous BPT diagram (see Fig. 1.3) is the ([N II] $\lambda 6583$ Å)/(Hα $\lambda 6563$ Å) vs. ([O III] $\lambda 5007$ Å)/(Hβ $\lambda 4861$ Å). The line ratios are chosen from nearby lines to minimize the effect of extinction. The solid line marks the demarcation between
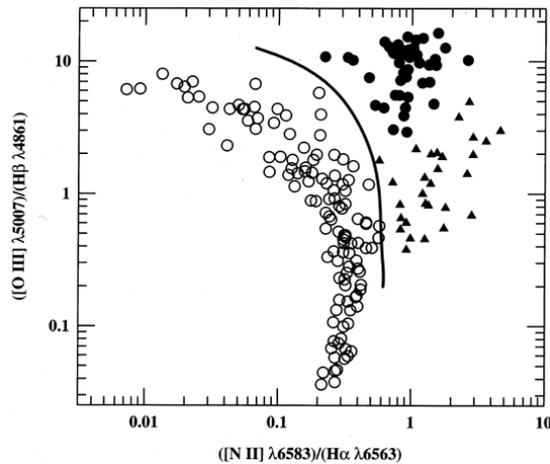
Figure 1.3: The BPT diagram showing ([N II] $\lambda 6583$ Å)/(Hα $\lambda 6563$ Å) vs. ([O III] $\lambda 5007$ Å)/(Hβ $\lambda 4861$ Å). Open circles represent H II region galaxies, filled circles represent Seyfert 2 like AGN and the filled triangle represent LINERs. The figure was taken from Peterson (1997).

galaxies dominated by star formation and galaxies dominated by nuclear AGN emission. In the NIR the line ratio (H$_2$(1-0)S(1) $\lambda 2.122$ μm)/(Brγ $\lambda 2.166$ μm) vs. ([Fe II] $\lambda 1.257$ μm)/(Paβ $\lambda 1.282$ μm) or modifications of it are used (see Fig. 4.6). These diagrams are not only to be used on apertures as big as the galaxy itself but also on subregions, e.g., nucleus, star forming regions, or shock regions, to determine the excitation mechanism in this part of the galaxy.

1.4.2 Continuum Decomposition

Normal galaxies show a variety of stellar populations from newly formed to old stars. These form the Spectral Energy Distribution (SED) of normal galaxies together with gas and dust emission at different temperatures. To estimate the fractions of these different components of the spectrum a decomposition of the SED is needed, which is a complicated task. Different stellar populations can be traced by imprints in the spectrum, e.g., occurrence of hydrogen recombination lines in absorption or other absorption lines like CO(2-0) $\lambda 2.29\ \mu$m. Bumps in the spectrum resulting from the black body emission peaks can be used to identify dust emission, e.g., hot dust at its sublimation temperature of $T \sim 1300$ K peaks at a wavelength of $\lambda \sim 2.23\ \mu$m. But for a sophisticated approach data from several wavelength regimes are required to disentangle the composition of an observed galaxy spectrum properly. For example, different compositions of star forming ages and metallicities can create similar absorption features. A good approach is a linear combination of several template stars, dust black body emission, and a power-law together with a dust screen component. Based on Smajić et al. (2012) following expression will be used

$$con_{obs} = \exp\left(-\tau\right) \times \left(\sum_i a_i star_i + bB_\lambda(T) + c\lambda^{\alpha-2} \right),$$

where con_{obs} is the observed continuum, $\exp\left(-\tau\right)$ is the absorption coefficient as described in Sect. 1.1.3, a_i, b, and c are scaling factors, $star_i$ are stellar template spectra, $B_\lambda(T)$ is the Planck function (see Sect. 1.1.1), and $c\lambda^{\alpha-2}$ is a power-law (see Sect. 1.1.1) for the decomposition of the observed galactic spectrum.

1.4.3 Star Formation Strength

To measure the strength of recent (a few 1 Myrs to a few 10 Myrs) star formation the UV is the most important observable, since only young hot stars are dominant in the UV regime. As mentioned above, the UV heats dust that then reemits the UV photons in the infrared, e.g., at 60 μm, and allows for an estimate also from this wavelength regime. Older cooler stars can also heat dust but due to their lower temperature the dust emission peaks at $\sim 100\ \mu$m. The general idea here is that the ionizing photons from the stars are measured, i.e., counted, which allows to estimate the number of ionizing stars using the underlying Initial Mass Function (IMF). Furthermore, the current formation rate of these stars can be given by dividing their current number by their calculated lifetime. This is called the Star Formation Rate (SFR). The hydrogen recombination lines scale well

with the Lyman continuum flux. Therefore they can be used as a measure for the SFR. The calibration by Panuzzo et al. (2003) will be used

$$\mathrm{SFR} = \frac{L_{\mathrm{Br}\gamma}}{1.585 \times 10^{32}\mathrm{W}} \mathrm{M}_\odot \mathrm{yr}^{-1},$$

with $L_{\mathrm{Br}\gamma}$ the luminosity of Brγ in W.

Another measure for star formation is the SuperNova Rate (SNR). Supernovae are stellar explosions that are distinguished into Type I (no Hydrogen lines) and Type II (Hydrogen lines) supernovae. They mark the end of a stellar life. The progenitor of a Type II supernova is a massive star (> 8 M$_\odot$) which means a liftetime of a few Myrs to some 10 Myrs. These stars become stellar black holes. Type I supernovae are distinguished in Type Ia (Si II $\lambda6150$Å emission) and Type I b/c (no Si II $\lambda6150$Å emission). Type Ia supernovae are those used for standard candles since the brightness always peaks to the same amount. This can be explained because their progenitors are white dwarfs that usually would not undergo supernova explosions but since they accrete mass from a binary companion they exceed the Chandrasekhar limiting mass of ≈ 1.4 M$_\odot$ and nuclear fusion is initiated in a few seconds in the whole star. The power generated disrupts the star completely. White dwarfs form out of stars with less than 3 M$_\odot$ hence the lifetime of the progenitors of Type Ia supernovae are of the order of 10^9 years or more therefore old stellar populations are traced. Type Ib/c supernova progenitors are intermediate mass stars ($\approx 3 - 8$ M$_\odot$) that after exploding end as a neutron star thus young stellar populations of less than 100 Myrs are traced. The empirically derived calibrations of the SNR in dependence of the [Fe II] $\lambda1.64\,\mu$m luminosity from Calzetti (1997)

$$\mathrm{SNR}_{\mathrm{Cal97}} = 5.38\,\frac{L_{\mathrm{[Fe\,II]}}}{10^{35}\mathrm{W}}\,\mathrm{yr}^{-1}$$

and Alonso-Herrero et al. (2003)

$$\mathrm{SNR}_{\mathrm{AlH03}} = 8.08\,\frac{L_{\mathrm{[Fe\,II]}}}{10^{35}\mathrm{W}}\,\mathrm{yr}^{-1}$$

will be used, respectively. The [Fe II] $\lambda1.64\,\mu$m emission line is very shock sensitive with a high ionization potential for Fe II of 16.4 eV. It is ionized in partially ionized hydrogen regions. The main ionization mechanisms are shocks, e.g., supernovae or X-rays in AGN. Both excitation mechanisms are also visible at 6 cm radio emission and correlate well with the [Fe II] emission (e.g., Forbes & Ward 1993). Young stars can ionize [Fe II] as well but at very low Fe II/H II ratios, e.g., [Fe II] $\lambda1.64\,\mu$m/Br$\gamma \lesssim 1.5$, than compared to supernova, e.g., [Fe II] $\lambda1.64\,\mu$m/Br$\gamma \gtrsim 8.5$, or X-ray excitation. These limits were empirically derived by Rodríguez-Ardila et al. (2005).

1.5   Rotation in Galaxies

The rotation of external galaxies has been first noticed in line shifts in galaxy spectra. These shifts are observable in nebular emission lines (e.g., H I 21 cm, Hα) and stellar absorption lines (e.g., CaT, CO(2-0)). Nebular emission lines describe the rotation of the gas and molecular clouds whereas the stellar absorption lines describe the stellar velocity field. In a sole disk system these two will not have differential velocity fields; however, most galaxies have a stellar bulge which is not coupled to the disk and which is stabilized by random motions of the stars. In these galaxies stellar rotational velocities are usually smaller than gaseous velocities due to the dissipative nature of gas and smaller asymmetric drift.
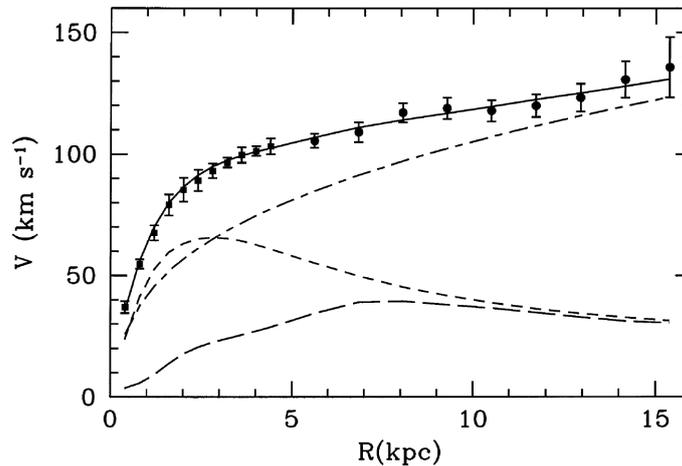

Figure 1.4: The rotation curve for the galaxy M 33 as measured by the H I 21 cm line (data points). The solid line is the best model fit with contributions from gas (long-dashed line), the stellar disk (short-dashed line), and halo (dot-dashed line). Credit: Corbelli & Salucci (2000)

The H I 21 cm line is the most important tracer of gas rotation. Most of what is known today has been based on observations of the this emission line because it can be traced far out from the center of galaxies. Rotation diagrams of H I 21 cm, e.g., Fig. 1.4, show a rotation curve that does not decline with the expected Keplerian $v \propto r^{-1/2}$ rotation and even keeps on rising as in the case of M 33, stay at a constant velocity or drop off slowly. These observations showed that there must be a significant amount of mass contributing to the potential that could not be observed (dark matter), i.e., not of stellar or gaseous origin. The rise before the expected drop off can be attributed to the stellar bulge potential. Similar to the gravitational potential within a filled sphere the velocity is propor-

tional to $\sim r$. Very close to the center of the galaxy the BH potential is dominant and a Keplerian motion with $v \propto r^{-1/2}$ can describe the the rotational velocity. Figure 1.5) illustrates this in a log-log rotation diagram. On scales $r < 1$ pc the BH dominates with Keplerian motion. On scales $\sim 10^3 > r > 1$ pc the bulge potential dominates. A peak in rotational velocity is observed at ~ 2 kpc in the case of Milky Way followed by a small drop that resembles Keplerian motion at first but then is strongly disturbed by the halo potential.
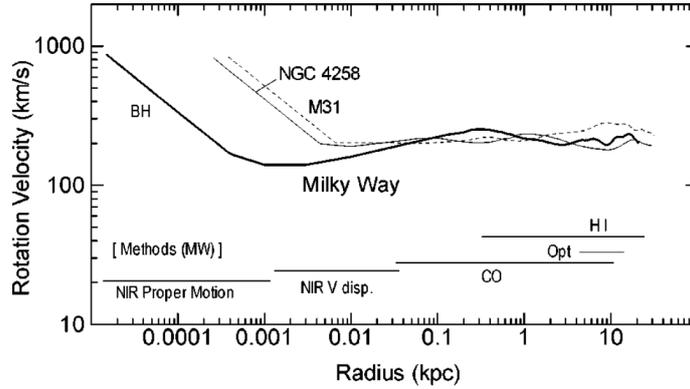
Figure 1.5: Log-Log rotation diagram for Milky Way, NGC 4258, and M 31. Innermost regions are calculated velocities for massive BHs. Observational methods are for the case of Milky Way. For more detail see text. Credit: Sofue & Rubin (2001)

The bulge potential can be described by the Plummer potential

$$\Phi(r) = -\frac{GM}{\sqrt{a^2 + r^2}}$$

with the radius r, a scalelength a, and the bulge mass M. This potential was introduced by Plummer (1911) to fit observations of globular clusters. Taking as an assumption that the stars are on closed orbits, the gravitational and centrifugal forces have to compensate each other at any given point. From this the velocity v of the star can be determined by

$$v^2 = r\frac{\mathrm{d}\Phi}{\mathrm{d}r}$$

$$\Rightarrow v = \sqrt{\frac{GM\,r^2}{(a^2 + r^2)^{\frac{3}{2}}}}.$$

It will be used for later analysis as an approximation of the bulge potential in the inner few 100 pc of NGC 1566.

Overview

2.1 The NUGA sample

The Nuclei of Galaxies (NUGA) project as initially defined by García-Burillo et al. (2003); García-Burillo et al. (2003) is a multi-wavelength approach on nearby AGNs. The main goal is to find answers on how gas from the host is allowed to fall towards the AGN, i.e., what mechanisms are responsible for removing angular momentum from the gas, and if these mechanisms are only prominent in AGNs or if the amount of available gas is the main difference between quiescent and active galaxies. For example, bars and galaxy interactions produce kiloparsec perturbations that are clearly related to the onset of activity in high-luminosity AGNs (Hutchings & Neff 1992).

There are several candidates which can lead to the feeding of an LLAGN, e.g., large-scale bars, nested bars, nuclear spirals, warps, and stellar winds. Theoretical models and numerical simulations indicate that not a single mechanism is responsible for the feeding but that several mechanisms work together on different scales to allow gas infall to the AGN (Hopkins & Quataert 2011a,b; Hopkins et al. 2011).

The sample is planned to complete to about 30 AGNs that span the activity categories of nearby AGNs (LINERs, Seyfert 1, and Seyfert 2). The idea behind the selection of the sample is to analyze high spatial resolution data, i.e., $< 1''$ angular resolution which corresponds to < 100 pc in physical units and to use multi-wavelength data in the optical, NIR, and mm wavelength regime.

The high resolution is needed especially for the very central few arcseconds since the feeding goes below scales of < 10 pc, e.g., the obscuring torus structure scale (see Sect. 1.2.2). To achieve these scales either space observations, e.g., by the Hubble Space Telescope (HST) for the NIR and optical, or (Adaptive Optics (AO) assisted) ground based observations, e.g., by Spectrograph for INtegral Field Observation in the Near Infrared (SINFONI) at the Very Large Telescope (VLT) in the NIR, or interferometric observations, e.g., by the Atacama Large Millimeter/Sub-millimeter Array (ALMA) for sub-mm and mm wavelength regime, are needed.

The multi-wavelength approach enables a thorough analysis of the observed

region. The optical provides information on dust distribution, e.g., dark regions in optical images, star formation history from well studied optical spectral features, and the distribution, excitation, and kinematics of ionized gas, e.g., Hα emission.

The NIR provides the distribution of the mass dominating old stellar population and with it the stellar potential that exerts torques on the gas distribution. Additionally, the NIR is not prone to obscuration by dust hence one can probe deeper than in the optical giving a more reliable estimate of the ionized gas and its characteristics. Furthermore, the hot molecular gas distribution, excitation, and kinematics can be analyzed, e.g., H$_2$ emission lines, which is of importance close to the nucleus on scales of < 100 pc where molecular gas can be easily excited by stars, the AGN directly, or outflows.

The sub-mm and mm observations detect the cold molecular gas distribution, e.g., CO transitions, which is one of the best molecular gas tracers. Most of the gas in the central kiloparsec is cold (< 100 K) and in molecular phase, making observations of CO transitions the ideal candidate to probe the distribution, excitation, and kinematics of the bulk of the gas.

The combination of these characteristics allows to derive the torque budget of the gas in the inner < 1 kpc of nearby galaxies and compare this to the observed regions of star formation, ionized gas, and excited gas.

The results of the so far observed NUGA sources are that one-third show a negative torque budget down to scales of < 100 pc, indicating removal of angular momentum, i.e., gas inflow. However, two-third of the observed sources show a positive torque budget down to scales < 300 pc, indicating outflowing gas. These sources were observed with the Institut de Radioastronomie Millimétrique (IRAM) Plateau de Bure Interferometer (PdBI) in CO and NIR imaging was used as input for the torque budget calculation.

These results infer that higher spatial resolution is needed for the central regions, e.g., using the newly operational ALMA interferometer for (sub)mm observations and (AO assisted) Integral Field Spectrograph (IFS) ground observations in the NIR with SINFONI. The higher spatial resolution will shed light on the central few parsecs to a few ten parsecs and give information on how the warm gas, which is strongest in emission at the very nucleus, behaves compared to the cold gas, e.g., H$_2$(1-0)S(1) to ^{12}CO(3-2) distribution, excitation and kinematics (see Smajić et al. 2014, 2015, and references therein).

2.2 Feeding and Feedback in AGNs

Unresolved, powerful, and highly ionizing emission detected in the centers of galaxies is believed to stem from accretion events onto a SMBH, the AGN of these galaxies. According to the unified model of AGNs this active nucleus consists of a SMBH surrounded by an accretion disk at scales of up to a few lightdays which ionizes the surrounding gas on scales from several lightdays, in Seyfert galaxies, up to lightyears, in Quasi Stellar Objects, (e.g., BLR) to several hundred parsecs (e.g., NLR) and up to even larger scales via jets. The torus, a dust and gas mantle, surrounds the AGN on parsec to tens of parsecs scales and is thought to be responsible for Seyfert 1 (torus almost face-on toward the observer) and Seyfert 2 (torus almost edge-on) classifications of AGNs. The existence of the torus can be inferred from high column densities toward Seyfert 2 AGNs and dust blackbody emission in Seyfert 1 AGNs with temperatures up to the sublimation temperature of dust (≈ 1300 K). For more details see Sect. 1.2.2.

The host galaxy and its SMBH have been empirically found to exhibit tight correlations. These correlations apply to the stellar bulge (e.g., Magorrian et al. 1998; Ferrarese & Merritt 2000; Marconi & Hunt 2003). The correlations connect the mass of the central SMBH with the mass, luminosity, and kinematics of the bulge. Latest studies show that these correlations may depend on the galaxy classification (e.g., barred galaxies, Graham & Scott 2013) and that several galaxies show an over-luminous bulge or an under-massive SMBH (Busch et al. 2014). Läsker et al. (2014) imply that the total luminosity of the host galaxy seems a more robust tracer of the SMBH mass than the bulge luminosity. The distribution of the gas in the host is essential to understand these correlations, since gas is the progenitor of stars which mainly contribute to mass, luminosity and kinematics of the bulge.

AGN feedback on galaxy size scales seems to be responsible for the observed relations. Several feedback models can be found in the literature (see Fabian 2012, and references therein). In general it is assumed that the BH blows away the surrounding material from the bulge, e.g., via radiation pressure or radio jets, as soon as it reaches a critical mass and strips the host from its gas content. This negative feedback eventually quenches star formation in the host and stops the growth of the BH itself by self-regulation. Depending on the parameters, however, the BH might not be able to expel the gas completely hence inducing star formation by compression of the ISM in the shell of the feedback (Ishibashi & Fabian 2012). However, gas in nearby $z \sim 0$ galaxies is available close to the SMBH allowing accretion to take place. The question remains how the gas returned from these galaxy scales to the SMBH and how accretion does look on tens to hundreds of pc scales?

Gravitational torques are one of the strongest form of force to act on the distribution of the gas on these scales. Gravitational mechanisms that exert gravitational torques such as galaxy-galaxy interactions (e.g., galaxy merger) or non-axisymmetries within the galaxy potential (e.g., spiral density waves or stellar bars on large scales) can lead to loss of angular momentum in the gas. Hydrodynamical mechanisms such as shocks and viscosity torques introduced by turbulences in the interstellar medium (ISM) can remove angular momentum from gas, too. The original NUGA (north) project has already studied the gaseous distribution in more than ten nearby galaxies ($\approx 4 - 40$ Mpc) with results that show a variety of morphologies in nuclear regions, including bars and spirals (García-Burillo et al. 2005; Boone et al. 2007; Hunt et al. 2008; Lindt-Krieg et al. 2008; García-Burillo et al. 2009), rings (Combes et al. 2004; Casasola et al. 2008; Combes et al. 2009) and lopsided disks (García-Burillo et al. 2003; Krips et al. 2005; Casasola et al. 2010).

On large scales, hundreds to thousands of parsecs, gravitational torques are the strongest mechanism to successfully transport gas close to the nucleus, whereas viscosity torques can take over on smaller scales (< 200 pc, e.g., Combes et al. 2004; van der Laan et al. 2011). Therefore, large-scale stellar bars are an important feature to transport gas toward the inner Lindblad resonance (ILR) (e.g., Sheth et al. 2005) where the formation of nuclear spirals and rings is induced.

So far, the NUGA sample studied the cold gas distribution. These studies are used as a complement to my SINFONI NIR observations by comparing the sites of hot molecular and ionized gas (Combes et al. 2013, 2014; Smajić et al. 2014, 2015). This enables the identification of ongoing star formation sites and regions ionized by shocks (i.e., super novae (SN) or outflows). Furthermore, comparing the distribution of cold (e.g., CO, HCN) and hot (e.g., H_2) molecular gas will give a more clear insight on feeding and feedback of the AGN through its ambient gas reservoir. Riffel et al. (2013, and references therein) assume that molecular gas (e.g., H_2) traces the ambient disk structure and in some cases the streaming motions, i.e., the feeding of the SMBH, whereas ionized gas often traces outflowing material that is above the galaxy disk plane, i.e., the feedback from the SMBH. However, molecular emission lines in the NIR (e.g., H_2(1-0)S(1) emission) are known shock tracer that are found in regions shocked by jets or outflows (e.g., Riffel et al. 2014; Davies et al. 2014, and references therein). Lately, García-Burillo et al. (2014) find that cold molecular gas (e.g., $^{12}CO(3-2)$ emission) can be found in outflows.

In this thesis I will analyze the interactions of nuclear star formation sites and the AGN with regard to fueling and feedback. Using the differently excited H_2 lines (e.g., H_2 $\lambda 2.12$ μm, 1.957 μm, 2.247 μm) and the hydrogen recombination

line Brγ in K-band and the forbidden transition [Fe $\textsc{ii}$] $\lambda 1.644$ μm in H-band allows to put constrains on the excitation type (e.g., thermal, non-thermal) of the warm gas and the excitation temperature (Mouri 1994; Rodríguez-Ardila et al. 2004; Zuther et al. 2007). The cold gas information can then be compared to the NIR results.

I will use the emission lines Brγ and [Fe $\textsc{ii}$] and the stellar absorption features (e.g., Si $\textsc{i}$, CO(6-3), Mg $\textsc{i}$, Na $\textsc{i}$, CO(2-0)) to get insight into the star formation history of the nuclear region (e.g., Davies et al. 2007). Star formation, recent or ongoing, on scales of $0.1 - 1$ kpc around the nucleus is an important process which is frequently found in all types of AGNs in contrast to quiescent galaxies (e.g., Cid Fernandes et al. 2004; Davies et al. 2006; Busch et al. 2015). The debate if outflows from the AGN quench or initiate star formation is current, but it is most probable that outflows can induce both effects.

CHAPTER 3
Data Reduction

The galaxies analyzed in this thesis were observed with the VLT integral field spectrograph SINFONI (Eisenhauer et al. 2003; Bonnet et al. 2004) on Cerro Paranal in Chile. It uses a 2k × 2k Hawaii 2RG infrared detector for observations in the J, H, K, and H+K bands covering a wavelength range from $1.10\mu m - 2.45\mu m$ at a spectral resolution of ~ 2000, ~ 3000, ~ 4000, and ~ 1500 respectively. Three different Field Of Views (FOVs) are available, $8'' \times 8''$ in no AO mode, and $3'' \times 3''$ and $0\rlap{.}''8 \times 0\rlap{.}''8$ with AO. An image slicer is used to cut the observed FOV into 32 slits. These slits are then reflected onto a grating which disperses the slits onto the infrared detector, see Fig. 3.1.

The raw image consists of the 32 horizontally placed slits which are vertically dispersed, i.e., spatial information is in horizontal direction and spectral information is in vertical direction. The slits are displaced with regard to the neighboring slit, i.e., neighboring slits detector pixel are not illuminated with light at the same wavelength.

The reduction of the raw images was conducted by the SINFONI pipeline version 2.3.2 for the following reduction steps:

- Checking the linearity of the detector pixels and flagging non-linear pixels from LINEARITY_LAMP exposures.

- Creating a master dark (current) frame from DARK exposures and flagging hot-pixels.

- Creating a master flat field frame from FLAT_LAMP exposures and flagging pixels above a given threshold.

- Computation of the optical distortion on the detector and estimation of the relative slit distances to the first slit with FIBER_NS exposures.

- Deriving wavelength dispersion coefficients and creating a wavelength calibration map using WAVE_LAMP exposures.

- Subtracting SKY from SCIENCE frames and divide by MASTER_FLAT. Reconstructing the FOV at every wavelength bin, i.e., creating a three dimensional cube with wavelength as the third dimension.
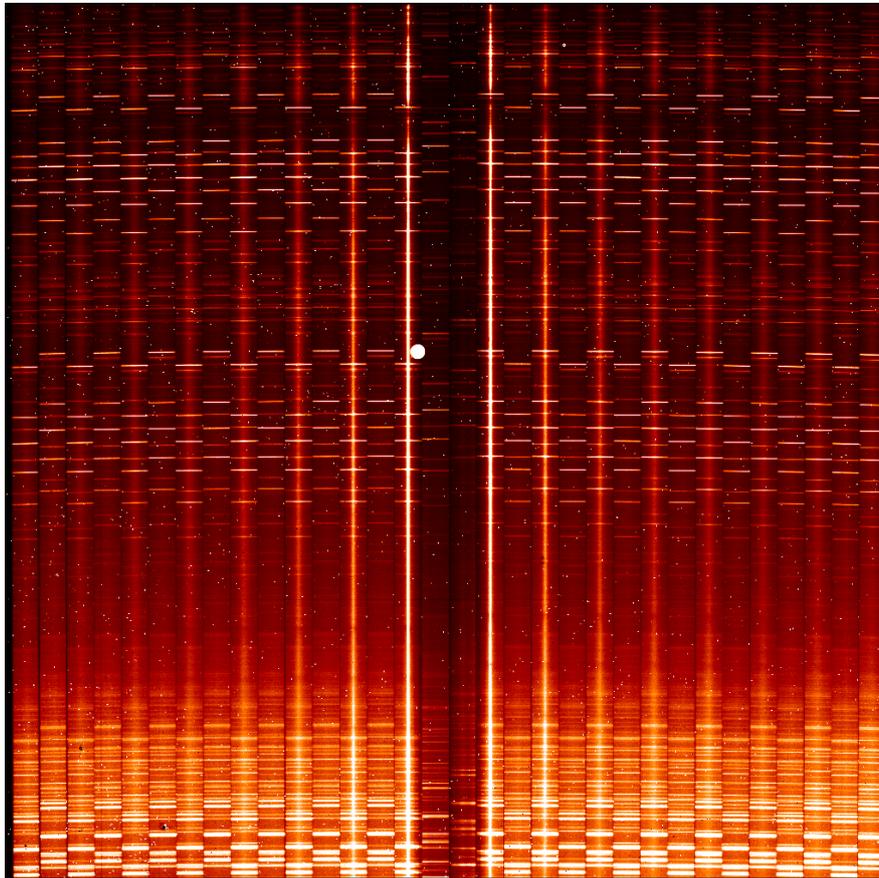
Figure 3.1: Raw SINFONI detector image from the observations. Long vertical lines are the observed object's center. The 32 displaced slits are distinguishable by dark pixel columns between them or by the displaced OH emission lines that are visible horizontally in the image. Note the characteristic cluster of bad pixels of the SINFONI detector in the upper central part of the image.

The creation of the mosaic out of all single exposure cubes was performed in Interactive Data Language (IDL) using scripts written by myself.

Further, I will discuss here two phenomena that showed up unexpectedly. In Sect. 3.1 a detector amplifier related problem is discussed. In Sect. 3.2 atmospheric emission line removal had to be refined since the pipeline was not able to give satisfactory results. Both phenomena were investigated and corrected using IDL scripts written by myself.

3.1 Detector Specific Pattern

During the data reduction a problem with the 32 SINFONI detector amplifiers had to be addressed that occurred during the observing period (Smajić et al. 2014). The detector amplifiers introduce two different types of variation in the arbitrary digital units (ADU) (see Fig. 3.2). These variations appeared and disappeared from one exposure to the next and were also found in the calibration data provided to the observation data. From the investigation of the affected files this problem was recognized in several particular amplifiers with random occurrence (from file to file), but fixed patterns were identified too. There are two different noise patterns within the amplifiers:

Pattern one is a constant offset in every other pixel column of an amplifier (see first row of Figs. 3.2 & 3.3). But the pattern is neither constant between two amplifiers nor between different exposures. It seems that this pattern occurs in several but not in all amplifiers and that there are amplifiers where it is usually stronger than in others.[1]

(a) Pattern One   (b) Pattern Two

Figure 3.2: The figure shows the last four pixels (from bottom to top). Shown are the two types of pattern that randomly show up on the SINFONI detector. When affected, it is always at least one amplifier (64 pixels or columns). Credit: Smajić et al., A&A, 567, A119, 2014, reproduced with permission © ESO.

Pattern two is a sinusoidal noise pattern in every four columns of one amplifier (see second row of Figs. 3.2 & 3.3). The pattern was fitted best with a sine function that added an offset of half a π to the next column. This pattern occurs only in amplifiers 14, 16, 18, and 20, counting from left to right and starting with 1.

The different patterns were observed in different as well as in the same data files, no superposition was observed. In one data file, an amplifier stopped showing a noise pattern after about 1000 rows.
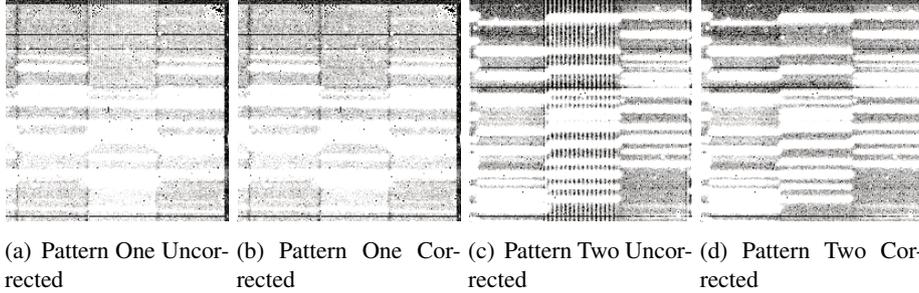
The last three pixels in every column of the detector were investigated. These pixels are control pixels which are not exposed to light but are influenced by the same electronic noise by which the exposed detector pixels are influenced.[2]

---

[1]Which amplifiers were affected by the pattern was not investigated in particular because the offset was sometimes very small. One could make it out by eye but the standard deviation was not much higher, if at all than in unaffected amplifier columns. A lot more time would have been needed to investigate the exact occurrence of this noise pattern.

[2]The first and last four pixels in every row and column are control pixels. Only the last three

(a) Pattern One Uncorrected   (b) Pattern One Corrected   (c) Pattern Two Uncorrected   (d) Pattern Two Corrected

Figure 3.3: The figure shows parts of the detector where the pattern was detected (a) & (c) and then corrected (b) & (d). Note that the dark horizontal lines are part of an already known detector problem. The bright extended horizontal lines are OH sky lines. The three darkish extended vertical lines in (a) & (b) are the slit borders of the 32 slitlets on the detector. Credit: Smajić et al., A&A, 567, A119, 2014, reproduced with permission © ESO.

These pixels allowed to determine if a noise problem is at hand in the amplifier columns by standard and mean deviation methods. The two problems were separated and the constant offset pattern was corrected first because it is easier to determine. The complication here was the automated correction due to a positive or negative ADU average combined with negative or positive constant offsets. After that the sinusoidal pattern was corrected by fitting a two-dimensional sine with 16 columns and four rows making up the 64 channels of every amplifier. The noise was detected and corrected in 66 data files (science and calibration data). The correction was successful as shown in figure 3.3. Weak noise patterns, which were not selected by our routines, can still make the resulting data files noisier, however, the difference to other noise sources (e.g., photon noise, readout noise) is almost not measurable.

3.2 Atmospheric Emission Correction

A more typical problem, i.e., the OH emission of the atmosphere (Smajić et al. 2014), had to be taken care of after correcting for the unusual detector noise features. The weather conditions were exceptional, i.e., photometric night, however, exposures of 150 seconds were too long for the fast changing atmospheric

---

in every column were used because in some exposures the first of the last four control pixel in a column seems to be slightly exposed, best seen in the fiber exposure data. In addition, the first four pixels in every column were not used because the noise offset here was usually different hence a combination of the first and last pixels in every column was not possible, also the very first and fourth pixel sometimes suffered from other effects (e.g., slightly exposed). The first and last pixels in every row are not interesting since this is a column wise problem.

(a) Method one (b) Method two
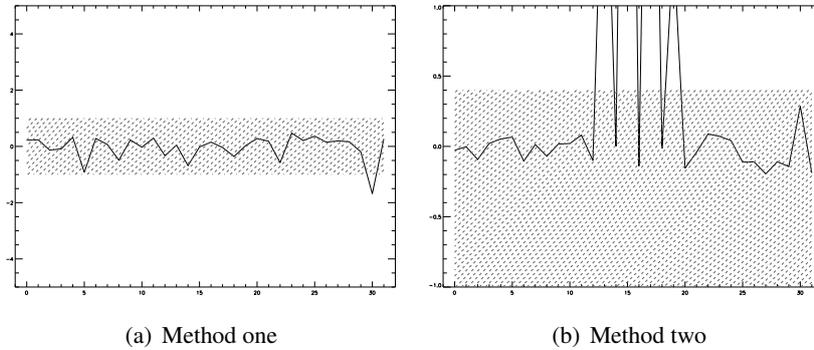
Figure 3.4: The selection criteria with which pattern one and pattern two were selected. The amplifiers are from the same affected exposure. All amplifier values outside the marked region flag the amplifier as infected. Method one finds that amplifier 30 is affected by pattern one (a) but it does not recognize anything in amplifiers 14, 16, 18, and 20. Method two (b) recognizes pattern two but does not find pattern one as effectively as method one.

OH line emission. The usual OH correction performed by the pipeline resulted in strong OH residuals. The higher density OH correction that was implemented following Davies (2007) resulted in a better correction in some parts but in a worse correction in others, for example 'P-Cygni' profiles in the OH lines were introduced. Comparing the raw target files with their pre/subsequent raw sky files, a change in the strength of the OH lines from target to sky was noticed by up to 10%. In addition, a random shift of about 0.04 pixel in the spectral direction of the detector was noticed. This was found by fitting Gaussian profiles to several OH lines. The selection of the OH lines used for investigation relied on lines with 100 peak counts above the continuum and on lines isolated enough to assume a reliable profile fit. Furthermore, OH lines were selected from every vibrational transition. All selected lines in one detector column were fitted simultaneously to improve the continuum fit.

A first result is that all fitted lines in a sky file differed by about the same factor, e.g., Fig. 3.5, and pixel difference, e.g., Fig. 3.6, with respect to the corresponding target file, in every detector column. Hence, the median of all OH lines (41 in H- and 16 in K-band) and all 32 slits (about 60 of 64 pixels per slit were used) was taken to determine the scaling factor and the shift of the OH lines. The fit did not work well at the edges of the slits due to contamination from the neighboring slit, hence the slit edges were neglected. As not to scale the continuum with the OH lines, the continuum was fitted in every detector column (spectral direction) and was subtracted before the OH line scaling. In H-band this was done by using a linear function. For the K-band continuum a blackbody
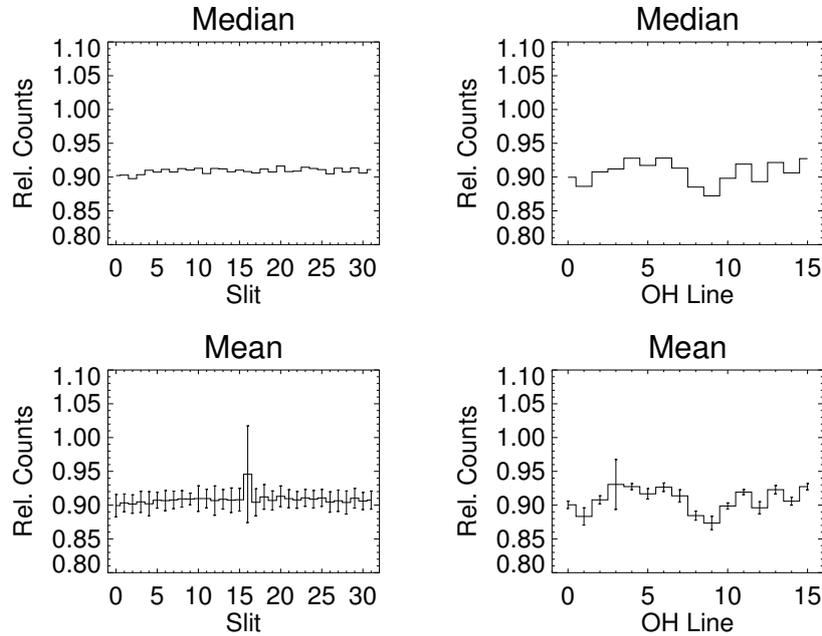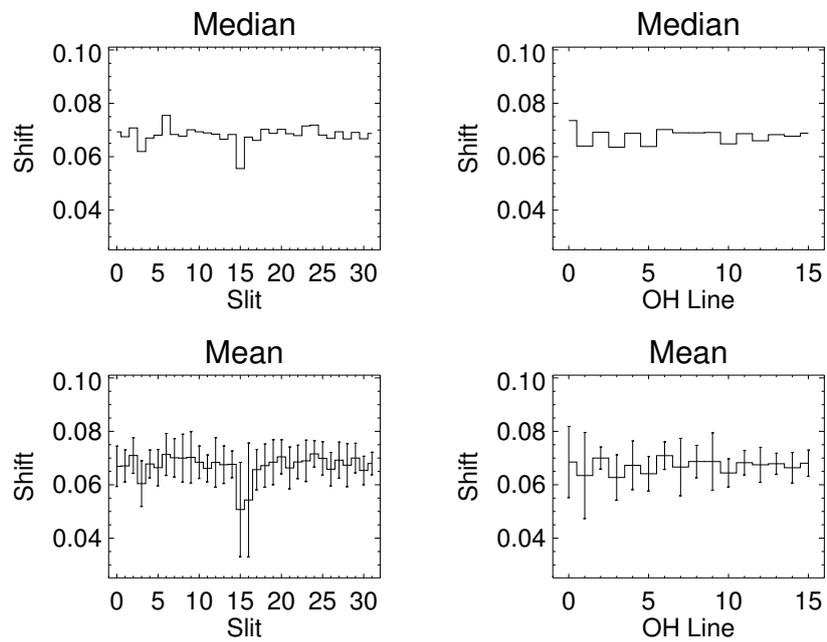
Figure 3.5: The relative flux difference in OH lines between consequent object and sky observations. *Top left*: Median over all OH lines in given detector slit. *Top right*: Median over all slits in given OH line. *Bottom left*: Mean over all OH lines in given detector slit with mean deviations. *Bottom right*: Mean over all slits in given OH line with mean deviations.

function was fitted, because the gray-body emission of the background becomes prominent at the red end of the K-band. The median of the fitted parameters over one slit was used to determine a robust continuum for the whole slit. After the subtraction of the continuum the remaining atmospheric emission features were scaled, the continuum was added back and then the full column was shifted by the determined subpixel shift. The scaling was done based only on the emission lines because the continuum does not vary. The spectral shift has to be performed on the full spectrum since the shift originates from a movement of the grating rather than from an atmospheric effect.

Figure 3.6: The shift in detector pixel of OH lines between consequent object and sky observations. *Top left*: Median over all OH lines in given detector slit. *Top right*: Median over all slits in given OH line. *Bottom left*: Mean over all OH lines in given detector slit with mean deviations. *Bottom right*: Mean over all slits in given OH line with mean deviations.

CHAPTER 4

The Seyfert 2 Galaxy NGC 1433

The barred, ringed, spiral SB(rs)ab galaxy, NGC 1433, is located in the Dorado group (Buta 1986; Kilborn et al. 2005; Buta et al. 2010) at a redshift of $z \approx 0.003586$ (see table 4.1, Koribalski et al. 2004). It is classified as Seyfert like by Veron-Cetty & Veron (1986), but Cid Fernandes et al. (1998) and Sosa-Brito et al. (2001) refined the classification in a low ionization narrow emission line region (LINER) galaxy using a stellar-continuum subtracted spectrum and extinction corrected optical emission lines. The position of the center of the galaxy coincides with the X-ray ROSAT source (Liu & Bregman 2005).

NGC 1433 shows a primary stellar bar of about 4 kpc in radius, located roughly in the east-west direction (PA 94°). Two rings, an outer ring at a PA of 15° and radius of 9.1 kpc and an inner ring with a radius of about 5.2 kpc and a PA of about 95° (see Fig. 4.1), can be identified. The secondary nuclear bar has a radius of 430 pc at PA 31° and is surrounded by a ring at the same PA and about 460 pc radius (see Fig. 4.1; Wozniak et al. 1995; Buta et al. 2001). The nuclear region shows no signs of recent star formation except for the nuclear ring which is the site of a starburst (Cid Fernandes et al. 1998; Sánchez-Blázquez et al. 2011). Measurements of the atomic H I 21 cm line show emission in the inner and outer rings and a depletion in the nuclear region (Ryder et al. 1996), whereas strong molecular CO emission is detected in the nuclear region (Bajaja et al. 1995). The H I measurement reveals a line of nodes at a PA of 201° and an inclination of 33°. The nuclear region is filled with dusty spiral arms visible in Hubble Space Telescope (HST, see Fig. 4.1) images (Maoz et al. 1996; Peeples & Martini 2006). These arms or filaments are very well traced by the molecular $^{12}CO(3–2)$ emission observed with ALMA (Combes et al. 2013). The $^{12}CO(3–2)$ emission just south of the nucleus shows a highly redshifted component at about 100 km s^{-1} indicating a possible outflow. Spitzer data imply that NGC 1433 harbors a pseudo-bulge (Fisher & Drory 2010).

The complex dynamical structure makes NGC 1433 a good candidate to search for the connection between warm molecular gas detected in the NIR, and cold molecular gas detected at a few hundred GHz. Are cold and warm gas following the same dusty spiral arms? Are bright emission regions of cold and warm gas coinciding? What evidences of an outflow can be seen in warm gas?
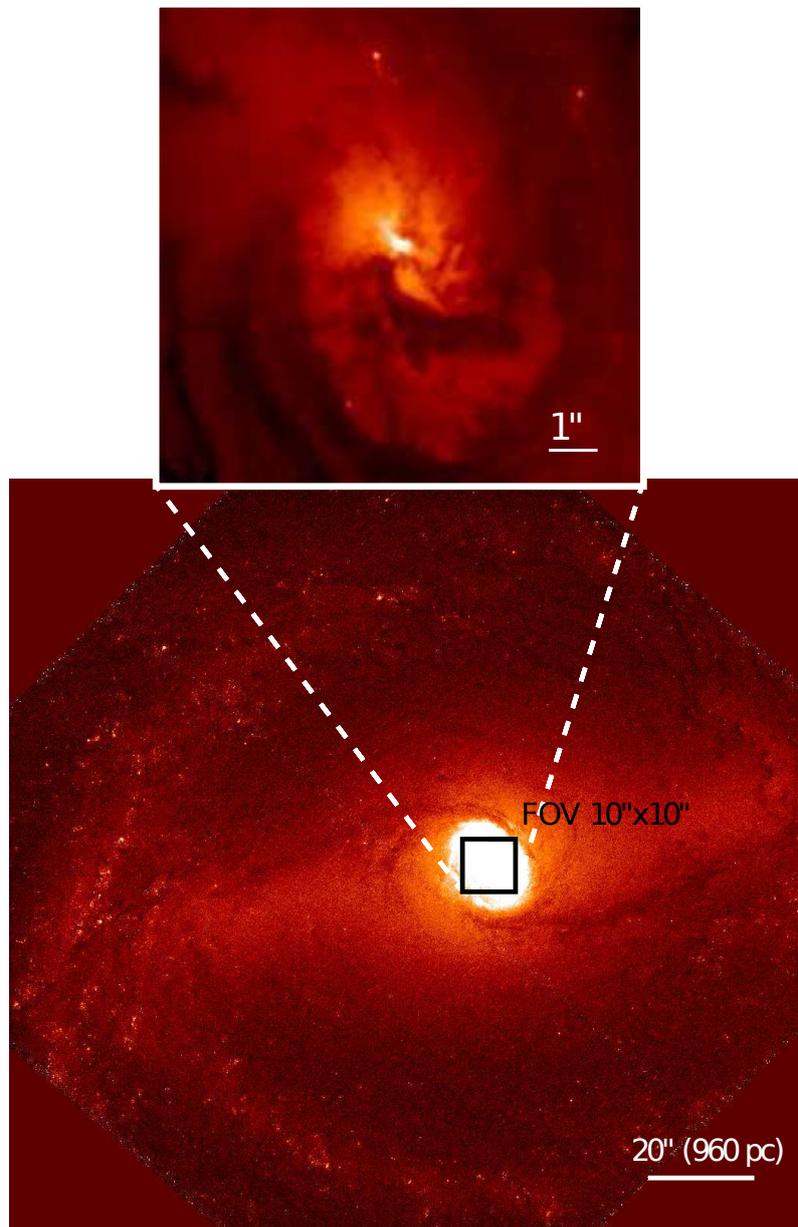
Figure 4.1: HST F438 wide field image of NGC 1433 taken from the ESA Hubble Science Archive. The SINFONI observation FOV of $10'' \times 10''$ is marked by a square. The color scale in the lower image was chosen to reflect the large scale structure of the host, e.g., main stellar bar. The top image shows the prominent dust lanes in the center of NGC 1433. Credit: Smajić et al., A&A, 567, A119, 2014, reproduced with permission © ESO.

4.1 Observation and Data Reduction

I present the results of my European Southern Observatory (ESO) SINFONI observations of NGC 1433 with the Unit Telescope 4 of the Very Large Telescope in Chile. The $0\rlap{.}''25$ plate scale was used with an $8'' \times 8''$ FOV without adaptive optics assistance. The average seeing during the observation was $0\rlap{.}''5$. A $\pm 2''$ dithering sequence was used, to increase the FOV and minimize the overlap of dead pixels in critical areas. Nine dithering positions were chosen in which the central $4'' \times 4''$ were observed with the full integration time. The resulting FOV is $12 \times 12''$, however, a FOV of $10 \times 10''$ is used for the analysis to increase the sinal-to-noise in the FOV. NGC 1433 was observed in the H-band grating with a spectral resolution of $R \approx 3000$ and in the K-band grating with a resolution of $R \approx 4000$. The digital integration time of 150 seconds per exposure was used in both bands with a ...TST... nodding sequence (T: target, S: sky), to increase on-source time. The overall integration time on the target source in H-band was 2400 seconds and in K-band 4500 seconds with additional 1200 seconds in H-band and 2250 seconds in K-band on sky. The G2V star HIP 017751 was observed in the H- and in K-band within the respective science target observation. Two object-sky pairs in H-band and four object-sky pairs in K-band were taken. The standard star was used to correct for telluric absorption of the atmosphere and to perform the flux calibration of the target. A high S/N solar spectrum (Maiolino et al. 1996) was used to correct the black body and intrinsic spectral features of the telluric G2V star. The solar spectrum was convolved with a Gaussian to adapt its resolution to the resolution of the standard star spectrum. The edges of the solar spectrum had to be interpolated by a black body with a temperature of $T = 5800$ K to get a correction at the edges of the bands. The standard star spectrum was extracted by taking the total of all spaxels within a $3 \times \mathrm{FWHM_{PSF}}$ radius of the point spread function (PSF) (Howell 2000), centered on the peak of a two-dimensional Gaussian fit. The flux calibration of the target source was performed during the telluric correction procedure. The standard star counts were calibradted at $\lambda 1.662\,\mu$m and $\lambda 2.159\,\mu$m, in H- and K-band, respectively, to the flux given by the 2MASS All-sky Point Source Catalog. A PSF FWHM of $0\rlap{.}''62$ in H-band and $0\rlap{.}''56$ in K-band was measured from the observed standard star (see Fig. 4.2). The PSF shows an elongation in the northeast to southwest direction at a PA of $69°$ (see Fig. 4.3).

Detector specific problems, which occurred during the observation period, were analyzed and corrected for and OH sky emission line corrections were applied (see Sect. 3.1).

The data reduction was performed with the SINFONI pipeline up to single-exposure-cube reconstruction. The wavelength calibration had to be refined by
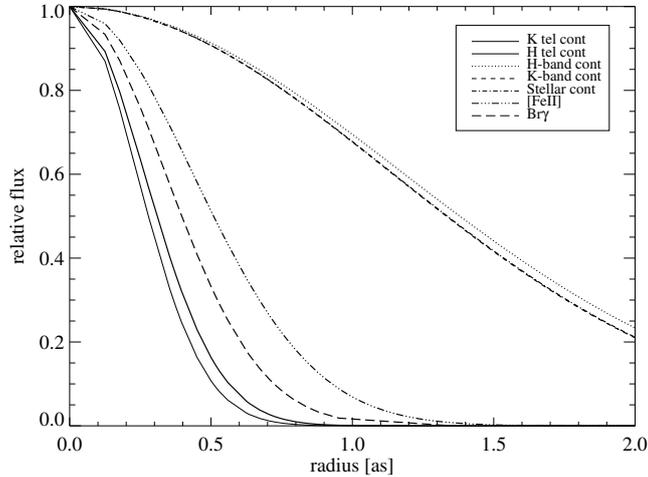
Figure 4.2: Shown are Gaussian fits to radial luminosity profiles of the K-band standard star continuum, the H-band standard star continuum, the H- and K-bands galaxy continuum, the fitted stellar continuum in the K-band, Fe II $\lambda 1.644$ μm, and Brγ. Note that K-band galaxy continuum and the fitted stellar continuum lie on top of each other. The Gaussian fit was centered on the galactic center. Credit: Smajić et al., A&A, 567, A119, 2014, reproduced with permission © ESO.

hand because of a constant offset introduced to the wavelength axis. The error introduced by this shift is ~ 3 km s^{-1}.

The linemap and spectra extraction was conducted using IDL scrpits written by me.

I use calibrated 350 GHz ALMA data from the ALMA archive for comparison with the SINFONI NIR results (Combes et al. 2013, observation and calibration details therein). Masks are used at 50 mJy, 30 mJy and 10 mJy emission levels. The map sizes are 720×720 pixels with a pixel size of $0\farcs05$ for cleaning. The line cube comprises 72 channels of 5 km s^{-1} width, centered on the systemic velocity, i.e., 1076 ± 180 km s^{-1}. The integrated intensity and continuum maps (line-free regions of all four spectral windows, i.e., 7 GHz) were corrected for primary beam attenuation. Imaging, cleaning, and parts of the analysis have been conducted with the CASA software (v3.3 McMullin et al. 2007).

4.2 Results and Discussion

The seeing limited imaging spectroscopy of SINFONI resolves the central 500 pc of NGC 1433 at a spatial resolution of 27 pc in K-band and 30 pc in H-band.

Several molecular ro-vibrational hydrogen lines and the narrow hydrogen recombination line Brγ $\lambda 2.166$ μm are identified. Stellar absorption features are detected in in H- and in K-band (e.g., CO(6-3) $\lambda 1.62$ μm, CO(2-0) $\lambda 2.29$ μm, NaD $\lambda 2.207$, CaT $\lambda 2.266$). The [Fe II] $\lambda 1.644$ μm line in the H-band, which is important for NIR diagnostics, is also detected. The emission lines properties were determined from Gaussian profile fits. A FOV of $10'' \times 10''$ instead of the available $12'' \times 12''$ is used because the signal-to-noise in the utmost outer regions is not good enough for a thorough analysis.

The new galaxy center is adopted in all figures shown (see table 4.1 and Sec. 4.2.4). The black $\times$ in all maps gives the position of the new adopted center of the galaxy, i.e., the location of the SMBH. The FWHM maps and values are not corrected for instrumental broadening, which is ~ 100 km s^{-1} in H-band and ~ 75 km s^{-1} in K-band, except when used to determine values, e.g., the black hole mass. Emission line properties, i.e flux and FWHM, of all discussed emission lines are summarized in table 4.2.

4.2.1 Gas Distribution

I will describe and compare the distribution of molecular, e.g., H$_2$(1-0)S(1), ^{12}CO(3-2), and ionized, e.g., Brγ, gas.

Ionized gas

In H-band, the forbidden line transition [Fe II] is detected in a resolved region at the center of about 38 pc in diameter (see Fig. 4.3). The flux peak is slightly offset to the south by one spaxel, i.e., $0''.125$. The shape of the emission looks slightly elongated in the northeast to southwest direction, similar to the PSF elongation. The Line-Of-Sight Velocity (LOSV) indicates that the line is redshifted with respect to the systemic velocity by ~ 20 km s^{-1}. The redshifted velocity maximum is ~ 18 pc south of the center with a velocity of -45 km s^{-1}. The blueshifted counterpart is at a velocity of ~ 20 km s^{-1} and lies north of the center. The line width is rather uniform with an FWHM of about 185 km s^{-1} and a faint broadening with an FWHM of 210 km s^{-1} in the center. The Equivalent Width (EW) peaks at the same position as the flux with ~ 2.2 Å indicating that the origin of the ionizing source is at the very center of the galaxy (see Fig. 4.5).
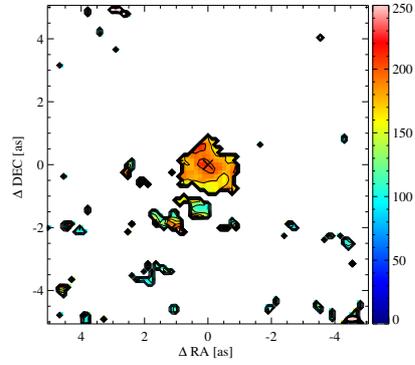
The hydrogen recombination line Brγ is detected only at the center, too, and is marginally resolved in a region of about 30 pc in diameter (see Fig. 4.3). Only a narrow component of this recombination line can be detected. The emission peaks at the center and is roughly elongated in the east-west direction. The line width peaks at the very center at an FWHM ~ 200 km s^{-1} and is similar to
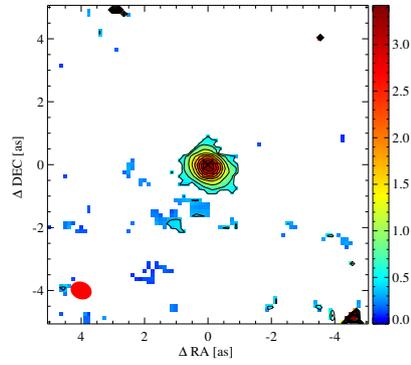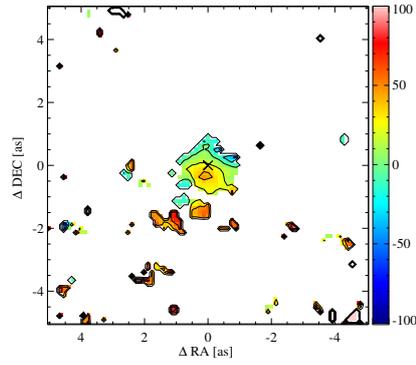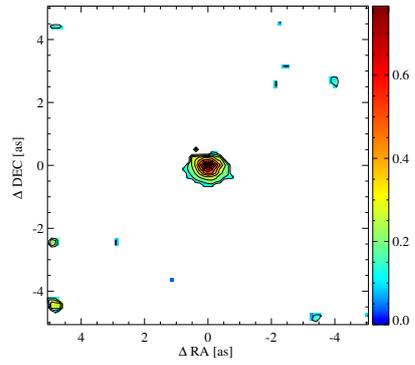
(a) Flux [Fe II]

(b) FWHM [Fe II]

(c) LOSV [Fe II]

(d) Flux Brγ
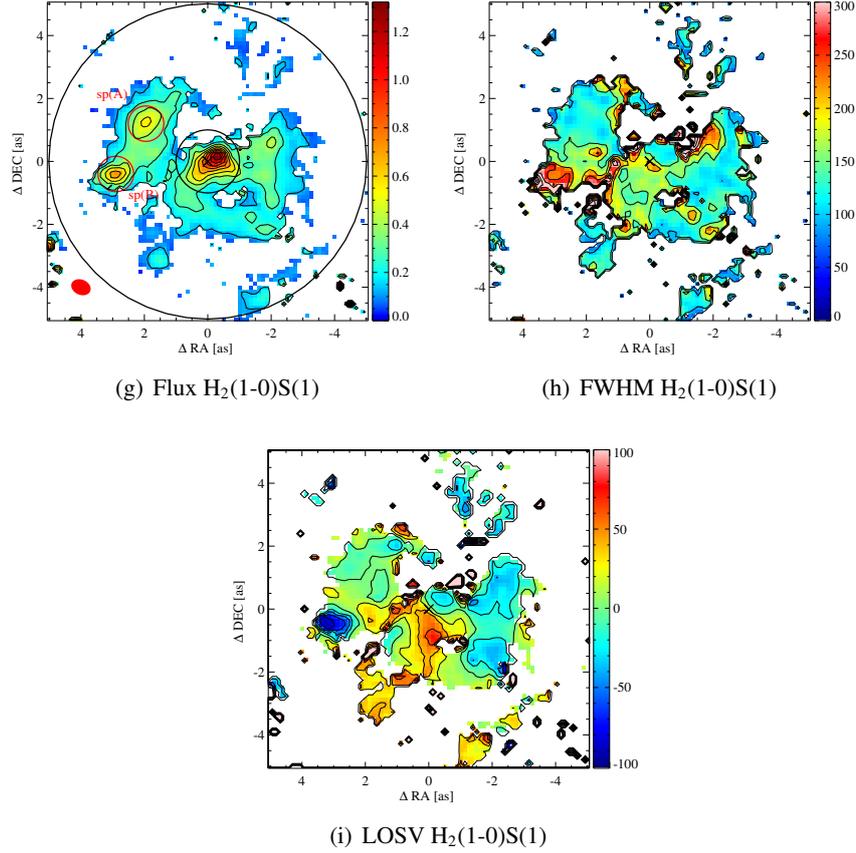
(e) FWHM Brγ

(f) LOSV Brγ

(g) Flux H$_2$(1-0)S(1)

(h) FWHM H$_2$(1-0)S(1)

(i) LOSV H$_2$(1-0)S(1)
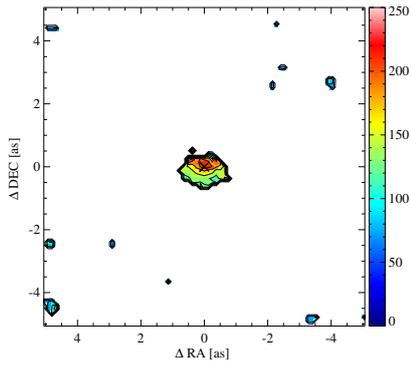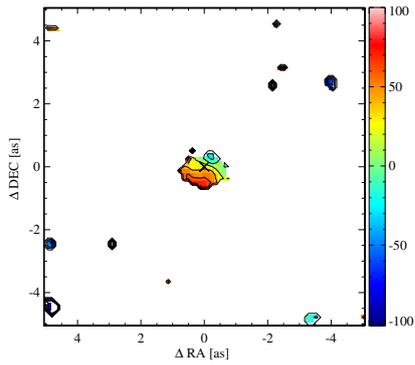
Figure 4.3: Shown are the flux [10^{-20} W m^{-2}], FWHM [km s^{-1}] and LOSV [km s^{-1}] maps (left to right) of the [Fe II], Brγ, and H$_2$ λ(1-0)S(1) lines (top to bottom). (a) and (g) show the beam size in the lower left corner for H- and K-band respectively. (g) shows the aperture sizes taken for the measurements. One angular resolution element (beam) corresponds to a PSF$_{\text{FWHM}}$ of 0$\farcs$62 in H-band and 0$\farcs$56 in K-band (see Fig. 4.2). The centered circles are of radius 1″ and 5″ respectively. The red circles marking the emission regions sp(A) and sp(B) are of radius 0$\farcs$56. The black cross marks the position of the adopted center. Credit: Smajić et al., A&A, 567, A119, 2014, reproduced with permission © ESO.

that of the [Fe II] emission line. Elsewhere in the emission region it drops to ~ 150 km s^{-1}. The LOSV shows a blueshifted end in the northwest direction and a redshifted end in the southwest. A rotation with the line of nodes in this direction (PA $\sim 114°$) can be assumed, however, the region Brγ is detected in is too small to say much more about the velocity field in the central region. The LOSV at the very center is redshifted to ~ 30 km s^{-1}. The EW is small with a maximum of about 0.8 Å on the nucleus hinting at a nuclear ionization (see Fig. 4.5).

The Star Formation Rates

The luminosity of Brγ can be used as a measure for recent star formation since it is proportional to the Lyman continuum flux (Panuzzo et al. 2003; Valencia-S. et al. 2012). When the central Brγ excitation is assumed to be originating from stars only, i.e., no excitation by AGN radiation is taken into account, the luminosity of Brγ in this region can be used to determine a star formation rate (SFR). An upper limit for the SFR within a $1''$ radius around the nucleus of $1.4 \times 10^{-3} M_\odot \text{yr}^{-1}$ is derived using

$$\text{SFR} = \frac{L_{\text{Br}\gamma}}{1.585 \times 10^{32} \text{W}} M_\odot \text{yr}^{-1} \tag{4.1}$$

and $L_{Br\gamma}$ from above. Furthermore, when outflows or jets are disregarded as excitation sources in this region and [Fe II] excitation is assumed from supernovae only, an upper limit for the supernova rate (SNR) in the central region can be estimated. Two different estimators are used (Bedregal et al. 2009)

$$\text{SNR}_{\text{Cal97}} = 5.38 \, \frac{L_{\text{[Fe II]}}}{10^{35} \text{W}} \, \text{yr}^{-1} \tag{4.2}$$

following Calzetti (1997) and

$$\text{SNR}_{\text{AlH03}} = 8.08 \, \frac{L_{\text{[Fe II]}}}{10^{35} \text{W}} \, \text{yr}^{-1} \tag{4.3}$$

following Alonso-Herrero et al. (2003). Both relations were derived from empirical data analysis. An [Fe II] luminosity of $L_{\text{[Fe II]}} = 1.92 \times 10^{30}$ W returns SNR estimates of 1.03×10^{-4} yr^{-1} and 1.55×10^{-4} yr^{-1}, respectively. The derived SFR and SNR values are low (e.g., Rosenberg et al. 2012; Esquej et al. 2014, and references therein) compared to other non-starburst galaxies, in particular with regard to the unlikely assumption that all of the central Brγ and [Fe II] emission is attributed to star formation.

Molecular gas

Several H_2 emission lines are detected at a five sigma confidence level: H_2(1-0)S(3) $\lambda 1.96$ μm, H_2(1-0)S(2) $\lambda 2.03$ μm, H_2(1-0)S(1) $\lambda 2.12$ μm, H_2(1-0)S(0) $\lambda 2.22$ μm, H_2(2–1)S(1) $\lambda 2.25$ μm, H_2(1-0)Q(1) $\lambda 2.41$ μm, H_2(1-0)Q(3) $\lambda 2.42$ μm. The most prominent lines are H_2(1-0)S(3) and H_2(1-0)S(1).

The molecular hydrogen in general, best seen in the H_2(1-0)S(1) line map, shows a distinct structure in the nuclear region of NGC 1433 (see Fig. 4.3(g)). First, the overall emission follows the dust lanes that can be seen in the HST image (see Fig. 4.12(a)). Second, the emission peaks about 0″.5 northwest offset to the K-band continuum peak and forms an arc-like structure from there toward the southeast, crossing the location of the continuum peak. The LOSV along the arc-like structure shows a strong gradient from about -40 km s^{-1} to 40 km s^{-1}.

Several local emission maxima are detected. The most prominent maxima are two spots 2″–3″ east-northeast of the nucleus and a less prominent emission region in the west about 2″.5 away from the center. The EW at the continuum peak is only $\sim$ 1Å whereas at the H_2(1-0)S(1) emission peak the EW is $\sim$ 2.1Å. Moreover, the strongest EWs are seen in the eastern emission spots ranging from about 1.8 Å in the east over 3.4 Å in the northeastern spot (sp(A)) and reaching about 8 Å in the spot (sp(B), see Fig. 4.5). Emission spot sp(B) shows an FWHM of more than 230 km s^{-1} and a blue-shifted LOSV of 90 km s^{-1} whereas the surrounding gas is rather systemic or slightly redshifted. The southern spot sp(B) belongs probably to a spiral arm that is not coupled with the inner nuclear (pseudo-) ring (see Figs. 4.3, 4.4) described by Combes et al. (2013). The LOSV is rather blueshifted in the arm west of the center whereas the eastern side is rather at a systemic velocity (see Fig. 4.3(i)). South of the nucleus the gas is redshifted up to 70 km s^{-1} in an 1″ distance, indicating a possible outflow. The FWHM in this region is 180 km s^{-1} whereas the FWHM at the center is around 210 km s^{-1}. To the northwest of the nucleus there is a probable blue counterpart to the redshifted part of the outflow at a velocity of only 30 km s^{-1} and a distance of 0″.5. An outflow scenario was thoroughly discussed in Combes et al. (2013). Another possible scenario that can explain this high LOSV gradient in all detected emission lines is a gaseous disk in the center of NGC 1433. The scenarios are discussed in section 4.2.5.

The emission line H_2(1-0)S(3) is distributed similarly to the H_2(1-0)S(1) emission line. The H_2(1-0)S(3) transition peaks in the same region as H_2(1-0)S(1) and has a tail along the K-band continuum peak toward the southeast. The two emission peaks in the east are detected as well as other emission spots that one can identify with bright regions in the H_2(1-0)S(1) emission map. The EWs are similar over the whole FOV. The FWHM is generally higher than the

49

line width of H$_2$(1-0)S(1).

All other detected molecular hydrogen lines show emission around the center and in the northeastern emission spot. The dust lane structure is barely traced in emission line maps other than H$_2$(1-0)S(1) and H$_2$(1-0)S(3), probably due to the low intensity of these lines.

(a) Flux ^{12}CO(3-2)

(b) Dispersion ^{12}CO(3-2)

(c) LOSV ^{12}CO(3-2)
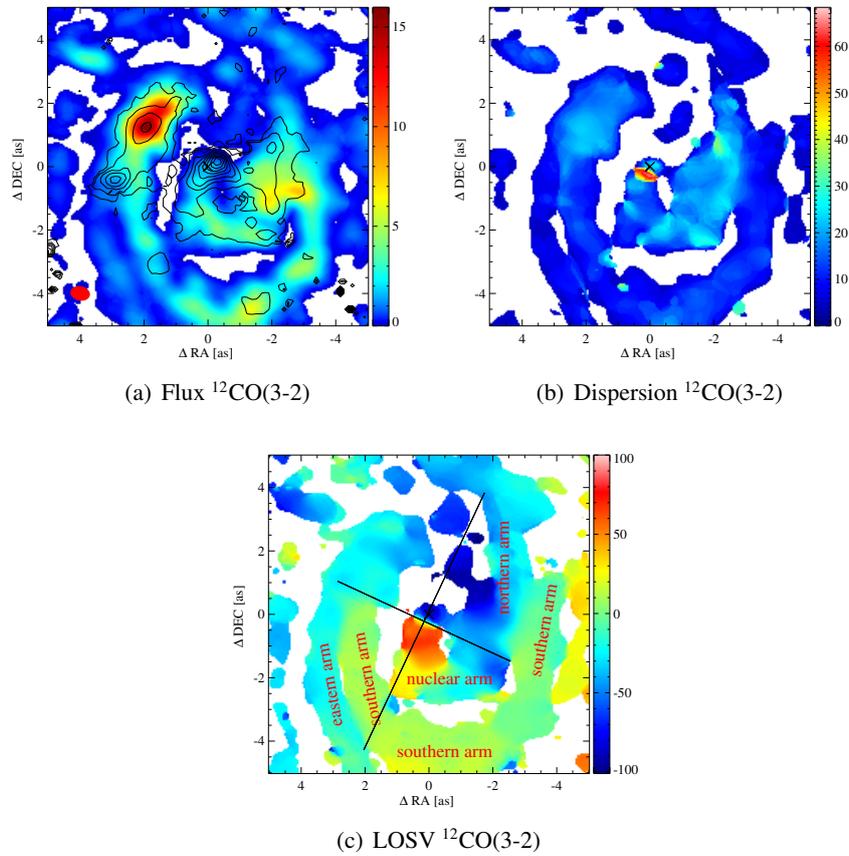
Figure 4.4: ALMA cycle 0 molecular ^{12}CO(3-2) maps. (a) shows the emission map of ^{12}CO(3-2) [Jy beam^{-1} km s^{-1}] overlayed with H$_2$(1-0)S(1) emission contours. The red ellipse at -4,4 depicts the beam size. The dispersion (moment 2) is shown in (b) and the LOSV is shown in (c), both maps are in [km s^{-1}]. (c) shows the cuts for the position velocity (PV) diagrams (see Fig. 4.14). The cuts were not set on the galactic center but along the central velocity gradient of the ^{12}CO(3-2) 1st moment map. Credit: Smajić et al., A&A, 567, A119, 2014, reproduced with permission © ESO.

(a) EW [Fe II]

(b) EW Brγ

(c) EW H$_2$ λ2.12 μm
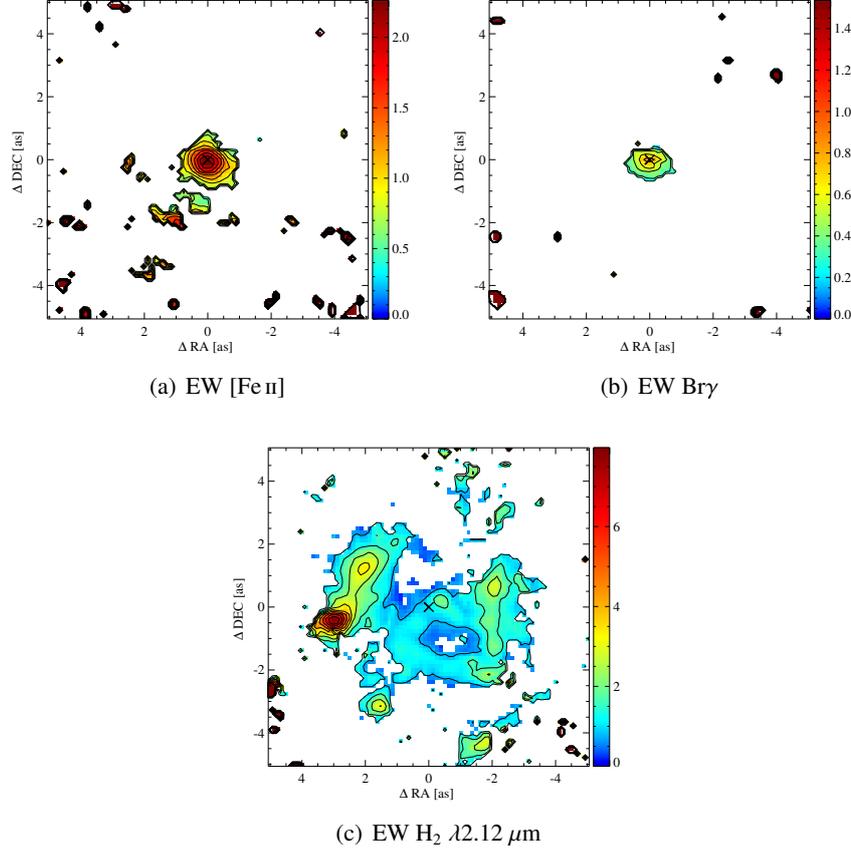
Figure 4.5: EW maps of narrow Brγ, [Fe II], and H$_2$ λ(1-0)S(1) emission lines in Å. For details, see Sect. 4.2. Credit: Smajić et al., A&A, 567, A119, 2014, reproduced with permission © ESO.

The H$_2$ mass estimation

The gas mass of the warm molecular hydrogen can be estimated following Turner & Ostriker (1977); Scoville et al. (1982); Wolniewicz et al. (1998) as

$$M_{\mathrm{H_2}} = 4.243 \times 10^{-30} \left(\frac{L_{\mathrm{H_2(1-0)S(1)}}}{\mathrm{W}} \right) \mathrm{M_\odot}. \qquad (4.4)$$

A warm H$_2$ gas mass of 4.89 $M_\odot$ can be estimated at the central 1″ (~54 pc) using an H$_2$ (1-0)S(1) luminosity of $L_{\mathrm{H_2(1-0)S(1)}}$ = 1.15×10^{30} W. Within 10″ × 10″ FOV a warm molecular hydrogen mass of 19.5 $M_\odot$ is estimated using a 5″ radius aperture centered on the nucleus. The conversion factor determined by Mazzalay

et al. (2013) yields

$$\frac{M_{H_2(cold)}}{M_{H_2(warm)}} = (0.3 - 1.6) \times 10^6. \tag{4.5}$$

is used to determine the cold molecular hydrogen mass. A cold H_2 gas mass of $(1.5 - 7.8) \times 10^6 M_\odot$ is derived for the $1''$ radius aperture and $(0.6 - 3.1) \times 10^7 M_\odot$ for the $5''$ radius aperture. This implies that one third of the H_2 in the central $10''$ can be found in the central $1''$ radius around the nucleus. Combes et al. (2013) derive an H_2 gas mass for their outflow region, which covers about the same area as the central $1''$ radius discussed here, of $3.6 \times 10^6 M_\odot$. This value is in good agreement with the measurements derived in this work. However, the $^{12}CO(3-2)$ luminosity measurements imply an H_2 gas mass of $2.1 \times 10^5 M_\odot$ for a $1''$ radius and $8.3 \times 10^6 M_\odot$ for a $5''$ radius, using the Milky Way dust-to-gas ratio (Solomon & Barrett 1991).

Table 4.1: NGC 1433 basic data.

Parameter	Value	References[a]
$\alpha^{(b)}_{J2000}$	$03^h42^m01.49^s$	(1)
$\delta^{(b)}_{J2000}$	$-47°13'20''.2$	(1)
$\alpha^{(c)}_{J2000}$	$03^h42^m01.49^s$	This work
$\delta^{(c)}_{J2000}$	$-47°13'18''.8$	This work
Nuclear activity	Seyfert	(2)
Redshift	0.003586	(3)
Distance	9.9 Mpc ($1'' = 48$ pc)	(1)
Inclination	$33°$	(4)
Position angle	$199° \pm 1°$	(4)

Notes. [a] (1) Combes et al. (2013); (2) Veron-Cetty & Veron (1986); (3) Koribalski et al. (2004); (4) Buta et al. (2001). [b] Galaxy center as adopted by Combes et al. (2013). [c] The new adopted center taken from the ALMA observations world coordinate system.

4.2.2 Line diagnostics

The nuclear region and emission spots sp(A) and sp(B) are the regions in the observed FOV which show a variety of line species that allow for a line diagnostic. One diagnostic diagram uses the logarithmic line ratios of $H_2(1-0)S(1)$ over $Br\gamma$ and [Fe II] over $Pa\beta$ to distinguish three different galaxy types. Starburst galaxies, in the lower left of Fig. 4.6, are photoionized and show very high H II emission. The LINERs are mainly shock ionized, hence shock tracers like

H$_2$(1-0)S(1) and [Fe II] $\lambda\lambda$1.257 μm,1.644 μm show stronger emission. Both excitation mechanisms can be found in Seyfert galaxies therefore this galaxy type is placed between the two extrema.

The nuclear region of NGC 1433 takes its place in the AGN regime (see Fig. 4.6), but given the error bars a LINER classification cannot be excluded, e.g., aperture effects might shift the classification into the LINER regime. This is caused mainly by a deficiency of H II in the central region where Brγ is detected only in the very center, the location of the nucleus. Earlier classifications are confirmed (e.g., Veron-Cetty & Veron 1986; Cid Fernandes et al. 1998) that describe this galaxy as being Seyfert and LINER like. Because of the borderline classification of NGC 1433 between Seyfert/LINER galaxy, scenarios that include outflows are further supported.

The conversion between the [Fe II] λ1.644μm flux, obtained from the SINFONI H-band data and the J-Band emission line [Fe II] λ1.257 μm was done using the factor

$$\frac{f_{\lambda1.644\mu m}}{f_{\lambda1.257\mu m}} = 0.744$$

(Nussbaumer & Storey 1988). The case B ratio of Brγ/Paβ = 0.17 was used for the conversion of Brγ to Paβ, with a temperature of $T = 10^4$ K and an electron density of $n_e = 10^4$.
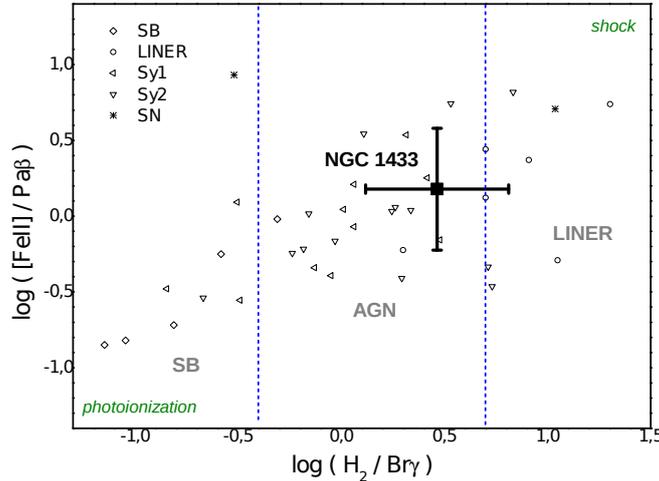
Figure 4.6: Diagnostic diagram for the classification of the nuclear emission. The [Fe II] λ1.257 μm and Paβ values were derived from the [Fe II] λ1.644 μm and the Brγ line. Credit: Smajić et al., A&A, 567, A119, 2014, reproduced with permission © ESO.

The detection of several molecular hydrogen emission lines enables for a line ratio diagnostic (Rodríguez-Ardila et al. 2005). The three main excitation mechanisms of molecular hydrogen in the NIR are: (i) UV flourescence (non-thermal); (ii) X-ray heating (thermal); and (iii) shocks (thermal).

i *UV-flourescence*: Highly energetic UV photons, which are created in the Lyman-Werner band (912-1108 Å), are absorbed by H_2 molecules and then reemitted at lower frequencies. This can occur in a warm high-density gas where one finds thermal emission line ratios for the lower levels. Because of the high-density, the lower levels are dominated by collisional excitation. Hence, observations of higher level transitions are required to distinguish collisional excitation (thermal) from UV pumping (non-thermal).

ii *X-ray heating*: X-ray dominated regions (XRDs) are observable in regions with temperatures < 1000 K. In these regions H_2 is mainly ionized by X-rays. At higher temperatures, shock excitation due to collisions populates the lower excitation levels. The ionization rate per H-atom is limited to < 10^{-15} cm^3 s^{-1} since higher rates will destroy the H_2 molecules (e.g., Tine et al. 1997; Draine & Woods 1990; Maloney et al. 1996). In dense and static photodissociation regions UV photons instead of X-ray photons can heat the molecular gas.

iii *Shock fronts*: The collisional excitation via shock fronts in a medium is a thermal mechanism and populates the electronic ground levels of H_2 molecules. This population of the ro-vibrational transitions is described by a Boltzmann distribution. The kinetic temperatures in these shock excited regions can be higher than 2000 K (Draine & McKee 1993).

Non-thermal excitation can be excluded as an excitation mechanism in all of the analyzed regions because all regions show (2-1)S(1)/(1-0)S(1) ratios of < 0.2 (see Fig. 4.7). The central region is situated above the thermal emission curve, which is probably due to an overestimation of the (1-0)S(3) line that is situated in a noisy spectral region. Nevertheless, Rodríguez-Ardila et al. (2005) show that the bulk of Seyfert galaxies, independent of Seyfert type, have similar or even higher (1-0)S(3)/(1-0)S(1) ratios than the nuclear region. Therefore, thermal excitation is the main mechanism in the center of NGC 1433 but further differentiation cannot be derived.

The off-nuclear emission region sp(A) lies on the thermal emission curve at an excitation temperature between 2000 K and 3000 K. This implies that the gas there is heated up, probably by a hidden star formation region. The $^{12}CO(3-2)$ map shows the brightest emission in this region. The star formation region has
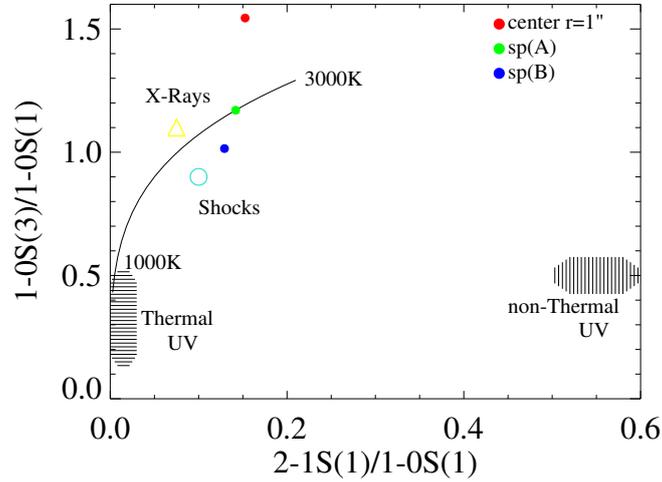
Figure 4.7: Molecular hydrogen diagnostic diagram to classify the emission at the nucleus in red and in emission spots sp(A) in green and sp(B) in blue. Line ratios are $H_2(2\text{-}1)S(1)/H2(1\text{-}0)S(1)$ and $H_2(1\text{-}0)S(3)/H_2(1\text{-}0)S(1)$. The curve represents thermal emission at 1000–3000 K. Horizontal stripes are thermal UV excitation models by Sternberg & Dalgarno (1989). Vertical stripes are nonthermal models by Black & van Dishoeck (1987). The area of X-ray heating models by Draine & Woods (1990) is marked by an open triangle (yellow). The open turquoise circle marks the region of the shock model by Brand et al. (1989). Credit: Smajić et al., A&A, 567, A119, 2014, reproduced with permission © ESO.

already formed stars by then, which explains that Combes et al. (2013) report a non-detection of the dense gas tracers $HCO^+(4\text{–}3)$ and $HCN(4\text{–}3)$ in this region. Since no Brγ emission is detected a high column density toward the star forming region's H II region can be inferred.

Emission spot sp(B) lies close to the thermal excitation curve at about 2000 K and is near to the predicted shock excitation models by Brand et al. (1989). The $^{12}CO(3\text{-}2)$ shows no increased flux in this region therefore sp(B) and sp(A) seem not to be excited by the same mechanisms. The broadness of the H_2 lines in sp(B) as well as the very blueshifted velocities indicate an interaction of the two gas arms, eastern and southern arm (see Fig. 4.4(c)). Due to the interaction of the arms shock fronts are induced in the gas, which then excite the H_2 molecules in sp(B). Another possibility is a strong star formation that shocks the surrounding gas. Brγ, $HCO^+(4\text{-}3)$, and $HCN(4\text{-}3)$ are not detected in sp(A) indicating either a high column density toward the region, low-density gas or a not strong enough ionization source.

4.2.3 Continuum Analysis and Black Hole Mass

The continuum analysis was conducted mainly by using a decomposition method, as described in Smajić et al. (2012), in the nuclear region of NGC 1433. The contribution to the continuum is of stellar origin only and extinction can be neglected. Therefore, the stellar and the K-band continuum peak in the same position and their photon distributions are very similar. The stellar continuum was obtained by fitting the CO(2-0) bandhead with a stellar spectrum. Stellar templates taken by Winge et al. (2009) were used as input for the fitting routine. The template spectra were convolved with a Gaussian to adapt their resolution to the SINFONI resolution of 4000 in K-band. The red giant HD2490 is a spectral class M0III star and fitted best without the need of additional stellar spectra (e.g., asymptotic giant branch stars). What might be surprising is the fact that the NIR continuum peak coincides with the optical, HST images from F450W, F660W, and F810W filters, and is not affected by the obvious dust lanes seen in Fig. 4.12(a). The spectra of the used template stars have a wavelength coverage from 2.2 μm to 2.4 μm only. Hence, the fitted spectral region is small. This might explain that no extinction component was needed for the fit, even at the spatial positions of the dust lanes.

The H-K color map (see Fig. 4.8) indicates a strong reddening toward the newly adopted center but reddening is not detected at the dust lane positions. The reddening at the center can be taken as a signature of hot dust at the sublimation temperature, which, in AGNs, is co-spatial with the inner edge of the circumnuclear torus and/or the outer edge of the accretion disk. The LOSV of the stars
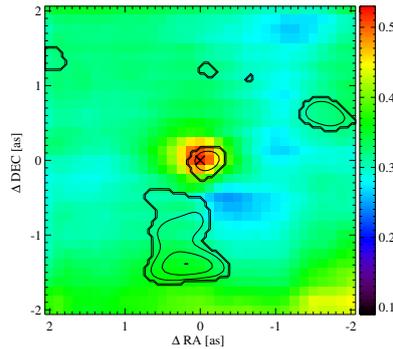
Figure 4.8: The H-K color diagram in magnitudes showing the center of NGC 1433 measured in the SINFONI H- and K-band. The contours are from the 0.87 mm continuum emission measured by ALMA. For detail, see section 4.2.3 & 4.2.4. Credit: Smajić et al., A&A, 567, A119, 2014, reproduced with permission © ESO.

is determined from the CO(2-0) band head fitting and a rotation direction at a PA of $\sim 201°$ is measured. The determined velocity field is systematically redshifted by a few $km\,s^{-1}$. This might be a result of the imperfect wavelength calibration as explained in section 4.1. The projected velocities range from about -50 to 60 $km\,s^{-1}$ and the 0 $km\,s^{-1}$ isovelocity contour lies close to the continuum center. The stellar velocity dispersion (SVD) ranges from about 90 to 160 $km\,s^{-1}$. The black hole mass can be estimated from the SVD, assuming that NGC 1433 lies on the M-σ relation. Following Gültekin et al. (2009),

$$M_{\bullet} = 10^{8.12\pm0.08} \times \left(\frac{\sigma_*}{200 \text{ km s}^{-1}}\right)^{4.24\pm0.41} M_{\odot}, \qquad (4.6)$$

a black hole mass of $M_{\bullet} = 7 \times 10^6 M_{\odot}$ is estimated using a velocity dispersion of $\sigma_* = 100$ km s^{-1} measured at the very center of the SVD map where a minimum is found. A minimum in the SVD is often detected in galaxies which harbor a not always resolved nuclear disk (Emsellem et al. 2001; Falcón-Barroso et al. 2006). By assuming that the fitted SVD over the observed FOV (see Fig. 4.9) follows a Gaussian distribution, a mean velocity dispersion of 125 ± 10 km s^{-1} is determined. Hence, a black hole mass of $M_{\bullet} = (1.8 \pm 0.8) \times 10^7 M_{\odot}$ is estimated. The first black hole mass estimate of $M_{\bullet} = 7 \times 10^6 M_{\odot}$ agrees with Buta (1986), however, the latter estimate represents the bulges SVD, which is needed for the equation given above.

The PA of the nuclear stellar bar or oval is estimated to a PA of $\sim 33°$ using the shape and angle of the K-band continuum isophotal ellipses (see Fig. 4.10(b), 4.11(c)). The PA changes to 15° at the isophotal lines that range from 25% to 35% of the peak luminosity then it shifts to a PA of about 70° for the inner isophotes. This change in PA toward the inner isophotal lines can be attributed to the PSF, which is elongated in the northeast to southwest direction at a PA of ~70°.
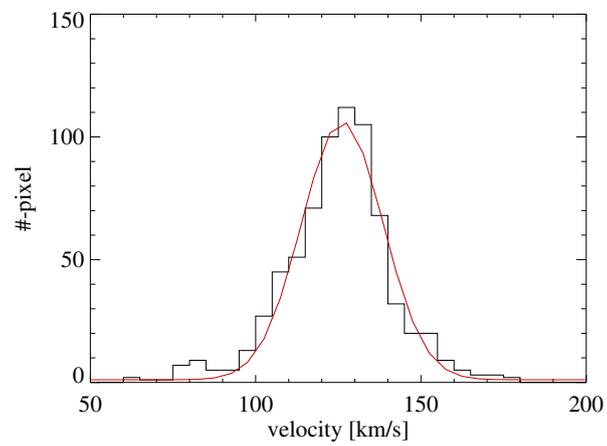
Figure 4.9: The fit over the stellar dispersion from the continuum decomposition in 5 km s^{-1} bins. The X-axis shows the fitted dispersion and the Y-axis the total number of spatial pixel that correspond to this dispersion bin. The red curve represents a Gaussian fit to the distribution. Credit: Smajić et al., A&A, 567, A119, 2014, reproduced with permission © ESO.

**Table 4.2:** NGC 1433 emission line flux and FWHM in regions center, sp(A), and sp(B).

Line λ [μm]	center Flux [10^{-18} W m^{-2}]	FWHM [km s^{-1}]	sp(A) Flux [10^{-18} W m^{-2}]	FWHM [km s^{-1}]	sp(B) Flux [10^{-18} W m^{-2}]	FWHM [km s^{-1}]
[Fe II] λ 1.644	1.94 ± 0.47	190 ± 50	—	—	—	—
H$_2$(1-0)S(3) λ 1.957	1.33 ± 0.13	210 ± 20	0.33 ± 0.02	180 ± 15	0.29 ± 0.02	230 ± 15
H$_2$(1-0)S(1) λ 2.122	0.86 ± 0.11	180 ± 25	0.28 ± 0.02	125 ± 10	0.28 ± 0.03	255 ± 25
Brγ λ 2.166	0.295 ± 0.095	185 ± 70	—	—	—	—
H$_2$(1-0)S(0) λ 2.223	0.36 ± 0.09	230 ± 75	0.065 ± 0.02	190 ± 70	0.05 ± 0.02	195 ± 115
H$_2$(2-1)S(1) λ 2.247	0.13 ± 0.06	110 ± 55	0.04 ± 0.015	140 ± 60	0.04 ± 0.02	235 ± 50
H$_2$(1-0)Q(1) λ 2.408	1.08 ± 0.20	185 ± 30	0.28 ± 0.03	155 ± 15	0.21 ± 0.04	250 ± 40
H$_2$(1-0)Q(2) λ 2.414	0.79 ± 0.265	290 ± 75	—	—	0.06 ± 0.02	115 ± 35
H$_2$(1-0)Q(3) λ 2.422	1.02 ± 0.20	205 ± 30	0.23 ± 0.015	135 ± 15	0.18 ± 0.02	235 ± 35

Notes. Region center: The region is centered on the nuclear position and adopted galactic center. The lines were measured in a 1″ radius aperture. Regions sp(A) and sp(B): A 0″56 radius aperture centered on the emission regions was used to measure the lines. See also Fig. 4.3(g). The FWHM is not corrected for instrumental broadening, which is ~ 100 km s^{-1} in H-band and ~ 75 km s^{-1} in K-band.

4.2.4 The nucleus of NGC 1433

A result from the continuum decomposition examined in Sect. 4.2.3 is that the 0.87 mm continuum peak measured with ALMA (see Fig. 4.10(c)) and the NIR stellar peak do not agree in spatial position. This issue was addressed by an overlay of the H_2(1-0)S(1) contours on the HST F450W map, the ALMA ^{12}CO(3-2) map, and the 0.87 mm continuum map (see Figs. 4.4(a), 4.10(c), 4.12(a)). The dust lanes are well covered by the H_2(1-0)S(1) emission when the stellar NIR peak (marked with an $\times$) is placed onto the brightest pixel in the HST image (see Fig. 4.12(a)). Furthermore, the molecular CO emission fits best to the H_2(1-0)S(1) emission when the stellar continuum center is placed on a small local CO peak about $1\rlap{.}''5$ north and $0\rlap{.}''2$ west from the center assumed in Combes et al. (2013). Additionally, the H_2(1-0)S(1) contours overlayed on the 0.87 mm continuum map and aligned to the same spatial pixel that was found from the overlay onto the ^{12}CO(3-2) map (see Fig. 4.10(c)) reveal that the NIR stellar continuum peak is situated on a local 0.87 mm peak, which is about three-quarters as strong as the brightest 0.87 mm peak. The eastern part of the central arclike structure found in the H_2(1-0)S(1) line map and described in section 4.2.1 traces 0.87 mm emission toward the peak of the 0.87 mm emission. In addition, the H-K color diagram in Fig. 4.8 confirms the newly adopted center because the color becomes significantly redder here, resulting from the warm dust emission of the SMBH surrounding torus. Unfortunately, the bright emission regions in the ^{12}CO(3-2) and the H_2(1-0)S(1) emission maps do not coincide exactly and can therefore not be used to align the NIR and the sub-mm maps.

The brightest ^{12}CO(3-2) region, which is in the northeast, and the bright clumps in the west are very well traced by the H_2(1-0)S(1), see Fig. 4.4(a). These emission regions can be used for a proper alignment as it is also appreciable in the correspondence of the extended flux of both emitting species. The error estimate of the center positioning turns out to be $0\rlap{.}''2$ with the described method. The estimated error becomes evident when studying the overlay of the 0th and 1st moment maps of ^{12}CO(3-2) with the corresponding H_2 maps. The error represents a shift of the ALMA data with respect to the NIR/optical center. A cross-correlation of the strongest ^{12}CO(3-2) emission spots with probable corresponding emission in the H_2 map is performed by a shift of the CO maps with respect to the H_2 emission line map . Additional support for the newly estimated nuclear position is the strong velocity gradient across this region in all emission lines, e.g., ^{12}CO(3-2), H_2(1-0)S(1), Brγ, and [Fe II]. Furthermore, [Fe II] and Brγ only show detectable emission at the position of the stellar continuum peak that is co-spatial with emission from the circum-nuclear hot dust. The exact position of the adopted new center is given in table 4.1. These arguments are convincing

(a) H-band continuum

(b) K-band continuum
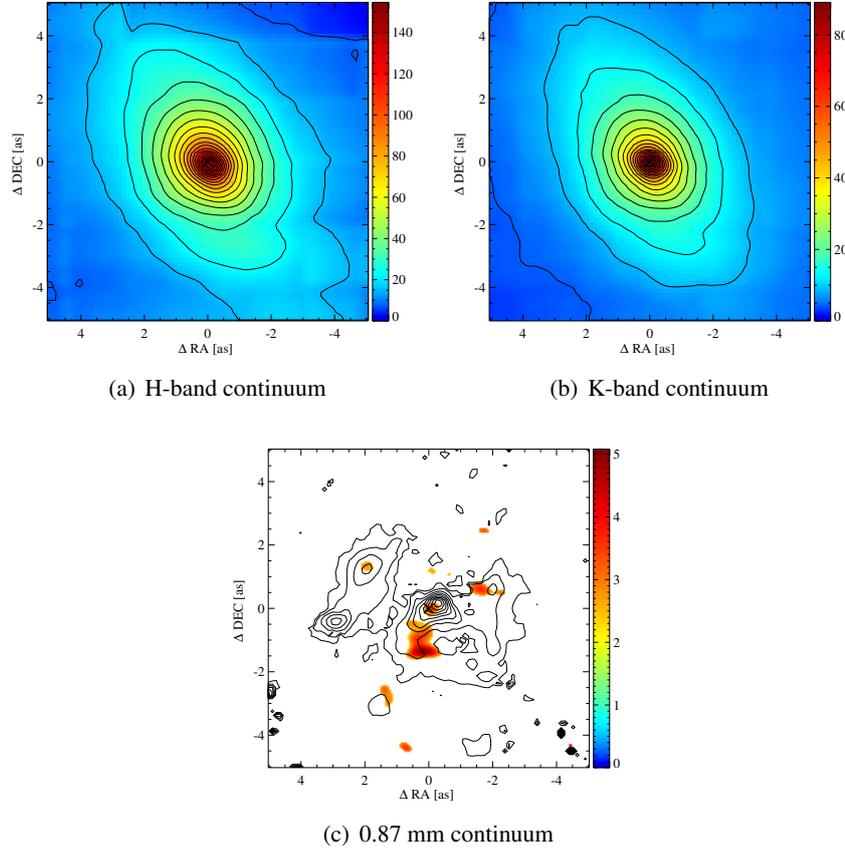
(c) 0.87 mm continuum

Figure 4.10: From left to right H-band, K-band [10^{-18} W m^{-2} μm^{-1}] and the 0.87 mm [Jy beam^{-1}] continuum are shown. (c) H$_2$(1-0)S(1) contour overlayed on the 3 sigma clipped 0.87 mm continuum. For details, see section 4.2.3 & 4.2.4. Credit: Smajić et al., A&A, 567, A119, 2014, reproduced with permission © ESO.

combined evidence for the presence of an AGN and a SMBH at the newly found position.

4.2.5 The central arcsecond

The high velocity gradients in the central region were already discussed for the ^{12}CO(3-2) line observed with ALMA by Combes et al. (2013). They argue mainly in favor of an outflow scenario and its origin. Although they place the center of NGC 1433 and therefore the AGN more than 1″ further south, their argument is still solid. However, because of the change in the position of the cen-

(a) Stellar LOSV

(b) Stellar dispersion

(c) Stellar continuum
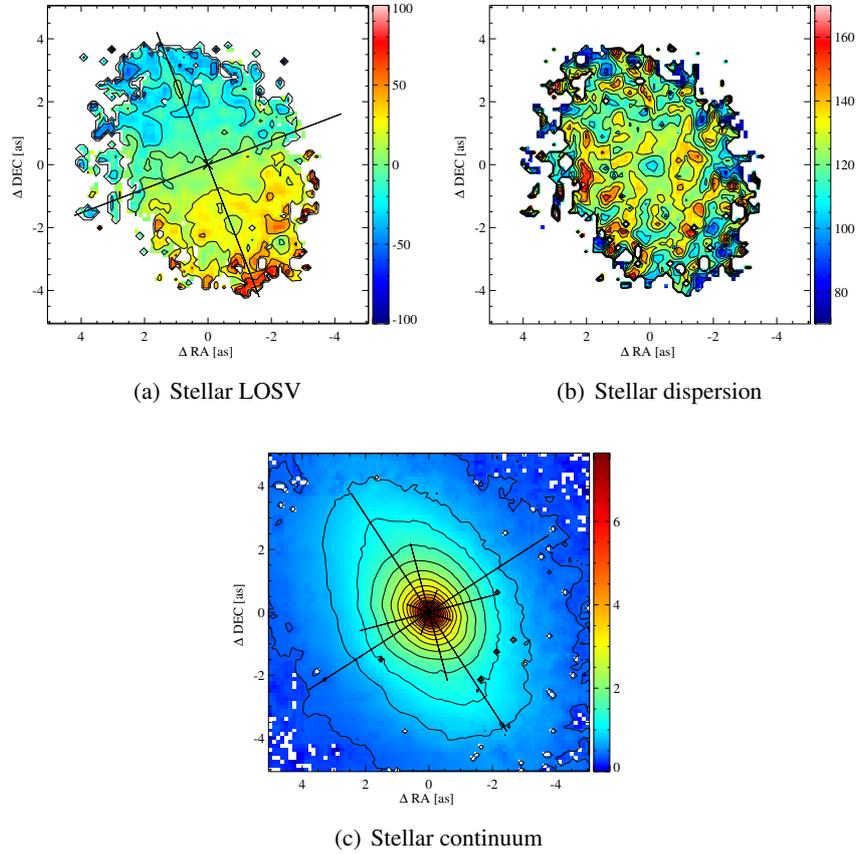
Figure 4.11: The fitted stellar LOSV map [km s^{-1}], stellar disperion [km s^{-1}] and stellar continuum (arbitrary unit) map are shown. In fig. (a) the LOSV PA of the galactic rotation is marked. Figure (c) shows probable PAs of the isophotes where the largest cross marks the PA of the nuclear bar and the smallest cross the orientation of the beam. The middle cross indicates a possible twist in the isophotal lines. Credit: Smajić et al., A&A, 567, A119, 2014, reproduced with permission © ESO.

ter a rotating gaseous disk surrounding the nucleus and the center of the stellar distribution of NGC 1433 needs to be considered an alternative solution.

A central nuclear disk?: In molecular hydrogen a velocity gradient of -40 km s^{-1} to 40 km s^{-1} is measured at a 1″ diameter distance over the nucleus (see Fig. 4.3(i)). In the same position in the ^{12}CO(3-2) map the gradient reaches higher velocities of - 80 km s^{-1} to 120 km s^{-1} (see Figs. 4.4(c), 4.14(a)). Using the H$_2$(1-0)S(1) velocities a central mass of M_{cent} of $7.3 \times 10^6 M_\odot$ is estimated. This mass is in-between the two measured black hole masses estimated using

(a) H_2(1-0)S(1) over F450W HST

(b) CO(3-2) over F450W HST
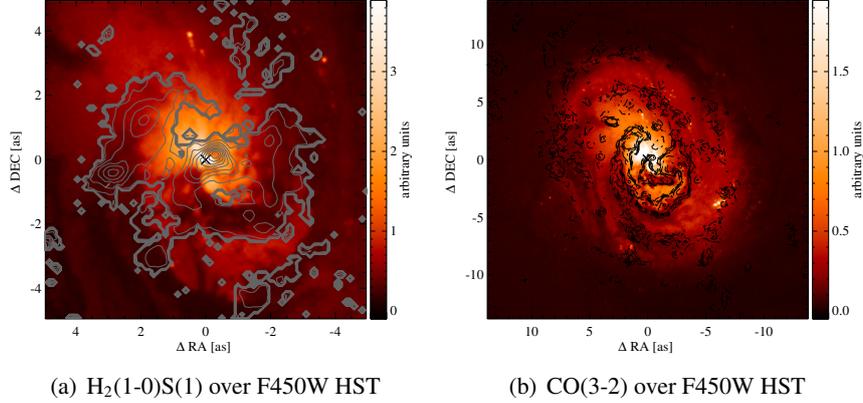
Figure 4.12: Figure (a) shows an HST map at about 4380 Å with H_2(1-0)S(1) contours overlayed. Figure (b) shows the same HST image in the ALMA FOV with the ^{12}CO(3-2) line emission in contours. The HST images were taken from the archive and were observed with the WFC3 instrument and the UVIS detector using the F438W filter. The images illustrate the remarkable overlap of dust lanes and molecular hydrogen (a) and ^{12}CO(3-2) emission (b), respectively. Credit: Smajić et al., A&A, 567, A119, 2014, reproduced with permission © ESO.

the M–σ relation (7×10^6 and $1.7 \times 10^7 M_\odot$, see also Sect. 4.2.3). The velocity gradient across the center is at a PA of 140° and is aligned with the farside of the galaxy whereas the stellar velocity gradient is at a PA of 201°. The nuclear velocity gradient is recognized in all detected NIR emission lines except for [Fe II], which can also resemble a north–south aligned gradient.

A discrepancy in the line of nodes angle between H_2 and ^{12}CO(3-2) is measured. For ^{12}CO(3-2) a line of nodes PA of 155° is found, this difference is visible in the LOSV maps of the respective lines (see Figs. 4.3(i),4.4(c)). The effect is probably introduced by PSF smearing since this region is barely resolved. A possible inclination (face-on to edge-on) of this gaseous nuclear disk cannot be determined from this data and since the PA differs strongly from the stellar PA a rotation in the galactic disk plane does not distinguish itself.
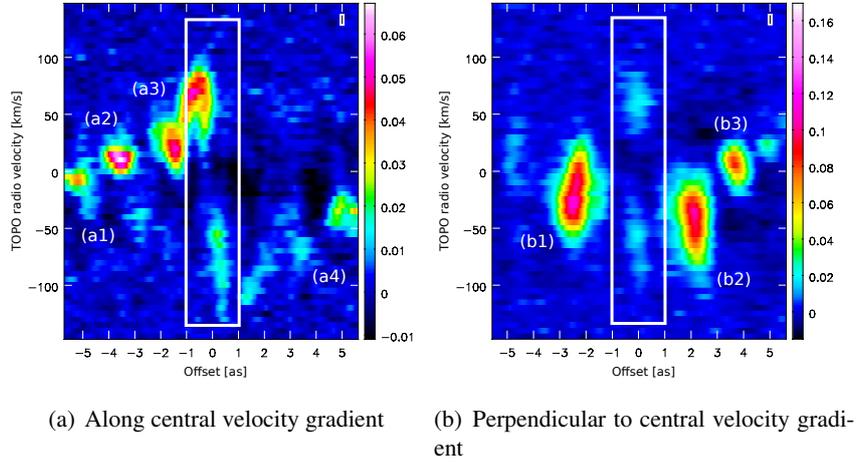
The position velocity (PV) diagram in Fig. 4.14(a) indicates a possible central rotating disk profile that reaches the maximum velocities of ± 100 km s^{-1} at $\pm 0\farcs 4$ from the center. The PA of the PV diagram cuts was chosen based on the velocity field in the central region (see Fig. 4.4(c)). Assuming an edge-on disk, a lower limit for the dynamical mass is estimated to be $4 \times 10^7 M_\odot$ with the measured velocity and radius. This mass is higher than the estimated BH mass values, as required. The dynamical mass is derived within an aperture of $0\farcs 4$ radius, which is supposed to be higher than the BH mass since it accounts

(a) H$_2$(1-0)S(1) – stellar LOSV

(b) CO(3-2) – stellar LOSV

(c) CO(3-2) – stellar LOSV + 20 km s^{-1}
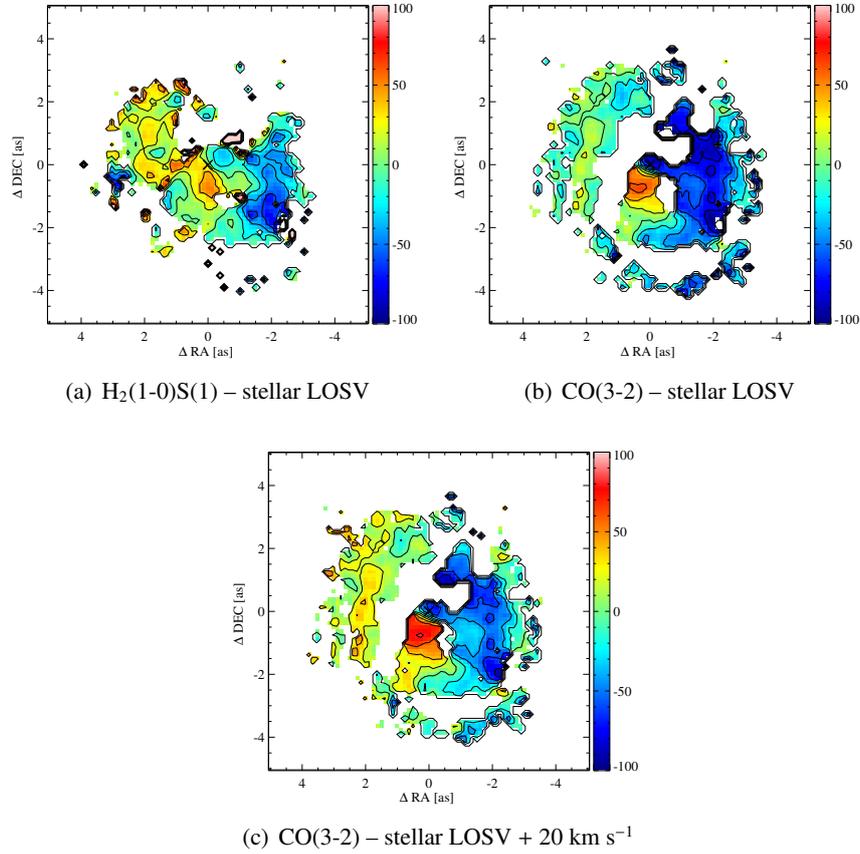
Figure 4.13: Stellar LOSV subtracted maps of H$_2$(1-0)S(1) and ^{12}CO(3-2). (c) is the same as (b) but 20 km s^{-1} were added to the residual to indicate the higher resemblance with Fig. (a). All color-bar units are in km s^{-1}. For details, see Sect. 4.2.5. Credit: Smajić et al., A&A, 567, A119, 2014, reproduced with permission © ESO.

for the stellar mass included in this aperture. Assuming that the inclination is $i = 33^o$ this implies a higher mass by a factor of 3 (see Combes et al. 2013). However, inclination and PA of a circum-nuclear disk do not at all have to agree with the corresponding values of the larger scale galaxy structure. When compared to the Milky Way a large stellar mass contribution for the inner 20 pc of NGC 1433 can be expected . For example, the mass density in the inner parsec of the center of the Milky Way reaches values of the order of 10^5 M$_\odot$ pc^{-3} (see Fig. 22 by Schödel et al. 2009, 2002). This results in an enclosed stellar mass of 4×10^7 M$_\odot$ pc^{-3} at a radius of 10 pc and about 10^8 M$_\odot$ pc^{-3} at a radius of 20 pc.

(a) Along central velocity gradient

(b) Perpendicular to central velocity gradient

Figure 4.14: PV diagrams from the ^{12}CO(3-2) ALMA cube (a) along the central velocity gradient (PA= 140°) and (b) perpendicular to the central velocity gradient (PA= 50°). The color-bar shows the flux density in [Jy beam^{-1}]. The position of the cuts is displayed in Fig. 4.4(c). The white rectangle marks the nuclear region in which the central velocity gradient is dominent. (a1) to (b3) mark dust arm positions: (a1) eastern arm, (a2) southern arm, (a3) nuclear arm, (a4) northern arm, (b1) overlap between eastern and southern arm, (b2) nuclear arm, (b3) southern arm (west). Credit: Smajić et al., A&A, 567, A119, 2014, reproduced with permission © ESO.

This implies also that in the case of NGC1433, the stellar mass contribution will be substantial.

The tips of the disk are located at the slightly increased dispersion spots as seen in the 2nd moment ^{12}CO(3-2) image (Fig. 4.4(b)). The lack of ^{12}CO(3-2) emission at the very center visible in the PV diagrams can be explained by highly excited, possibly even optically thin, molecular gas at temperatures of >55 K that is suppressed in its emission by the ^{12}CO(3-2) transition. For example, molecular rings filled in by line emission of higher rotational transitions are a commonly observed phenomenon in galactic nuclear regions. In the case of I Zw 1 Staguhn et al. (2001); Eckart et al. (2001); Eckart et al. (2000) have shown that the circum-nuclear ring structure, which is present in interferometric ^{12}CO(1-0) maps, is not evident in ^{12}CO(2-1) maps. The center of the ring has been filled up by ^{12}CO(2-1) line emission enhanced by means of higher molecular excitation toward the nucleus. Regarding the ^{12}CO(3-2) emission, there is ample evidence of elevated ^{12}CO(3-2)/(1-0) ratios toward the central positions of galactic nuclei, as demonstrated by Irwin et al. (2011). Their Fig.7 shows that at densities of 10^4 cm^{-3} a variation of that ratio by a factor of up to 4 can be

obtained if the molecular gas temperature varies between T~50 K and T~10 K, typical nuclear (Muraoka et al. 2007; Tilanus et al. 1991; Israel et al. 2006) and off-nuclear values (Mauersberger et al. 1999; Wilson et al. 2009). Theoretical three-dimensional non-LTE calculations of CO lines (Wada & Tomisaka 2005) imply that a behavior such as this is expected from the molecular gas structure around AGN.

The H_2 mass derived in the nuclear region is an indicator that the gas close to the nucleus is indeed highly excited since a lower mass from the $^{12}CO(3-2)$ transition is derived than from the $H_2(1-0)S(1)$ transition. To resolve this issue, however, sub-mm observations of the central region at higher frequencies and higher angular resolution is needed.

A central nuclear outflow: The newly determined nuclear position agrees well with the kinematic origin of a potential molecular outflow. Interpreting the observed nuclear [Fe II] and Brγ line emission as tracers of star formation activity (see Sec. 4.2.1) make star formation an unattractive source for driving such an outflow. In fact, it is very likely that intermittent nuclear accretion events are the driving force (see also Combes et al. 2013).

The above explained rotation profile might as well be produced by an outflow, which is then smeared out by the PSF to look like a rotation profile. The distance of the absolute disk velocity maxima from the center is taken as the radius of the disk radius, which yields a disk radius of about 0″4. The PV diagram perpendicular to the velocity gradient (see Fig. 4.14(b)) shows conspicuous faint emission lobes at the 0″ position and at velocities of about ±60 km s^{-1}. Almost no emission is detected in-between these velocities on the nucleus, which is expected for a molecular disk, but not necessary (see above). Other emission lobes in the PV diagram are molecular arms.

A combined model: A third possibility to create the observed profile is a combination of rotating disk and outflow. This scenario explains the rotational character of the center as well as the red tail south of the nucleus visible in $H_2(1-0)S(1)$ and $^{12}CO(3-2)$. A disk with a single sided outflow away from the observer explains then the higher redshifted velocity compared to the blueshifted velocity in the SINFONI observation. The different PAs of the central velocity gradients in H_2 and CO might then be introduced by PSF smearing due to the higher outflow velocity in $^{12}CO(3-2)$ compared to the H_2 velocities. This approach matches the increased redshifted velocity 1″ south of the nucleus seen in the H_2 and CO LOSV images (Fig. 4.3(i), 4.4(c)) that follow the 0.87 mm continuum tail.

The newly determined position of the center of NGC1433 places the outflow's origin at position of the SMBH, located at the connection point of blueshifted
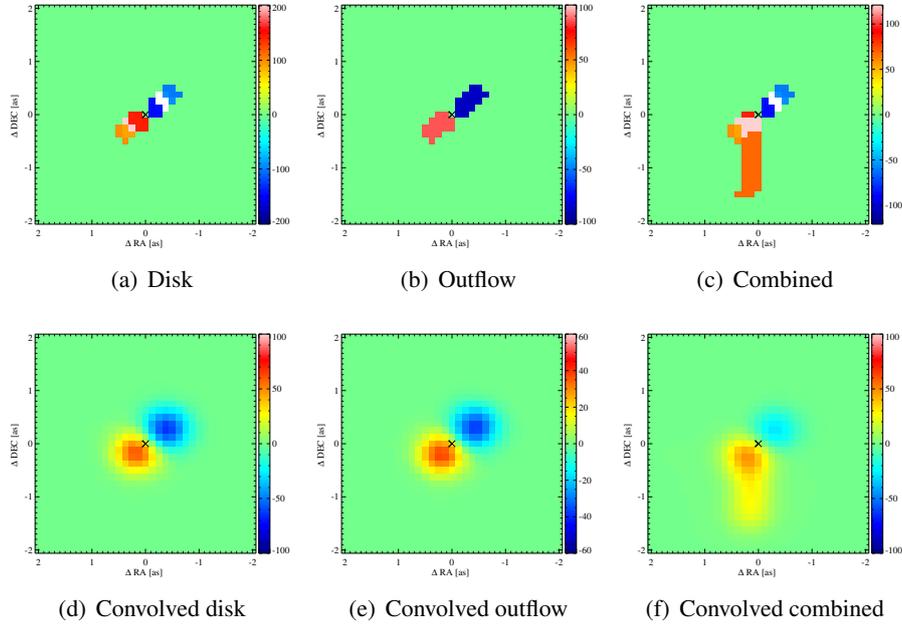
and redshifted gas in the center. In addition, the new central position helps explain the off-nuclear dust continuum emission. Fig. 4.10(c) shows the 0.87 mm emission and an overlay of H_2(1-0)S(1) emission contours. Comparing these two emission maps shows that radio continuum emission is present at least at the center and with its emission peak about $1\rlap{.}''5$ south of it. Following the H_2(1-0)S(1) emission from nucleus to radio continuum peak one traces also weak radio continuum emission. Though weak, the radio emission is a three sigma detection. The overlap of radio continuum and H_2 emission is remarkable. This radio continuum trail puts the combined model, i.e., outflow and disk scenario, at least in front of the rotational disk only scenario. The trail can be explained by gray body dust emission heated by the outflow. Interestingly, the EW of H_2(1-0)S(1) is nearly constant along this trail and around the nucleus except for the emission peak. One might expect an increase of the EW in the outflow regions with respect to the surroundings because of higher H_2 fluxes, but none can be detected in any of the emission lines. The dust lane $2''$ south of the nucleus shows the same EW as the outflow regions.

A simple model approach

Three simple models for the central velocity gradients were derived to substantiate the discussion. The disk model was created based on a differentially rotating edge-on disk with a rotational velocity of $v \sim 100$ km s^{-1} at the outer edge (see Fig. 4.15(a)). Inclination was not introduced as a parameter since this would mainly change the value of the LOSV of the disk. The outflow model was created assuming a constant velocity of $v \sim 100$ km s^{-1} up to a radius of $0\rlap{.}''625$ (see Fig. 4.15(b)). The inclination was fixed to $30°$ for the outflow. The orientation for both models is at a PA of $130°$. The scale height, i.e., disk thickness and width of the outflow, was chosen to be 3 spatial pixels. A change in scale height results directly in a change in the observed LOSV, therefore, it was fixed. The two models were then convolved with a Gaussian PSF, using the FWHM measurements of the telluric standard star in K-band, and placed on an emissionless background.

The result of these two models after convolution is that both models, disk and outflow, look very similar and cannot unambiguously be traced back to their underlying model. Both models fit well in the central $1''$ diameter region. However, the redshifted part shows an elongated tail southward, which cannot be accounted for with these two isolated models.

To address this issue, a third model was chosen as a combination of the disk model as described above and a one-sided outflow model. The outflow's PA is now chosen to be $\sim 175°$ and only the redshifted part is taken into account. The

67

(a) Disk   (b) Outflow   (c) Combined

(d) Convolved disk   (e) Convolved outflow   (f) Convolved combined

Figure 4.15: The models used in section 4.2.5 are presented. (a)-(c) are the constructed models, (d)-(f) are the PSF convolved models. For details, see Sect. 4.2.5. Credit: Smajić et al., A&A, 567, A119, 2014, reproduced with permission © ESO.

disk radius is the same as in the single model. The radius for the outflow is $1\overset{''}{.}5$. The velocities chosen for this combined model are 60 $\mathrm{km\,s^{-1}}$ for the disk and 80 $\mathrm{km\,s^{-1}}$ for the outflow. The convolution was done with the same PSF as explained above. The combined model is shown in Fig. 4.15(c). To derive similar velocities as in the $H_2(1\text{-}0)S(1)$ LOSV map, the velocities of disk and outflow and the PA of the outflow were adjusted compared to the single models. All other parameters have the same values as in the single model description. Regarding a one-sided outflow, this can be justified if an otherwise double-sided nuclear wind makes contact with a molecular cloud on only one side.

This third approach describes the central gradient and the southward going redshifted tail very well. A $4'' \times 4''$ detail of the $H_2(1\text{-}0)S(1)$ velocity field centered on the nucleus and the model subtracted residual are shown in Fig. 4.16. The residual is at 0 ± 10 $\mathrm{km\,s^{-1}}$ in the vicinity of the central gradient. The redshifted tail shows higher residuals at $\sim 1''$ distance from the center, however, these can mainly be attributed to the underlying galactic rotation.

68

(a) H$_2$(1-0)S(1) detail (b) H$_2$(1-0)S(1) − model
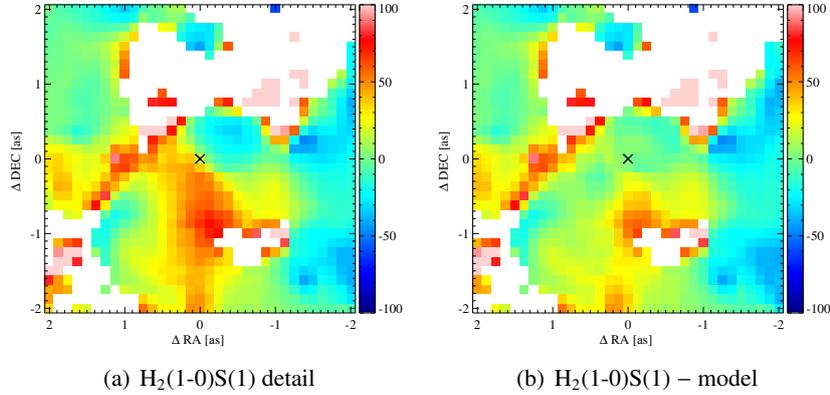
Figure 4.16: (a) shows the central $4'' \times 4''$. (b) shows the same detail but subtracted by the combined model (see Fig. 4.15(f)). For details, see Sect. 4.2.5. Credit: Smajić et al., A&A, 567, A119, 2014, reproduced with permission © ESO.

4.2.6 The dusty nuclear spiral arms

NGC 1433 shows a prominent nuclear ring at a radius of about $10''$ (see Fig. 4.1). The nuclear ring is fed efficiently by the primary bar and the induced gravitational torques. The ring is the sight of several star formation regions, for example Fig. 4.12(b) shows several bright spots, probably stellar clusters. Dust lanes wind from the nuclear ring toward the center where a pseudo-ring r=4$''$ in radius is formed right outside the inner ILR (iILR) at r=3$.''$6 (Buta et al. 2001). The dust arms that form the pseudo-ring show differential LOSV patterns as seen in Fig. 4.3(i) and 4.4(c).

At least three differential arms are identified in the $10'' \times 10''$ FOV. From the north along the western side the northern arm winds toward the center and is blueshifted. The southern arm stretches from the west and arcs along the south toward the emission peak in ^{12}CO(3-2) and is rather redshifted. The eastern arm is situated in the east and stretsches from the south in the $10'' \times 10''$ FOV toward the ^{12}CO(3-2) emission peak but is blueshifted, in contrast to the southern arm (see Fig. 4.4(c)). The western part in the central 2$''$ is blueshifted and seems connected to the nuclear peak in H$_2$(1-0)S(1). This nuclear arm arcs from the west southward and then north toward the nucleus and becomes more redshifted on its path.

The arms are nicely detected in ^{12}CO(3-2) and the LOSVs are similar to the H$_2$(1-0)S(1) LOSVs except in a region that can be associated with the eastern arm. This H$_2$(1-0)S(1) emission region, i.e., sp(B) (see Sect. 4.2.1), is the most

blueshifted region in the molecular hydrogen LOSV map. It reaches almost $-100\,\mathrm{km\,s^{-1}}$ at a distance of $3\farcs5$ to the nucleus. In the region north of sp(B), i.e., emission region sp(A) (see Sect. 4.2.1), the strongest $^{12}CO(3\text{-}2)$ emission is neither as blue as the eastern arm nor as red as the southern arm, but rather an average of both. This region is situated where eastern and southern arm interact or overlap, which would explain the strong $^{12}CO(3\text{-}2)$ and H_2 emission. Note that although there is a maximum in $^{12}CO(3\text{-}2)$ emission the dust lane here becomes seemingly more transparent as seen in the HST images. The southern spot sp(B) is stronger in H_2 than sp(A) and shows an FWHM of up to $250\ \mathrm{km\ s^{-1}}$. The cause for these observables is either an interaction between the two arms or a massive star formation region hidden behind and pushing at all the dust and gas. The star formation scenario would explain the strong blueshift and the strong H_2 emission excited by UV photons. But, the linewidth of the H_2 line in sp(B) speaks in favor of a collision of the two arms. Additionally, no Brγ emission can be detected in sp(B), which would imply, in the case of star formation, that the column density of the dust and molecular gas,e.g, H_2, between observer and star forming region is very high so that the H II region cannot be detected even in the NIR. In addition, no CO emission peak coincides with the position of sp(B). The velocity dispersion in the arms at $2''$ distance from the nucleus is up to $50\ \mathrm{km\ s^{-1}}$ and more (see Fig. 4.14), which may indicate an arm-arm interaction or hidden star formation activity.

The derived stellar LOSVs at a PA of 21° are consistent with measurements by Buta et al. (2001). The stellar continuum map indicates a PA of 33° for the nuclear bar, which is confirmed by Combes et al. (2013). The stellar luminosity distribution in the NIR does not indicate greater disturbances. A twist from the nuclear bar orientation of 33° to 15° and then to 69° toward the central isophotes is visible. However, the central isophotes are obviously dominated by the PSF, which is elongated at a PA of 69°. An ellipses fit to the continuum in optical and NIR confirms the PA measurements.

4.2.7 Computation of the torques

My thanks go to Francoise Combes who provided me with the computation of the torques in this subsection.

In near-infrared images the nuclear bar is well detected (see, for example, Jungwiert et al. 1997). It is situated inside the nuclear ring, and extends out to about 400 pc in radius at a PA of 30°. Inside the nuclear ring Peeples & Martini (2006) find a patchy nuclear spiral structure in HST images. The I-band image, because of the lowest dust extinction of the present HST data, is selected to trace

the old stellar distribution, and derive the gravitational potential at high spatial resolution. No bulge-disk-deconvolution was applied, considering that the bulge is highly flattened as concluded by Buta et al. (2001) on the basis of both photometry and kinematic arguments. They find that the inner part of the bulge is as highly flattened as the disk. The dark matter fraction is also negligible in the central kpc. The HST I-band image has been rotated and deprojected according to a PA of 19° (equivalent to 199°) and an inclination of i=33°, and then Fourier transformed to compute the gravitational potential and forces. A stellar exponential disk thickness of ~1/12th of the radial scale-length h_r=3.9 kpc of the galaxy has been assumed, giving h_z=328pc. This is the average scale ratio for galaxies of this type (e.g., Barteldrees & Dettmar 1994; Bizyaev & Mitronova 2002, 2009). The potential has been derived assuming a constant mass-to-light ratio of M/L = 0.5 $M_\odot/L_\odot$ in the I-band over the considered part of the image of 2 kpc in size. This mass-to-light ratio is realistic in view of what is found statistically for spiral galaxies (Bell & de Jong 2001). The pixel size of the map is 0.1″=4.8 pc. The stellar M/L value was fit to reproduce the observed CO rotation curve.

Following Combes et al. (2014), the potential was decomposed into its different Fourier components. The radial distribution of their normalized amplitudes and their radial phase variations are shown in Fig. 4.17.

The torques at each pixel are derived from the potential, as described in García-Burillo et al. (2005). The sign of the torque is determined relative to the sense of rotation in the plane of the galaxy. The product of the torque by the gas density Σ is shown in Fig. 4.18.

The torque weighted by the gas density $\Sigma(x, y)$ is then averaged over azimuth, and allows the estimation of the variations of the specific angular momentum L of the gas over time. By normalizing the angular momentum and rotation period at each radius, the efficiency of the torque in driving gas flows is obtained, see Fig. 4.19.

The uncertainty on the torques introduced by the uncertainty in the center position, see Sect. 4.2.4, is about 20%. The error estimation was conducted by computing the torques for several centers displaced by ±0″.2 in RA and DEC.

The estimated torques show that the nuclear bar has a high efficiency, although its strength is diluted by the flattened bulge. In one rotation, that is in ~ 40 Myr, the gas gains up to 50% of its angular momentum at a distance of 88 to 200 pc. At distances > 200 pc the torque becomes negative. The pseudo-ring, which was interpreted as the inner ILR of the bar, i.e., the ILR of the nuclear bar, by Combes et al. (2013), is found at this distance. The derived torques drive the gas toward the pseudo-ring and reinforce it. At distances lower 88 pc the derived torques cannot be interpreted in terms of average torques because the gas is
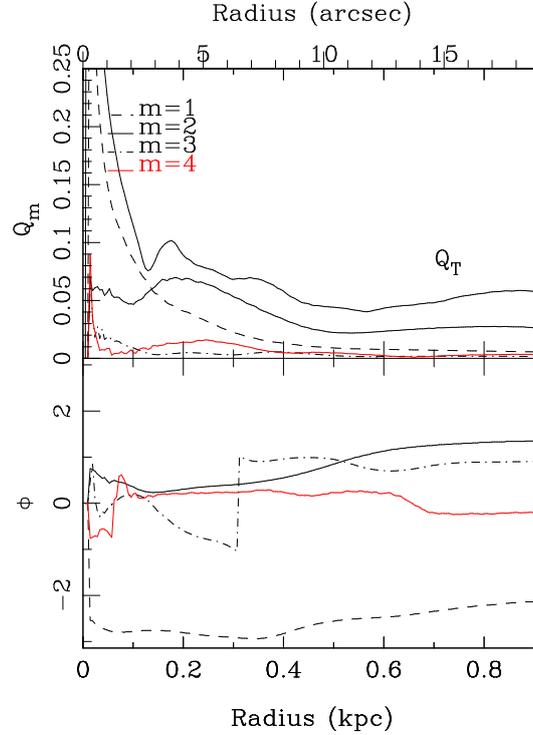
Figure 4.17: *Top:* Strengths (Q_m and total Q_T) of the $m = 1$ to $m = 4$ Fourier components of the stellar potential within the central kpc. Inside a radius of 130 pc, the $m = 1$ term dominates, and the nuclear bar extends until 350 pc radius. *Bottom:* Corresponding phases in radians of the Fourier components, taken from the major axis, in the deprojected image. Credit: Smajić et al., A&A, 567, A119, 2014, reproduced with permission © ESO.

not in quasi-stationary orbits in rotation around the center of the galaxy, aligned on the galaxy plane. The observed gas here is outflowing, probably dragged by AGN jets, at some angle from the plane (Combes et al. 2013). Therefore, the torque computation and deprojections do not apply here.

In summary, the in molecular gas observed pseudo-ring at distance r=200 pc, the ILR of the nuclear bar, is created by gas accumulations due to negative torques at r>200 pc and positive torques at r<200 pc. Hence, viscous torques or dynamical friction has to be invoked as mechanisms to drive gas further in toward the AGN.
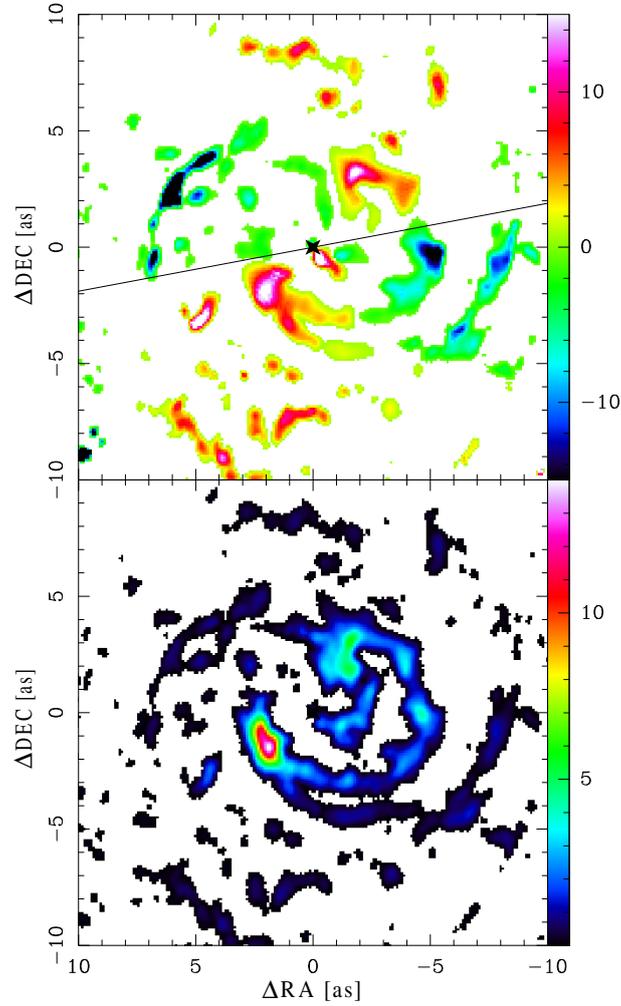
Figure 4.18: *Top:* Map of the gravitational torque, t(x,y) × Σ(x,y), weighted by the gas surface density Σ, assumed proportional to the ^{12}CO(3-2) emission. The torque per unit mass is $t(x, y) = x F_y - y F_x$ at each pixel (x,y), where F_x and F_y are the forces per unit mass, derived from the potential. The torques change sign as expected in a four-quadrant pattern (or butterfly diagram). The orientation of the quadrants follows the nuclear bar's orientation. In this deprojected picture, the major axis of the galaxy is oriented parallel to the horizontal axis. The inclined line reproduces the mean orientation of the bar (PA = 101° on the deprojected image). *Bottom:* The deprojected image of the ^{12}CO(3-2) emission, at the same scale, and with the same orientation, for comparison. The axes are labeled in arcsecond relative to the center. The color scales are linear, in arbitrary units. Credit: Smajić et al., A&A, 567, A119, 2014, reproduced with permission © ESO.
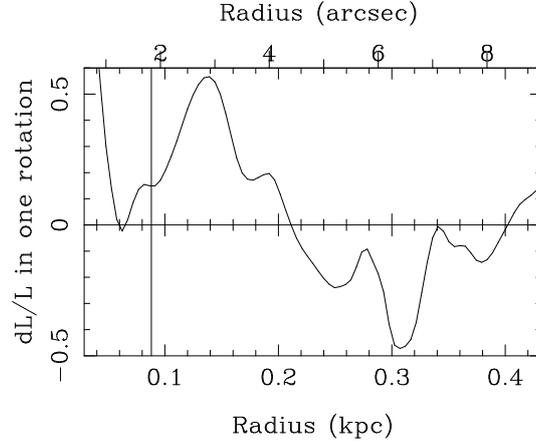
Figure 4.19: The radial distribution of the torque, quantified by the fraction of the angular momentum transferred from the gas in one rotation–dL/L, estimated from the ^{12}CO(3-2) deprojected map. The vertical line at 88 pc radius delimits the extent of the central gas outflow, and the computation has no meaning here. The torque is positive inside a 200 pc radius and then negative outside. Credit: Smajić et al., A&A, 567, A119, 2014, reproduced with permission © ESO.

4.3   Conclusion and summary

I present the first ALMA backed SINFONI results **of** the nearby LINER/Seyfert 2 galaxy NGC 1433 from the extended NUGA south sample. The center of the galaxy and the black hole position are constrained to the optical and NIR stellar luminosity peaks. The newly adopted center of NGC 1433 is situated $1''\!.5 \pm 0''\!.2$ north-northwest of the central position assumed by Combes et al. (2013), see table 4.1.

The velocity field of the H_2 and CO gas in the very center is discussed, with the newly adopted center as a reference. Three interpretations of the results are proposed: gaseous disk, molecular outflow, and a combination of both. Outflow characteristics were not observed in X-ray, however, the $2''$ resolution is insufficient to trace the possible small scale outflow that is discussed here. The simple modeling approach shows that, there is no observable difference between a nuclear disk model and a small scale nuclear double-sided outflow. The nuclear disk might be decoupled, depending on the yet unknown inclination. The third model, a combination of a circum-nuclear disk and a one-sided outflow, is a scenario that explains the southward reaching redshifted tail as well as the central velocity field, however, it also has a higher number of degrees of freedom.

An analysis of the spiral arms and their LOSVs hints at an inflow scenario for the nuclear region of NGC 1433 (see Fig. 4.13). The dust arms appear to leave

the disk, which can be implied by the observed blueshifted LOSV about 2″ west of the nucleus, but turn around, become redshifted, and fall in the direction of the nucleus. However, here the spiral arm encounters the strong nuclear velocity gradient that is oriented at a PA ~ 140°. The torque calculations show that the gas is driven toward a pseudo-ring at r=200 pc radius, which is interpreted by Combes et al. (2013) as the ILR of the nuclear r=430 pc bar. The estimated torque budget requires that possible gas infall toward the very center (< 200 pc) is induced by other mechanisms, e.g., viscous torques and dynamical friction. In fact, several dust arms are detected within a 2″ radius, i.e., the nuclear-arm and several faint dust lanes (see Fig. 4.12) that could be driven inward by viscosity torques (Combes et al. 2004; van der Laan et al. 2011). The observed minimum in SVD of the stars at the nucleus can then be explained by infalling gas that creates a nuclear disk in which stars are formed with a lower velocity dispersion than the bulge's SVD (Emsellem et al. 2001; Falcón-Barroso et al. 2006).

The PV diagrams agree with an outflow (see Fig. 4.14) scenario. The newly adopted center, i.e., the position of the SMBH, is now situated at the probable kinematic origin of the outflow. The lower molecular hydrogen velocity with respect to the CO velocity in the nuclear region indicates shock ionization of the gas. However, a small circum-nuclear disk cannot be excluded.

The measured stellar LOSV is consistent with literature values. The stellar isophotes follow the nuclear bar, however, small deviations may be detected toward the center (see Fig. 4.11).

The detected emission lines allow a line diagnostic on the nucleus and in emission spots sp(A) and sp(B). A Seyfert-to-LINER like excitation mechanism at the nucleus of NGC 1433 can be confirmed from the diagnostic diagram in Fig. 4.6. Star formation as the driving force for the possible nuclear outflow in the center can be excluded due to a very low SFR. Thermal excitation dominates the emission regions sp(A) and sp(B). The thermal emission temperature is higher in sp(A) than in sp(B) whereas sp(B) is close to the shock excitation models by Draine & McKee (1993). Region sp(A) lies exactly on the thermal emission curve at ~ 2500 K. Either strong but highly extincted star formation is detected here or a strong spiral arm-arm interaction takes place, due to strong $^{12}CO(3-2)$ and H_2 emission in sp(A), and strong and turbulent H_2 emission in sp(B).

The stellar mean SVD is estimated to 124 km s^{-1}. This yields a black hole mass of $M_{\bullet} = 1.74 \times 10^7 M_{\odot}$, which is higher than literature values by a factor 2. The molecular hydrogen mass is derived from $^{12}CO(3-2)$ and from $H_2(1-0)S(1)$ measurements. Within the central 1″ radius aperture a molecular hydrogen mass of ~ $10^6 M_{\odot}$ is estimated from the warm NIR gas, which is a factor 2 higher than the value from the cold CO gas. At larger apertures, e.g., the central r= 5″

75

aperture, a mass of $\sim 10^7 M_\odot$ is derived from both emission lines. The mismatch in the center may result from a lack of emission of the ^{12}CO(3-2) transition due to highly excited gas at temperatures higher than 55 K.

Gas and dust arms are connected to the center. But is the nucleus accreting the gas through a disk? Or possible infall repelled by an outflow from the AGN? Are maybe both mechanisms working without any larger interaction? Higher spatial resolution in forthcoming ALMA cycles and AO assisted SINFONI observations as well as higher excited CO transitions are needed to sufficiently resolve the nuclear region and the mechanisms that create the strong gradient that is not aligned with the stellar velocity field.

The Seyfert 1 Galaxy NGC 1566

The barred, ringed, spiral SAB(s)bc galaxy, NGC 1566, is part of the Dorado group (Mulchaey & Regan 1997; Reunanen et al. 2002) and harbors a low luminosity AGN (LLAGN) at a redshift of $z \approx 0.005017$ (Koribalski et al. 2004). The orientation of the bar is in north-south direction (PA~ 5°) and the ring has a diameter of 1.7 kpc (see Fig. 5.1). Broad Balmer lines are detected by Alloin et al. (1985) with widths of $FWHM_{H\beta} = 2400\pm300$ km s^{-1}. They also measure an increase in flux of the broad Hβ line by a factor of $4 - 5$ within 24 days. But they find the narrow line ratio of Hα/Hβ to be ≈ 3.1, which is typical for Seyfert 2 galaxies, however, the broad line flux variation and the broad to narrow line ratio Hβ(b)/Hβ(n) ≈ 10 shows that NGC 1566 is in a high activity state typical for Seyfert 1.2 galaxies. The light crossing time of the NLR is about $10^2 - 10^3$ years, hence, the NLR line ratios suggest that in the past few 100 years NGC 1566 has shown more the characteristics of a Seyfert 2 galaxy than that of a Seyfert 1. Kriss et al. (1991) measure a redshift of the broad emission lines of $200 - 1000$ km s^{-1}. This might result from gravitational redshift (Netzer 1977) but can also be induced by an infall of clouds at the near side of the BLR where the far side is obscured from the observers view or by an outflow of optically thick clouds at the far side.

NGC 1566 shows variability from IR wavelengths to X-ray. Baribaud et al. (1992) conclude that X-ray flickering should occur on time scales of 5×10^3 s. Additionally, they note that the NIR flux variation (heated dust reacting to UV flux changes) happens within the central 450 pc from the center at time scales similar to the broad Hα variability time scale. The extinction toward the nuclear region of NGC 1566 from NLR and BLR line ratios seems to be negligible. Baribaud et al. (1992) also calculate a dust mass $M_{dust} \approx 7\times10^{-4}$ M$_\odot$ and a dust evaporation radius of about 47 light-days. Reunanen et al. (2002) used slit spectroscopy on the nucleus of NGC 1566. They detect [Fe II] in the H-band and the H$_2$ $\lambda2.122$ μm line in the K-band. They note that the lines and the continuum appear weaker along the NLR cone than perpendicular to it. They do not detect narrow Brγ emission only a broad Brγ component with an $FWHM_{Br\gamma} = 2100$ km s^{-1}.

NGC 1566 is an interesting candidate to investigate the feeding and feedback
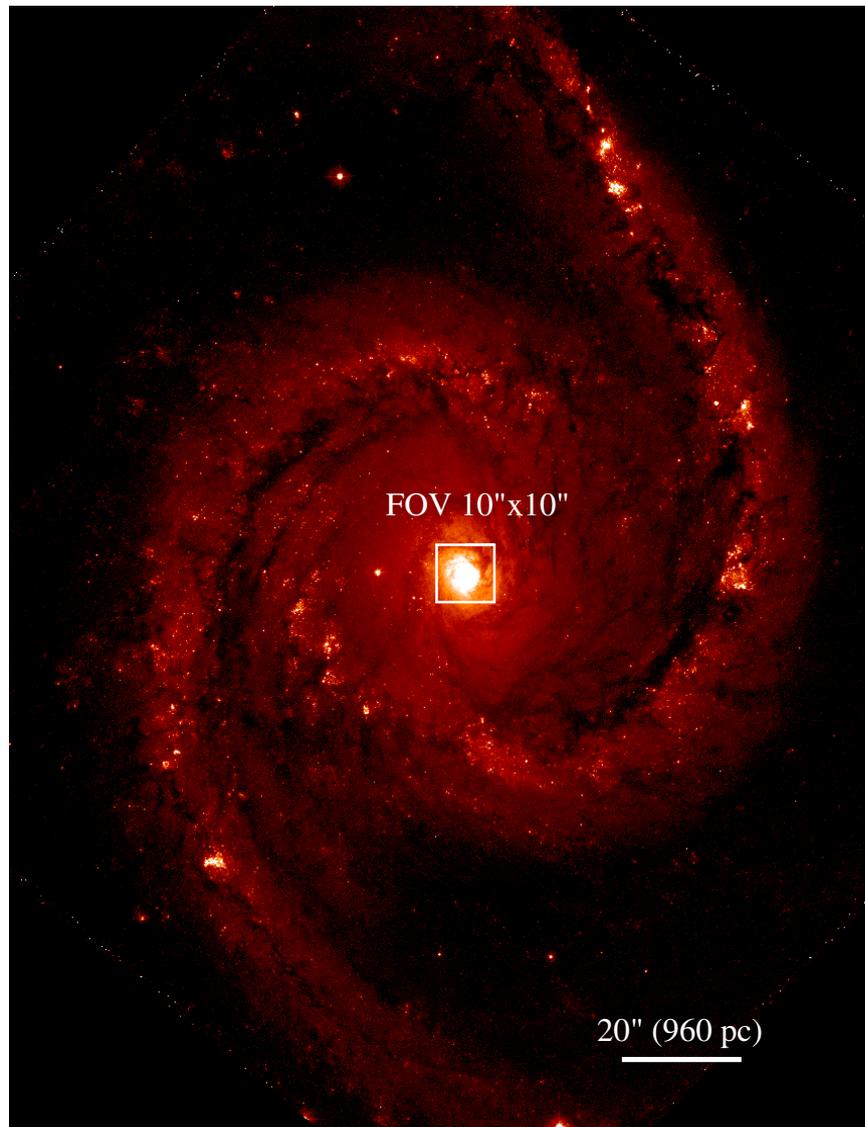
Figure 5.1: An HST image of NGC 1566 taken with the WFC3 UVIS2 F438W filter at a pivot wavelength of 4326 Å. North is up and east is left. The white rectangle marks the $10'' \times 10''$ field of view (FOV). Credit: Smajić et al., A&A, 583, A104, 2015, reproduced with permission © ESO.

of the nuclear region and the AGN. The galaxy, i.e., its AGN, seems to be waking up from a low activity state in the past few hundred years (low ionization level in the NLR) and shows signs of high activity with strong variability and high ionization on scales smaller than the NLR. Combes et al. (2014) find from ALMA ^{12}CO(3-2) and HST data that gravitational torques are a very likely cause to drive gas infall in NGC 1566. They derive negative torques from 300 pc down to 50 pc. From this point dynamical friction can drive the gas to the nucleus.

I will investigate the central $10'' \times 10''$ to find if the hot gas distribution and kinematics are similar to the cold gas observed with ALMA. Are there any signs of a feeding of the SMBH (e.g., strong ionization of the nuclear region, streaming gas motion)? How strongly is it accreting? Is any strong feedback (e.g., jets) visible in the hot gas? Is gas infall accompanied by star formation or is star formation rather hindered by the torque budget found by Combes et al. (2014)?

A systemic velocity of 1504 $\mathrm{km\,s^{-1}}$ and a distance of 10 Mpc are adopted for NGC 1566, following Alloin et al. (1985); Combes et al. (2014).

5.1 Observation and Data Reduction

I present results of my ESO SINFONI (Eisenhauer et al. 2003; Bonnet et al. 2004) observation of NGC 1566 with the Unit Telescope 4 of the Very Large Telescope in Chile. The $8'' \times 8''$ FOV with an $0\rlap{.}''25$ plate scale without adaptive optics assistance was used. The average seeing during observation was $\approx 0\rlap{.}''5$. A dithering sequence of the FOV by $\pm 2''$ was introduced to increase the FOV to $12'' \times 12''$ and minimize the overlap of dead pixels in critical areas. However, the outer $2''$ have a too low quality data, hence for the analysis a FOV of $10'' \times 10''$ was used. The dithering was done at 9 positions and the central $4'' \times 4''$ were observed with the full integration time, i.e., these are in all target exposures. The H-band grating, with a spectral resolution of R $\approx$ 3000, and the K-band grating, with a resolution of R $\approx$ 4000, were used. Both bands were observed at a digital integration time of 150 seconds and an TST... nodding sequence (T: target, S: sky), to increase on-source time. The overall integration time on the target source in H-band is 2550 seconds and in K-band 3000 seconds with an additional 1200 seconds in H-band and 1500 seconds in K-band on sky. The G2V star HIP 33144 was observed in H-band and in K-band within the respective science target observation. The observing strategy was to observe it twice (star in opposite corners of the FOV) with an integration time of 2 seconds. The ESO SINFONI pipeline was used for data reduction except for atmospheric OH line correction and final cube creation which were done manually. Detector specific

corrections were performed manually, as well. For more details on the reduction see Sect. 3. The standard star was used to correct for telluric absorption in the atmosphere and to perform a flux calibration of the target. The black body and intrinsic spectral features of the G2V star were corrected by a high S/N solar spectrum (Maiolino et al. 1996). The solar spectrum was convolved with a Gaussian to adapt its resolution to the resolution of the standard star spectrum. The solar spectrum edges were interpolated by a black body with a temperature of T = 5800 K. The telluric standard star spectrum was extracted by taking the total of all pixels within the radius of 3×FWHM$_{PSF}$ of the point spread function (PSF; Howell 2000), centered on the peak of a two-dimensional Gaussian fit. The flux calibration of the target source was performed during the telluric correction procedure. The standard star counts were referenced at λ1.662 μm and λ2.159 μm in H- and K-band respectively to the flux given by the 2MASS All-sky Point Source Catalogue[1].

To determine the spatial resolution achieved in the observation the radial profiles of the telluric star, the continuum emission in H- and K-band, and the radial profiles of the emission lines [Fe II], narrow Brγ, and broad Brγ (see Fig. 5.2) were analyzed. The unresolved broad component of the hydrogen recombination line Brγ is used to determine an accurate value of the FWHM of the PSF for the K-band because this value is measured from the science data itself. Figure 5.2 shows that the narrow component of Brγ and [Fe II] as well as the telluric stars in H- and K-band exhibit about the same spatial extent. This infers that the spatial resolution in H- and K-band is similar. A FWHM of the broad Brγ component of $\sim$ 0$''$59 is measured which corresponds to $\sim$ 29 pc. Spatially the PSF shows an elongation in the east-west direction slightly rotated by 10° (Fig. 5.3).

The correction of the OH lines, cube alignment, final cube creation, and the linemap and spectra extraction was conducted using IDL routines written by me.

Calibrated 350 GHz ALMA data is used as complementary data to the NIR results. The final product data is publicly available from the ALMA archive under project ID 2011.0.00208.S (PI: Combes). Details on observational setup, calibration, imaging and quality are stated in Combes et al. (2014) and in the project reports in the ALMA archive. The line cube comprises 50 channels of 10 km/s width and a beam of 0$''$64 × 0$''$43 at an PA of 123°. The rms achieved is 0.05 mJy beam^{-1} in the continuum and $\sim$ 1.3 mJy beam^{-1} in the line cubes. Imaging and parts of the analysis have been conducted with the CASA software (v3.3 McMullin et al. 2007).

---

[1]This publication makes use of data products from the Two Micron All Sky Survey, which is a joint project of the University of Massachusetts and the Infrared Processing and Analysis Center/California Institute of Technology, funded by the National Aeronautics and Space Administration and the National Science Foundation.
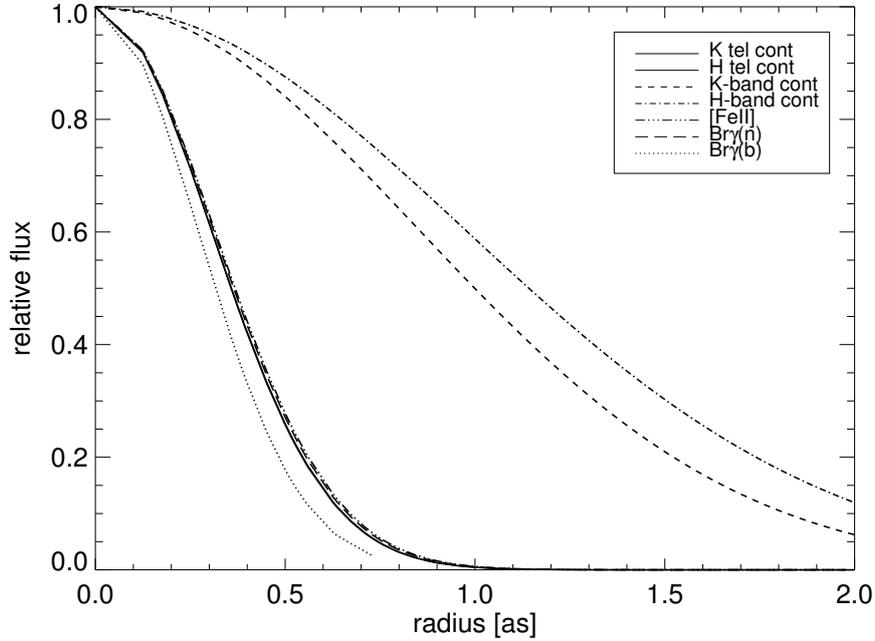
Figure 5.2: The radial profiles of the telluric star in K- and H-band, the K- and H-band galaxy continuum, [Fe II], narrow Brγ and broad Brγ. Credit: Smajić et al., A&A, 583, A104, 2015, reproduced with permission © ESO.

5.2 Results

With the seeing limited imaging spectroscopy of VLT SINFONI the central 485 pc of NGC 1566 are resolved at a spatial resolution of 29 pc. Several rovibrational molecular hydrogen lines (e.g. H_2(1-0)S(1) $\lambda 2.12\,\mu m$) and narrow and broad components of the hydrogen recombination line Brγ $\lambda 2.166\,\mu m$ are identified. Additionally, several stellar absorption features in K-band (e.g. CO(2-0) $\lambda 2.29\,\mu m$, NaD $\lambda 2.207\,\mu m$, CaT $\lambda 2.266\,\mu m$) are detected. The H-band shows a variety of stellar absorption features (e.g. Si I λ 1.59 μm, CO(6-3) $\lambda 1.62\,\mu m$) and it harbors the [Fe II] $\lambda 1.644\,\mu m$ line, which is important for NIR line diagnostics. The flux and the FWHM of all detected emission lines are summarized in tables 5.1 and 5.2 for the regions: center $r = 1''$, center $r = 5''$, center $r =$ PSF, star formation region (SFr), star formation region at PSF sized aperture (SF PSF), and center at PSF sized aperture (cPSF), see Fig. 5.3 for more detail. The emission line FWHMa presented in this chapter are corrected for instrumental broadening.

5.2.1 Ionized Gas

The forbidden transition [Fe II] $\lambda 1.644$ μm is slightly blended by the CO(7-4) $\lambda 1.641$ μm absorption but is very strong. With an FWHM of 350 km s^{-1} it is the broadest narrow emission line at the center (Figs. 5.3(a) & 5.3(b)). The line map of the [Fe II] emission shows a triangular shape pointing in north, east and southwest directions. The FWHM and equivalent width (EW) maps both show elongated features in the east-west direction. Toward the north the FWHM decreases quickly to about 100 km s^{-1}. To the south-west it stays for about one arcsecond above 300 km s^{-1} before it drops to $\sim$ 150 km s^{-1}. The eastern part extends to about 1$''$5 with an FWHM of about 250 km s^{-1}. The [Fe II] emission is point-like on the nucleus with a stronger eastern wing and a weaker south-western wing best seen in the EW map (Fig. 5.3(c)). The EW is 6.8 Å on the nucleus and only 0.6 Å in the south-west. A small plateau is detected to the east with an EW of $\sim$ 0.9 Å.

The Brγ line shows, spatially and spectrally, two components. Narrow and broad Brγ emission is detected at the center. The broad component shows an FWHM of about 2000 km s^{-1} and is redshifted by 340 km s^{-1}. This broad line emission is supposed to be excited in clouds close to the SMBH that are virialized and therefore are rotating fast around the center. From the spatial distribution of the BLR emission a reliable value for the PSF of $\sim$ 29 pc is determined (Sect. 5.1). The broad component is a clear indicator for a SMBH. The narrow component at the center has an FWHM of about 230 km s^{-1} and suggests a region size of 13.5 pc, after deconvolution with the PSF width. The excitation can be caused by the AGN meaning that the Brγ emission is excited in the NLR by the AGN, or by a nuclear star forming region, or most probably by a combination of both. Hence, the Brγ line can only be used as an upper limit for star formation at the nucleus itself. In addition, a spatially resolved strong narrow Brγ emission is detected about 1$''$ southwest from the nucleus (Fig. 5.3(j)). The off-nuclear Brγ emission shows a rather elliptical shape in the south-east to north-west direction. The FWHM in this region is $\sim$ 100 km s^{-1} with a maximum of 150 km s^{-1} in the south-east and a minimum of 70 km s^{-1} in the north-west. The EW of the narrow Brγ line at the nucleus is about 1.0 Å. At the off-nuclear region it is about 2.6 Å in the brightest spot and falls to about 2 Å along the ellipse.

To investigate the excitation mechanism in the center and the south-western Brγ emission region he line ratio $\log([\text{Fe II}]/\text{Br}\gamma)$ can be used (Alonso-Herrero et al. 1997). A ratio of about 1 on the nucleus confirms the assumption that a mixture by X-ray photons from the AGN ($\log([\text{Fe II}]/\text{Br}\gamma) \lesssim 1.3$), from stellar thermal UV emission, and shocks is responsible for the ionization. For the off-

nuclear region the line ratios of -0.3 to -0.4 are typical for a star forming region ($\log([\text{Fe\,\textsc{ii}}]/\text{Br}\gamma) < 0.3$, see also Fig. 5.16) whose young bright stars ionize the gas by UV photons. The luminosity of Brγ, $L_{\text{Br}\gamma}$, is proportional to the Lyman continuum flux and can be used as a measure for the star formation rate (SFR) (Panuzzo et al. 2003; Valencia-S. et al. 2012) in the emitting region

$$\text{SFR} = \frac{L_{\text{Br}\gamma}}{1.585 \times 10^{32}\,\text{W}}\ \text{M}_\odot\ \text{yr}^{-1}. \tag{5.1}$$

The two regions of interest are at the nucleus with an $1''$ radius and a luminosity of $L_{\text{Br}\gamma} = 8.45 \times 10^{29}$ W and the lenticular region $1\rlap.''5$ southwest from the center with a luminosity of $L_{\text{Br}\gamma} = 4.15 \times 10^{29}$ W over an area of ~ 1.33 arcsec^2. A SFR of $\sim 5.3 \times 10^{-3}$ M$_\odot$ yr^{-1} is derived at the center and of $\sim 2.6 \times 10^{-3}$ M$_\odot$ yr^{-1} at the southwestern region. Additionally, the supernova rate (SNR) can be estimated in these regions using the [Fe\,\textsc{ii}] emission. Following Bedregal et al. (2009) and two different calibrations are used

$$\text{SNR}_{\text{Cal97}} = 5.38\ \frac{L_{[\text{Fe\,\textsc{ii}}]}}{10^{35}\,\text{W}}\ \text{yr}^{-1} \tag{5.2}$$

after Calzetti (1997) and

$$\text{SNR}_{\text{AlH03}} = 8.08\ \frac{L_{[\text{Fe\,\textsc{ii}}]}}{10^{35}\,\text{W}}\ \text{yr}^{-1} \tag{5.3}$$

after Alonso-Herrero et al. (2003). The luminosity of [Fe\,\textsc{ii}] is measured to be $L_{[\text{Fe\,\textsc{ii}}]} = 7.1 \times 10^{30}$ W at the center and $L_{[\text{Fe\,\textsc{ii}}]} = 2.51 \times 10^{29}$ W at the southwest. The SNRs are $\sim 3.82 \times 10^{-4}$ yr^{-1}, and $\sim 5.74 \times 10^{-4}$ yr^{-1}, respectively, at the center and $\sim 1.35 \times 10^{-5}$ yr^{-1}, and $\sim 2.03 \times 10^{-5}$ yr^{-1}, respectively, in the southwest. The estimates at the central region are upper limits since star formation and the AGN are responsible for the excitation of Brγ and [Fe\,\textsc{ii}].
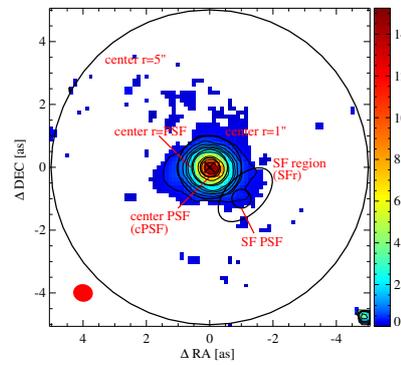
The broad Brγ line flux and FWHM are used to estimate the mass of the central SMBH of NGC 1566. A conversion factor of Paα/Br$\gamma \sim 12$ is used to translate the Brγ to Paα flux and be able to use the equation

$$\text{M}_\bullet = 10^{7.29\pm0.1} \left(\frac{L_{\text{Pa}\alpha}}{10^{42}\,\text{erg s}^{-1}}\right)^{0.43\pm0.03} \left(\frac{FWHM_{\text{Pa}\alpha}}{10^3\,\text{km s}^{-1}}\right)^{1.92\pm0.18}\ \text{M}_\odot \tag{5.4}$$
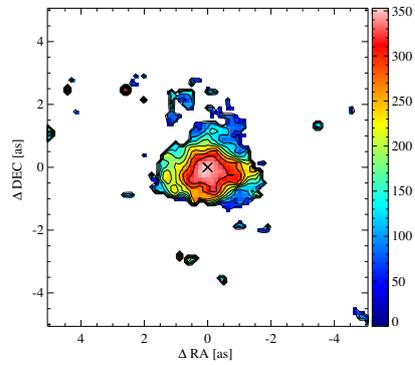
derived by Kim et al. (2010). The BH mass is estimated to be $\text{M}_\bullet = (3.0 \pm 0.9) \times 10^6$ M$_\odot$ using a luminosity of $L_{\text{Br}\gamma} = 5 \times 10^{38}$ erg s^{-1} and a $FWHM_{\text{Br}\gamma} = 2000$ km s^{-1}. Kriss et al. (1991) find a black hole mass of 5×10^6 M$_\odot$ based on optical studies of the BLR size and broad emission line profiles.

In addition, the He\,\textsc{i} $\lambda 2.06$ μm emission line is detected. The emission is strongest at the center but is also very prominent in the southwestern region
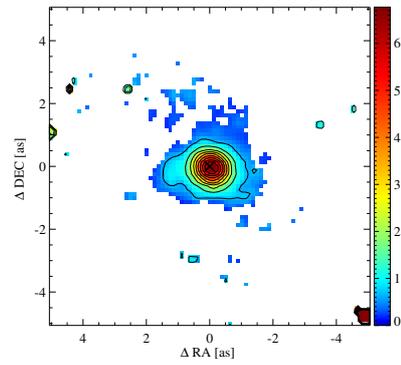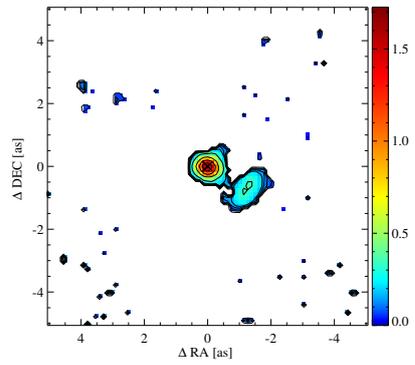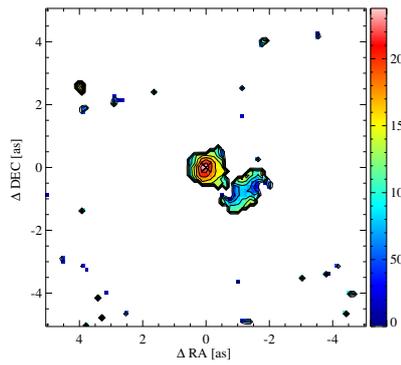
(a) Flux [Fe II]

(b) FWHM [Fe II]

(c) EW [Fe II]

(d) Flux He I

(e) FWHM He I

(f) EW He I

(g) Flux H$_2$(1-0)S(1)

(h) FWHM H$_2$(1-0)S(1)

(i) EW H$_2$(1-0)S(1)

(j) Flux Brγ

(k) FWHM Brγ

(l) EW Brγ
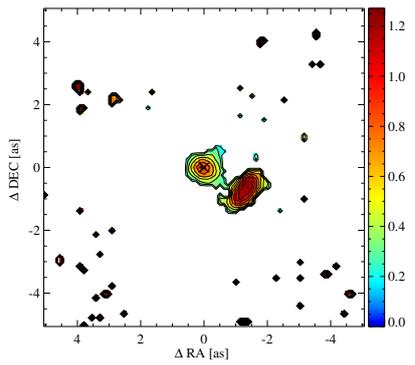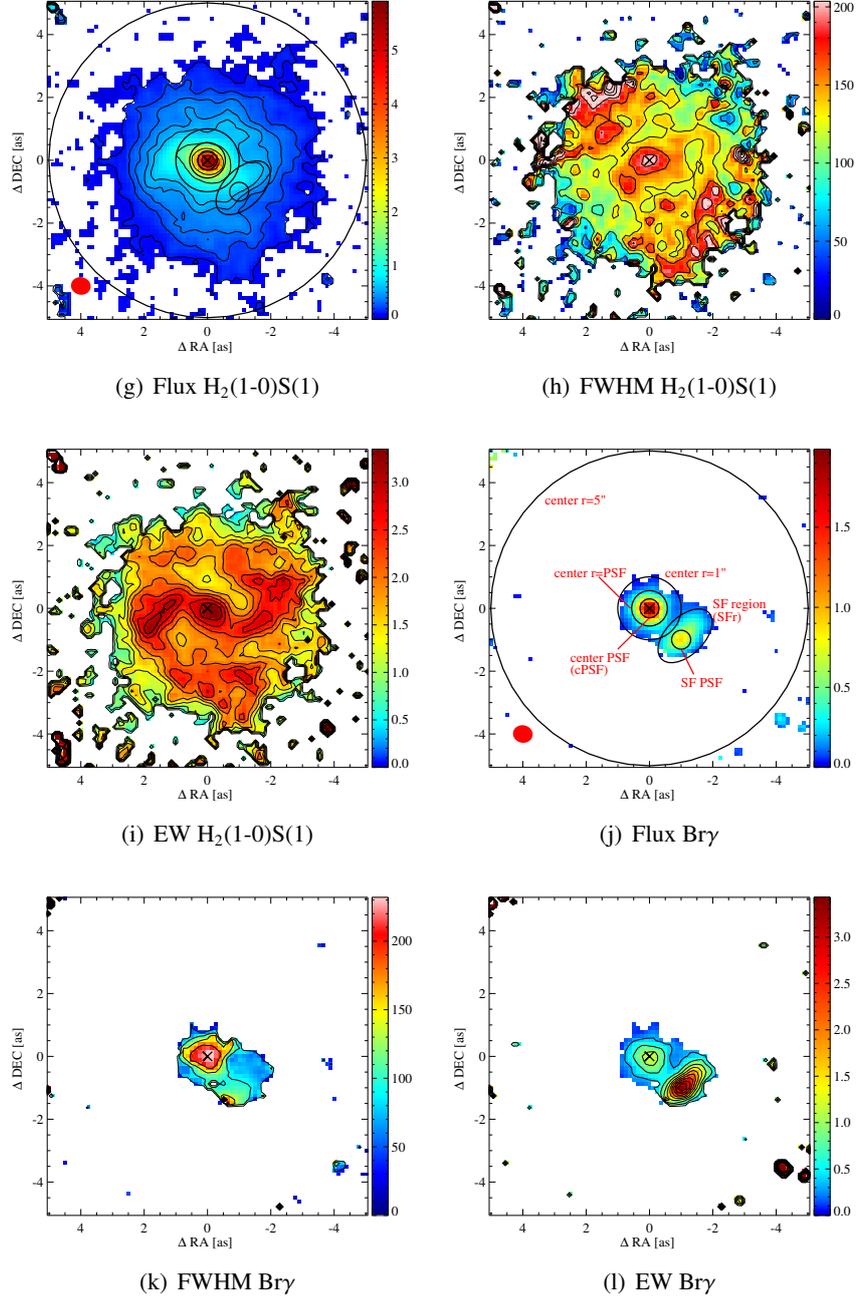
Figure 5.3: From left to right: flux [10^{-20} W m^{-2}], FWHM (corrected for instrumental broadening) [km s^{-1}] and EW [Å] maps of, from top to bottom: [Fe ɪɪ], He ɪ, H$_2$(1-0)S(1), and narrow Brγ emission lines. The regions discussed in this work are marked in the flux maps (a), (g), and (j). Credit: Smajić et al., A&A, 583, A104, 2015, reproduced with permission © ESO.

where the strong narrow Brγ emission is detected. The FWHM peaks on the center with $250\,\mathrm{km\,s^{-1}}$ whereas the south-western region shows a broadness $\sim$ 120 km s^{-1} similar to that of the Brγ. The flux distribution and with it the EW of both lines is not as similar. The southwestern emission region shows a peak in Brγ in its lower part, whereas He I is uniformly distributed over the whole ellipse. The EW of He I is up to 0.8 Å at the nucleus and up to 1.3 Å at the southwestern emission region.

5.2.2 Molecular Gas

In K-band several molecular hydrogen lines are detected. Most prominent are the H$_2$(1-0)S(1) λ2.12 μm and H$_2$(1-0)S(3) λ1.96 μm lines. Other detections are: H$_2$(1-0)S(2) λ2.03 μm, H$_2$(1-0)S(0) λ2.22 μm, H$_2$ (2–1)S(1) λ2.248 μm, H$_2$(1-0)Q(1) λ2.41 μm H$_2$(1-0)Q(3) λ2.42 μm.

The molecular emission line H$_2$(1-0)S(1) shows strong emission on the nucleus and reveals a nuclear spiral structure (Figs. 5.3(g), 5.3(i)). The EW map reveals the full extent of the nuclear structure. The arms are clearly visible, with the eastern arm having a higher EW than the western, which is visible in the flux map as well. The center in EW looks like a gaseous bar with a hump at the very center. The spiral does not seem to become narrow here, however, this might be a resolution effect. The strong off-nuclear Brγ emission is situated along the southern edge of the western arm, where the EW is lower. Both arms are oriented at a PA of $\sim$ 90° and point counter-clockwise, when moving from the center outward. The eastern arm and the nuclear region both show the maximum in EW of about 3.4 Å, outside these regions the EW drops to $\sim$ 1.75Å. Both arms show concentrated cigar-shaped emission in the parts connected to the nucleus and then turn over by about $\sim$ 90° into more diffuse emission. The arms do not look like a geometrical spiral close to the center. Inferred from the EW map a bar seems to connect the spiral arms toward the nucleus. The line of sight velocity (LOSV) shows a rotation at a PA of $\sim$ 45° that reaches a LOSV of about $\pm$150 km s^{-1} at a radius of about 2$''$5 (Fig. 5.6). In addition, a strong gradient is observed in the central region with the line of nodes at a PA $\sim$ 0°. This change in the PA is indicative of a bar or spiral density wave. The FWHM reaches a velocity of $200\,\mathrm{km\,s^{-1}}$ at the center and in regions $\sim$ 2$''$5 to the northeast and to the southwest of the nucleus. Along the spiral arms the FWHM is $\sim 130\,\mathrm{km\,s^{-1}}$. Along the minor axis of the galactic rotation the FWHM does not fall to the width of the spiral arms but stays at about 160 km s^{-1}. In the northwest and southeast the FWHM drops down to $70\,\mathrm{km\,s^{-1}}$ (Fig. 5.3).

H$_2$(1-0)S(3) and all other detected molecular hydrogen emission lines look very similar to H$_2$(1-0)S(1) in shape and value (e.g., similar velocities, similar

flux distribution, see Figs. 5.17 and 5.18). Therefore, the H_2(1-0)S(1) emission line is used as the general description of all molecular hydrogen lines.

From the detected molecular hydrogen lines the warm H_2 gas mass can be determined using the luminosity of the H_2(1-0)S(1), $L_{H_2(1\text{-}0)S(1)}$, and the equation

$$M_{H_2} = 4.243 \times 10^{-30} \left(\frac{L_{H_2(1\text{-}0)S(1)}}{W} \right) M_\odot \qquad (5.5)$$

following Turner & Ostriker (1977); Scoville et al. (1982); Wolniewicz et al. (1998); Riffel et al. (2008). The warm H_2 gas mass in a $5''$ radius aperture, which corresponds to all the H_2 emission detected in the FOV, is derived to 57 $M_\odot$. The cold gas mass is estimated using the conversion factor derived by Mazzalay et al. (2013)

$$\frac{M_{H2(cold)}}{M_{H2(warm)}} = (0.3 - 1.6) \times 10^6. \qquad (5.6)$$

The cold H_2 gas mass in the central $10'' \times 10''$ is found to be $(1.7 - 9.1) \times 10^7$ $M_\odot$. Combes et al. (2014) detect $7 \times 10^7 M_\odot$ in their $r = 18''$ FOV from CO(3-2) observations with ALMA. The values are in good agreement since the bulk of the molecular mass in NGC 1566 is located in the inner $6''$ (Fig. 5.3, 5.8 and Combes et al. 2014, and their Fig. 3).

In the mm-regime the cold molecular gas distribution is traced by the ^{12}CO(3-2) line observed with ALMA. This emission line is compared the ro-vibrational H_2 line emission which traces the hot molecular gas distribution. In general, the ^{12}CO(3-2) emission is very similar to the H_2(1-0)S(1) emission. In both lines an $r = 3''$ disk is detected with a nuclear spiral inside these $3''$. The nuclear spiral looks almost identical when comparing the ^{12}CO(3-2) emission and the H_2(1-0)S(1) EW maps (Fig. 5.3(i) and 5.8(a)).

5.2.3 Continuum

The mm-continuum at 0.87 mm peaks in the same region as the NIR continuum but the distribution is different compared to the NIR (Fig. 5.7, 5.8(c)). The 0.87 mm emission is distributed similar to the molecular lines. Apart from the peak in the center 0.87 mm emission is detected in the south-western spiral arm coinciding with the Brγ emission and in the north-east coinciding with the regions that show an increased width in the molecular lines (Fig. 5.8(b)). Combes et al. (2014) find that the 0.87 mm emission is dominated by dust emission.

The flux density is higher in H- than in K-band. It becomes redder at the center, as is expected in a Seyfert 1 galaxy, hence the slope becomes flatter but it is not inverted. The H-K map (Fig. 5.4) shows a clear reddening toward the

Table 5.1: NGC 1566 emission line flux and FWHM, part one.

	Flux [10^{-18} W m^{-2}]		
Line	Center $r = 1''$	Center $r = 5''$	Center $r = $ PSF
[Fe II]	5.93 ± 0.68	—	4.82 ± 0.38
H$_2$(1-0)S(3)	3.80 ± 0.33	15.15 ± 3.18	2.35 ± 0.19
H$_2$(1-0)S(2)	1.66 ± 0.18	5.46 ± 1.35	1.01 ± 0.10
He I	0.51 ± 0.14	—	0.42 ± 0.09
H$_2$(2-1)S(3)	—	—	0.12 ± 0.07
H$_2$(1-0)S(1)	3.41 ± 0.15	11.21 ± 1.2	2.25 ± 0.09
Brγ	0.71 ± 0.16	—	0.60 ± 0.10
H$_2$(1-0)S(0)	1.04 ± 0.12	3.68 ± 1.06	0.64 ± 0.07
H$_2$(2-1)S(1)	0.55 ± 0.11	—	0.35 ± 0.07
H$_2$(1-0)Q(1)	3.68 ± 0.35	33.64 ± 8.44	2.23 ± 0.17
H$_2$(1-0)Q(3)	3.23 ± 0.24	49.70 ± 5.7	1.80 ± 0.12
	FWHM [km s^{-1}]		
[Fe II]	321 ± 48	—	333 ± 34
H$_2$(1-0)S(3)	211 ± 17	227 ± 43	211 ± 15
H$_2$(1-0)S(2)	221 ± 28	214 ± 63	219 ± 26
He I	150 ± 54	—	165 ± 43
H$_2$(2-1)S(3)	—	—	70 ± 46
H$_2$(1-0)S(1)	191 ± 10	189 ± 25	199 ± 9
Brγ	165 ± 44	—	199 ± 37
H$_2$(1-0)S(0)	173 ± 22	210 ± 67	178 ± 22
H$_2$(2-1)S(1)	172	—	176
H$_2$(1-0)Q(1)	166 ± 14	153 ± 36	171 ± 12
H$_2$(1-0)Q(3)	171 ± 14	150 ± 20	185 ± 14

**Notes.** Flux and FWHM table for regions Center $r = 1''$, $r = 5''$, and $r = $ PSF (see also Fig. 5.3 for abbreviations). During the fit the linewidth of the emission line H$_2$(2-1)S(1) was tied to the width of the emission line H$_2$(1-0)S(0), hence no error can be given for the linewidth. The values for the FWHM are corrected for instrumental broadening.

Table 5.2: NGC 1566 emission line flux and FWHM, part two.

Flux [10^{-18} W m^{-2}]			
Line	SFr	SF PSF	cPSF
[Fe II]	0.21 ± 0.09	0.06 ± 0.02	2.39 ± 0.13
H$_2$(1-0)S(3)	0.57 ± 0.05	0.14 ± 0.01	0.93 ± 0.07
H$_2$(1-0)S(2)	0.28 ± 0.03	0.08 ± 0.01	0.39 ± 0.04
He I	0.17 ± 0.02	0.05 ± 0.006	0.23 ± 0.04
H$_2$(2-1)S(3)	0.03 ± 0.02	0.012 ± 0.006	0.05 ± 0.03
H$_2$(1-0)S(1)	0.52 ± 0.03	0.13 ± 0.008	0.96 ± 0.03
Brγ	0.35 ± 0.03	0.14 ± 0.008	0.31 ± 0.04
H$_2$(1-0)S(0)	0.17 ± 0.02	0.05 ± 0.005	0.25 ± 0.03
H$_2$(2-1)S(1)	0.11 ± 0.02	0.03 ± 0.005	0.14 ± 0.03
H$_2$(1-0)Q(1)	0.74 ± 0.11	0.16 ± 0.02	0.86 ± 0.07
H$_2$(1-0)Q(3)	0.81 ± 0.11	0.17 ± 0.03	0.69 ± 0.05
FWHM [km s^{-1}]			
[Fe II]	130 ± 89	84 ± 60	344 ± 24
H$_2$(1-0)S(3)	144 ± 14	124 ± 12	207 ± 14
H$_2$(1-0)S(2)	177 ± 25	183 ± 26	210 ± 24
He I	89 ± 19	82 ± 16	197 ± 37
H$_2$(2-1)S(3)	14 ± 10	56 ± 32	84 ± 44
H$_2$(1-0)S(1)	139 ± 10	129 ± 10	204 ± 8
Brγ	96 ± 11	103 ± 7	225 ± 31
H$_2$(1-0)S(0)	116 ± 16	112 ± 16	179 ± 25
H$_2$(2-1)S(1)	115	111	177
H$_2$(1-0)Q(1)	115 ± 19	95 ± 17	177 ± 12
H$_2$(1-0)Q(3)	171 ± 26	170 ± 30	195 ± 14

Notes. Flux and FWHM table for regions SFr, SF PSF, and cPSF (see also Fig. 5.3 for abbreviations). The linewidth of H$_2$(2-1)S(1) was tied to the width of emission line H$_2$(1-0)S(0) during the fit, hence no error can be given for the linewidth. The FWHM values are corrected for instrumental broadening.

center with an H-K value of > 0.8 mag at the very center. This implies a warm to hot dust emission in the galaxy center (Fischer et al. 2006; Busch et al. 2014). Since a broad Brγ component is detected it can be assumed that emission from the inner edge of the dust torus surrounding the AGN is detected.
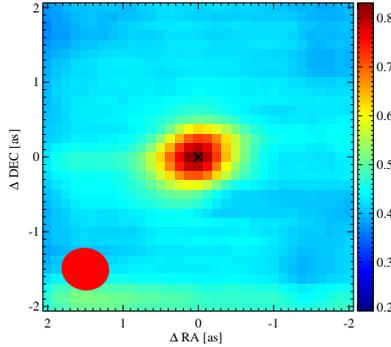

Figure 5.4: The H-K color diagram in magnitudes of the central $4'' \times 4''$ of NGC 1566. The red ellipse at $(1.5'', -1.5'')$ shows the beam size. For details see Sect. 5.2.3 & 5.3.2. Credit: Smajić et al., A&A, 583, A104, 2015, reproduced with permission © ESO.

To analyze the NIR continuum further a decomposition was performed. The continuum components: stellar template, hot dust blackbody, power-law and an overlaying extinction component were used to determine the continuum composition. The stellar component was fitted using resolution adapted template stars from Winge et al. (2009). Since these stars are only available in K-band from 2.2 μm to 2.4 μm the decomposition had to be performed in this wavelength range. For more details on the decomposition see Smajić et al. (2012) and Smajić et al. (2014).

The decomposition provides two interesting results. The blackbody, responsible for fitting hot dust, returns a hot $\sim$ 1000 K component with a significant contribution at the very center. This is expected in Seyfert 1 nuclei and is consistent with the reddening seen in the H-K map toward the center. The stellar component produces best results when HD2490, an M0III star, representing the old stellar population, and HD1737, a G5III star are used. The contribution of G5III-like stellar emission becomes apparent at the center.

The stellar velocity dispersion, LOSV, and intensity are shown in Figs. 5.5, 5.6, and 5.7. The stellar LOSV shows a rather regular rotational field at velocities of ± 60 km s^{-1} with a boxy redshifted side. The stellar velocity dispersion shows velocities of 90 to 125 km s^{-1} with the very center being at 100 km s^{-1}. To use the M$-\sigma_*$ relation and estimate the mass of the SMBH the dispersion of the bulge is needed. To determine the bulge dispersion a Gaussian fit was performed
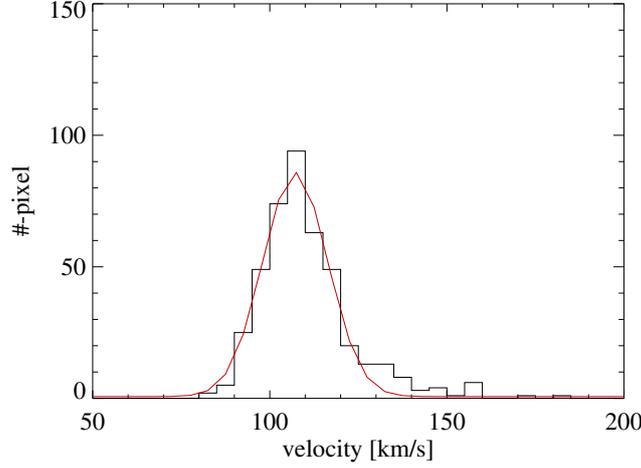
Figure 5.5: Stellar velocity dispersion histogram. The X-axis shows the fitted dispersion in 5 km s^{-1} bins. The Y-axis shows the total number of spatial pixel that correspond to the dispersion bin. The red curve is a Gaussian fit to the distribution. Credit: Smajić et al., A&A, 583, A104, 2015, reproduced with permission © ESO.

on the distribution of the stellar velocity dispersion values (Fig. 5.5). The fit yields a dispersion of 105 ± 10 km s^{-1}. Following Gültekin et al. (2009)

$$M_\bullet = 10^{8.12 \pm 0.08} \times \left(\frac{\sigma_*}{200 \text{ km s}^{-1}} \right)^{4.24 \pm 0.41} M_\odot, \qquad (5.7)$$

the mass of the SMBH is then estimated to $M_\bullet = 8.6 \pm 4.4 \times 10^6$ M$_\odot$. Graham & Scott (2013) have investigated the M$-\sigma_*$ relation for barred galaxies. Their best fit

$$M_\bullet = 10^{7.92 \pm 0.23} \times \left(\frac{\sigma_*}{200 \text{ km s}^{-1}} \right)^{5.29 \pm 1.47} M_\odot, \qquad (5.8)$$

returns a BH mass of $M_\bullet = 2.8 \times 10^6$ M$_\odot$, unfortunately the errors are higher than the actual result. When their fit with the least root-mean-square scatter is used

$$M_\bullet = 10^{7.78 \pm 0.1} \times \left(\frac{\sigma_*}{200 \text{ km s}^{-1}} \right)^{4.14 \pm 0.55} M_\odot, \qquad (5.9)$$

the result is a BH mass of $M_\bullet = (4.2 \pm 2.4) \times 10^6$ M$_\odot$. The latter two results agree within the errors with mass estimates using the broad emission lines, i.e., broad Hα (Kriss et al. 1991) and broad Brγ (see Sect. 5.2.1).
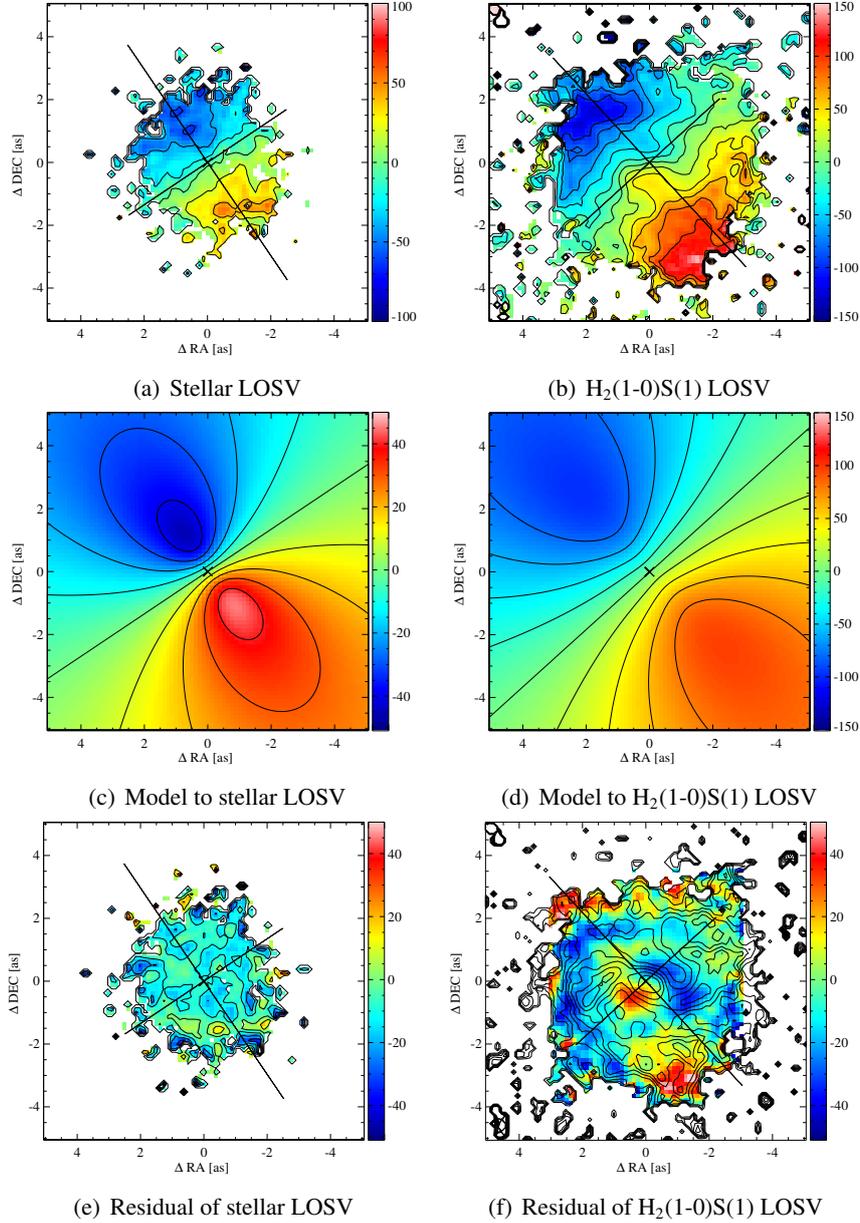
5.3 Discussion

5.3.1 The Active Nucleus

The BH mass of NGC 1566 can be estimated by the broad Brγ component and the M$-\sigma_*$ relation. The Brγ approach returns a BH mass of $(3.0 \pm 0.9) \times 10^6$ M$_\odot$, less than a factor two smaller than the 5×10^6 M$_\odot$ estimated from optical broad line measurements (Kriss et al. 1991). This difference might be introduced by variations in the activity of the AGN. A flux increase in the broad Hβ line was measured by a factor of four to five within only 24 days (Alloin et al. 1985). Assuming a low activity state during the observation, an increase of a factor four in luminosity will increase the BH mass derived from the Brγ broad line to $(5.5 \pm 1.7) \times 10^6$ M$_\odot$, a factor of two. Hence, the derived value of $(3.0 \pm 0.9) \times 10^6$ M$_\odot$ is in good agreement with the literature value.

Using the M$-\sigma_*$ relation with the determined stellar dispersion of 105 km s^{-1} a BH mass of $(8.6 \pm 4.4) \times 10^6$ M$_\odot$ is estimated, using the relation by Gültekin et al. (2009). This value is similar to the 8.3×10^6 M$_\odot$ from Woo & Urry (2002) but a factor two to three higher than the BH mass estimate from the broad emission lines. Graham & Scott (2013) find that barred galaxies follow a slightly different M$-\sigma_*$ relation than non-barred galaxies. Using their values a BH mass of $(4.2 \pm 2.4) \times 10^6$ M$_\odot$ is derived. This value is a factor two lower than the one obtained when using the relation from Gültekin et al. (2009) and agrees very well with the broad emission line BH mass estimates.

The scatter of the individually estimated BH masses is higher than their uncertainties. Therefore, a mean BH mass is derived from the four relations used in this work (see sections 5.2.1 and 5.2.3) to estimate the BH mass of NGC 1566. The mean BH mass is $(5.3 \pm 2.9) \times 10^6 M_\odot$. All individual BH mass values are within the standard deviation of the mean BH mass.

NGC 1566 is obviously a Seyfert 1 galaxy inferred from the broad lines it exhibits and it is actively accreting mass due to the observed variabilities. The $2 - 10$ keV X-ray luminosity of the AGN was measured by Levenson et al. (2009) to $L_{X,D20} = 10^{41.5}$ erg s^{-1} for a distance of 21.2 Mpc, hence an $L_X = 7.0 \times 10^{40}$ erg s^{-1} is estimated for a distance of 10 Mpc. From the derived mean BH mass an Eddington luminosity of $L_{Edd} = (6.6 \pm 3.7) \times 10^{44}$ erg s^{-1} can be determined. Using the relation $L_{bol} \approx 16 \times L_X = (1.1 \pm 0.4) \times 10^{42}$ erg s^{-1} for LLAGN (Ho 2008, 2009) the Eddington ratio of the active nucleus in NGC 1566 can be estimated to $\lambda_{Edd} = (2 \pm 1) \times 10^{-3}$. This is a typical value for Seyfert 1 LLAGN (Ho 2008). Although Kawamuro et al. (2013) use different parameters, e.g. BH mass, distance, L_X conversion factor etc., they find a similar value of 3.2×10^{-3}.

(a) Stellar LOSV

(b) H$_2$(1-0)S(1) LOSV

(c) Model to stellar LOSV

(d) Model to H$_2$(1-0)S(1) LOSV

(e) Residual of stellar LOSV

(f) Residual of H$_2$(1-0)S(1) LOSV

Figure 5.6: Top panel: Stellar LOSV, fitted LOSV model and the subtracted residual in units of [km s^{-1}]. Bottom: H$_2$(1-0)S(1) LOSV, fitted LOSV model and the subtracted residual overlayed with contours of the EW map of H$_2$(1-0)S(1) in units of [km s^{-1}]. The EW map was overlayed to display the nuclear spiral onto the residual velocity field of the gas. The straight lines denote the orientation of the major and minor rotation axis as determined by the LOSV model. For more details, see Sect. 5.3.3. Credit: Smajić et al., A&A, 583, A104, 2015, reproduced with permission © ESO.

(a) K-band continuum

(b) Stellar continuum

(c) Stellar dispersion
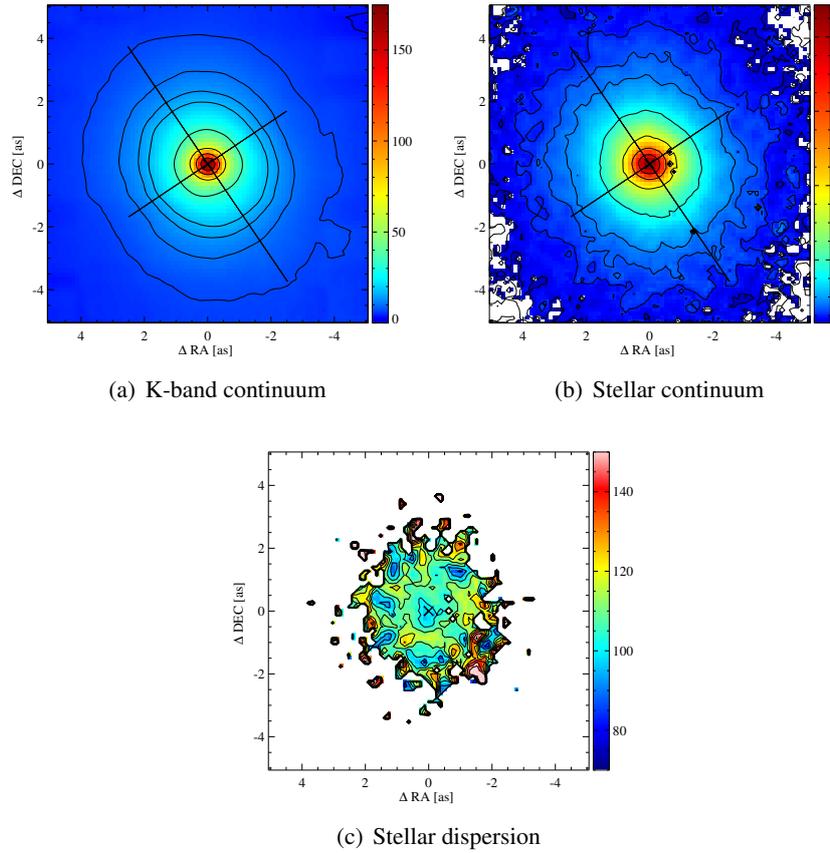
Figure 5.7: K-band continuum (a) [10^{-18} W m^{-2} μm^{-1}], the fitted stellar continuum (b) [arbitrary units] and the SVD (c) [km s^{-1}] obtained from the continuum decomposition. For more details, see Sects. 5.2.3 and 5.3.2. Credit: Smajić et al., A&A, 583, A104, 2015, reproduced with permission © ESO.

The mass accretion onto the SMBH can then be estimated with

$$\frac{\mathrm{d}M}{\mathrm{d}t} = \frac{L_{\mathrm{bol}}}{\eta c^2}, \tag{5.10}$$

where η is an efficiency factor which is usually of the order of 0.1. The mass accretion rate is calculated to $(2.0 \pm 0.7) \times 10^{-4}$ $M_\odot$ yr^{-1} using L_{bol} from above. The cold H$_2$ gas mass in the $10'' \times 10''$ FOV was measured to be $\sim 5.4 \times 10^7$ M$_\odot$. This mass is enclosed in the central $r = 3''$ gas disk (see Fig. 5.3(g)) which then has a column density of $\sim 1.9 \times 10^6$ M$_\odot$ arcsec^{-2} or $\sim 7.7 \times 10^2$ M$_\odot$ pc^{-2}. A gas mass density of 3.6×10^2 $M_\odot$ pc^{-3} is derived from the H$_2$ cPSF flux measurement by assuming that the emission stems from a spherical region 29 pc in diameter. Hence, the black hole of NGC 1566 has enough mass enclosed in its central parsec to accrete at the current rate for a few Myrs. The H$_2$ mass estimates for these two regions are in agreement with estimates from the ^{12}CO(3-2) emission observed with ALMA (see Fig. 5.8). A ^{12}CO(3-2) flux of ~ 570 Jy km s^{-1} measured for the central $r = 3''$ gas disk and ~ 12 Jy km s^{-1} for the cPSF region. Furthermore, H$_2$ masses of $\sim 6.6 \times 10^7$ M$_\odot$ and $\sim 1.6 \times 10^6$ M$_\odot$ respectively are calculated, using the Milky Way conversion values from Bolatto et al. (2013).

Due to the narrow line ratio of Hα/H$\beta \sim 3.1 \pm 0.3$, which are typical for Seyfert 2 galaxies, Alloin et al. (1985) conclude that NGC 1566 might be a waking up Seyfert 1, which was in a low ionization state in the past few hundred years as inferred from emission line ratios in the NLR, beginning the harder ionization of the nuclear region. The AGN would have enough fuel to do so and start ionizing hydrogen outside the $r = 16$ pc at the center. On the one hand, the line ratio from Alloin et al. (1985) might have been created by an aperture effect and the H ii deficiency in the central region of NGC 1566 (Comte & Duquennoy 1982). On the other hand, the H ii deficiency might result from the low activity state in the past of NGC 1566 since there is hydrogen in the nuclear region but in molecular form mainly. The activity of NGC 1566 over the last ~ 20 yr is a variable one (e.g., Alloin et al. 1985; Kriss et al. 1991; Baribaud et al. 1992; Levenson et al. 2009) without a specific trend of in- or decrease.

5.3.2 Continuum Emission

The continuum emission in the central $10'' \times 10''$ of NGC 1566 is mainly produced by stars. The continuum decomposition, however, reveals a hot dust component at the nucleus. The fits at the center, $r = 1''$, $r = $ PSF, and center PSF (cPSF), need a hot dust component. The hot dust exhibits only 4% of the flux density in the $r = 1''$ region, whereas the $r = $ PSF region exhibits 7% of the flux density and the cPSF region exhibits even 16% flux density as hot dust emission

(a) Flux ^{12}CO(3-2)

(b) Dispersion ^{12}CO(3-2)
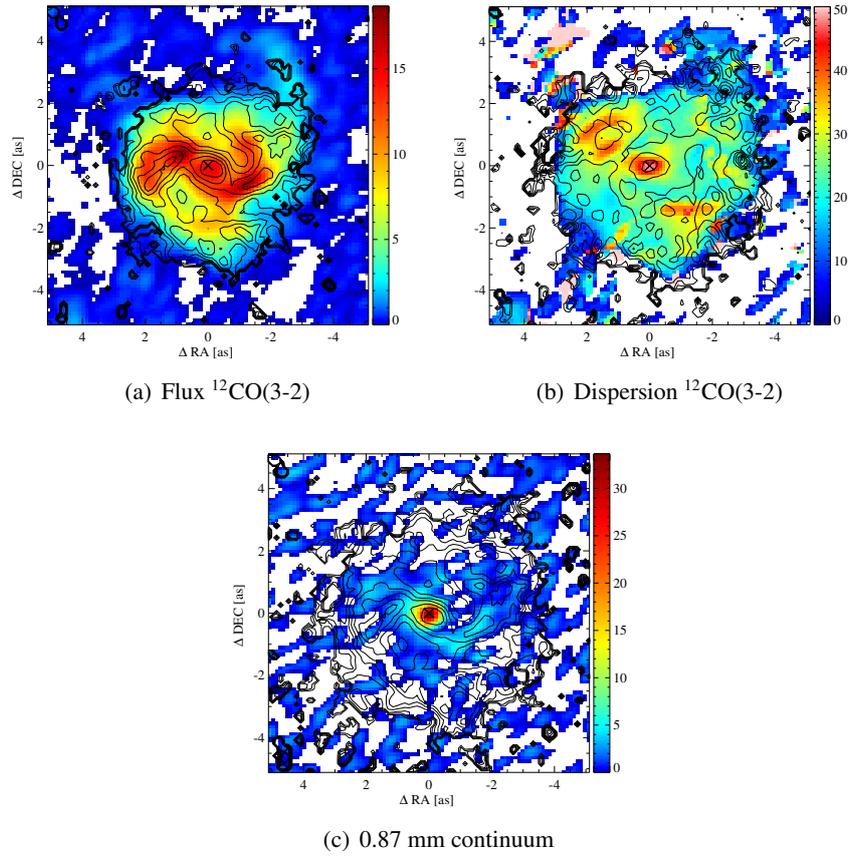
(c) 0.87 mm continuum

Figure 5.8: Panel (a) & (c) show the ^{12}CO(3-2) and continuum at 0.87 mm flux maps in [Jy beam^{-1} km s^{-1}] overlayed with H$_2$(1-0)S(1) EW contours. Panel (b) shows the ^{12}CO(3-2) second moment map in [km s^{-1}] overlayed with H$_2$(1-0)S(1) FWHM contours.

at a temperature of $\sim$ 1000 K. The hot dust emission is not strong enough to create a steep red continuum in K-band. The difference in percentage here is caused by the aperture size of the central regions. All regions exhibit a hot dust flux density of $\sim 500 \times 10^{-18}$ W m^{-1} μm^{-1} (Fig. 5.9). This hot dust emission at the nucleus is visible in the H-K map as well (Fig. 5.4). The nucleus of NGC 1566 apparently shows characteristics of Seyfert 1 nuclei, i.e. broad hydrogen lines, and hot dust continuum emission, but on smaller scales, e.g. the AGN ionizing range of $r \lesssim 16$ pc.[2] The effect of aperture on the features is essential. Apertures of more than 100 pc or $2''$ would probably not be able to detect and measure the hot dust component. NGC 1566 would then show the characteristics of a quiescent galaxy without any narrow H II emission at the nuclear region, the broad Brγ emission might be detected further out, depending on its strength (e.g., Reunanen et al. 2002).

The stellar continuum in the FOV is best fitted by an M0III star, a giant. The central $r \sim 1''$ needs a G5III giant as well for the fit. The G-type star contributes one third of the flux in the central $r = 1''$ region. Outside this region the G-type star is not needed. The differences between the two stars are the temperature, i.e. the spectral slope, and the absorption features, e.g. CO(2-0). The G5III stellar contribution indicates a need for bluer continuum emission or for more shallow features in the continuum emission at the center of NGC 1566. The need for bluer continuum emission might stem from uncertainties in the hot dust contribution, however, the hot dust flux stays constant over several apertures. The main argument for a G-type star here is the EW of the CO absorption feature. The EW in CO(2-0) of the M0III star is too high, i.e. the CO absorption feature is too deep, although a hot dust contribution is taken into account. A higher hot dust contribution can be excluded since the spectral shape of the residual galaxy spectrum becomes too blue for an K- or M-type star to fit. Star formation at the center of Seyfert galaxies and in the torus itself is not unusual (e.g. Davies et al. 2007) and can account for additional featureless continuum.

The spatial shape of the continuum emission is roundish with a slight elongation at a PA of $34°$. This is the same PA as the line-of-nodes of the stellar velocity field. Hence, the stars in the center do not follow the main stellar bar distribution, which is at a PA of $\sim 0°$. The $34°$ that are measured are either created by a small nuclear bar within the $r = 9''.7$ pseudo-ring (Comerón et al. 2010) or the angle stems from the bulge population and is affected by projection effects. However, to disentangle this a sophisticated decomposition of the galaxy structure using high resolution imaging in the NIR is required (e.g. Busch et al.

---

[2]The Brγ region size at the center is taken here as a measure for the ionizing range of the central ionizing source.

(a) Center $r = 1''$

(b) Center $r = 5''$

(c) Center r = PSF

(d) SFr

(e) SF PSF

(f) cPSF
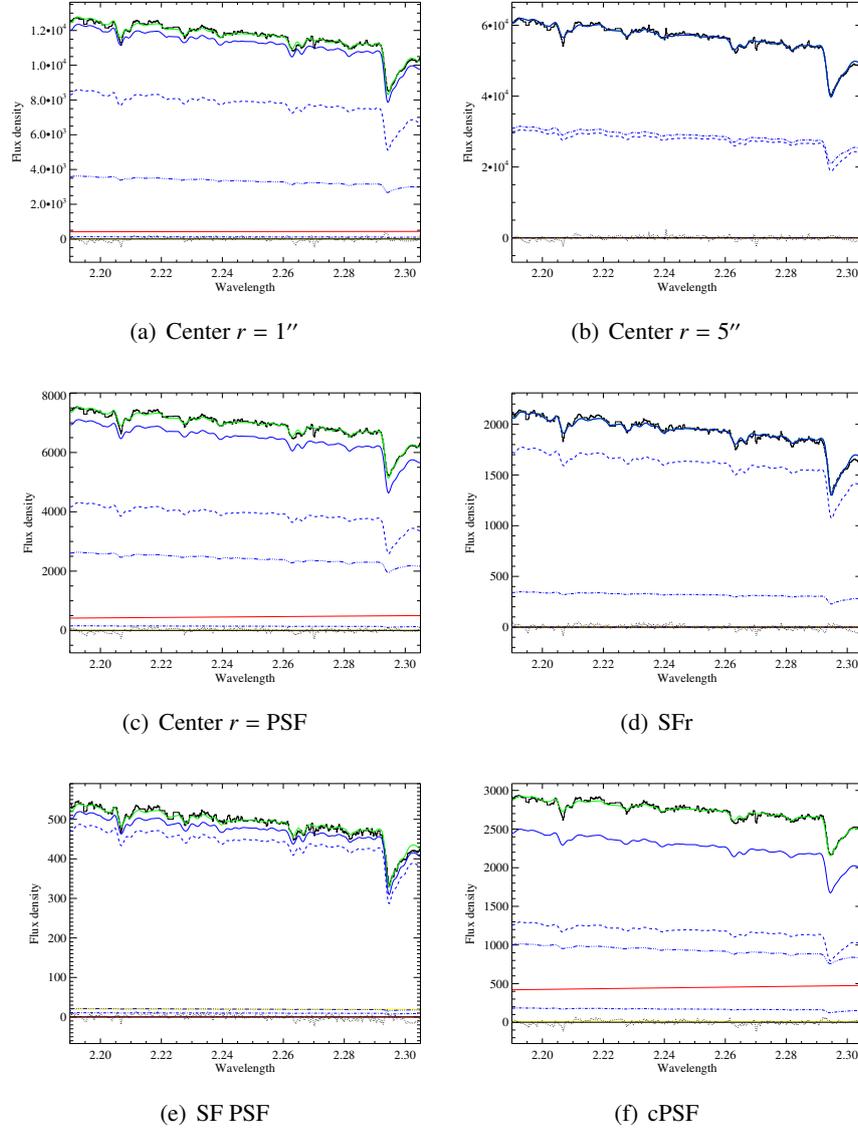
Figure 5.9: The continuum decomposition for six different regions. The axes are flux density [10^{-18} W m^{-2} μm^{-1}] versus wavelength [μm]. The components are: *Red curve*: hot dust component; *Yellow curve*: power-law component; *blue curve*: total stellar component; *dashed blue curve*: M0III star; *dash-dot blue curve*: K3III star; *Triple-dot-dashed blue curve*: G5III star. The combined components curve is in green and the original input spectrum is in black. The dotted black curve around zero is the residual of spectrum minus combined curve. Note that the emission lines at $\lambda 2.223$ μm and $\lambda 2.247$ μm were masked. Credit: Smajić et al., A&A, 583, A104, 2015, reproduced with permission © ESO.

2014).

5.3.3 Kinematics

The kinematics in the center of NGC 1566 show rotations at a PA of $\sim 214°$ for the stellar kinematics (Fig. 5.6(a)) and at a PA of $\sim 222.5°$ for the molecular gas (e.g., $H_2(1\text{-}0)S(1)$, Fig. 5.6(b)). The observed velocity field of the molecular gas shows strong deviations from rotation at the center.

Stellar Kinematics

The line of nodes of the stellar rotation is aligned with the stellar continuum major axis at a PA of $34°$. The PA of $42°5$, derived from the $H_2(1\text{-}0)S(1)$ line, is in good agreement with Agüero et al. (2004). They find a PA of $44° \pm 8°$ from optical emission lines. The stellar LOSV map shows a smooth rotation field. A model is fited to the observed velocity using the Plummer potential to represent the bulge gravitational potential (Barbosa et al. 2006). The model subtracted map shows low residuals (Fig. 5.6(e)). The stellar velocity dispersion shows a slight drop at the very center (Sect. 5.2.3). This is often an indication for a stellar disk (e.g. Emsellem et al. 2001; Falcón-Barroso et al. 2006) at scales < 100 pc. However, there are no features in the stellar residual LOSV map (Fig. 5.6(e)) that would support a stellar disk.

The difference in stellar and gaseous PA might be explained by streaming motions of the gas related to a strong spiral wave. But the gaseous PA over the central $8'' \times 8''$ is in agreement with measurements at larger scales, hence the effect has to stem from larger scale spiral density waves rather than the nuclear spiral discussed here. To substantiate any misalignment between gaseous and stellar disk, however, a much better estimate of the PAs is needed. Hence, the gaseous and stellar disk are oriented very similar but might be misaligned.

Gas Kinematics

On scales of $200 - 300$ pc Combes et al. (2014) showed that the gravitational torques are able to transport almost half of the angular momentum of the gas in one rotation period. Here gas is able to move in spiral arms that connect the inner Lindblad resonance (ILR) of the nuclear bar with the central ≤ 200 pc. On smaller scales the angular momentum transport is smaller per rotation period, but the period becomes smaller as well. The inner 200 pc show the molecular nuclear gas disk which exhibits a clear two-arm spiral structure (Figs. 5.3(g), 5.3(i)). The flux map indicates the arms direction and shows some intriguing

elongation along the minor axis. The spiral is clearly outlined in the H_2(1-0)S(1) EW map (Fig. 5.3(i)). The EW along the minor axis is surprisingly low, but strong perpendicular to it, indicating a gaseous bar-like structure between the two arms. The southwestern arm is weaker in EW than the northeastern arm, which is indicative of additional continuum (e.g. star formation). In the outer part the two-arm spiral becomes flocculate and forms a ring-like structure at a $2''$ radius. This ring might correspond to an inner ILR due to a secondary nuclear bar (Sect. 5.3.2) or is rather created by gas falling in from the $200 - 300$ pc scales toward the lower angular momentum transport region at ≤ 150 pc scales.

The nuclear spiral disturbs the velocity field of the molecular gas and creates a strong S-shaped feature at the center. To remove the rotational part from the spiral disturbance again a model is fitted to the observed velocity using the Plummer potential to represent the bulge gravitational potential. The residual of the fit (Fig. 5.6(f)) highlights the difference in the observed LOSV (Fig. 5.6(b)) and the model (Fig. 5.6(d)). The center of the residual map shows blueshifted residuals to the west and redshifted residuals to the east of the nuceleus. The nucleus is situated at 0 km s^{-1}. Contrary to the case of NGC 1068, discussed by García-Burillo et al. (2014), where non-virial outflow motions are required to explain the residual velocity field derived for the nuclear 200 pc gas disk of that Seyfert 2 galaxy, in NGC 1566 residuals shown in Fig. 5.6(f) can be accounted for by streaming motions produced by the spiral/bar structure. The S-shape shows non-circular motion in one surface as it is the case for bars or warps. Non-circular orbits, e.g. a closed elliptical orbit with axes not parallel to one of the symmetry axis (minor or major), can produce residual velocities as observed in Fig. 5.6(f).

The orientation of the galaxy toward the observer can be inferred from considerations of the winding sense of the spiral arms (Fig. 5.1). These kind of spiral arms are always seen to be trailing. Hence, the near side has to be in the northwest when the arms are trailing because there is blueshifted motion in the northeast and the arms are oriented as seen in Fig. 5.1.

There are no signs for an outflow from the center. Schmitt & Kinney (1996) detect a faint one-sided cone in [O III] pointing toward the southeast. The cone is smaller than $0.''5$ and can probably be associated with the NLR of NGC 1566. The increase of the FWHM of H_2 along the minor axis is in the same direction as the [O III] cone but is probably caused by beam smearing along the 0 km s^{-1} velocity gradient. At a size of $r \sim 0.''5$ the [O III] cone occupies spatially the nuclear Brγ and [Fe II] emission region, i.e. these lines originate from the same region. However, a one-sided emission on the nucleus is not detected in the data from any emission line (Fig. 5.3). The [Fe II] emission has a triangular shape but is centered on the nucleus. There is extended flux toward the southeast and also

a broadening of the [Fe II] line. These are only hints at a possible weak outflow from the nuclear region of NGC 1566 and can as well be associated with the NLR. The LOSV residuals up to $1''$ from the center in Fig. 5.6(f) fit an outflow along the minor axis, but these residuals are easily explained due to deviations introduced by the density waves of the nuclear spiral. Higher angular resolution observations are needed to be able to compare the [O III] emission with shock tracers in the NIR (e.g., H_2(1-0)S(1) and [Fe II]) and look for signs of outflowing gas in the LOSV and FWHM.

An interesting region in the gas kinematics lies $1''\!.5$ to the east and $1''$ to the north. The dispersion here increases over the nuclear disk average in both investigated molecular species, i.e. H_2(1-0)S(1) and ^{12}CO(3-2), Fig. 5.8. No increase in line flux can be measured, only the 0.87 mm continuum shows some substantial emission. What is creating this turbulence is not clear. As mentioned above an outflow from the nucleus is rather improbable as the only signs for an outflow are hinting toward the southeast. Other possibilities are interactions of nuclear disk and spiral arms, e.g. the nuclear spiral. However, these are only speculations since the data is not giving any substantial hints toward the origin of this turbulence.

5.3.4 Emission Line Diagnostics

The detection of several emission lines in NGC 1566 gives the opportunity to analyze the emission at the center. The broad Brγ emission was already discussed in Sect. 5.3.1. Here, I analyze the ratios of the narrow ionized and molecular emission lines with the goal of finding the nature of their excitation. I investigate apertures centered on the nucleus and on the ionization region situated $\sim 1''\!.5$ southwest of the nucleus.

Ionized and Molecular Line Diagnostics

The narrow Brγ emission line as well as [Fe II] and H_2(1-0)S(1) transitions can be used in a diagnostic diagram to disentangle photoionization by young, bright stars and shock ionization (e.g., supernovae). In contrast to Reunanen et al. (2002), a narrow Brγ emission is detected. They probably were not able to detect the narrow Brγ emission due to the width of their aperture since the slit positions do coincide with the positions of narrow Brγ emission (Sect. 5.3.2). Young and bright stars can be found in systems with recent and strong star formation like starburst galaxies. LINER galaxies exhibit high [Fe II] and H_2(1-0)S(1) fluxes. These species are good shock tracers as they are often found in regions of supernovae or outflows/jets.
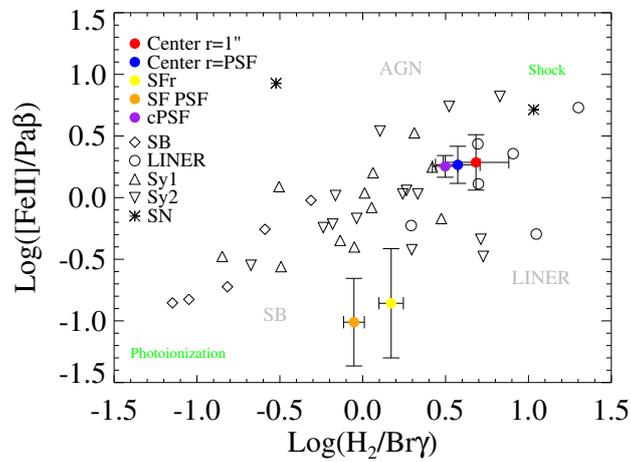
Figure 5.10: Diagnostic diagram of log [Fe II]/Paβ and log H$_2$/Brγ for the central r = PSF, r = 1″ and the star formation region (SFr). The conversion factor of 0.744 was used for [Fe II]λ1.644 μm over [Fe II]λ1.257 μm (Nussbaumer & Storey 1988). For the conversion of Brγ to Paβ the case B ratio of 0.17 was used. Open symbols correspond to literature values from Larkin et al. (1998, LINER), Dale et al. (2004, SB), Rodríguez-Ardila et al. (2004, 2005, Sy1, Sy2). Credit: Smajić et al., A&A, 583, A104, 2015, reproduced with permission © ESO.

The nuclear regions cPSF, r = PSF, and r = 1″ lie on the linear transition relation from SB over AGN to LINER. The r = PSF region is well situated in the AGN regime indicating mixed ionization mechanisms, typical for AGN. Interestingly, the r = 1″ region with its slightly bigger aperture moves further toward the LINER regime. This trend is caused by aperture effects only. The Brγ flux at the center stems from a deconvolved region of 13.5 pc, whereas the H$_2$ emission stems from everywhere in the r = 3″ molecular gas disk. Hence, larger apertures will shift the H$_2$ over Brγ ratio toward higher H$_2$ fluxes and in this case toward the LINER domain.
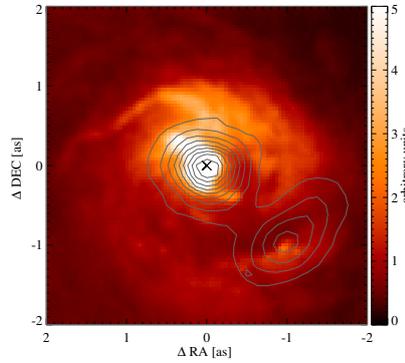
Figure 5.11: Brγ contours plotted over the HST image at 4326 Å. Note the bright emission spots at the SFr emission region at (-1,-1). Credit: Smajić et al., A&A, 583, A104, 2015, reproduced with permission © ESO.

The star formation region SFr lies off the linear correlation seen in Fig. 5.10. Its situated in the AGN regime, but below the relation where the Seyfert galaxies reside. Due to the bright Brγ emission in this region I already assumed SFr to be a possible star formation region. The ratio log [Fe II]/Paβ puts SFr into the H II galaxy region, however, the ratio log H$_2$/Brγ shifts it to the AGN regime. This behavior can be explained by an H$_2$ overabundance. As mentioned above, the high H$_2$ fluxes shift the central r = 1″ aperture toward the LINER like excitation regime. This is the case for SFr as well. The high H$_2$ flux shifts the SFr region from the photo ionization or star formation regime toward the mixed ionization or AGN regime. The H$_2$ over Brγ ratio is five to ten times higher than in typical H II galaxies. Indeed, when examining Fig. 5.11 it looks like the star formation here is partly hidden by dust and probably molecular gas within the spiral arms. Additionally, the mm-continuum shows substantial dust emission in this region. The high molecular gas flux can be explained by gas infall along the spiral arms from the pseudo-ring toward the center as well (Sect. 5.3.3). There simply seems

to be a lot of molecular gas at the center of NGC 1566 that could create an overabundance in H_2(1-0)S(1) when it is ionized, which appears to be the case. Furthermore, PSF smearing due to the earlier mentioned H II deficiency at the center of NGC 1566 supports the shift in the diagnostic diagram of this region.

Molecular Hydrogen Diagnostics

The rich molecular gas disk in the central $r = 3''$ shows a variety of H_2 transitions in the NIR (see Tab. 5.1). There are three main excitation mechanisms for molecular hydrogen in the NIR (Mouri 1994; Rodríguez-Ardila et al. 2005) which can be discriminated with the detected H_2 species:

i) *UV fluorescence* (non-thermal) can occur in warm high-density gas where highly energetic UV photons from the Lyman-Werner band ($912 - 1108$ Å) are re-emitted by the H_2 molecules. To distinguish the UV pumping (non-thermal) from collisional excitation (thermal) higher level transitions need to be detected since the lower levels are populated by collisions.

ii) *X-ray heating* (thermal) is responsible for H_2 excitation in regions with temperatures of < 1000 K. At higher temperatures collisional excitation populates the lower levels.

iii) *Shocks* (thermal) can collisionaly populate the electronic ground levels of H_2 molecules. The rovibrational transitions are populated following a Boltzmann distribution where kinetic temperatures can be higher than 2000 K (Draine & McKee 1993).

Both diagnostic diagrams (Fig. 5.12) show similar behavior for the investigated regions. The H_2(2-1)S(1)/H_2(1-0)S(1) ratio ranges from ~ 0.15 to ~ 0.25 for all regions. The central regions, i.e. center $r = 1''$, center $r =$ PSF, and cPSF, show the lowest ratio in H_2(2-1)S(1)/H_2(1-0)S(1) declining with aperture. The star forming region SFr and the PSF sized aperture taken here SF PSF exhibit the highest value and the ratio is increasing with smaller apertures. This is not surprising since higher values in this ratio mean a higher contribution from non-thermal UV photons. The estimated ratios are close to the predicted ratios of Black & van Dishoeck (1987) for a mixture of thermal and low-density fluorescence models (Fig. 5.12(a)). The contribution of non-thermal excitation is about $10\% - 20\%$ for the central regions (cPSF, $r =$ PSF and $r = 1''$). The estimated ratio of non-thermal to thermal excitation for region SFr would imply a contribution of $\sim 30\%$. This is a strong hint at young star formation taking place at

(a)

(b)
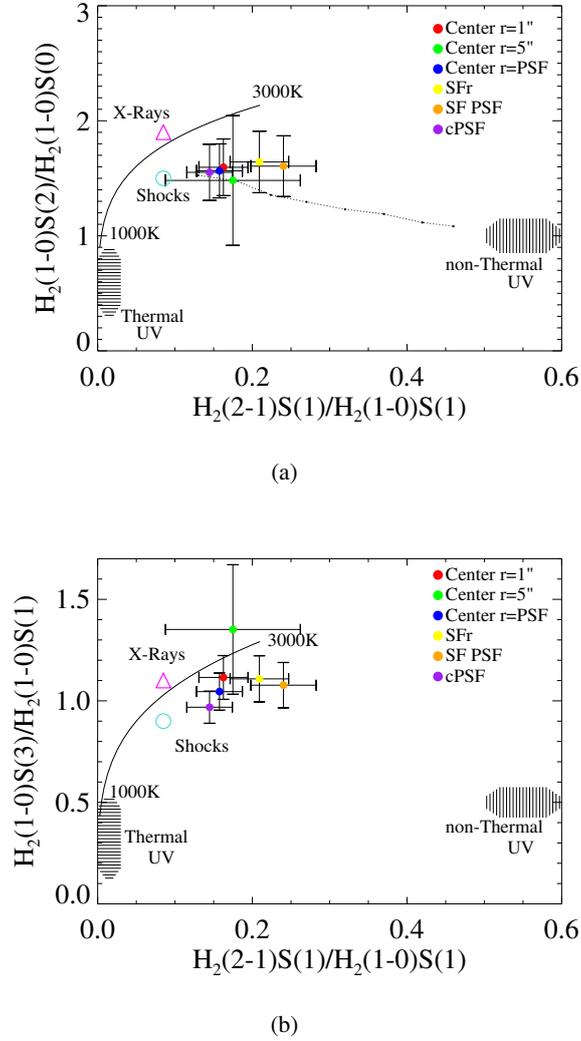
Figure 5.12: Molecular hydrogen line ratio diagrams. The ratios of $H_2(2-1)S(1)/H_2(1-0)S(1)$ versus $H_2(1-0)S(2)/H_2(1-0)S(0)$ are shown in (a). The ratios of $H_2(2-1)S(1)/H_2(1-0)S(1)$ versus $H_2(1-0)S(3)/H_2(1-0)S(1)$ are shown in (b). The curves represent the thermal emission at $1000 - 3000$ K. Vertical stripes represent the region where models by Black & van Dishoeck (1987) predict non-thermal UV excitation. Horizontal stripes are thermal UV excitation models by Sternberg & Dalgarno (1989). The open, magenta triangle represents thermal X-ray models by Draine & Woods (1990) and the open, turquoise circle represents a shock model from Brand et al. (1989). The filled dark bullets connected with a dotted line in Fig. (a) are the predicted line ratios from a mixture of thermal and low-density fluorescence models of Black & van Dishoeck (1987). The first bullet from the left represents 10% non-thermal and 90% thermal UV-fluorescence, the second 20% non-thermal and 80% thermal UV-fluorescence and so on. Credit: Smajić et al., A&A, 583, A104, 2015, reproduced with permission © ESO.

regions SFr and SF PSF. The SF data points lie off the mixture of thermal and non-thermal model in the $H_2(1-0)S(2)/H_2(1-0)S(0)$ ratio but are within the error bars (Fig. 5.12(a)). The thermal component for central and star forming regions is not clear but it is very probably somewhere between 2000 K and 3000 K. The central regions move with smaller aperture toward the shock model at ~ 2000 K indicating a stronger thermal ionization close to the nucleus. However, dense gas ionized by UV-fluorescence can show similar emission compared to thermally ionized gas. The $v = 1$ transitions are thermalized by collisions and with higher density of the gas the $v = 2$ transitions are thermalized as well and hence underpredicted with respect to lower density gas excited by UV-fluorescence (e.g., Sternberg & Dalgarno 1989, 1995; Sternberg & Neufeld 1999; Davies et al. 2003, 2005). All regions are situated beneath the thermal Boltzmann distribution indicating rather a shock than an X-ray origin of the thermally excited molecular emission. The line ratio measured for the full FOV ($r = 5''$) is not very reliable. This ratio exhibits the highest error bars, probably due to contamination of the low flux continuum in the outer parts of the FOV by OH line correction residuals.

The level population diagram in Fig. 5.13 compares the measured level population of the H_2 emission lines to UV-excitation models derived by Davies et al. (2003). The $v = 1$ transitions scatter around the higher density models (model 2,3,4,5). The SF region tends toward lower density gas, e.g. model 1, and indicates the characteristic ortho-to-para shift of fluorescent excitation (Sternberg & Neufeld 1999). The $v = 2$ transitions show a similar effect but the differences in the models are here more evident than for the $v = 1$ transitions.

The ro-vibrational levels will be populated according to the Boltzmann equation when thermal excitation is assumed. Then the excitation temperature T_{exc} can be derived from the inverse of the gradient of the line fitted to the thermalized levels in the graph shown in Fig. 5.13. These will be on a linear relation if the excitation is thermal. The estimate of the population density can be inferred from the observed column density (Lester et al. 1988):

$$N_{col} = \frac{f}{A_{ul}} \frac{\lambda}{hc} \times \frac{4\pi}{\Omega}, \tag{5.11}$$

with flux f in W m^{-2}, A_{ul} the transition probability (Wolniewicz et al. 1998), λ the rest frame line wavelength, h the Planck constant, c the speed of light, and Ω the aperture size in radian. In thermal equilibrium the ratio of two levels can be written as

$$\frac{N'}{N''} \frac{g_J''}{g_J'} = \exp\left(\frac{-\Delta E}{k_B T}\right), \tag{5.12}$$

with column densities N' and N'', statistical weights g'_J and g''_J, Boltzmann constant k_B, and the temperature of the thermal equilibrium T.

For the central regions, e.g. cPSF, the $v = 1$ transitions seem to be thermalized with an excitation temperature of $T_{exc} \sim 1800$ K (Fig. 5.13). However, none of the investigated regions are purely thermalized. This is shown by the $v = 2$, $J = 3$ level which lies off the excitation temperature line fitted to the $v = 1$ levels. This should not be the case for a thermal ionization process. Hence, other ionization processes, e.g. UV-fluorescence, have to be taken into account. The $v = 2$, $J = 5$ level seems suppressed with regard to the $v = 2$, $J = 3$ level and fits the thermal equilibrium fit. This effect is seen in the X-ray models of Draine & Woods (1990) which predict a decrement in the $v = 2$ $J = 5$ level.
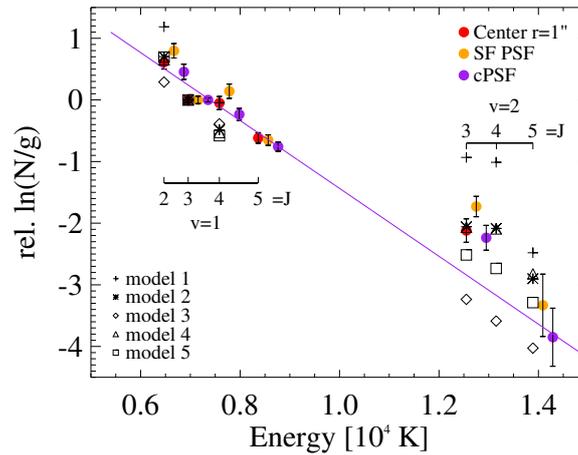
Figure 5.13: Molecular hydrogen level population diagram relative to the H_2(1-0)S(1) transition. The column density N is given in [m^{-2}]. The center $r = 1''$ region marks the energy of the level, the other regions are shifted for a better presentation in the plot. The models are for dense UV-excited gas taken from Davies et al. (2003). The linear fit is to the $v = 1$ levels of region cPSF which yields a kinetic excitation temperature of $T_{exc} \sim 1800$ K. Credit: Smajić et al., A&A, 583, A104, 2015, reproduced with permission © ESO.

To conclude, the H_2 line ratios for the central apertures and the SF apertures in the H_2 line ratio diagrams behave similar to the diagnostic diagram in Fig. 5.10. The difference in aperture is apparent in all three diagrams. For the central regions (i.e. center $r = 1''$, center $r = $ PSF and cPSF) the ratio for smaller apertures moves away from the shock ionization in the diagnostic diagram in Fig. 5.10, whereas in the H_2 line ratio diagrams the smaller apertures go towards the shock model region at temperatures of ~ 2000 K (Fig. 5.12). The regions SFr

and SF PSF in all diagrams show a trend toward young stellar populations/star formation.

5.3.5 Stellar Emission and Absorption

The off-nuclear Brγ emission in NGC 1566 is a strong indicator for star formation. The EW of Brγ is relatively high here (see table 5.3). The H$_2$(1-0)S(1) EW in that region goes down with respect to the same region in the eastern spiral arm. The diagnostic diagram in Fig. 5.10 places this region into the AGN regime, however, it is off the linear correlation. It is most likely that an over-abundance in H$_2$ flux is responsible for the shift from the photoionization region to the mixed ionization region. The $\log$ H$_2$/Brγ line ratio has values of down to -0.2 at the position of the brightest spots in the HST images (Figs. 5.16(a), 5.11). These at least three distinct bright emission regions in the HST image are probably the brightest or least attenuated star formation regions. However, the elongated shape of the Brγ emission there indicates more star formation behind the dust and molecular gas of the nuclear spiral.

Table 5.3: Equivalent widths after Mannucci et al. (2001).

	Center $r = 1''$	Center $r = 5''$	Center $r = $ PSF
Si I	2.64	2.34	2.60
CO(6-3)	6.45	6.52	6.24
Brγ	0.55	...	0.79
Na I	3.41	3.27	3.26
Ca I	4.51	4.26	4.53
CO(2-0)	15.84	16.91	14.68
	SFr	SF PSF	cPSF
Si I	2.38	2.31	2.47
CO(6-3)	6.71	7.05	5.88
Brγ	1.60	2.59	1.03
Na I	3.61	3.50	3.22
Ca I	4.79	4.73	4.70
CO(2-0)	18.45	18.07	13.50

Notes. Equivalent width of the stellar absorption features and of Brγ given in Å of all discussed regions (see also Fig. 5.3 for abbreviations). For all absorption features the line range and continuum range were taken from Mannucci et al. (2001) and the hot dust component in the center was subtracted prior to measuring the EW.

The star formation observed in this region does not show significant EW
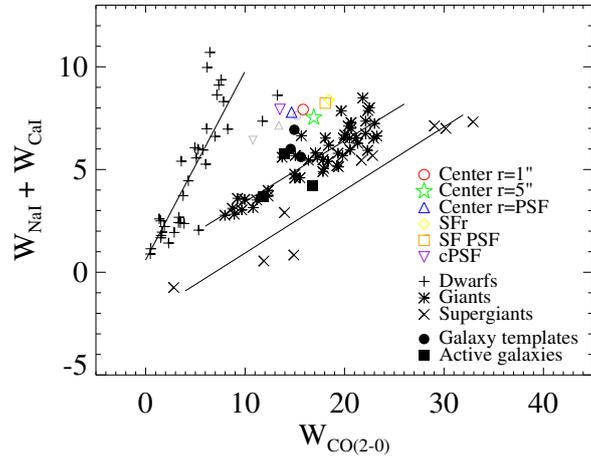
(a)
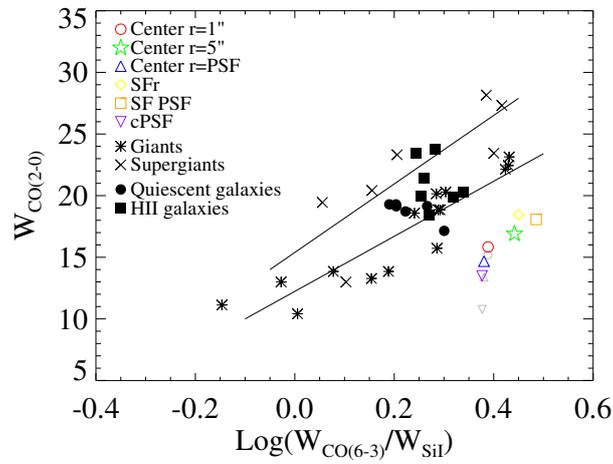
(b)

Figure 5.14: The EW of stellar absorption feature diagrams of Si I, CO(6-3), Na I, Ca I, and CO(2-0). The diagrams are based on Mannucci et al. (2001). The lines are linear fits to the distribution of dwarf, giant and supergiant stars in the diagrams. Note that the galaxy data points, filled symbols, are taken from apertures of ∼ 1 kpc whereas this observations data points are from regions of less than 50 pc in diameter, except the center $r = 5''$ region. The smaller grey symbols are EW values derived before subtracting the non-stellar continuum.

absorption feature values. The EW diagrams of stellar absorption features in Fig. 5.14 show that all regions discussed here show EWs between giants and main sequence stars (dwarfs). A major contribution from supergiants can be excluded. These stars with masses $> 8\ M_\odot$ have lifespans of only a few 10 Myr, hence, the age of the star formation has to be either $\gtrsim 100$ Myr, the supergiants already died, or < 10 Myr, the stars did not yet evolve to supergiants. The population synthesis model starburst99 (Leitherer et al. 1999) is used to investigate the stellar population and stellar history with regard to the stellar absorption features of Si I, CO(6-3), and CO(2-0). These can be compared to the measured values in interesting regions. The starburst99 data were calculated with standard settings: instantaneous burst of star formation that produces a Kroupa IMF with exponents of 1.30 and 2.30, an upper mass cutoff of $100\ M_\odot$, and a total involved mass of $10^6\ M_\odot$. The Padova tracks with AGB stars and a metalicity of 0.02 were used. The two PSF apertures (cPSF and SF PSF) are drawn into Fig. 5.15. The population synthesis EWs are consistent with two star forming ages, $\lesssim 9$ Myr and ~ 100 Myr. Since strong Brγ emission is detected in the SF PSF region and the [Fe II] is low here it is probable that the star formation here is very young, < 9 Myr. This would explain the lack of supergiants in this region because they did not have the chance to form, yet. The very low [Fe II] emission supports the age estimate from above since only a few stars have reached the age to undergo supernova explosions and ionize [Fe II] through shocks. Although, low [Fe II] emission is expected for ages of $\gtrsim 40$ Myr too. The continuum decomposition in this region needs a featureless component of up to 4% of the total K-band continuum. Assuming that this featureless, i.e. no absorption lines, continuum is produced by the young stars that ionize the Brγ emission line an estimate of the Brγ EW for this star formation can be estimated to be > 70Å. This value is expected for instantaneous bursts at an age of $\lesssim 8$ Myr. Therefore, I conclude that this region is indeed a very recent star forming region, located in a spiral arm which is connected to the very center of NGC 1566.

The EW diagrams (Fig. 5.14) indicate a trend for the central region where with lower aperture on the nucleus the EW in CO(2-0) becomes lower. This effect can be introduced by non-stellar continuum, however, before measuring the EWs the hot dust continuum as determined by the continuum decomposition was subtracted. The effect of the correction is seen in Fig. 5.14(a), if the non-stellar continuum was not accounted for, the central region would be on a linear correlation with a positive gradient. The three regions lie on a line with a gradient of zero. Also, the differences of the three regions are much more severe in Fig. 5.14(b) when no hot dust continuum subtraction was performed. Therefore, the inner most region (cPSF) is indeed tendentiously moving toward the main

sequence stars (dwarfs) with lower aperture.

The [Fe II] emission in the central region is strong. Brγ emission is detected as well but not as strong as [Fe II]. Both emission lines originate in a region of ~ 32 pc in diameter, as measured from the linemaps without deconvolution with the PSF width, centered on the nucleus. The contribution from AGN and star formation to the [Fe II] and Brγ emission cannot be disentangled in the center. Hence, no arguments towards a young (e.g., < 10 Myr) burst of star formation at the center can be made. But the tendency toward dwarf EWs in the central region indicates a burst of star formation at ages > 40 Myr which might be ongoing.

From Brγ and [Fe II] arguments the star formation in SFr is probably younger than 9 Myrs. The EWs of Si I, CO(6-3) and CO(2-0) for an instantaneous star burst agree with this assumption (Fig. 5.15). For the nucleus this is not as easy to disentangle since a differentiation between Brγ and [Fe II] excitation by the AGN and by star formation is not possible. The EWs agree with a very young star formation but also with star formation older than 90 Myr. The tendency that the smaller the aperture is the more the EWs in Fig. 5.14 tend toward the dwarf branch speaks in favor of an older star burst (> 90 Myrs). However, especially at the center a mix of very old and young star formation is possible, which might explain the EWs similar to dwarfs (Fig. 5.14) and non-thermally excited Brγ and H_2 emission at the cennter. Other star forming histories are possible, e.g. exponentially declining bursts, but the conclusions are similar to the instantaneous star burst discussed here (e.g., Davies et al. 2007).

Table 5.4: Equivalent widths Origlia et al. (1993).

	SF PSF	cPSF
Si I	2.33	1.90
CO(6-3)	3.66	3.24
CO(2-0)	10.76	9.10

Notes. Equivalent width of the stellar absorption features given in Å of the discussed regions (see also Fig. 5.3 for abbreviations). For all absorption features the line range and continuum range were taken from Origlia et al. (1993) and the hot dust component in the center was subtracted prior to measuring the EW.

5.4 Conclusion and Summary

I have analyzed the central $10'' \times 10''$ of the Seyfert 1 galaxy NGC 1566 using NIR IFS data. The reported H II deficiency (Comte & Duquennoy 1982) is confirmed. I make a first detection of narrow Brγ emission at the center and at

(a) EW of Si ɪ

(b) EW of CO(6-3)

(c) EW of CO(2-0)
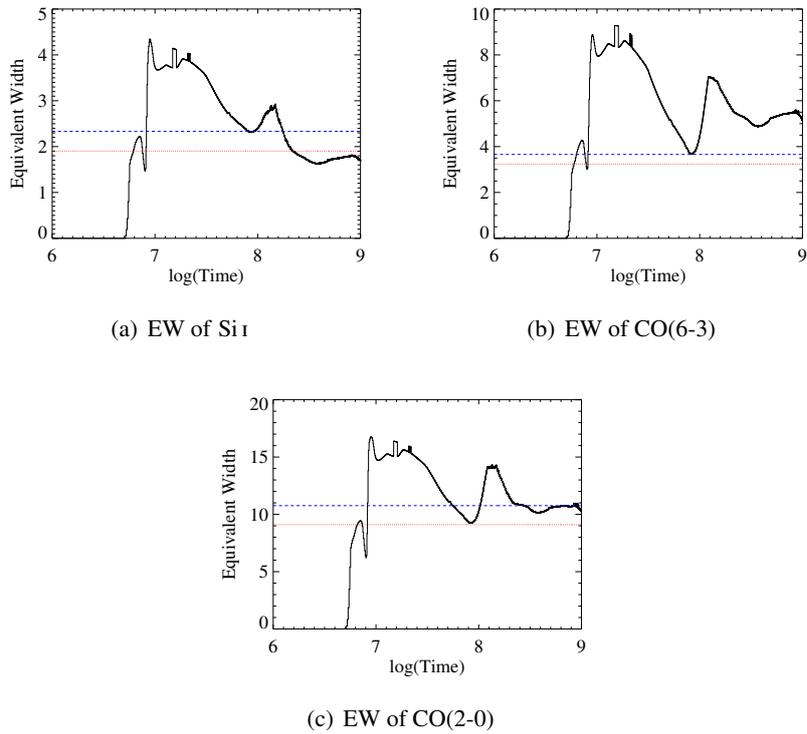
Figure 5.15: Equivalent width [Å] of Si ɪ, CO(6-3), and CO(2-0) vs. time [log yr] for an instanta-
neous burst of star formation (for details see Sect. 5.3.5). The blue dashed line represents the EW
values for region SF PSF and the red dotted line the values for region cPSF, see Fig. 5.3 for ab-
breviations and table 5.4. The absorption line range and continuum range were taken from Origlia
et al. (1993).

one region offset to the southwest. From the detection of a broad Brγ component a BH mass of $(3.0 \pm 0.9) \times 10^6 \ M_\odot$ is estimated similar to other BH mass measurements from broad lines (Kriss et al. 1991).

From the continuum decomposition I derive the mass dominating stellar distribution and its velocities. Using the velocity dispersion of the stars in the bulge the BH mass is estimated independently from broad emission lines. The BH mass is estimated to $(4.2 \pm 2.4) \times 10^6 \ M_\odot$, and is in excellent agreement with the BH estimate from broad emission lines. The hot dust blackbody emission of ~ 1000 K at the nuclear position is one more evidence that the AGN at the center of NGC 1566 is a Seyfert 1 nucleus.

A mean value for the BH mass of $(5.3 \pm 2.9) \times 10^6 M_\odot$ is derived from all methods and relations used in this work. Combining the BH mass with the bolometric luminosity gives an Eddington ratio of $\lambda_{Edd} = (2 \pm 1) \times 10^{-3}$ which is in good agreement with other Seyfert 1 LLAGN.

NGC 1566 is a mass accreting Seyfert 1 galaxy with a huge molecular gas reservoir in a nuclear disk of radius $r = 3''$. The disk is filled up with gas allowed to fall in due to the torque budget on scales of $200 - 300$ pc (Combes et al. 2014). The nuclear spiral might be able to transport the gas further toward the nucleus where strong H_2 emission is detected. Star formation seems to have just started in the nuclear disk at the outer edge of the southwestern spiral arm. Inferring from the huge molecular gas reservoir of the nuclear disk with a mass of $(1.7 - 9.1) \times 10^7 \ M_\odot$ NGC 1566 has the potential to brighten up considerably and transform that gas reservoir into stars.

Molecular hydrogen is very strong in the observed FOV particularly in an $r = 3''$ disk and in a spiral structure within this disk. Disk and spiral are both detected as well in the warm H_2 emission lines with SINFONI as in cold H_2 gas from the $^{12}CO(3\text{-}2)$ emission with ALMA. The shape of the spiral looks similar when comparing the EW of $H_2(1\text{-}0)S(1)$ with the flux map of $^{12}CO(3\text{-}2)$. However, $H_2(1\text{-}0)S(1)$ shows the strongest emission on the nucleus whereas $^{12}CO(3\text{-}2)$ shows several strong emission spots. The southwestern emission spot of $^{12}CO(3\text{-}2)$ coincides with the Brγ emission seen in the SF region. From the H_2 emission a cold H_2 gas mass of $(1.7 - 9.1) \times 10^7 \ M_\odot$ is determined which is in agreement with results based on the ALMA observation by Combes et al. (2014). In the NIR the warm molecular gas seems to form a ring-like structure at $r \sim 2''$ best seen in the EW map in Fig. 5.3(i) and the $^{12}CO(3\text{-}2)$ emission line map (see Fig. 5.8(a).

Along the southern arm a star forming region is detected at a distance of $\sim 1''\!.5$ from the center. The measured SFR over a surface area of ~ 1.33 arcsec^2 is $2.6 \times 10^{-3} \ M_\odot$ yr^{-1}. Comparing this to the global Schmidt law (Kennicutt

1998) I find that the data point for SFr lies very close to the relation. However, the value for the nuclear $3'' \times 3''$ disk is situated below the relation with an SFR of 8.0×10^{-3} $M_\odot$ yr^{-1} over a surface area of $\pi \times 9$ arcsec^2. The nuclear region of NGC 1566 has a large molecular gas reservoir which is not being used efficiently for star formation.

The excitation mechanism of the molecular gas is partly due to thermal processes (e.g., shocks) and partly due to non-thermal excitation (e.g., UV fluorescence). The diagnostic diagrams in Figs. 5.10 & 5.12 show a clear distinction between the nuclear region and the SF region. The nuclear regions are situated in the AGN regime in the diagnostic diagram in Fig. 5.10. The SF region is situated right of the starburst region due to the above mentioned H_2 overabundance. The H_2 line ratios (Fig. 5.12) imply young star formation at regions SFr and SF PSF due to a non-thermal excitation fraction of up to 30%. These implications are supported by the EW ratios of the stellar absorption lines (Fig. 5.15 and Sect. 5.3.5) which hint at a star formation younger than 9 Myr.

The central regions are closer to the shock models but show a smaller non-thermal component as well (Fig. 5.12). The level population diagram (Fig. 5.13) shows that the $v = 2$ levels are not thermalized with the $v = 1$ levels indicating that the region is excited by a combination of thermal and non-thermal processes in dense gas, i.e. shocked gas and gas ionized by UV-fluorescence from young newly formed bright stars. Both methods hint at star formation at the nucleus which are not distinguishable further from ionizing emission of the AGN.

The central $\sim 1''$ is very interesting harboring possible nuclear star formation. No strong feedback can be detected but hints from shock tracers (e.g., H_2(1-0)S(1) and [Fe II]) and of non-thermal excitation (e.g., UV photons from young bright stars) are detected. High angular resolution measurements with SINFONI are needed to identify possible feedback and star formation in the central arcsecond of the seemingly waking up Seyfert 1 nucleus. The lack of strong feedback could be a reason for the lack of strong star formation in the nuclear disk if the nuclear spiral is not able to condense gas strong enough to enable star formation.

Additional Figures

The line maps to all important emission lines that were detected except for the H_2 Q-branch are given here. The Q-branch is situated at the end of K-band and therefore the maps show noise features as well. However, the flux and FWHM of these lines are given in tables 5.1 and 5.2 for the regions discussed here. Additionally, several line ratio maps are presented in Fig. 5.16

Figure 5.17 shows the flux, FWHM, and EW of all other detected H_2 lines

detected up to 2.3 μm. The flux distribution is very similar in all H_2 lines and peaks on the nucleus. The FWHM is increased in the center along the minor axis and H_2(1-0)S(3) shows an increased width in the northeast and a decreased width in the northwest, similar to H_2(1-0)S(1). The nuclear spiral is detected in all EW maps which show an increased EW at the position of the spiral density wave.

Figure 5.18 shows the LOSV of all H_2 lines from 5.17 and additionally the LOSV maps of the detected ionized gas. The LOSV in the molecular lines is very similar, as are flux and EW, indicating that they all originate from the same region, i.e. the nuclear molecular gas disk. For the ionized lines it is hard to tell because the region in which they are detected is not large enough to give information about the spatial velocity distribution. However, the LOSV fields do not look very different from the molecular LOSV fields (e.g., Brγ).

(a) log(H_2(1-0)S(1)/Brγ)　　(b) log([Fe II]/Brγ)　　(c) log(H_2(1-0)S(1)/He I)

(d) H_2(2-1)S(1)/H_2(1-0)S(1)　(e) H_2(1-0)S(2)/H_2(1-0)S(0)　(f) H_2(1-0)S(3)/H_2(1-0)S(1)
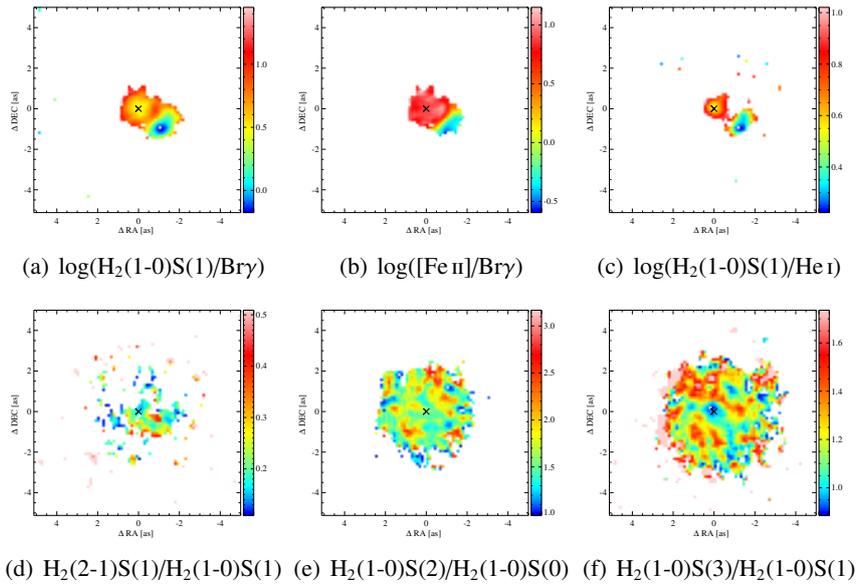
Figure 5.16: Shown are the logarithmic line ratios of H_2(1-0)S(1) over Brγ and [Fe II] over Brγ in (a) and (b). Panel (c) shows the logarithmic H_2(1-0)S(1) over He I ratio. Panel (d),(e),(f) show H_2(2-1)S(1) over H_2(1-0)S(1), H_2(1-0)S(2) over H_2(1-0)S(0) and H_2(1-0)S(3) over H_2(1-0)S(1). Credit: Smajić et al., A&A, 583, A104, 2015, reproduced with permission © ESO.

(a) Flux H$_2$(1-0)S(3) (b) FWHM H$_2$(1-0)S(3) (c) EW H$_2$(1-0)S(3)

(d) Flux H$_2$(1-0)S(2) (e) FWHM H$_2$(1-0)S(2) (f) EW H$_2$(1-0)S(2)

(g) Flux H$_2$(1-0)S(0) (h) FWHM H$_2$(1-0)S(0) (i) EW H$_2$(1-0)S(0)

(j) Flux H$_2$(2-1)S(1) (k) FWHM H$_2$(2-1)S(1) (l) EW H$_2$(2-1)S(1)
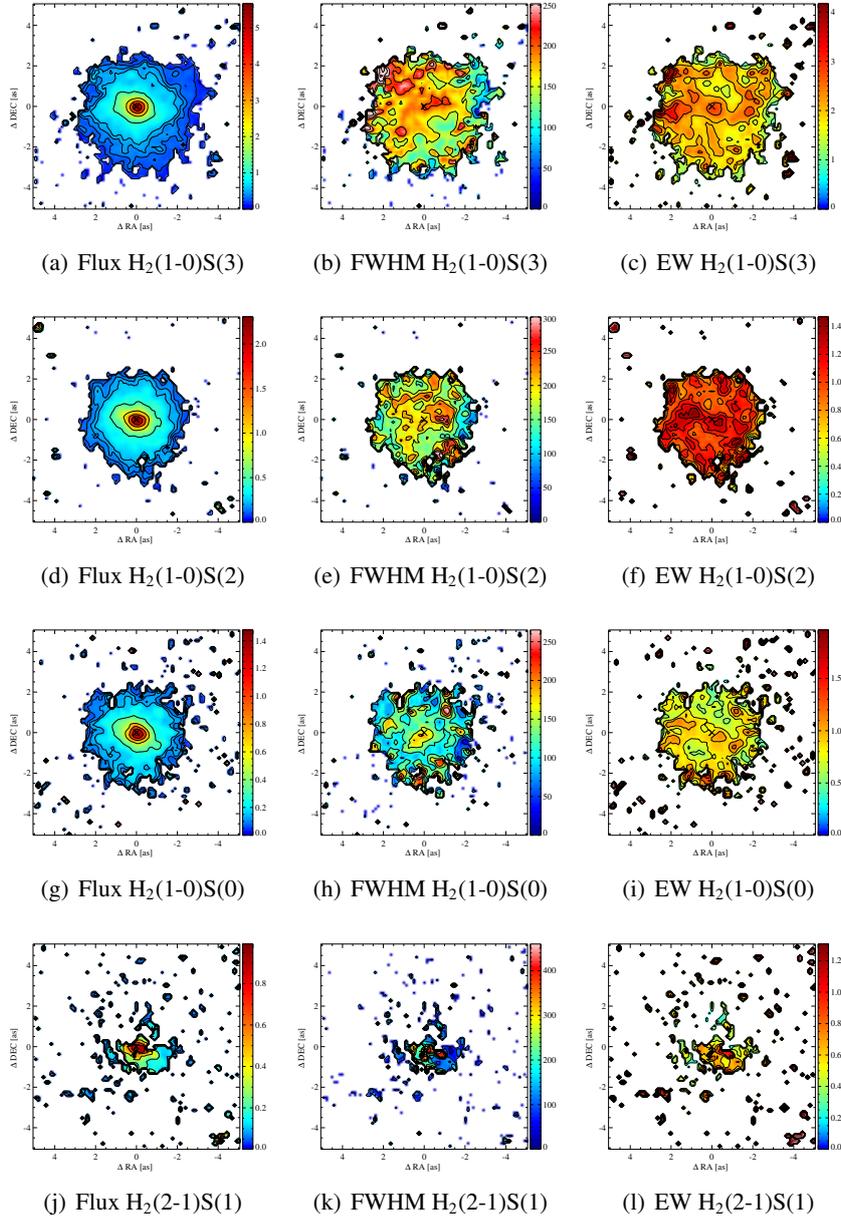
Figure 5.17: Molecular hydrogen emission lines. From left to right: flux [10^{-20} W m^{-2}], FWHM (corrected for instrumental broadening) [km s^{-1}] and EW [Å] maps of, from top to bottom: H$_2$(1-0)S(3), H$_2$(1-0)S(2), H$_2$(1-0)S(0), and H$_2$(2-1)S(1). Credit: Smajić et al., A&A, 583, A104, 2015, reproduced with permission © ESO.

116

(a) [Fe II]

(b) He I

(c) Brγ

(d) H$_2$(1-0)S(3)

(e) H$_2$(1-0)S(2)
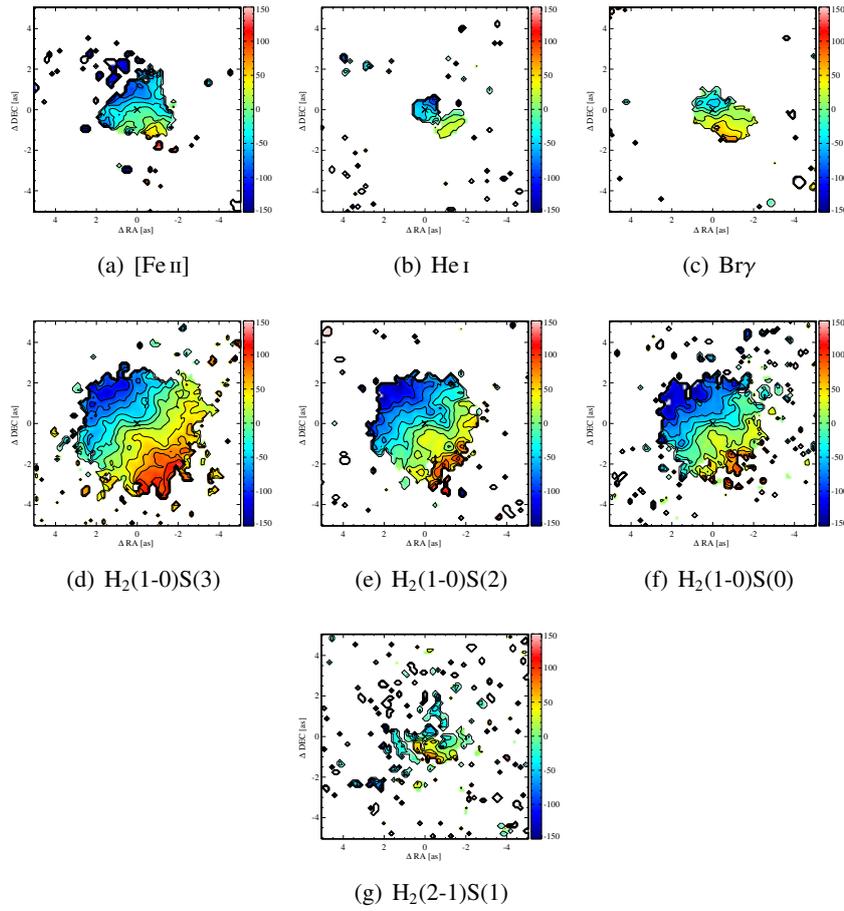
(f) H$_2$(1-0)S(0)

(g) H$_2$(2-1)S(1)

Figure 5.18: Presented are the LOSV [km s^{-1}] maps of, from left to right and top to bottom: [Fe II], He I, narrow Brγ, H$_2$(1-0)S(3), H$_2$(1-0)S(2), H$_2$(1-0)S(0), H$_2$(2-1)S(1). Credit: Smajić et al., A&A, 583, A104, 2015, reproduced with permission © ESO.

Part II

A Fringe and Flexure Tracker
for LINC-NIRVANA at the LBT

The two science cases studied in this work show the complexity of the central regions of nearby AGNs. These regions, as shown in the first part of this work, are very eventful but compared to their luminous siblings, e.g., LLQSOs (Busch et al. 2015, and references therein), the scales of the regions on which these events are detected are smaller by more than two magnitudes, i.e., regions of up to kpc scales translate to regions below 10 pc in scale. Hence, to study these cases in more detail and to find explicit answers, telescopes and instruments that can achieve a higher spatial resolution, e.g., interferometry, and integrate deeper, e.g., higher photon collecting area, i.e., larger mirrors, are needed.

To improve the observing capabilities astrophysicists, together with engineers, design, build, and test the future instruments and telescopes, i.e., the Large Binocular Telescope, the European Extremely Large Telescope, the Giant Magellan Telescope. These new telescopes are going to give us answers to some of the mentioned questions and at the same time will leave us puzzled with new fascinating and exciting surprises of nature.

Therefore, the second part of my work addresses the (re-)design and tests of the Fringe and Flexure Tracker (FFTS) for LBT INterferometric Camera and the NIR/Visible Adaptive iNterferometer for Astronomy (LINC-NIRVANA) at the Large Binocular Telescope (LBT). This instrument will give astronomers the opportunity to observe galaxies which are for example at a distance of about 10 Mpc, the distance of NGC 1433 and NGC 1566, at a spatial resolution of about 1 pc and at the same time give spatial information over a $10'' \times 10''$ FOV.

Introduction

6.1 The Large Binocular Telescope

The LBT is a joint project of U.S. American, German, and Italian institutions (Herbst et al. 2004). It is an optical to NIR telescope on Mt. Graham, Arizona USA, equipped with two primary mirrors of 8.4 m in diameter on a single mount. The baseline of the mount is 14.4 m resulting in a telescope with a light collecting area of 110 m^2, i.e., the area of an 11.8 m mirror, and an effective resolution of a $\sim$ 22.8 m single mirror telescope, i.e, $\sim$ 0$''$02 at 2.2μm. Not only is it the largest telescope in this wavelength range, but it provides the basic body for Fizeau interferometry. The two mirrors, on a single mount, can be seen as the free holes of a masked 22.8 m mirror telescope. Therefore, long delay lines that account for optical path difference between two telescopes are not needed.

This particular structure of the LBT allows three different operation modes. In *individual beam mode* the two mirrors can be pointed to arbitrary positions on sky up to a few arcminutes apart observing different regions at the same time.
In *incoherent beam combination mode* both mirrors are observing the same target and in the same wavelength regime. This gives a light gathering area of an $\sim$ 11.8 m telescope. However, the spatial resolution stays that of an $\sim$ 8.4 m telescope.
In *coherent beam combination mode* the phase information is preserved which results in a fringe pattern that reflects the Young experiment with a pinhole diamter to seperation ratio of 8.4 m to 14.4 m. This mode improves the spatial resolution to that of a 22.8 m telescope. In combination with homothetic imaging (see Sect. 6.2.1), i.e., exit pupil is a scaled version of the entrance pupil, the interferometric high spatial resolution is combined with a large FOV of 10$''$ × 10$''$. Homothetic imaging is the LBT unique observing mode compared to other interferometers in this wavelength regime, e.g., the VLT interferometer.

Current instruments on the LBT are:
The *Large Binocular Camera* (LBC) Red and Blue, each above one primary mirror. These two cameras are optimized in the blue (3500 − 6500 Å) and red (5500 − 10000 Å) and are used simultaneously.
The *Multi-Object Double Spectrograph* (MODS) is a seeing-limited spectro-
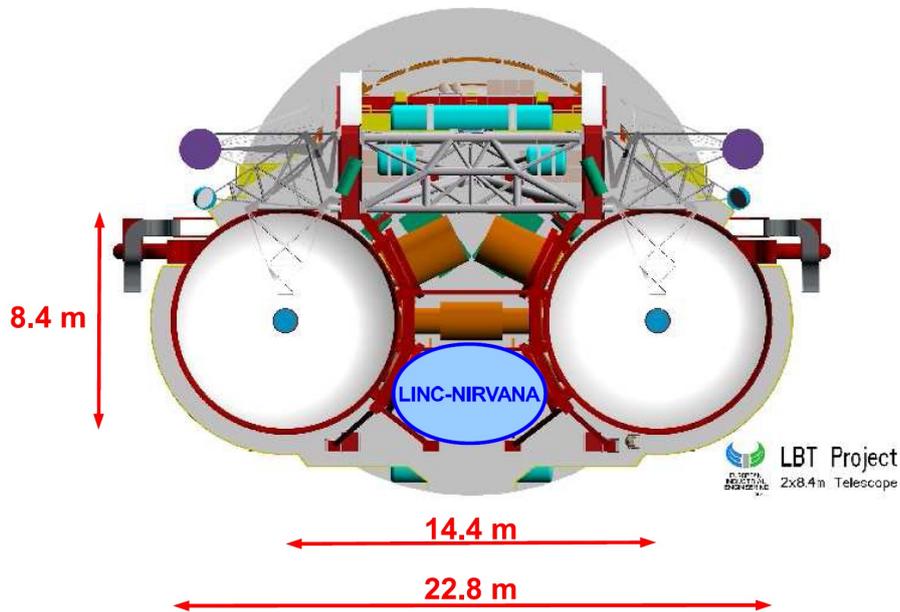
Figure 6.1: The LBT design with its two 8.4 m mirrors. The place holder for LINC-NIRVANA is is shown in blue in the central lower part of the image. Image source: LINC-NIRVANA in a nutshell, LN-MPIA-GEN-SCI-001

graph and imager with a wavelength range of $3200 - 11000$ Å. There are two identical instruments built for the two mirrors of the LBT.

The *LBT Near Infrared Spectroscopic Utility with Camera and Integral Field Unit for Extragalactic Research* (LUCI, formerly LUCIFER) is made twice, one for each mirror, and is capable of long-slit and multi-slit spectroscopy as well as imaging at $0.85 - 2.4$ μm and will be available in AO-mode.

The *LBT Mid-Infrared camera* (LMIRcam) is an imager/spectrograph which will work mainly at $3 - 5$ μm and use the LBT interferometer's (LBTI) sensitivity and resolution.

The *Potsdam Échelle Polarimetric and Spectroscopic Instrument* (PEPSI) is a fiber-fed high-resolution Échelle spectrograph which will work in the wavelength range of 3830-9070 Å.

6.2 LINC-NIRVANA

The highly sophisticated instrument for the LBT is the LINC-NIRVANA, also LN, (Herbst et al. 2004). It is the combination of a NIR homothetic imaging camera, using the distinctive characteristic single mount of the LBT, and state of

the art AO system, Multi-Conjugate Adaptive Optics (MCAO), for the LBT.

6.2.1 Homothetic Imaging

A single mirror telescope with a masked pupil, e.g., a mask in front of the telescope with two holes, is called a Fizeu interferometer. The telescope then acts as a beam combiner for the apertures created by the mask. The FOV in this constellation corresponds to that of the telescope whereas the resolution depends on the separation of the masked apertures and is therefore limited by the telescope. To be able to use an improved resolution and FOV two telescopes that act as one larger masked telescope are needed. This setup is described in Traub's golden rule of separated telescopes[1] (Traub 1986). An interferometer that obeys the golden rule and has more than one aperture is referred to as a homothetic imager. The setup has to guarantee that no optical path-length difference in the focal plane is introduced for any wavefront seen by the interferometer, i.e., for wavefronts at off-axis directions, see Fig. 6.2. The big advantage is that a large FOV is seen and resolved and is not fixed to the diffraction limit of the single mirror aperture, as it is the case for radio interferometers where the accessible FOV equals the beam of a single dish. The resulting data, i.e., image recorded by the detector, will be a fringe pattern convolved with an 8 m telescope PSF.

6.2.2 Multi Conjugate Adaptive Optics

An AO system corrects the perturbations in the incoming and plane wavefront, which were introduced by the atmosphere. This is achieved by splitting a part of the incoming light, e.g., optical light during NIR observations, away from the optical path towards a wavefront sensor. The wavefront sensor analyses the speckle pattern in real-time and sends the correction to a deformable mirror, which is placed before the light-splitting, to correct for the distortions of the wavefront (see Fig. 6.3). This system works well if the AO system can be used on the target itself, i.e., the target has to be bright enough to allow for short enough integration of the wavefront sensor (WFS), see Fig. 6.3(a).

When this is not the case an off-axis target can be used as a reference for the AO system. In this case the problem arises that the path through the atmosphere is different for observed science target and reference star. For example in Fig. 6.4(a) the central star is a faint star that is supposed to be observed with AO, however, the AO won't work on-axis because it is magnitude limited. A nearby

---

[1] "As viewed from a point in the focal plane, beams from separated telescopes must be recombined so that they appear to be coming directly from a single large telescope which has been masked so as to reproduce exactly the ensemble of collecting telescopes."
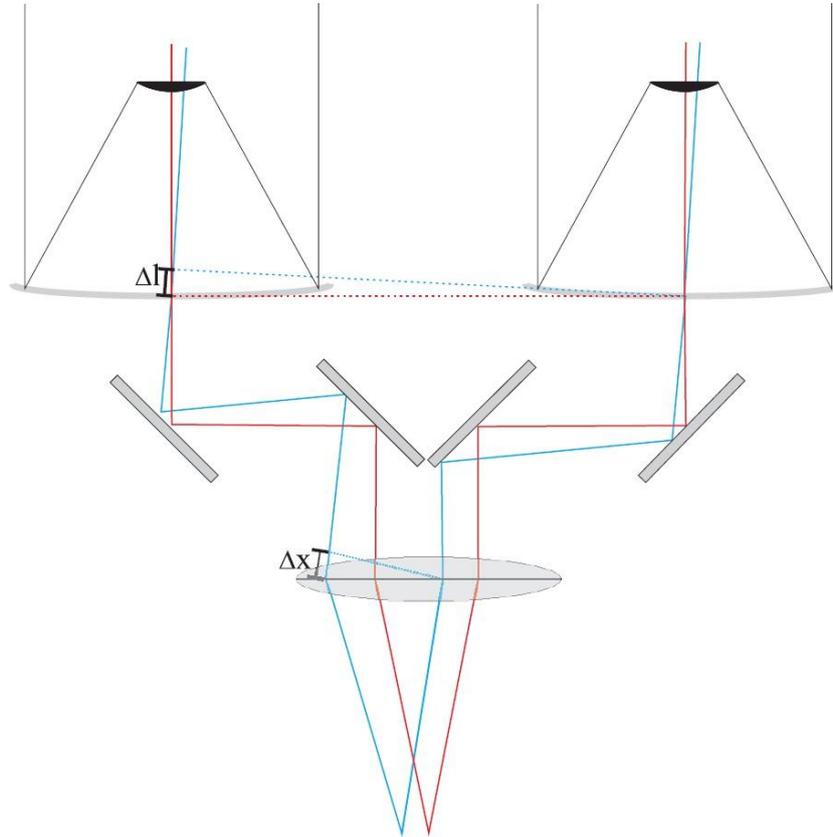
Figure 6.2: Sketch of an optical design representing a homothetic imager with two apertures, e.g., the LBT. The optical path-length difference in the focal plane has to be zero, i.e., $\Delta x = \Delta l$ has to be fulfilled. Image credit: Bertram (2007)

bright star can be used as a reference for the AO system. However, the intersection of the path through the atmosphere is far from identical for the two stars. The AO will correct for the reference stars perturbations but the science target wavefront moves partly through a different part of the atmosphere's distortions. This effect is called anisoplanetism. Single conjugate AO systems are limited by high layer anisoplanetism to a reference star that typically has to be closer than $30''$ to the science target. An additional limit is the magnitude of the reference star. The star has to be bright enough for the AO system to record, analyze and correct the incoming wavefront before it changes.[2]

---

[2] The Fried parameter r_0 (Fried 1965) describes the scale length over which the phase coherence is preserved. It is proportional to the wavelength λ and is a function of the zenith angle ξ,
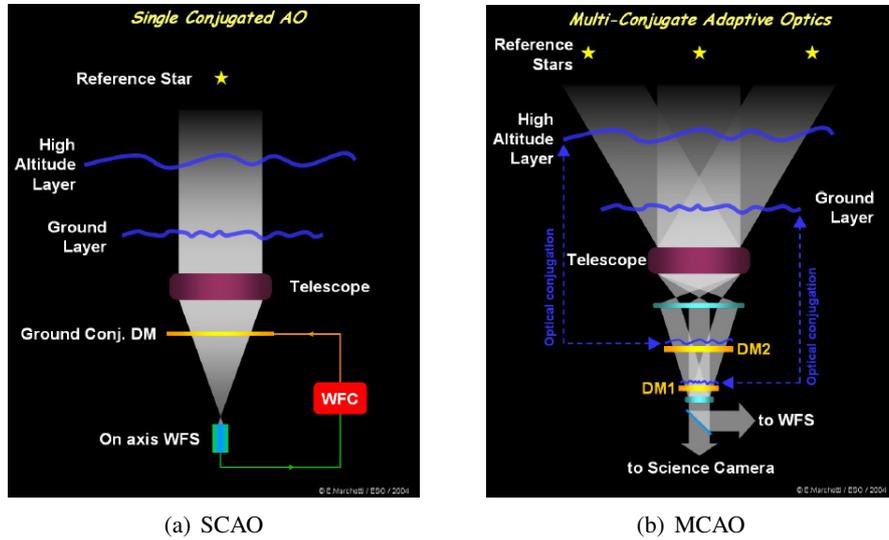
Figure 6.3: A sketch depicting (a) single conjugate AO and (b) multi conjugate AO. Image credit: ESO

Instead of a natural guide star (NGS) a laser guide star (LGS) can be used. However, since the LGS is created in earth's atmosphere ($\sim$ 90 km) the light path forms a cone towards the telescope (see Fig. 6.4(b)). This cone does not pass all of the atmospheric pathway that the science target light does and leads to imperfect correction.

MCAO helps to solve the problem of anisoplanetism particularly for the high layer corrections and therefore increases the observable FOV (see Fig. 6.3(b)). By correcting not only an on-axis star but also stars at a higher angles the anisoplanetism problem can be solved. Furthermore, when a bright science target is observed or the reference stars are close enough, i.e., the seeing cells of the reference stars overlap with the science target seeing cell, the MCAO enables the correction in higher atmospheric layers.

Due to the good overlap at the ground layer the light of the different stars can be combined so that the magnitude limit for the reference stars is not that of the single stars individually but of their combined light.

The use of several LGS and MCAO can minimize the cone effect and improve the efficiency of the AO for small FOV's.

---

i.e., $r_0 \propto \lambda^{6/5} f(\xi)$. The coherence time t_0 can then be determined from $t_0 = 0.314 r_0/\bar{v}$ with $\bar{v}$ the windspeed in the correcting layer. A typical value for the scale length at 2.2 μm is $r_0 \sim 60$ cm with typical wind speeds of 10 m s^{-1}. These parameters give a typical coherence time of $t_0 \sim 20$ ms.

(a) Anisoplanetism
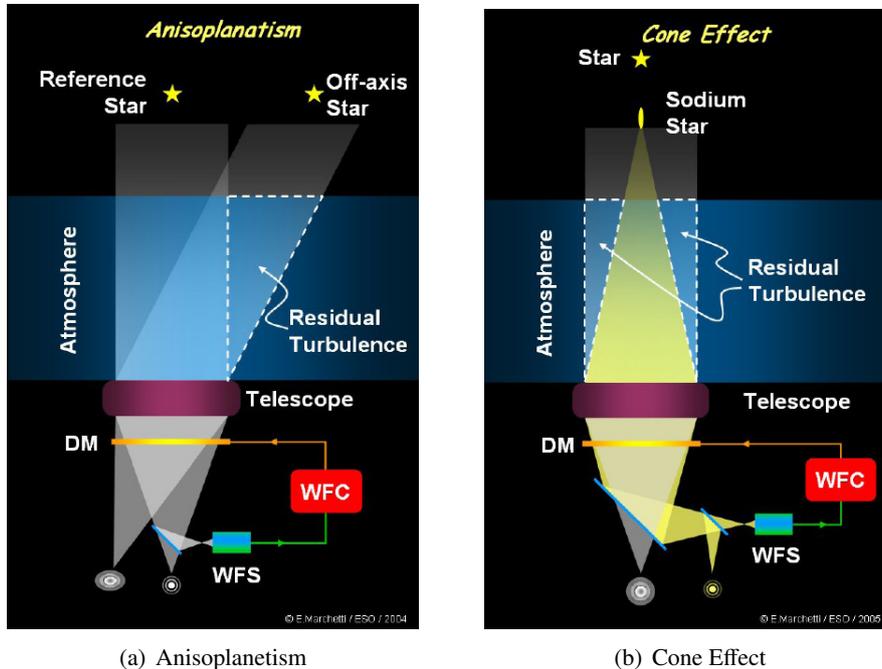
(b) Cone Effect

Figure 6.4: A sketch depicting (a) the effect of anisoplanetism and (b) the cone effect. Image credit: ESO

The MCAO of LN is necessary to make full use of the large FOV of the homothetic imaging abilities of the LBT.

6.2.3   Fringe Tracking

The two primary mirrors of the LBT are on a single mount which annihilates the use of long delay lines to recombine the beams. The installation of the optical systems is not without error and has to be corrected to achieve a perfect beam recombination. Also, vibration within the system can lead to misalignments of optical parts during an observation. However, the main source of misalignment for the two wavefronts propagating through the two single apertures is the atmospheres piston. For single apertures this effect is not present and the correction of atmospheres tip/tilt and higher modes is taken over by the AO system. For the case of beam combination the AO corrects all modes but the piston mode which translates into a path-length difference between the two wavefronts.

In order to correct the path difference the interference pattern of the two apertures is analyzed. The interference pattern is the fringe pattern of a double-slit

experiment, also known as Young's experiment, convolved with an 8 m telescope PSF. This pattern can only be detected if the differential path-length of the two beams is smaller than the coherence length

$$l_c = \frac{\bar{\lambda}^2}{\Delta\lambda}$$

with $\bar{\lambda}$ the mean wavelength and $\Delta\lambda$ the observed bandwidth.

Fringe tracking can be used in different modes. In *cophasing* mode, the path-length difference is controlled to always remain zero, i.e., the central fringe has to be centered and should not move. In *phase tracking* mode the the path-length difference is kept constant within the coherence length but does not have to be zero. In *coherencing* mode the path-length difference is kept within the coherence length with no other constrain.

6.3 The Fringe and Flexure Tracker

The fringe and flexure tracking system (FFTS) is the part of LINC-NIRVANA that enables homothetic imaging. Fringe and flexure tracking allows for the correction of optical path-length difference (OPD) between the two mirrors, which is induced by the atmosphere and by the telescope itself (e.g. vibration). This OPD, or piston, is not corrected by the AO because it is not detectable with single dish telescopes. The correction is done by two mirrors, which are single mounted on a piezo-driven stage.

The FFTS detector is a HAWAII focal plane array with a resolution of 1024× 1024 pixel. However, for faster readout parts of 64×64 and 32×32 pixel subarrays will be used. Therefore, frame rates of up to 1 kHz are achieved to correct the point spread function (PSF) for OPD. The residual OPD is required to be less than $\lambda/10$. The fringe tracking and also the OPD correction will be done by piezo-staged mirrors, however, the flexure correction needs to be given to the AO system to deal with. To be able to track the fringes and the flexure independently the beam is split and placed on two distinctive positions of the detector by the use of a periscope (Zuther et al. 2012).

6.3.1 General Design

The FFTS mechanics is supported by an outer GFRP casing (1), which is double-walled and reinforced by GFRP rods that are attached to cold ring (6) and base plate (9). The base plate is designed to be stiff and light by using aluminum and pocket milling. It has to hold the three heavy moving stages (4) that are movable
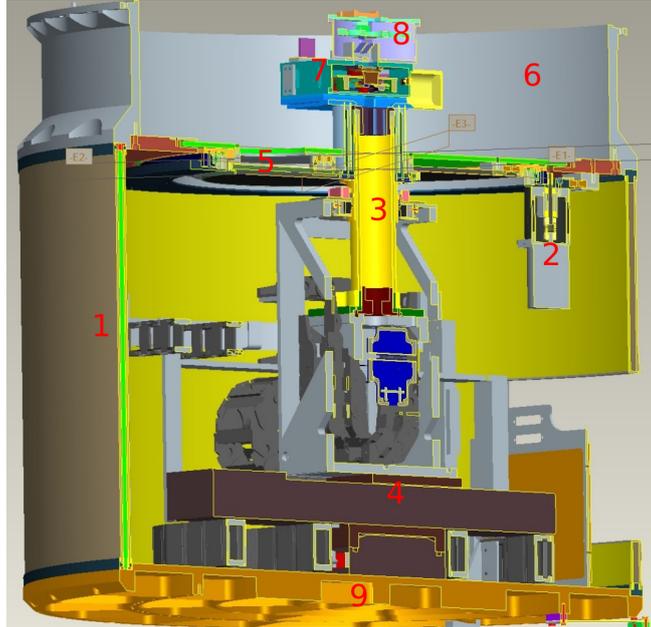
Figure 6.5: The Fringe and Flexure Tracking System mechanics in cross section with the old baffle system (5). Everything below the baffle (5) is in an ambient temperature environment and everything above it is in a cryogenic environment. For details see text.

in x-, y-, and z-direction. Mounted onto the z-stage is the GFRP pin (3). This pin carries the detector head (7) and filter wheel (8). An interlock protection surrounds the pin right under the baffle and can be actuated by a GFRP tube connected to the baffle and held in position by springs. All electronics are connected to a patchboard that is situated at a rectangular hole in the GFRP casing and is then further lead to an exit out of the cryostat. The cold ring (6) is made of aluminum. This part will be attached to the heat exchanger and has to keep the cold side below 110 K. The baffle (5) shields the cold from the warm part and is made of three overlapping aluminum disks. The outer ring is connected to the cold ring. The inner two movable parts mostly cool via radiation. The inner two baffle are rotating. The larger disk is attached to a gear on a bearing via springs and is rotated actively by the baffle motor (2). The bearing is placed on a steel structure that is attached to the outer ring with springs. The inner disk is moved passively by the pin. The a baffle motor with a double-walled GFRP attachment and a GFRP axle is attached to the steel structure. An encoder is attached similarly to the baffle motor to track the exact rotation steps of the baffle, see Sect. 7.2. The detector head (7) contains the FFTS detector and has to be cooled

and shielded from all kind of electro-magnetic radiation (e.g., reflection of incoming science photons, filter wheel motor, thermal photons). The periscope is attached at the beam entrance opening. The filter wheel (8) with the filter wheel motor consists of 13 filters (including open and closed). Especially the motor adds additional weight to the detector head and induces a high torque when the instrument is tilted. The cold part is anodized to prevent reflection, the ambient temperature part is coated with high reflective multi-layer insulation (MLI) foil to keep the heat in the ambient temperature part.

6.3.2 FFTS oddities

The FFTS is divided into an ambient temperature and a cryogenic part (Smajic et al. 2012), see Figure 6.5. The cryogenic part consists of the baffle, the detector head and the filter wheel. This part has to be cooled to about 77 K because the instrument operates in the near-infrared (NIR). Therefore, the detector needs to be placed in a cold and dark environment as not to be exposed to thermal photons radiated by warm bodies and as not to be bothered by reflection. The moving stages that position the detector head for a given FOV in three spatial dimensions, however, need to be in an ambient temperature environment (about 280 K). As a consequence, the connection between these two parts needs to exhibit a temperature gradient of more than 200 K. Additionally, this connection needs to be stiff enough to support about 4 kg without breaking or being greatly distorted. The baffle encoder and motor have contact to the cold baffle but are situated in the ambient temperature part and therefore need to be connected with a low heat conduction. Also, the detector positioning unit (DPU) needs to be protected if a mechanical or software error occurs and the movement of the stages and/or baffle cannot be controlled anymore. This protection is realized by switches that turn off the system if they are activated. This can occur for example if the baffle stops moving but the linear stages do not. The result would be that the pin, which supports the detector head, would get under high stress by being pressed against the not moving baffle. Once again a connection between cold baffle and ambient temperature DPU has to be established, which is not allowed to cool the ambient temperature part, too. This connecting part has the responsibility to actuate the switches before the pin hits the not moving baffle.
The ambient temperature part of the FFTS is very massive due to the base plate, which in addition to its own weight carries the moving stages, the detector head, and the filter wheel. The cryostat of LINC-NIRVANA will have to be turned by 90 degrees, with respect to the gravity vector. The FFTS will be hanging attached to the heat exchanger at the end of the 3m cryostat. The rotation axis is placed in the center, perpendicular to the cylindric cryostat mantle. Hence, the

torque will be high owing to the 1.5 m lever arm. Therefore, a stiff and light cylindric mantle is needed to hold the ambient temperature part as to minimize the weight and the flexure introduced by the base plate and all parts attached to it.

In conclusion, a material is needed with

- a low heat conduction,

- a high E-module, and

- a low density,

which all are characteristics of Glass Fiber Reinforced Plastics (GFRP).

The FFTS's GFRP put to test

In this chapter the GFRP tests for the FFTS of LINC-NIRVANA are explained. The pins task is to hold the detector head of about 4kg at a lever arm of more than 350 mm. The DPU (including the pin) has to be able to reproduce all movements so that the detector can be positioned accurately with a lever arm of up to 700 mm. Therefore, the flexure of the whole FFTS cryostat is measured with respect to the plane where it is attached to the LINC-NIRVANA cryostat.

For several applications the GFRPs had to be cut and trimmed to fit the instruments purposes. The institutes workshop had no problems working the material with their machines and there were no problems with sharp or unraveling edges. The gluing was also very efficient using the epoxy encapsulant STYCAST 1266. Stycast 1266 is known for its impact strength and adheres well to metals and glass. The low viscosity ensures an excellent wicking and flow around parts in the tightest clearance applications to give the best possible adherence behavior and to expel air from the glued areas. The latter is very important for vacuum applications. The hardening takes several hours, however, it does not need to be cared about during this time and therefore can be hardened over night. Due to its low viscosity one has to take care that the encapsulant does not flow where it is not supposed to. Hence, a hardening form is needed or it has to checked and turned for a few hours after mixing. The thinner the encapsulant the faster it hardens!

7.1 Glass fiber reinforced plastics

For all characteristics mentioned in Chapt. 6.3.2 GFRP offers a solution. It connects high stiffness with a low density and offers a low electric and thermal conduction. An industrial use for GFRP's are airplane wings owing to the materials low density, high stiffness and low electric conduction. Other fiber options are aramid, carbon, zylon (PBO), polyethylene (PE) and various other fibers. All differentiate in their price and their mechanical, chemical and physical properties, e.g., resistance to acids, high temperature resistance, low/high heat conduction. GFRPS's are glass fibers glued with a matrix, e.g., epoxy resins, venylester

resins. The matrix similar to the fiber type has its own properties from which one can choose. The main purpose of the matrix is to hold the fibers in line and at a distance to each other to minimize abrasion. The matrix also transfers force between fibers and different layers. Furthermore, the matrix, since it is glued to the fibers, has to compensate for some of the incoming force especially if the direction of the force is perpendicular to the fiber direction. The matrix also protects the fibers from external influences, e.g., acids.

Fiber and matrix are chosen with respect to the cost and the area of application. Epoxy resins, which are used here, yield a good adhesion to the fiber, are electric insulators and have a great fatigue limit. Epoxy resins are usually used in aviation and astronautics (Schuermann 2005). The combination glass fiber and epoxy resin yields the perfect tool to fulfill the instruments requirements.

Table 7.1: GFRP technical data.

Properties	Fabric: F012	
	0°	90°
Compressive Strength [MPa]	600	85
Compressive Modulus [GPa]	40	6
Flexural Strength [MPa]	875	125
Flexural Modulus [GPa]	39	6
Tensile Strength [MPa]	665	95
Tensile Modulus [GPa]	40	6
ILSS [MPa]	70	10

Notes. Values are given in the Technical Data Sheet SM350 of the *Advanced Composites Group*. The GFRP described here was used for the construction of the pin.

7.2 Baffle motor and encoder

In a minor pre-test the vacuum performance and stability of the baffle motor and encoder attachments to the baffle and the axles of these two instruments were tested. Both, attachments and axles, are made of GFRP and glued with the two component, low viscosity, epoxy encapsulant and impregnant STYCAST 1266.

The baffle motor and encoder are both screwed to the baffle and use GFRP axles and a steel coupling (motor axle to GFRP axle) to achieve contact to the baffle gear. Stycast 1266 is used to glue gears to the axles. Both gear parts, baffle

gear and gears on the axles, are made of the same low contracting stainless steel, to minimize the gear backlash when the baffle is cooled to 77 K. The baffle gear has an effective diameter of 500 mm whereas the axles gears have an effective diameter of 10 mm. The motor is supposed to run highest at an ω of 2.8 s^{-1}. Its holding torque is 350 mNm and the detent torque is 13 mNm. The Phytron VSS 52.200.5 stepper motor, which is designed for extreme environments (e.g., vacuum of 10^{-11} mbar and temperatures of 77 K), is used. To stabilize the axles in radial direction, two uncoated steel bearings are used (see Figure 6.5 #2).

The axles were tested at room temperature and normal pressure for stability. Also, the baffle gear was jammed so that the motor was forced to jump-over to ensure that the axles won't break at the highest possible torque. Several long-term runs were run to test the abrasion behavior of the axles. Both tests proved to be satisfactory. The extreme test showed no cracks in the axles and no abrasion traces on the axles or around these (e.g., dust traces from the axles) were found. Additionally, the baffle behavior in vacuum was tested at 10^{-5} mbar without cooling down. Everything ran smoothly several times. In addition, the GFRP connecting baffle and motor/encoder showed no signs of cracks or abrasion which may have occurred during the above described tests within the GFRP or epoxy resin.
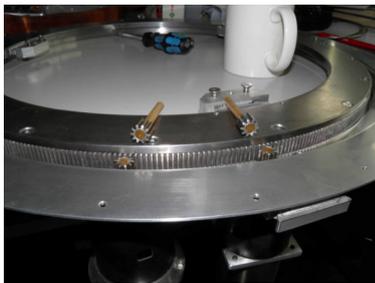
(a) GFRP axles   (b) Baffle motor and encoder

Figure 7.1: Shown are the two GFRP axles and their two spare parts in (a) and the baffle motor (right hand side) and encoder (left hand side) in (b). The baffle motor and the encoder are attached to the baffle ring and to the baffle gear. The motor moves the baffle gear and the encoder is moved by the baffle gear. The encoder is supposed to give information about how far the baffle gear was actually moved by the motor if problems occur with the motor, i.e., the motor misses steps.

7.3 Flexure of the FFTS

The flexure measurement of the full FFTS cryostat flexure (including the stages, pin, detector head and filterwheel dummy)[1] is presented. The FFTS will be at the bottom end of the LINC-NIRVANA cryostat and will be attached over its cold-ring. The lower FFTS cryostat part is at an ambient temperature and is supported by a GFRP double walled structure inlaid with GFRP rods. The full DPU is attached to the base plate of the FFTS cryostat hence the full weight of it is contributing to the flexure. In the test setup it has a lever arm of about 600 mm. The detector head and filter wheel dummy weigh more than 4kg and are attached to the GFRP double walled pin at a lever arm of about 350 mm. Hence, this may introduce a not negligible part of flexure.

The flexure is tested at rest and for different trajectories. The needed absolute positioning accuracy is several 10 μm. The accuracy, needed during the tracking of a guide star, is 4 μm over 10 minutes.

7.3.1 Test setup

The flexure of the FFTS was tested by attaching the system to a steel skeleton resembling the LINC-NIRVANA cryostat. The skeleton can be tilted from 0 to 90 degrees at a resolution of 5 degrees around the x-axis (defined as parallel to the x-stage). Data processing and recording is done by the Heidenhain KGM 182 encoder, which uses interference position measurement at a resolution better than 0.1 μm. The needed accuracy for the detector trajectory during the tracking is 4 μm in x-direction, since the x-axis lies along the baseline of the telescope which defines the high-resolution of the PSF. The Heidenhain grid plate is attached to the skeleton and does not add any load to the FFTS cryostat. The Heidenhain detector head, which transfers the analogue signal to the readout electronics (either an IK 220 interface card or the EIB 741 portable interface box)[2] is attached to the FFTS detector head. The test setup is presented in Figure 7.2. The TwiceAsNice[3] common LINC-NIRVANA software is used in combination with the Motion Control (MoCon) for the movement test.

---

[1] Note that the baffle is missing in this test, however, although it is heavy it has a small lever arm (less than 150 mm) and therefore won't contribute much to the flexure.

[2] For more information about the Heidenhain encoder and interface card/box visit www.heidenhain.us

[3] For more information about TwiceAsNice vist https://svn.mpia.de/trac/gulli/TwiceAsNice

(a) FFTS cryostat

(b) Tilt ring

(c) Top view
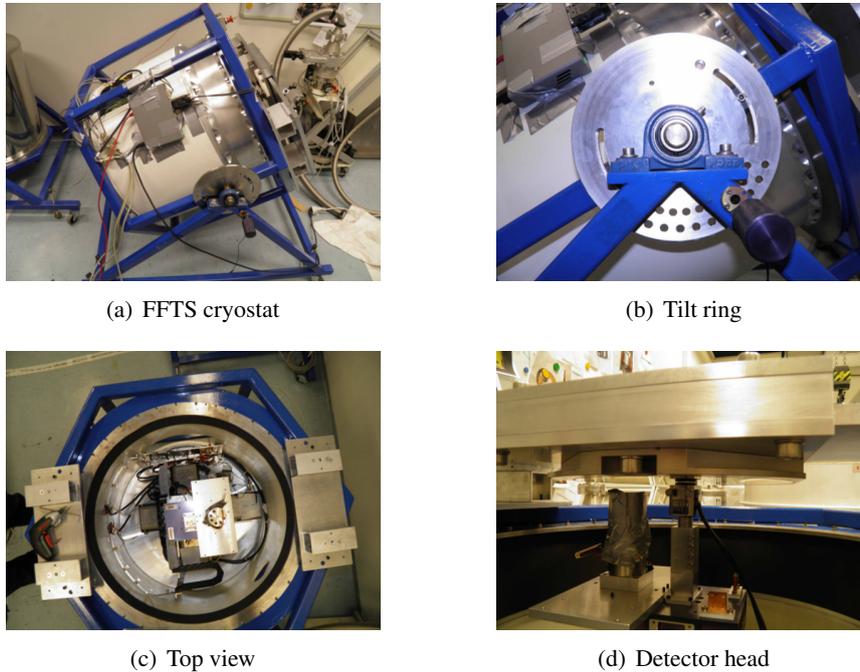
(d) Detector head

Figure 7.2: The test setup for the full flexure measurement.

7.3.2 Results and Discussion

The detector head position (the Heidenhain detector) was recorded over several time ranges for 0 to 90 degrees tilts. The flexure above 60 degrees tilt was not monitored in detail, because it is not expect that the telescope will be tilted far more than 60 degrees for observations owing to the high airmass and high light pollution by city lights at lower telescope positions. In addition to the Heidenhain plate above the detector head, a Heidenhain absolute encoder (LIC 4015) is used for the x-stage that monitors only the movement of this stage. Hence, one can distinguish between stage movement and pure flexure. Unfortunately, the absolute encoder of the y-stage, which is the direction of tilt, is broken and could not be replaced for the test campaign. The accuracy of the Heidenhain plate is better than ±0.1 μm and that of the absolute encoder is about ±0.01 μm. The main results of this test-campaign are explained in the following.

First of all the DPU can support the detector head and filter wheel at full load with a minor consequence that if the stages do not get current they cannot support the DPU and roll down if the cryostat is tilted. Hence, a parking position is needed for the disk-in-disk baffle when the FFTS is not running. However,

with the new simplified baffle, see Sect. 8.2, the stages are free to move until the limit switches hit the FFTS GFRP housing. From the active limit switches the position will be known immediately.

Secondly, the full flexure of the DPU does not exceed 1.6 mm even at 90 degrees tilt and over two days of staying in that position.

The third result is that the time behavior of the flexure indicates that tracking the guide star continuously over 10 minutes will not be an issue. A linear relationship of the flexure is measured at a 60 degree tilt of 0.6 μm per hour in negative y-direction and only 0.3 μm in x-direction, see Fig. 7.3. However, a
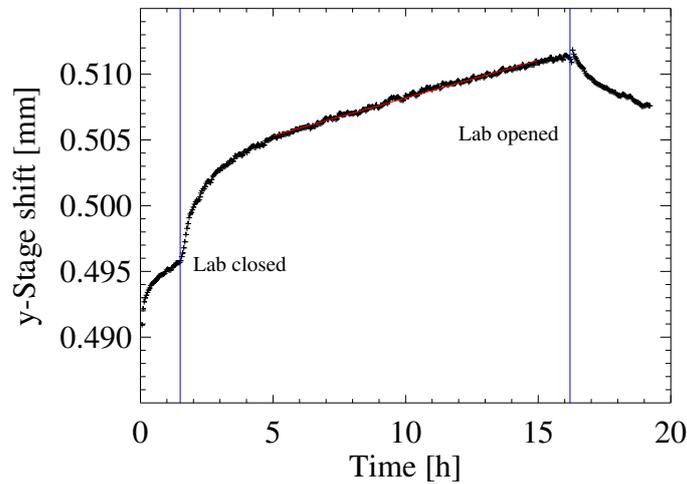
Figure 7.3: Flexure behavior of the y-stage at 60° tilt. The blue vertical lines indicate closing and opening of the laboratory. The red line is a linear fit to the slope. The fit yields a gradient of 0.6μm h^{-1}.

temperature dependency of the measured flexure is noticed, which is very strong in y-direction. This temperature features occur always after the laboratory is either shut down in the evening or opened again the next day. The reaction of the DPU to the temperature change is always the same: the y-stage 'falls' after the laboratory is closed, i.e., tilts in the negative y-direction (tilt direction), and returns in the morning when the laboratory is opened. The temperature effects seem to follow an exponential decay law but this problem was not addressed further since the temperature of the FFTS cryostat will be controlled. Nonetheless, the temperature induced flexure can be high on timescales of about 10 minutes, e.g., for the 60 degree tilt a decline of the detector head in y-direction of 3 μm

in 800 seconds was measured after the lab was closed. The x-direction is not affected as much as the y-direction if at all. For the 60 degree tilt no x-stage reaction can be measured which can be seen as coincidental with the y-direction but for the 0 degree measurement there seems to be a reaction that shows a gradient of 0.7 μm over 1000 seconds in positive x-direction. After that, the slope turns again and a gradient of 0.5 μm per hour and declining is measured. For the y-direction a gradient of 12.8 μm per hour is measured for the temperature feature in negative y-direction which dominates the graph only for about 1000 seconds after which the slope turns towards the positive y-direction with a gradient of 0.9 μm per hour declining to 0.3 μm per hour. This amount of deviation is also visible in a periodic pattern with a gradient of about 0.4μm per 600 seconds which can attributed to temperature variations owing to the air conditioning cooling phase, see Fig. 7.4.

(a) y-Stage at 0° tilt.

(b) Detail of y-stage at 0° tilt.
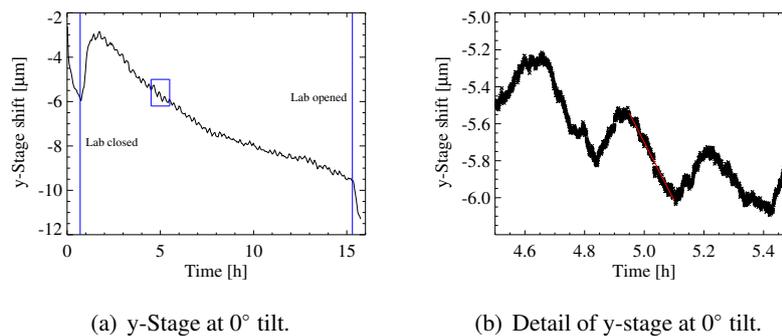
Figure 7.4: Flexure behavior of the y-stage at 0° tilt. The blue vertical lines in (a) indicate closing and opening of the laboratory. The blue rectangle indicates the region from which the detail shown in (b) is taken. The red line in (b) is a linear fit that yields a gradient of 3μm h^{-1}.

The fourth result is the positioning of the detector head with respect to xy-movement. The positioning accuracy of the DPU as measured by the Heidenhain plate is derived to be up to ± 8 μm for telescope inclinations of 0 to 60 degrees. This may seem a big number but the detector pixel size is even larger with a size of 18 μm, hence the positioning of the detector will be good enough to get the fringes on the detector. The more important thing is that the detector head stays within 4 μm of the acquired position during an observation (max. 600s). In this part of the test campaign the movement was paused about 1 minute before driving on to see how the DPU behaves when it stopped moving. What is noticed is a "bleeding" of the DPU in the direction of its movement, see Fig. 7.5. The DPU seems to move although the software used to move it says it has reached its

destination. This bleeding is only important for about the first 20 to 30 seconds where it can change for about 1 μm. After this time the bleeding is still detectable but it shows a gradient of only 0.3 μm per 60 seconds. The effect lasts only about 1 minute in full after which it ceases and cannot be distinguished from the thermally induced variation. Both stages were moved for 6×10^6 steps back
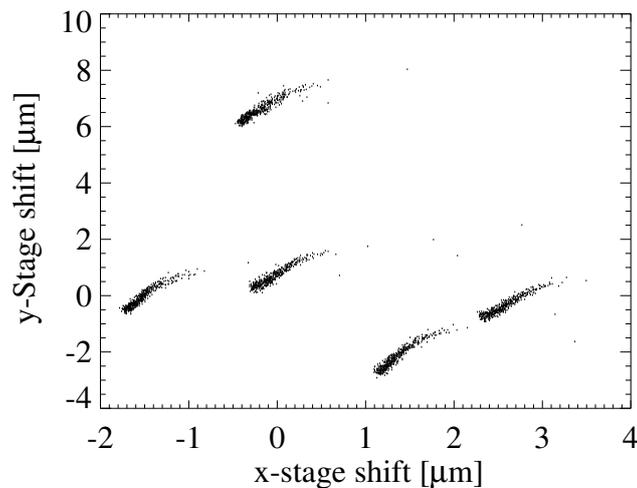
Figure 7.5: Positioning accuracy of the x- and y-stage at 30° tilt. The mentioned "bleeding" is indicated by the coma-like end points of the tracks. For more detail see text.

and forth always from the upper-left to the bottom-right and vice versa corners to achieve a synchronous acceleration of the stages. This was important because a stage that reaches its position is not being controlled anymore by the MoCon, which introduces an additional error that is not supposed to occur (Rauch et al. 2012). Another issue here is that over the travel distance, if only the endpoint is given but not an exact route, the motors drive at full speed. Since the path is not controlled a deviation of several ten microns is measured for the different tracks although the start and end points are only a few microns apart. What is also seen is a fragmentation of back tracks and forth tracks which deviate up to 10 μm within their tracks. However, since the tracking will be controlled (e.g., acceleration, positioning) this is not supposed to happen while tracking a star.

The fifth result shows the positioning accuracy of the DPU with respect to the tilted angle of the telescope. It is not possible to reproduce the telescope tilting exactly but in a minimum of 5 degree steps which is good enough for the positioning but not good enough if the flexure gradient during a 10 minute

exposure is to be tested over which the telescope will be tilted by a maximum of 2.5 degrees continuously. The positioning of the DPU by tilting the cryostat shows small deviations of a few microns at high inclinations for both stages. For 60 to 30 degrees the deviation is not higher than 3 μm, see Fig. 7.6. For smaller angles the deviation gets higher with the highest at 5 degrees with 20 μm in y-direction and 7 μm in x-direction. Nonetheless, this is only the positioning which is again good enough. The gradient (deviation over time) is similar to the ones further up, hence there is no problem keeping the track stable (within 4 μm over 10 minutes) during an observation.
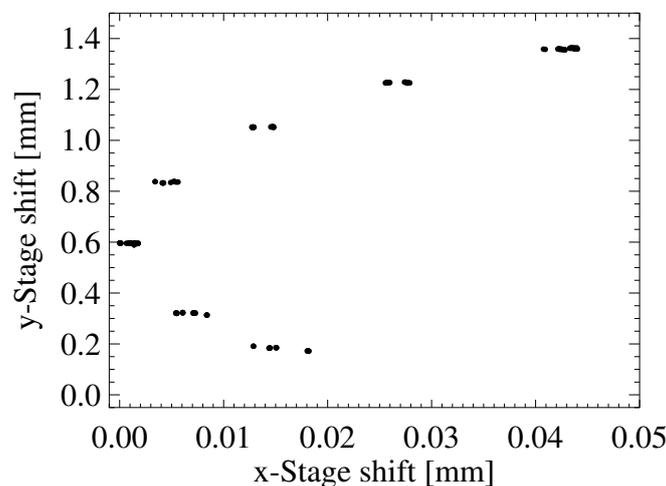
Figure 7.6: Flexure of the x- and y-stage at (lowest y-stage shift) 5°, 10°, 20°, 30°, 40°, 50°, and 60°.

Several runs were performed in a tracking sequence to demonstrate that the tracking of a guide star is possible. An elliptical track was chosen which was run through four times per run. In Figure 7.7 two consecutive runs are shown. A single run is about 5 minutes long adding up to a total of 10 minutes. The deviation within one run and also from one run to the next is less than 1 μm which indicates that very good results can be expected for the fringe tracking. Note that the software for these tracks was not written in full detail and that there still are some problems with the MoCon. For example, the software needs to be written in more detail as to get rid of the ringing at the beginning of the ellipse which can be achieved by controlling the acceleration at the beginning of the track. Another issue with either the software or the MoCon is that at a particular

point before the last track ends one of the stages stops moving whereas the other finishes the track, as seen in Figure 7.7 where the y-stage stops but the x-stage finishes its movement.

(a) Ellipse track

(b) Lower left quarter of the track
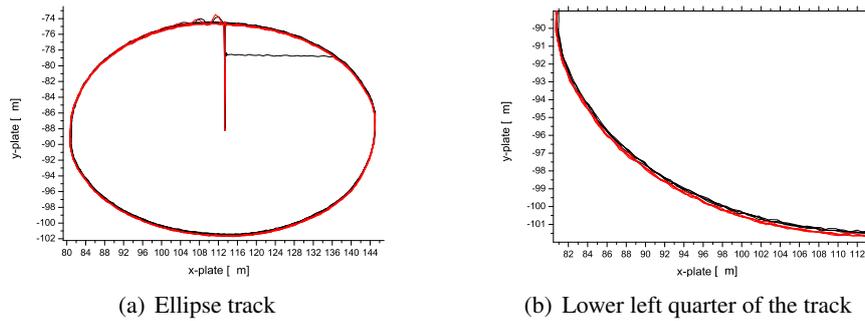
Figure 7.7: Shown in (a) is the full ellipse run through eight times (two times consecutively with four full ellipses at each run). (b) shows the lower left quarter of the ellipse. At no time the critical 4 μm deviation is overrun. The maximum deviation is 0.5 μm in x and y direction. Plotted are the -x and -y coordinates of the Heidenhain measurement plate attached above the detector head (see Figure 7.2(d)).

7.4 Summary

The use of glass fiber reinforced plastics in the fringe and flexure tracker a part of LINC-NIRVANA an instrument for the large binocular telescope is presented. The stiffness, robustness and low heat conduction of this material can be used for several applications. In the case of the FFTS these are: axles made of GFRP which are not damaged by using two good bearings to lead them, attachments connecting cryogenic parts (T=77 K) with ambient temperature parts (T=300 K) without transferring too much heat, a double walled pin that holds and positions the detector head at inclinations of 0 to 90 degrees with respect to the gravitational force (0 to 60 during observations), the DPU protection made to trigger a soft and a hard break if baffle and DPU choose to go separate ways and the double walled casing of the FFTS cryostat that makes the whole instrument weigh only a fraction of which it would be by using aluminum.

The results show that it is possible to track a guide star over up to 10 minutes with a deviation of less than 4 μm as needed to make full use of the fringe tracking and guarantee a diffraction limited PSF. These results are promising that the whole system will work in full cryogenic environment.

CHAPTER 8

The FFTS Baffle System

The FFTS baffle is the key element in keeping the warmth of the ambient temperature part from the cryogenic temperature part, for more details see Sect. 6.3.2. It was first designed by Bertram (2007). The idea was to have a large correction area for the FFTS resulting in an FFTS detector travel range of 200 mm×300 mm in the $x - y -$ plane. Therefore a complicated disk-in-disk system was designed that allowed the baffle to rotate without any limitation to rotation. The system was redesigned several times (e.g., Bertram et al. 2006; Bertram et al. 2008) but the general idea of limitless rotation and cooling only via radiation and the ball bearing was not disregarded until the very last.

8.1 The Disk-in-Disk System

The final design of the disk-in-disk system is shown in Fig. 8.1. An outer ring (2)

(a) FFTS with the old baffle   (b) FFTS old baffle model
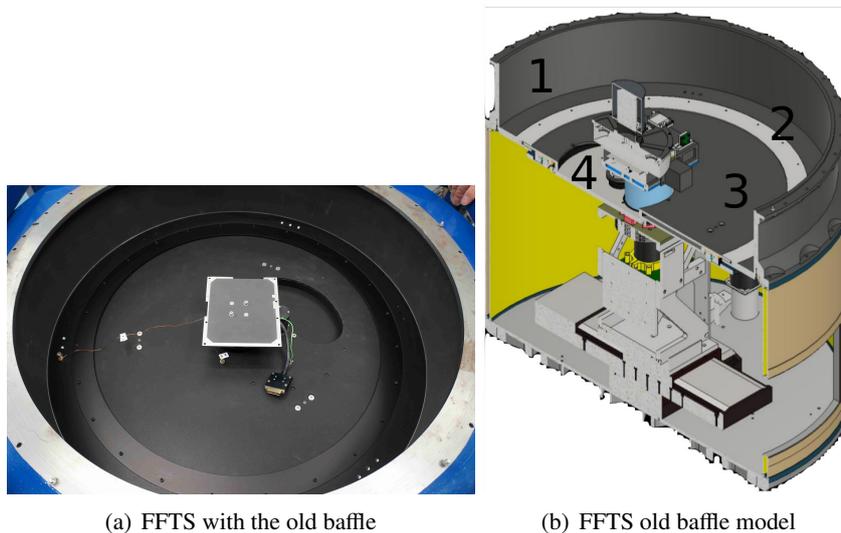
Figure 8.1: The FFTS equipped with the disk-in-disk baffle. For details see text.

is connected to the cold ring (1), see also Fig. 6.5, and therefore can be cooled down efficiently. All other parts of the baffle could not be attached to this cold part directly, e.g., copper strap connections, because of the mentioned movability of the baffle. Therefore the actual baffle, the outer (3) and inner (4) baffle, had to be cooled via radiation only. On the warm side these were shielded by attached MLI. Due to the large size of the outer baffle the bearing has to be approximately of the same radius. The consequence of this is that the steel bearing had to be attached to another steel part as not to be squeezed and twisted due to differential reactions of steel and aluminum to the cooling. These two steel parts made up most of the weight of the baffle hence the highest heat load. Therefore this steel part was connected at three points to the outer ring. To keep the ambient part warm a 50 Ω resistor is installed on the base plate of the FFTS.

The FFTS with the disk-in-disk system was attached to the LN cryostat at the Max Planck Institut für Astronomie (MPIA) in Heidelberg and cooled to see the baffles reaction to the final environment. The warm part of the system was fully equipped including the motor and encoder, see Sect. 7.2 and Fig. 8.2(a). The cold part was missing the detector head and filter wheel, see Fig. 8.1(a).

(a) FFTS warm part

(b) FFTS in LN cryostat
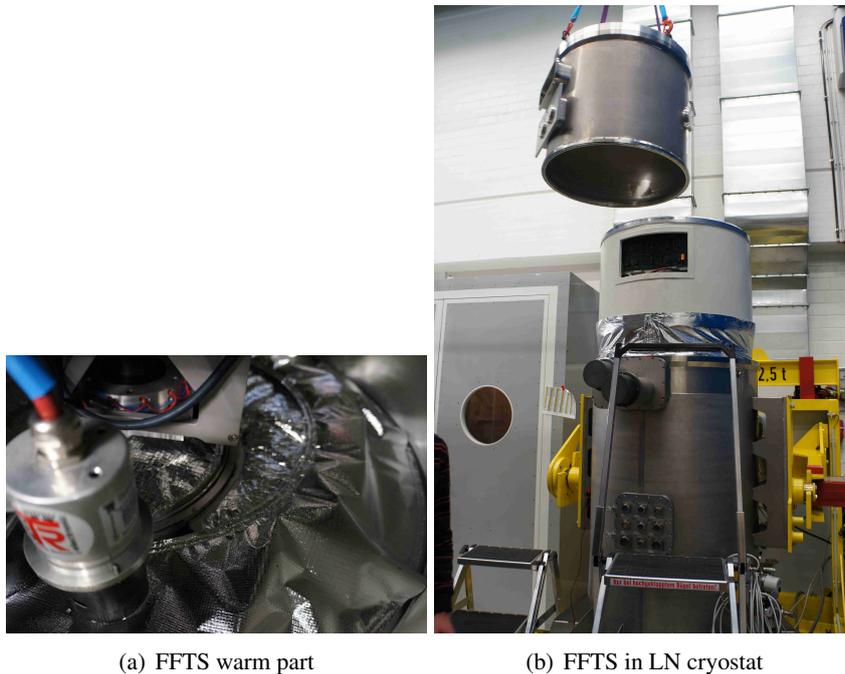
Figure 8.2: The final cooldown test setup for the disk-in-disk baffle in the LN cryostat at the MPIA.

The graph in Fig. 8.3 shows the cooldown of the system. The outer ring comes close to the reference plates, i.e., the heat exchanger. Note that the final temperature of the heat exchanger is supposed to be ∼ 60 K which was not achieved in this test due to problems with the heat exchanger system. The inner and outer baffle system is with ∼ 140 − 170 K far away from its requirements of ≤ 110 K.
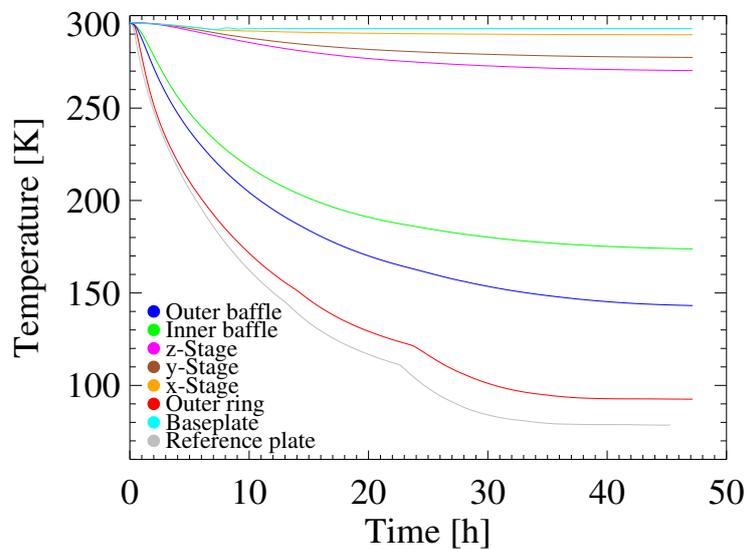
Figure 8.3: The final cooldown temperature graph for the disk-in-disk baffle in the LN cryostat at MPIA. For details see text.

Several factors can be responsible for the measured temperatures of the baffle system. The not achieved 60 K of the heat exchanger which was at about 80 K hence 20 K too warm surely has an impact though not accountable for the 30 − 60 K excess. Another problem might have been the heat load of the steel parts which take longer to cool down due to their high mass and low thermal radiation and conduction to cold baffle parts. It was not possible to install additional sensors in this test to monitor the steel parts temperature. Another reason for the temperature of the two critical baffle parts (3 and 4) is that the radiative cooling[1] goes with the temperature to the power of 4. Hence, the lower

---

[1] The Stefan-Boltzmann law states that the radiative power of a black body P scales as $P = A\epsilon\sigma T^4$, with its surface area A, emissivity ϵ, the Stefan-Boltzmann constant $\sigma = 5.67 \times 10^{-8}$ W m^{-2} K^{-4}, and its temperature T.

the temperature becomes the lower the radiative dissipation. As an example a temperature change from 270 K to 150 K reduces the radiative power by a factor of 10.

Due to scheduling issues it was not possible to get enough time (approximately six weeks) on the LN cryostat to find out and fix the too warm baffle system parts. Ideas to lower the temperature values of the critical baffle parts are for example to improve thermal conduction between steel parts and cold outer ring and give inner and outer baffle more time to cool down.

As a consequence of this tight schedule the baffle system was redesigned.

8.2 The Simplified Baffle System

To be able to guarantee a functioning system within the requirements it was decided to exchange the disk-in-disk baffle, see Fig. 8.4, for a more simple but effective designed baffle.

The benefit of the simplification is that no rotating system is required hence the heavy steel parts can be removed. Additionally, the cold baffle can be connected via copper straps directly to the cold ring which assures a temperature of ≤ 110 K. The new design reduces the FFTS correction area to a movable range of 150 mm $\times$ 150 mm ($45'' \times 45''$). However, this is no drawback because the first estimate of a correction area of $90'' \times 60''$ did not take into account the telescope uncertainties, e.g., tertiary reflection to the combined focus. New estimates show that at very best a correction area for the FFTS of $30'' \times 30''$ can be achieved[2]. Therefore the new $45'' \times 45''$ area is more than required due to telescope restrictions.

The new design is presented in Fig. 8.4 in real and as a model sketch, numbers in brackets can be found in Fig. 8.4(b). The first and most important part here are the springy copper straps (6). In the earlier design only four copper straps were included (three for the detector head and one for the filter wheel). Two additional straps were added for the filter wheel motor and cold baffle (3). The cold ring (1) stayed the same. The outer ring (2) is now much bigger with an inner hole diameter of ~ 207 mm and the side looking into the ambient temperature part is coated with MLI layers. This assures a bigger area that is directly screwed to the cold ring (1). The new cold baffle (3) consists of one round plate with a cylindric ring screwed to it. It is attached via one copper strap to the cold ring (1) to make possible cooling via conduction. The cylindric component adds another photon stop to this simple photon trap. The inner two cylindric parts (5), one in the cryogenic and one in the ambient temperature part are photon traps

---

[2] Detailed calculations are based on Beckers (1990).

(a) FFTS with the new baffle   (b) FFTS new baffle model
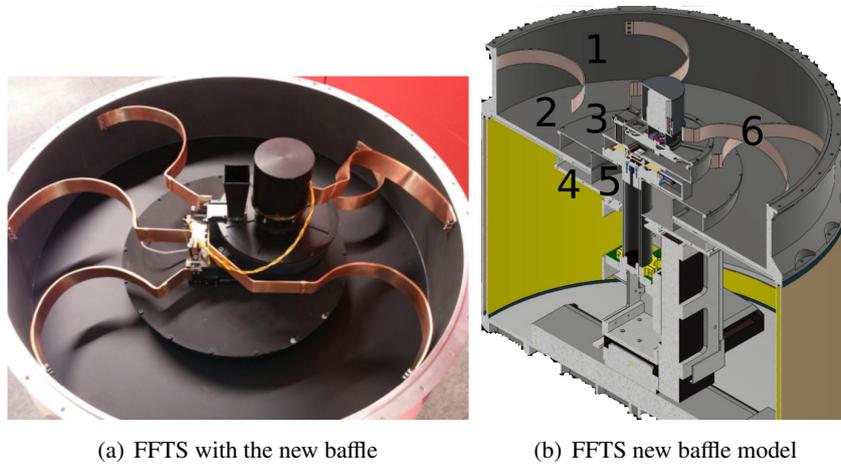
Figure 8.4: The FFTS equipped with the new baffle. For details see text.

and are attached to the outer ring (2). The upper part is connected well to the outer ring to assure the same temperature between these two components. The lower part is only connected at the screwing points since it is part of the warm system and is not supposed to transfer heat out of the ambient part. The warm part of the baffle is shown in (4). It is used as a photon trap from the ambient temperature surrounding and its cold part facing dish is coated with MLI layers. In addition to the new design, an MLI coating was added to the upper part of the FFTS GFRP outer structure, see Fig. 8.5(a). This new MLI is supposed to isolate

(a) MLI at warm structures   (b) MLI at outer ring
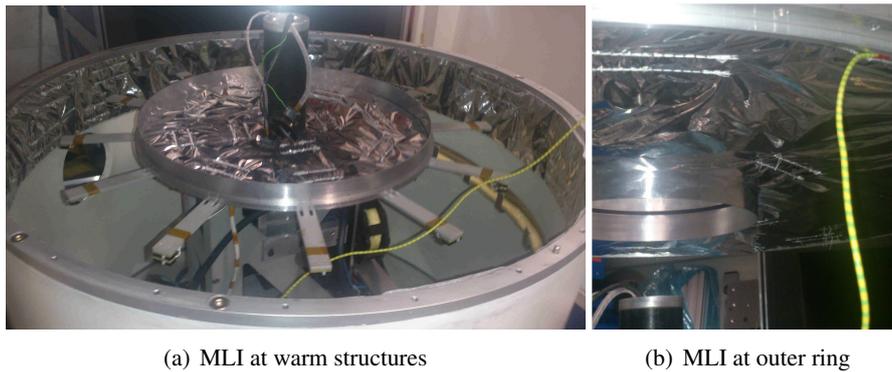
Figure 8.5: The MLI used in the new FFTS baffle system.

the upper part of the GFRP, which is directly connected to the cold ring, from the

ambient temperature photons. In this way the surface area of the GFRP structure is reduced and the photons that would have been absorbed by the "cold" part of the GFRP are mainly reflected and kept in the ambient part.

8.3 Final Cooldown in Cologne

Presented here is the final result of the cooldown tests with the new baffle in Cologne. Due to the tight schedule it is very probable that no tests will be done at MPIA before delivery to LBT.

8.3.1 Test Setup

For the cooldowns in Cologne four aluminum attachments were used to connect the cold plate of the cryostat and the cold ring of the FFTS, see Fig. 8.6(a) and (c). The design takes into account the form of the flange of the FFTS to achieve

(a) Cryostat coldplate   (b) FFTS closed from top

(c) FFTS in cryostat
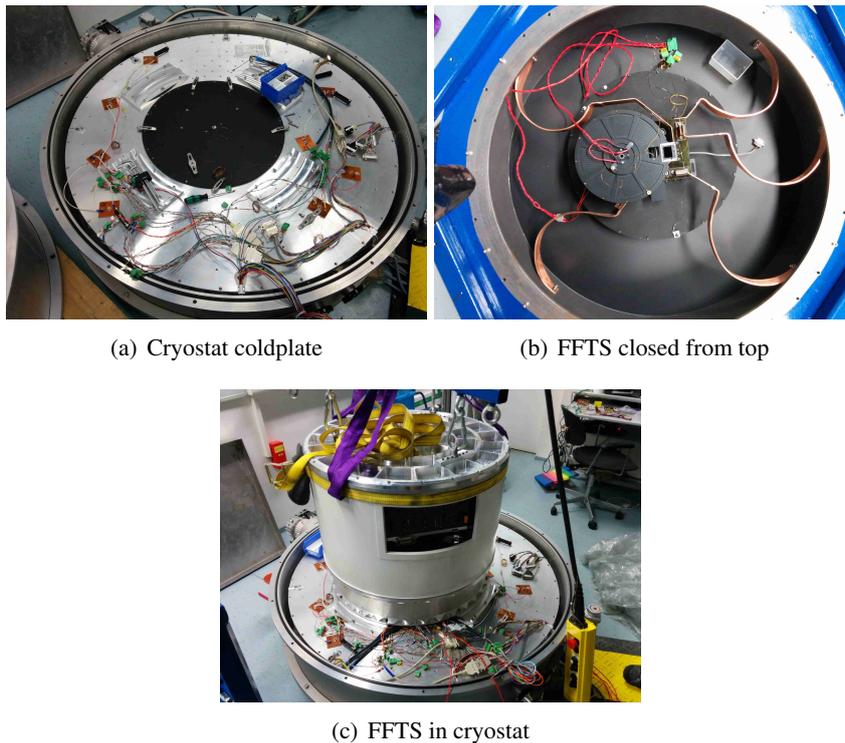
Figure 8.6: The final cooldown test setup in the cryostat in Cologne for the FFTS equipped with the new simplified baffle.

the best possible thermal conduction. Additionally, a black aluminum plate was screwed to the cold plate, see Fig. 8.6(a), to allow for a better photon absorption from baffle photons. Between cold plate and black aluminum plate a graphite mat was placed to guarantee a good thermal conduction. The warm part of the FFTS was fully equipped as seen in Fig. 8.5. In the cold part only the filter wheel motor is missing, see Fig. 8.6(b). It could not be built in because of height issues with the cryostat.

A final adjustment to the heating of the ambient part was done for the final test in Cologne. The heating resistor on the base plate was parallel split into a 68 Ω resistor on base plate and two 100 Ω resistors, in series, on the bottom part of the z-stage, see Fig. 8.7. Added up the resistors are a 50 Ω resistor to achieve the best energy output from the controller system. This assured a better heat distribution since the conduction from stage to stage was proven in earlier tests to be very low.

Twelve temperature sensors were built into the system to monitor the temperature behavior of the different components. These are attached to:

- One sensor on the baseplate, this sensor is also used to control the ambient heaters.

- Three sensors in total for x-, y-, and z-stage.

- One sensor on the anodized side of the cold baffle, see Fig. 8.6(b).

- Two sensors at the filter wheel (at motor flange and housing, see Fig. 8.6(b)).

- One sensor at the center of the black cold plate, see Fig. 8.6(a).

- Two sensors at the outer wall of the cold ring. One at the connection point to the GFRP structure and one at the connection point to the aluminum attachments.

- One sensor on the aluminum attachments.

- And one sensor at the lower part of the cryostat tank.

Four additional sensors were attached to a heating system for the cryostat which are not of use for this analysis. The temperature control was carried out with the temperature controller LakeShore Model 331.

8.3.2 Results and Discussion

The result of the final FFTS cooldown in Cologne is very satisfactory.

(a) Baseplate resistor   (b) z-stage resistors
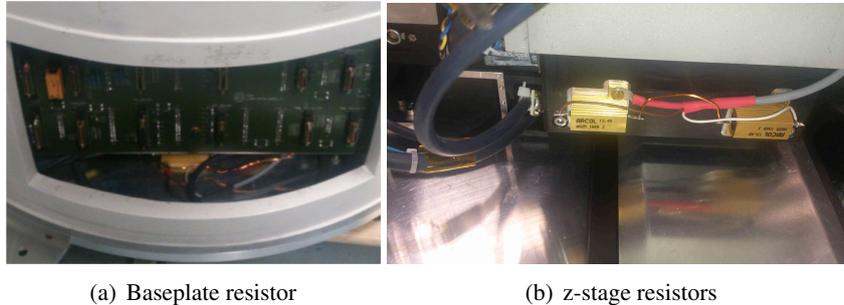
Figure 8.7: The resistors that keep the ambient temperature part warm.

The First Hours

The temperature behavior for the first 18 hours of the cooldown is shown in Fig. 8.8. After approximately three hours of filling with liquid nitrogen the tank of the cryostat was full and below 80 K. The aluminum attachments follow at about 80 K after $\approx$ 5 h. The black cold plate is at about the same temperature after $\approx$ 7 h. The cold ring reaches a temperature of $\leq$ 90 K after $\approx$ 7 h. Baffle and filter wheel need $\approx$ 11 h to reach a stable temperature of $<$ 100 K. After $\approx$ 5 h base plate and stages reach the critial 290 K temperature and the temperature control turns on. All subsystems behave in an expected manner.

The initial setting for the temperature control was set to linear interpolation by a periodic power output to the heater. From the base plate temperature plot it is clear that it is an easy task for the heater to keep the base plate at $\approx$ 290$\pm$1.5 K. The x-stage is kept warm at $\approx$ 288 K oscillating with $\pm$1 K. After 18 h the y-stage converges to a temperature of $\approx$ 280 K. The z-stage shows strong temperature variations due to the two attached heaters but oscillates periodically at 287 $\pm$ 4 K after 18 h.

The Last Hours

The last 7 hours of the $\approx$ 60 h cooldown and the beginning of warming up after the tank is empty are shown in Fig. 8.9. The tank temperature sensor stays below 80 K at all times as long as there is liquid nitrogen inside. The components directly attached to the cryostat cold plate, e.g., aluminum attachments, show a very slow increase in temperature. This is a normal behavior since the liquid nitrogen in the tank is getting lower and the thermal conduction via the copper cylinders, which connect to the cold plate, is getting slightly worse due to the in-
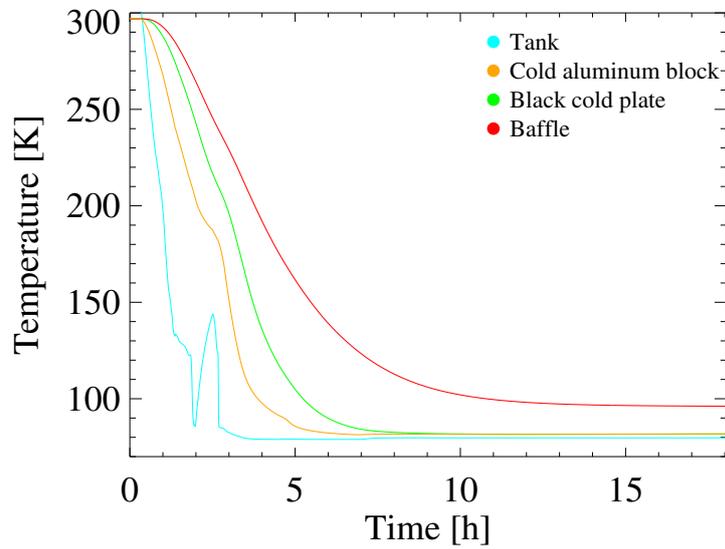
(a)
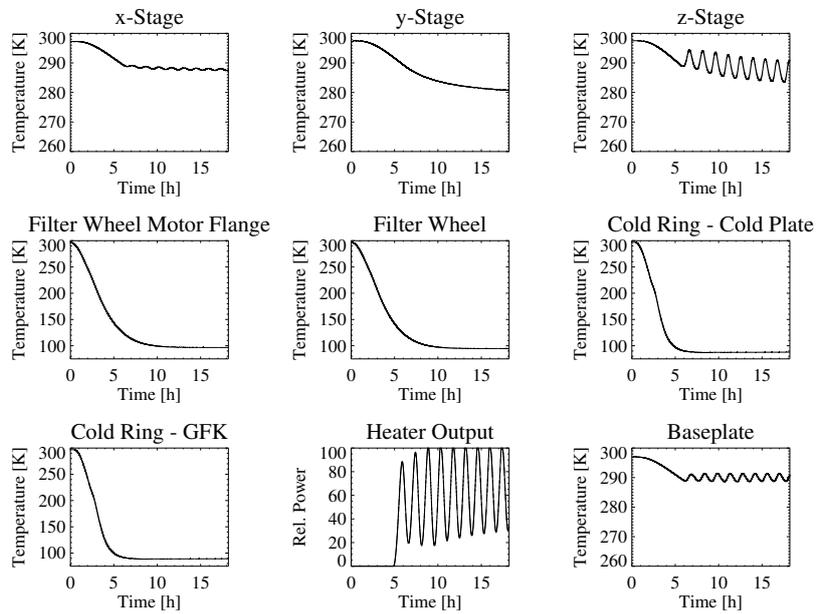
(b)

Figure 8.8: The final cooldown temperature plots and heater behavior over the first 18 hours. For details see text.
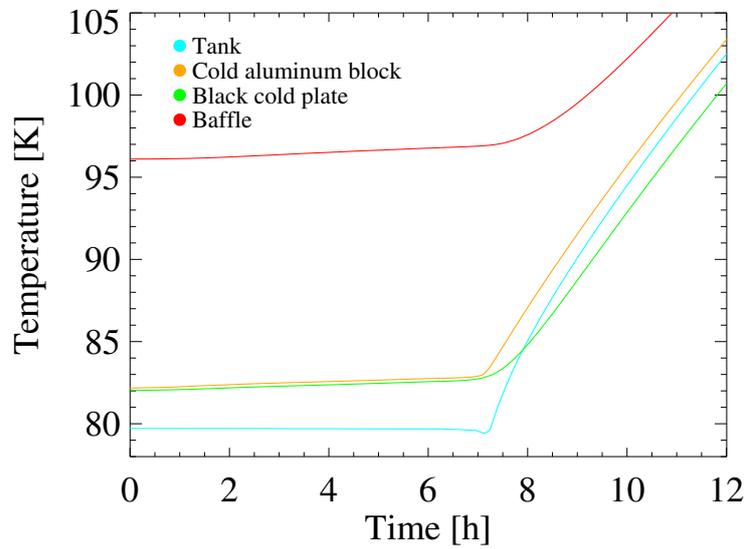
(a)
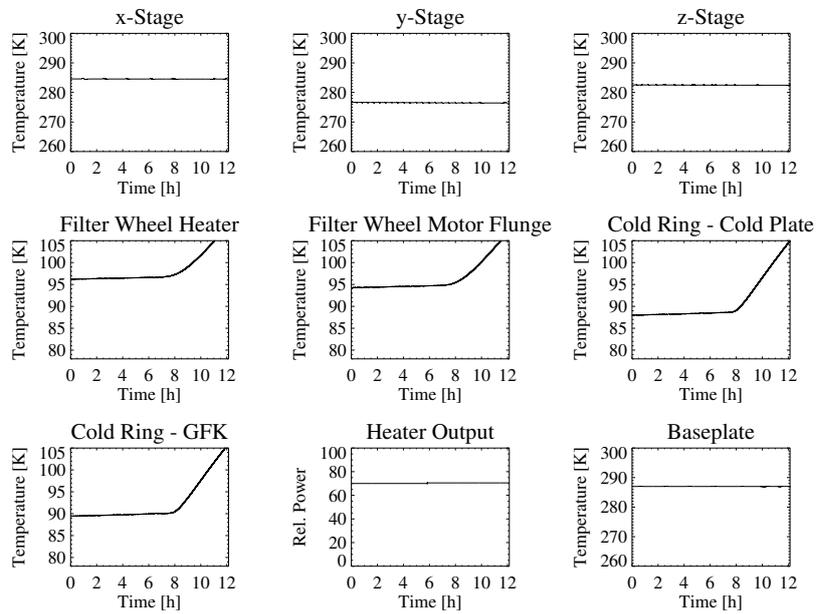
(b)

Figure 8.9: Temperature plots and heater behavior of the final cooldown over the last twelve hours. For details see text.

creasing length over which the gradient is built up[3]. The same effect is observed in components that are attached further down the conduction chain, e.g., baffle, but gradually later in time.

To stop the oscillation the Proportional Integral Derivative (PID) control[4] was turned on. The oscillation stopped and the subsystems were brought to constant temperature values. The base plate is at 287 K with a constant power output of about 70% of the heater. Giving the PID control more time or better initial settings will lead to a better control to 290 K on the base plate. The moving stages are all about 273 K with a temperature for the x-stage of 284.5 K, 276.5 K for y-stage, and 282.5 K for z-stage. The y-stage has the lowest temperature, due to the afore mentioned poor conduction between the stages.

The cold subsystems are all well below 110 K. Before the tank is empty the photon shield baffle is at $\leq$ 97 K, as is the filter wheel housing. The two cold ring sensors are below 90 K. Hence, all cold system parts tested here are within the requirements.

8.4 Summary

The FFTS baffle system was redesigned from a disk-in-disk system to a simple photon shield system. The disk-in-disk system ensured a large FFTS correction area but had the drawback that no heat conduction could be applied to it for cooling. The main cooling mechanism was radiation, which becomes ineffective with lower temperature due to its T^4 dependency. Therefore, during an imperfect cooldown in Heidelberg the baffle stayed too warm. Due to a tight schedule at the LINC-NIRVANA cryostat in Heidelberg there was not sufficient time to try and improve the cooling hence it was decided to redesign the baffle system. The new baffle system can be directly attached to the cold ring to ensure a fast cooldown. The warm part of the FFTS is efficiently shielded so that heat dissipation to

---

[3] The heat flow rate of a solid body is proportional to the cross-sectional surface area A and anti proportional to the length l. For two endpoints at constant temperature it is defined as Fourier's law

$$\dot{Q} = -\alpha \frac{A}{l} \Delta T,$$

with $\dot{Q}$ heat transfer per time, thermal conductivity α, cross-sectional surface area A, distance between the endpoints l and difference between the two temperatures ΔT.

[4] The controller finds the best fit power output by analyzing the error ϵ defined as the difference of setpoint temperature and feedback reading. The heater output P_H is then calculated from

$$P_H = P\left(\epsilon + I \int \epsilon \, dt + D \frac{d\epsilon}{dt}\right),$$

with a proportional P, an integral I, and a derivative D setting.

the cryogenic part is kept low and a heating system with 3 resistors can ensure the needed ambient temperature. The new solid baffle has an FFTS correcting area to $45'' \times 45''$ which is more than the $30'' \times 30''$ limitation due to telescope uncertainties.

The FFTS was successfully delivered to Heidelberg and is awaiting its implementation into the LINC-NIRVANA system. Additionally, the whole LINC-NIRVANA system has passed the preliminary acceptance Europe by the LBT Observatory with a number of tasks to be fulfilled before shipment.

Back matter

Acronyms

AGN Active Galactic Nucleus.

ALMA Atacama Large Millimeter/Sub-millimeter Array.

AO Adaptive Optics.

BH Black Hole.

BLR Broad-Line Region.

BLRG Broad-Line Radio Galaxy.

BPT Baldwin, Phillips & Terlevich.

ESO European Southern Observatory.

EW Equivalent Width.

FFTS Fringe and Flexure Tracker.

FIR Far-Infrared.

FOV Field Of View.

FWHM Full Width at Half Maximum.

GFRP Glass Fiber Reinforced Plastics.

HST Hubble Space Telescope.

IDL Interactive Data Language.

IFS Integral Field Spectrograph.

IMF Initial Mass Function.

IRAM Institut de Radioastronomie Millimétrique.

ISM InterStellar Medium.

LBT Large Binocular Telescope.

LINC-NIRVANA LBT INterferometric Camera and the NIR/Visible Adaptive iNterferometer for Astronomy.

LINER Low Ionization Nuclear Emission Region.

LLAGN Low-Luminosity AGN.

LOSV Line-Of-Sight Velocity.

MCAO Multi-Conjugate Adaptive Optics.

MoCon Motion Control.

MPIA Max Planck Institut für Astronomie.

NIR Near-Infrared.

NLR Nroad-Line Region.

NLRG Narrow-Line Radio Galaxy.

NUGA Nuclei of Galaxies.

PdBI Plateau de Bure Interferometer.

PDR PhotoDissociation Region.

PID Proportional Integral Derivative.

QSO Quasi Stellar Object.

Quasar Quasi Stellar Radio source.

SED Spectral Energy Distribution.

SFR Star Formation Rate.

SgrA* Sagittarius A*.

SINFONI Spectrograph for INtegral Field Observation in the Near Infrared.

SMBH Super Massive Black Hole.

SNR SuperNova Rate.

SVD Stellar Velocity Dispersion.

UM Unified Model.

UV UltraViolet.

VLBI Very Long Baseline Interferometer.

VLT Very Large Telescope.

Bibliography

Agüero, E. L., Díaz, R. J., & Bajaja, E. 2004, Astronomy and Astrophysics, 414, 453

Alloin, D., Pelat, D., Phillips, M., & Whittle, M. 1985, The Astrophysical Journal, 288, 205

Alonso-Herrero, A., Rieke, G. H., Rieke, M. J., & Kelly, D. M. 2003, The Astronomical Journal, 125, 1210

Alonso-Herrero, A., Rieke, M. J., Rieke, G. H., & Ruiz, M. 1997, The Astrophysical Journal, 482, 747

Antonucci, R. R. J. & Miller, J. S. 1985, The Astrophysical Journal, 297, 621

Bajaja, E., Wielebinski, R., Reuter, H.-P., Harnett, J. I., & Hummel, E. 1995, Astronomy and Astrophysics Supplement Series, 114, 147

Barbosa, F. K. B., Storchi-Bergmann, T., Cid Fernandes, R., Winge, C., & Schmitt, H. 2006, Monthly Notices of the Royal Astronomical Society, 371, 170

Baribaud, T., Alloin, D., Glass, I., & Pelat, D. 1992, Astronomy and Astrophysics, 256, 375

Barteldrees, A. & Dettmar, R.-J. 1994, Astronomy and Astrophysics Supplement Series, 103, 475

Beckers, J. M. 1990, in Society of Photo-Optical Instrumentation Engineers (SPIE) Conference Series, Vol. 1236, Advanced Technology Optical Telescopes IV, ed. L. D. Barr, 379–389

Bedregal, A. G., Colina, L., Alonso-Herrero, A., & Arribas, S. 2009, The Astrophysical Journal, 698, 1852

Bell, E. F. & de Jong, R. S. 2001, The Astrophysical Journal, 550, 212

Bentz, M. C., Peterson, B. M., Netzer, H., Pogge, R. W., & Vestergaard, M. 2009, The Astrophysical Journal, 697, 160

Bentz, M. C., Peterson, B. M., Pogge, R. W., Vestergaard, M., & Onken, C. A. 2006, The Astrophysical Journal, 644, 133

Bertram, T. 2007, PhD thesis, University of Cologne

Bertram, T., Arcidiacono, C., Straubmeier, C., et al. 2006, in Society of Photo-Optical Instrumentation Engineers (SPIE) Conference Series, Vol. 6268, Society of Photo-Optical Instrumentation Engineers (SPIE) Conference Series, 3

Bertram, T., Eckart, A., Lindhorst, B., et al. 2008, in , 701327

Bizyaev, D. & Mitronova, S. 2002, Astronomy and Astrophysics, 389, 795

Bizyaev, D. & Mitronova, S. 2009, The Astrophysical Journal, 702, 1567

Black, J. H. & van Dishoeck, E. F. 1987, The Astrophysical Journal, 322, 412

Blandford, R. D. & McKee, C. F. 1982, The Astrophysical Journal, 255, 419

Bolatto, A. D., Wolfire, M., & Leroy, A. K. 2013, Annual Review of Astronomy and Astrophysics, 51, 207

Bonnet, H., Abuter, R., Baker, A., et al. 2004, The Messenger, 117, 17

Boone, F., Baker, A. J., Schinnerer, E., et al. 2007, Astronomy and Astrophysics, 471, 113

Brand, P. W. J. L., Toner, M. P., Geballe, T. R., et al. 1989, Monthly Notices of the Royal Astronomical Society, 236, 929

Burtscher, L., Meisenheimer, K., Tristram, K. R. W., et al. 2013, Astronomy and Astrophysics, 558, A149

Busch, G., Smajić, S., Scharwächter, J., et al. 2015, Astronomy and Astrophysics, 575, A128

Busch, G., Zuther, J., Valencia-S., M., et al. 2014, Astronomy and Astrophysics, 561, 140

Buta, R. 1986, The Astrophysical Journal Supplement Series, 61, 631

Buta, R., Ryder, S. D., Madsen, G. J., et al. 2001, The Astronomical Journal, 121, 225

Buta, R. J., Sheth, K., Regan, M., et al. 2010, The Astrophysical Journal Supplement Series, 190, 147

Calzetti, D. 1997, The Astronomical Journal, 113, 162

Cardelli, J. A., Clayton, G. C., & Mathis, J. S. 1989, The Astrophysical Journal, 345, 245

Casasola, V., Combes, F., García-Burillo, S., et al. 2008, Astronomy and Astrophysics, 490, 61

Casasola, V., Hunt, L. K., Combes, F., et al. 2010, Astronomy and Astrophysics, 510, 52

Cid Fernandes, R., Gu, Q., Melnick, J., et al. 2004, Monthly Notices of the Royal Astronomical Society, 355, 273

Cid Fernandes, R., Storchi-Bergmann, T., & Schmitt, H. R. 1998, Monthly Notices of the Royal Astronomical Society, 297, 579

Combes, F., Baker, A. J., Schinnerer, E., et al. 2009, Astronomy and Astrophysics, 503, 73

Combes, F., García-Burillo, S., Boone, F., et al. 2004, Astronomy and Astrophysics, 414, 857

Combes, F., García-Burillo, S., Casasola, V., et al. 2013, Astronomy and Astrophysics, 558, 124

Combes, F., García-Burillo, S., Casasola, V., et al. 2014, Astronomy and Astrophysics, 565, A97

Comerón, S., Knapen, J. H., Beckman, J. E., et al. 2010, Monthly Notices of the Royal Astronomical Society, 402, 2462

Comte, G. & Duquennoy, A. 1982, Astronomy and Astrophysics, 114, 7

Corbelli, E. & Salucci, P. 2000, Monthly Notices of the Royal Astronomical Society, 311, 441

Dale, D. A., Roussel, H., Contursi, A., et al. 2004, The Astrophysical Journal, 601, 813

Davies, R. I. 2007, Monthly Notices of the Royal Astronomical Society, 375, 1099

Davies, R. I., Maciejewski, W., Hicks, E. K. S., et al. 2014, The Astrophysical Journal, 792, 101

Davies, R. I., Müller Sánchez, F., Genzel, R., et al. 2007, ApJ, 671, 1388

Davies, R. I., Sternberg, A., Lehnert, M., & Tacconi-Garman, L. E. 2003, The Astrophysical Journal, 597, 907

Davies, R. I., Sternberg, A., Lehnert, M. D., & Tacconi-Garman, L. E. 2005, The Astrophysical Journal, 633, 105

Davies, R. I., Thomas, J., Genzel, R., et al. 2006, The Astrophysical Journal, 646, 754

Dibai, E. A. 1977, Soviet Astronomy Letters, 3, 1

Dopita, M. A. & Sutherland, R. S. 2003, Astrophysics of the diffuse universe

Draine, B. T. & McKee, C. F. 1993, Annual Review of Astronomy and Astrophysics, 31, 373

Draine, B. T. & Woods, D. T. 1990, The Astrophysical Journal, 363, 464

Eckart, A. & Genzel, R. 1996, Nature, 383, 415

Eckart, A., Genzel, R., Ott, T., & Schödel, R. 2002, Monthly Notices of the Royal Astronomical Society, 331, 917

Eckart, A., Schinnerer, E., & Staguhn, J. 2001, in IAU Symposium, Vol. 205, Galaxies and their Constituents at the Highest Angular Resolutions, ed. R. T. Schilizzi, 344

Eckart, A., Schinnerer, E., & Tacconi, L. 2000, New Astronomy Reviews, 44, 523

Eisenhauer, F., Abuter, R., Bickert, K., et al. 2003, in Society of Photo-Optical Instrumentation Engineers (SPIE) Conference Series, Vol. 4841, Society of Photo-Optical Instrumentation Engineers (SPIE) Conference Series, ed. M. Iye & A. F. M. Moorwood, 1548–1561

Emsellem, E., Greusard, D., Combes, F., et al. 2001, Astronomy and Astrophysics, 368, 52

Esquej, P., Alonso-Herrero, A., González-Martín, O., et al. 2014, The Astrophysical Journal, 780, 86

Fabian, A. C. 2012, Annual Review of Astronomy and Astrophysics, 50, 455

Falcón-Barroso, J., Bacon, R., Bureau, M., et al. 2006, Monthly Notices of the Royal Astronomical Society, 369, 529

Ferrarese, L. & Merritt, D. 2000, The Astrophysical Journal Letters, 539, L9

Fischer, S., Iserlohe, C., Zuther, J., et al. 2006, Astronomy and Astrophysics, 452, 827

Fisher, D. B. & Drory, N. 2010, The Astrophysical Journal, 716, 942

Forbes, D. A. & Ward, M. J. 1993, The Astrophysical Journal, 416, 150

Fried, D. L. 1965, Journal of the Optical Society of America (1917-1983), 55, 1427

García-Burillo, S., Combes, F., Eckart, A., et al. 2003, in Astronomical Society of the Pacific Conference Series, Vol. 290, Active Galactic Nuclei: From Central Engine to Host Galaxy, ed. S. Collin, F. Combes, & I. Shlosman, 423

García-Burillo, S., Combes, F., Hunt, L. K., et al. 2003, Astronomy and Astrophysics, 407, 485

García-Burillo, S., Combes, F., Schinnerer, E., Boone, F., & Hunt, L. K. 2005, Astronomy and Astrophysics, 441, 1011

García-Burillo, S., Combes, F., Usero, A., et al. 2014, Astronomy and Astrophysics, 567, 125

García-Burillo, S., Fernández-García, S., Combes, F., et al. 2009, Astronomy and Astrophysics, 496, 85

Gavazzi, G. 1993, The Astrophysical Journal, 419, 469

Gebhardt, K., Bender, R., Bower, G., et al. 2000, The Astrophysical Journal Letters, 539, L13

Genzel, R., Eckart, A., Ott, T., & Eisenhauer, F. 1997, Monthly Notices of the Royal Astronomical Society, 291, 219

Graham, A. W. & Driver, S. P. 2005, Publications of the Astronomical Society of Australia, 22, 118

Graham, A. W. & Driver, S. P. 2007, The Astrophysical Journal, 655, 77

Graham, A. W. & Scott, N. 2013, The Astrophysical Journal, 764, 151

Greene, J. E. & Ho, L. C. 2005, The Astrophysical Journal, 630, 122

Gültekin, K., Richstone, D. O., Gebhardt, K., et al. 2009, The Astrophysical Journal, 698, 198

Herbst, T. M., Ragazzoni, R., Eckart, A., & Weigelt, G. 2004, in Society of Photo-Optical Instrumentation Engineers (SPIE) Conference Series, Vol. 5492, Ground-based Instrumentation for Astronomy, ed. A. F. M. Moorwood & M. Iye, 1045–1052

Ho, L. C. 2008, Annual Review of Astronomy and Astrophysics, 46, 475

Ho, L. C. 2009, The Astrophysical Journal, 699, 626

Hopkins, P. F. & Quataert, E. 2011a, Monthly Notices of the Royal Astronomical Society, 415, 1027

Hopkins, P. F. & Quataert, E. 2011b, Monthly Notices of the Royal Astronomical Society, 411, L61

Hopkins, P. F., Quataert, E., & Murray, N. 2011, Monthly Notices of the Royal Astronomical Society, 417, 950

Howell, S. B. 2000, Handbook of CCD Astronomy

Hunt, L. K., Combes, F., García-Burillo, S., et al. 2008, Astronomy and Astrophysics, 482, 133

Hutchings, J. B. & Neff, S. G. 1992, The Astronomical Journal, 104, 1

Häring, N. & Rix, H.-W. 2004, The Astrophysical Journal Letters, 604, L89

Irwin, J. A., Wilson, C. D., Wiegert, T., et al. 2011, Monthly Notices of the Royal Astronomical Society, 410, 1423

Ishibashi, W. & Fabian, A. C. 2012, Monthly Notices of the Royal Astronomical Society, 427, 2998

Israel, F. P., Tilanus, R. P. J., & Baas, F. 2006, Astronomy and Astrophysics, 445, 907

Jungwiert, B., Combes, F., & Axon, D. J. 1997, Astronomy and Astrophysics Supplement Series, 125, 479

Kaspi, S., Smith, P. S., Netzer, H., et al. 2000, The Astrophysical Journal, 533, 631

Kawamuro, T., Ueda, Y., Tazaki, F., & Terashima, Y. 2013, The Astrophysical Journal, 770, 157

Kennicutt, R. C. & Evans, N. J. 2012, Annual Review of Astronomy and Astrophysics, 50, 531

Kennicutt, Jr., R. C. 1998, The Astrophysical Journal, 498, 541

Kilborn, V. A., Koribalski, B. S., Forbes, D. A., Barnes, D. G., & Musgrave, R. C. 2005, Monthly Notices of the Royal Astronomical Society, 356, 77

Kim, D., Im, M., & Kim, M. 2010, The Astrophysical Journal, 724, 386

Koribalski, B. S., Staveley-Smith, L., Kilborn, V. A., et al. 2004, The Astronomical Journal, 128, 16

Kormendy, J. & Ho, L. C. 2013, Annual Review of Astronomy and Astrophysics, 51, 511

Krips, M., Eckart, A., Neri, R., et al. 2005, Astronomy and Astrophysics, 442, 479

Kriss, G. A., Hartig, G. F., Armus, L., et al. 1991, The Astrophysical Journal Letters, 377, L13

Larkin, J. E., Armus, L., Knop, R. A., Soifer, B. T., & Matthews, K. 1998, The Astrophysical Journal Supplement Series, 114, 59

Leitherer, C., Schaerer, D., Goldader, J. D., et al. 1999, The Astrophysical Journal Supplement Series, 123, 3

Lester, D. F., Harvey, P. M., & Carr, J. 1988, The Astrophysical Journal, 329, 641

Levenson, N. A., Radomski, J. T., Packham, C., et al. 2009, The Astrophysical Journal, 703, 390

Lindt-Krieg, E., Eckart, A., Neri, R., et al. 2008, Astronomy and Astrophysics, 479, 377

Liu, J.-F. & Bregman, J. N. 2005, The Astrophysical Journal Supplement Series, 157, 59

Läsker, R., Ferrarese, L., van de Ven, G., & Shankar, F. 2014, The Astrophysical Journal, 780, 70

Magorrian, J., Tremaine, S., Richstone, D., et al. 1998, AJ, 115, 2285

Maiolino, R., Rieke, G. H., & Rieke, M. J. 1996, The Astronomical Journal, 111, 537

Maloney, P. R., Hollenbach, D. J., & Tielens, A. G. G. M. 1996, The Astrophysical Journal, 466, 561

Mannucci, F., Basile, F., Poggianti, B. M., et al. 2001, Monthly Notices of the Royal Astronomical Society, 326, 745

Maoz, D., Filippenko, A. V., Ho, L. C., et al. 1996, The Astrophysical Journal Supplement Series, 107, 215

Marconi, A. & Hunt, L. K. 2003, The Astrophysical Journal Letters, 589, L21

Mauersberger, R., Henkel, C., Walsh, W., & Schulz, A. 1999, Astronomy and Astrophysics, 341, 256

Mazzalay, X., Saglia, R. P., Erwin, P., et al. 2013, Monthly Notices of the Royal Astronomical Society, 428, 2389

McMullin, J. P., Waters, B., Schiebel, D., Young, W., & Golap, K. 2007, in Astronomical Society of the Pacific Conference Series, Vol. 376, Astronomical Data Analysis Software and Systems XVI, ed. R. A. Shaw, F. Hill, & D. J. Bell, 127

Mihalas, D. & Binney, J. 1981, Galactic astronomy: Structure and kinematics /2nd edition/

Mouri, H. 1994, The Astrophysical Journal, 427, 777

Mulchaey, J. S. & Regan, M. W. 1997, The Astrophysical Journal Letters, 482, L135

Muraoka, K., Kohno, K., Tosaki, T., et al. 2007, Publications of the Astronomical Society of Japan, 59, 43

Netzer, H. 1977, Monthly Notices of the Royal Astronomical Society, 181, 89P

Nussbaumer, H. & Storey, P. J. 1988, Astronomy and Astrophysics, 193, 327

168

Origlia, L., Moorwood, A. F. M., & Oliva, E. 1993, Astronomy and Astrophysics, 280, 536

Osterbrock, D. E. & Ferland, G. J. 2006, Astrophysics of gaseous nebulae and active galactic nuclei

Panuzzo, P., Bressan, A., Granato, G. L., Silva, L., & Danese, L. 2003, Astronomy and Astrophysics, 409, 99

Peeples, M. S. & Martini, P. 2006, The Astrophysical Journal, 652, 1097

Peterson, B. M. 1997, An Introduction to Active Galactic Nuclei

Plummer, H. C. 1911, Monthly Notices of the Royal Astronomical Society, 71, 460

Rauch, C., Eckart, A., Horrobin, M., et al. 2012, in Society of Photo-Optical Instrumentation Engineers (SPIE) Conference Series, Vol. 8445, Society of Photo-Optical Instrumentation Engineers (SPIE) Conference Series, 38

Reunanen, J., Kotilainen, J. K., & Prieto, M. A. 2002, Monthly Notices of the Royal Astronomical Society, 331, 154

Riffel, R. A., Storchi-Bergmann, T., & Winge, C. 2013, Monthly Notices of the Royal Astronomical Society, 430, 2249

Riffel, R. A., Storchi-Bergmann, T., Winge, C., et al. 2008, Monthly Notices of the Royal Astronomical Society, 385, 1129

Riffel, R. A., Vale, T. B., Storchi-Bergmann, T., & McGregor, P. J. 2014, Monthly Notices of the Royal Astronomical Society, 442, 656

Rodríguez-Ardila, A., Pastoriza, M. G., Viegas, S., Sigut, T. A. A., & Pradhan, A. K. 2004, A&A, 425, 457

Rodríguez-Ardila, A., Riffel, R., & Pastoriza, M. G. 2005, MNRAS, 364, 1041

Rosenberg, M. J. F., van der Werf, P. P., & Israel, F. P. 2012, Astronomy and Astrophysics, 540, 116

Ryder, S. D., Buta, R. J., Toledo, H., et al. 1996, The Astrophysical Journal, 460, 665

Schmidt, M. & Green, R. F. 1983, The Astrophysical Journal, 269, 352

Schmitt, H. R. & Kinney, A. L. 1996, The Astrophysical Journal, 463, 498

Schuermann, H. 2005, Konstruieren mit Faser-Kunststoff-Verbunden (Springer)

Schödel, R., Merritt, D., & Eckart, A. 2009, Astronomy and Astrophysics, 502, 91

Schödel, R., Ott, T., Genzel, R., et al. 2002, Nature, 419, 694

Scoville, N. Z., Hall, D. N. B., Ridgway, S. T., & Kleinmann, S. G. 1982, The Astrophysical Journal, 253, 136

Sheth, K., Vogel, S. N., Regan, M. W., Thornley, M. D., & Teuben, P. J. 2005, The Astrophysical Journal, 632, 217

Shuder, J. M. 1981, The Astrophysical Journal, 244, 12

Silk, J. & Rees, M. J. 1998, Astronomy and Astrophysics, 331, L1

Smajic, S., Eckart, A., Horrobin, M., et al. 2012, in Society of Photo-Optical Instrumentation Engineers (SPIE) Conference Series, Vol. 8445, Society of Photo-Optical Instrumentation Engineers (SPIE) Conference Series, 27

Smajić, S., Moser, L., Eckart, A., et al. 2015, Astronomy and Astrophysics, 583, A104

Smajić, S., Moser, L., Eckart, A., et al. 2014, Astronomy and Astrophysics, 567, A119

Smajić, S., Fischer, S., Zuther, J., & Eckart, A. 2012, Astronomy and Astrophysics, 544, 105

Sofue, Y. & Rubin, V. 2001, Annual Review of Astronomy and Astrophysics, 39, 137

Solomon, P. M. & Barrett, J. W. 1991, in IAU Symposium, Vol. 146, Dynamics of Galaxies and Their Molecular Cloud Distributions, ed. F. Combes & F. Casoli, 235

Sosa-Brito, R. M., Tacconi-Garman, L. E., Lehnert, M. D., & Gallimore, J. F. 2001, The Astrophysical Journal Supplement Series, 136, 61

Staguhn, J., Schinnerer, E., & Eckart, A. 2001, in IAU Symposium, Vol. 205, Galaxies and their Constituents at the Highest Angular Resolutions, ed. R. T. Schilizzi, 340

Sternberg, A. & Dalgarno, A. 1989, The Astrophysical Journal, 338, 197

Sternberg, A. & Dalgarno, A. 1995, The Astrophysical Journal Supplement Series, 99, 565

Sternberg, A. & Neufeld, D. A. 1999, The Astrophysical Journal, 516, 371

Sánchez-Blázquez, P., Ocvirk, P., Gibson, B. K., Pérez, I., & Peletier, R. F. 2011, Monthly Notices of the Royal Astronomical Society, 415, 709

Tilanus, R. P. J., Tacconi, L. J., Sutton, E. C., et al. 1991, The Astrophysical Journal, 376, 500

Tine, S., Lepp, S., Gredel, R., & Dalgarno, A. 1997, The Astrophysical Journal, 481, 282

Traub, W. A. 1986, Applied Optics, 25, 528

Tremaine, S., Gebhardt, K., Bender, R., et al. 2002, ApJ, 574, 740

Tristram, K. R. W., Burtscher, L., Jaffe, W., et al. 2014, Astronomy and Astrophysics, 563, A82

Turner, E. L. & Ostriker, J. P. 1977, The Astrophysical Journal, 217, 24

Valencia-S., M., Zuther, J., Eckart, A., et al. 2012, Astronomy and Astrophysics, 544, 129

van der Laan, T. P. R., Schinnerer, E., Boone, F., et al. 2011, Astronomy and Astrophysics, 529, 45

Veron-Cetty, M.-P. & Veron, P. 1986, Astronomy and Astrophysics Supplement Series, 65, 241

Wada, K. & Tomisaka, K. 2005, The Astrophysical Journal, 619, 93

Wandel, A., Peterson, B. M., & Malkan, M. A. 1999, The Astrophysical Journal, 526, 579

Wilson, C. D., Warren, B. E., Israel, F. P., et al. 2009, The Astrophysical Journal, 693, 1736

Winge, C., Riffel, R. A., & Storchi-Bergmann, T. 2009, The Astrophysical Journal Supplement Series, 185, 186

Wolniewicz, L., Simbotin, I., & Dalgarno, A. 1998, The Astrophysical Journal Supplement Series, 115, 293

Woo, J.-H. & Urry, C. M. 2002, The Astrophysical Journal, 579, 530

Wozniak, H., Friedli, D., Martinet, L., Martin, P., & Bratschi, P. 1995, Astronomy and Astrophysics Supplement Series, 111, 115

Zuther, J., Eckart, A., Bertram, T., et al. 2012, in Society of Photo-Optical Instrumentation Engineers (SPIE) Conference Series, Vol. 8445, Society of Photo-Optical Instrumentation Engineers (SPIE) Conference Series, 36

Zuther, J., Iserlohe, C., Pott, J.-U., et al. 2007, Astronomy and Astrophysics, 466, 451

List of Figures

174

List of Tables

Danksagung

Acknowledgments, well... well..., lets see what we can find here.

First and foremost, I thank Prof. Dr. Andreas Eckart for making it possible to study observational astronomy and take part in building an instrument, which will perform thousands of observations for other astronomers thus help us understand the "world" a little more. His daily morning tour conversations, on and off topic, are a great way to start the working-day.

My gratitude goes also to Prof. Dr. Anton Zensus for refereeing my thesis and to Prof. Dr. Bülent Tezkan for being the chairman of my thesis defense committee.

Additional thanks go to Dr. Sebastian Fischer and Dr. Jens Zuther for the guidance a beginner needs in dealing with raw data. I thank Dr. Matthew Horrobin for tips and tricks in dealing with compromised data and also Dr. Steffen Rost for great, exciting, and sometimes frustrating work in the laboratory.

I thank the whole aegroup for a great working atmosphere. To mention a few: Dr. Macarena García-Marín, my office colleague, that IDL Å symbol..., Lydia Moser, all these molecular transitions..., Marzieh Parsa, break time..., Imke Wank, the poor LN baffle..., Dr. Mónica Valencia-S., these blobs..., Gerold Busch, the LLQSO host..., and all the other former and current members of the group.

Ein sehr großer Dank geht an die Feinmechanik Werkstatt, die sich immer Zeit genommen haben um mit mir geduldig die Zeichnungen zu besprechen und bei eiligen Aufträgen immer bereit waren etwas dazwischen zu schieben. Ebenso ein großer Dank geht an die Sekretärinnen, die einem die Verwaltungsarbeit sehr einfach und angenehm gemacht haben.

Beste Grüße an meine Freunde, allen voran Trick und Track, und an das Kommilitonen-Mensa-Team, gemeinsames mensen seit 2005.

Mein ganz besonderer Dank gebührt meiner Familie (nah und fern), insbesondere:

meinen Eltern, die immer alles dafür getan haben, dass ich und meine Schwester es einfach haben und uns in Allem unterstützt haben;

Hvala vam za sve što ste za nas učinili i što smo zajedno preživjeli i uživali, na primjer putovanja za BiH, od Audia 80 do Opela Vektre;

Armin und Anna, die mich die letzten 10 Jahre begleitet und unterstützt hat;

meiner Schwester, Nervensäge. . . haha;

und mit Sicherheit nicht zuletzt meinen Großeltern, für die Zeit, die mir mit Ihnen gegeben war und ist;

majki Vasvi, đedu Esadu, majki Subhi i đedu Hasibu.

Erklärung

Ich versichere, dass ich die von mir vorgelegte Dissertation selbständig angefertigt, die benutzten Quellen und Hilfsmittel vollständig angegeben und die Stellen der Arbeit – einschließlich Tabellen, Karten und Abbildungen –, die anderen Werken im Wortlaut oder dem Sinn nach entnommen sind, in jedem Einzelfall als Entlehnung kenntlich gemacht habe; dass diese Dissertation noch keiner anderen Fakultät oder Universität zur Prüfung vorgelegen hat; dass sie – abgesehen von unten angegebenen Teilpublikationen – noch nicht veröffentlicht worden ist sowie, dass ich eine solche Veröffentlichung vor Abschluss des Promotionsverfahrens nicht vornehmen werde. Die Bestimmungen dieser Promotionsordnung sind mir bekannt. Die von mir vorgelegte Dissertation ist von Prof. Dr. Andreas Eckart betreut worden.

Köln, den 11. Mai 2015

Teile der Dissertation sind in den folgenden Publikationen enthalten:

Smajić, S., Moser, L., Eckart, A., et al. 2015, Astronomy and Astrophysics, 583, A104

Smajić, S., Moser, L., Eckart, A., et al. 2014, Astronomy and Astrophysics, 567, A119

Horrobin, M., . . . , **Smajic, S.**, et al. 2014, SPIE, 9146, 91462G

Smajic, S., Eckart, A., Horrobin, M., et al. 2012, SPIE, 8445, 844527

Weitere Publikationen

Smajić, S., Fischer, S., Zuther, J., & Eckart, A. 2012, Astronomy and Astrophysics, 544, A105

Smajić, S., Fischer, S., Zuther, J., & Eckert, A. 2012, Journal of Physics Conference Series, 372, 012015

Smajic, S., Fischer, S., Valencia-S., M., Zuther, J., & Eckart, A. 2012, Proceedings of Nuclei of Seyfert galaxies and QSOs - Central engine & conditions of star formation (Seyfert 2012). 6-8 November, 2012. Max-Planck-Insitut für Radioastronomie (MPIfR), Bonn, Germany. id.9, 9

Busch, G., **Smajić, S.**, Scharwächter, J., et al. 2015, Astronomy and Astrophysics, 575, A128

Busch, G., **Smajić, S.**, Moser, L., et al. 2015, IAU Symposium, 309, 30

Valencia-S., ..., **Smajic, S.**, et al. 2015, The Astrophysical Journal, 800, 125

Valencia-S., M., Busch, G., **Smajić, S.**, et al. 2014, IAU Symposium, 304, 274

Eckart, A., ..., **Smajic, S.**, et al. 2014, The Astronomer's Telegram, 6285, 1

Rost, S., ..., **Smajic, S.**, et al. 2012, SPIE, 8445, 844539

Rauch, C., ..., **Smajić, S.**, et al. 2012, SPIE, 8445, 844538

Zuther, J., ..., **Smajic, S.**, et al. 2012, SPIE, 8445, 844536

Eckart, A., ..., **Smajic, S.**, et al. 2012, SPIE, 8445, 84451F

Fischer, S., **Smajic, S.**, Valencia-S, M., et al. 2012, Journal of Physics Conference Series, 372, 012057

Valencia-S, M., ..., **Smajic, S.**, et al. 2012, Journal of Physics Conference Series, 372, 012048

Valencia-S., ..., **Smajic, S.**, et al. 2012, Proceedings of Nuclei of Seyfert galaxies and QSOs - Central engine & conditions of star formation (Seyfert 2012). 6-8 November, 2012. Max-Planck-Insitut für Radioastronomie (MPIfR), Bonn, Germany. id.17, 17

Eckart, A., ..., **Smajic, S.**, et al. 2012, Proceedings of Nuclei of Seyfert galaxies and QSOs - Central engine & conditions of star formation (Seyfert 2012). 6-8 November, 2012. Max-Planck-Insitut für Radioastronomie (MPIfR), Bonn, Germany. id.4, 4

Tremou, E., ..., **Smajic, S.**, et al. 2010, SPIE, 7734, 773441

Horrobin, M., ..., **Smajic, S.**, et al. 2010, SPIE, 7734, 77341X

Rost, S., ..., **Smajic, S.**, et al. 2010, SPIE, 7734, 77341V